frontiers | Research Topics

Next generation in vitro models to study chronic pulmonary diseases

Edited by
Simon D. Pouwels, Alen Faiz and Emmanuel Twumasi Osei

Published in
Frontiers in Medicine
Frontiers in Oncology

FRONTIERS EBOOK COPYRIGHT STATEMENT

The copyright in the text of individual articles in this ebook is the property of their respective authors or their respective institutions or funders. The copyright in graphics and images within each article may be subject to copyright of other parties. In both cases this is subject to a license granted to Frontiers.

The compilation of articles constituting this ebook is the property of Frontiers.

Each article within this ebook, and the ebook itself, are published under the most recent version of the Creative Commons CC-BY licence. The version current at the date of publication of this ebook is CC-BY 4.0. If the CC-BY licence is updated, the licence granted by Frontiers is automatically updated to the new version.

When exercising any right under the CC-BY licence, Frontiers must be attributed as the original publisher of the article or ebook, as applicable.

Authors have the responsibility of ensuring that any graphics or other materials which are the property of others may be included in the CC-BY licence, but this should be checked before relying on the CC-BY licence to reproduce those materials. Any copyright notices relating to those materials must be complied with.

Copyright and source acknowledgement notices may not be removed and must be displayed in any copy, derivative work or partial copy which includes the elements in question.

All copyright, and all rights therein, are protected by national and international copyright laws. The above represents a summary only. For further information please read Frontiers' Conditions for Website Use and Copyright Statement, and the applicable CC-BY licence.

ISSN 1664-8714
ISBN 978-2-8325-4163-0
DOI 10.3389/978-2-8325-4163-0

About Frontiers

Frontiers is more than just an open access publisher of scholarly articles: it is a pioneering approach to the world of academia, radically improving the way scholarly research is managed. The grand vision of Frontiers is a world where all people have an equal opportunity to seek, share and generate knowledge. Frontiers provides immediate and permanent online open access to all its publications, but this alone is not enough to realize our grand goals.

Frontiers journal series

The Frontiers journal series is a multi-tier and interdisciplinary set of open-access, online journals, promising a paradigm shift from the current review, selection and dissemination processes in academic publishing. All Frontiers journals are driven by researchers for researchers; therefore, they constitute a service to the scholarly community. At the same time, the *Frontiers journal series* operates on a revolutionary invention, the tiered publishing system, initially addressing specific communities of scholars, and gradually climbing up to broader public understanding, thus serving the interests of the lay society, too.

Dedication to quality

Each Frontiers article is a landmark of the highest quality, thanks to genuinely collaborative interactions between authors and review editors, who include some of the world's best academicians. Research must be certified by peers before entering a stream of knowledge that may eventually reach the public - and shape society; therefore, Frontiers only applies the most rigorous and unbiased reviews. Frontiers revolutionizes research publishing by freely delivering the most outstanding research, evaluated with no bias from both the academic and social point of view. By applying the most advanced information technologies, Frontiers is catapulting scholarly publishing into a new generation.

What are Frontiers Research Topics?

Frontiers Research Topics are very popular trademarks of the *Frontiers journals series*: they are collections of at least ten articles, all centered on a particular subject. With their unique mix of varied contributions from Original Research to Review Articles, Frontiers Research Topics unify the most influential researchers, the latest key findings and historical advances in a hot research area.

Find out more on how to host your own Frontiers Research Topic or contribute to one as an author by contacting the Frontiers editorial office: frontiersin.org/about/contact

Next generation in vitro models to study chronic pulmonary diseases

Topic editors

Simon D. Pouwels — University Medical Center Groningen, Netherlands

Alen Faiz — University of Technology Sydney, Australia

Emmanuel Twumasi Osei — University of British Columbia, Canada

Citation

Pouwels, S. D., Faiz, A., Osei, E. T., eds. (2023). *Next generation in vitro models to study chronic pulmonary diseases*. Lausanne: Frontiers Media SA.

doi: 10.3389/978-2-8325-4163-0

Table of contents

frontiers | Frontiers in Medicine

TYPE Editorial
PUBLISHED 05 December 2023
DOI 10.3389/fmed.2023.1338939

Check for updates

OPEN ACCESS

EDITED AND REVIEWED BY
Dawei Yang,
Fudan University, China

*CORRESPONDENCE
Emmanuel T. Osei
✉ emmanuel.osei@ubc.ca

†These authors have contributed equally to this work and share last authorship

RECEIVED 15 November 2023
ACCEPTED 22 November 2023
PUBLISHED 05 December 2023

CITATION
Thiam F, Faiz A, Pouwels SD and Osei ET (2023) Editorial: Next generation *in vitro* models to study chronic pulmonary diseases. *Front. Med.* 10:1338939. doi: 10.3389/fmed.2023.1338939

COPYRIGHT
© 2023 Thiam, Faiz, Pouwels and Osei. This is an open-access article distributed under the terms of the Creative Commons Attribution License (CC BY). The use, distribution or reproduction in other forums is permitted, provided the original author(s) and the copyright owner(s) are credited and that the original publication in this journal is cited, in accordance with accepted academic practice. No use, distribution or reproduction is permitted which does not comply with these terms.

Editorial: Next generation *in vitro* models to study chronic pulmonary diseases

Fama Thiam[1], Alen Faiz[2†], Simon D. Pouwels[3,4,5†] and Emmanuel T. Osei[1,6*†]

[1]Department of Biology, University of British Columbia, Kelowna, BC, Canada, [2]Faculty of Science, Respiratory Bioinformatics and Molecular Biology, University of Technology Sydney, Sydney, NSW, Australia, [3]Department of Pulmonology, University Medical Center Groningen, University of Groningen, Groningen, Netherlands, [4]Department of Pathology and Medical Biology, University Medical Center Groningen, University of Groningen, Groningen, Netherlands, [5]University Medical Center Groningen, Groningen Research Institute for Asthma and Chronic Obstructive Pulmonary Disease, University of Groningen, Groningen, Netherlands, [6]Centre for Heart Lung Innovation, St. Paul's Hospital, Vancouver, BC, Canada

KEYWORDS

***in vitro* models, chronic pulmonary disease, air liquid interface (ALI), precision cut lung slice, CAD modeling, *ex vivo* models**

Editorial on the Research Topic
Next generation *in vitro* models to study chronic pulmonary diseases

Chronic pulmonary diseases, such as chronic obstructive pulmonary disease (COPD), tuberculosis (TB), and idiopathic pulmonary fibrosis (IPF), impact millions of people and are leading causes of death worldwide (1–3). Hence, a vast amount of research effort has been made to find early detection and curative therapies for these diseases. Researchers utilize several novel *in vitro* and *ex vivo* models to investigate the underlying mechanisms behind respiratory diseases. This is intended to help create targeted treatments that can aid in assessing and understanding novel disease mechanisms to subsequently improve the prognosis and quality of life of patients living with chronic pulmonary illnesses.

The use of bioinformatics and surgical models to improve diagnostics in respiratory diseases has the potential to impact clinical outcomes. In this Research Topic, studies from Oloko-Oba and Viriri and Gupta et al. assessed computer-aided diagnostic (CAD) systems related to TB diagnosis from the common and sensitive chest X-ray (CXR), which use deep learning techniques as well as a cellulose matrix absorptive probe for bronchial epithelial lining fluid (bELF) in the airways, respectively. From the systematic review of Oloko-Oba and Viriri, it was found that although most studies were developmental instead of being used in the clinic, the use of public and training datasets presented great potential for the use of CAD systems to improve TB diagnosis. In line with lung disease clinical diagnostics, Gupta et al. also discovered that the newly established bELF probes maintained their integrity with no residual fibers *in vivo* and obtained samples rich in proteins and with higher levels of inflammatory cytokines compared to the samples obtained from bronchial wash fluid. Ultimately, this high-precision probe is a novel technique for analyzing biomarkers in a consistent and accurate manner that will aid in early detection of lung disease (Gupta et al.).

In addition to diagnostics, air liquid interface (ALI) cultured cells have been used to assess different factors in disease severity, which is necessary to advance therapeutic treatments. In this Research Topic, Ito et al. used ALIs to show that age was a significant factor affecting respiratory syncytial virus (RSV) infection, with increased viral load and

viral genome copies, lower viral clearance, higher inflammation, increased cell damage, mucin production, and cellular senescence in ALIs of older people (>65 years) compared to younger individuals (≤60 years). Additionally, Kasper et al. compared an ALI model to a submerged culture model to show that SARS-CoV-2 entry genes, such as angiotensin converting enzyme 2 (ACE2), transmembrane serine protease 2 (TMPRSS2), cathepsin L (CTSL), and tyrosine protein kinase receptor UFO (AXL) in human primary small airway epithelial cells (SAEC) or bronchial epithelial cells (HBEC), are affected more by culture conditions than individual donor conditions.

Lung organoids are another *in vitro* model that is used to assess cell mechanisms and their implications in pulmonary diseases [Wisman et al.; (4, 5)]. Here, Wisman et al. developed organoids of MRC-5 and unfractionated lung cell suspensions or isolated $EpCAM^+$ distal lung tissue pulmonary epithelial cells from individuals with/without IPF. Organoids from IPF-derived cells were larger compared to isolated $EpCAM^+$ cell-organoids, suggesting intrinsic progenitor dysfunction. Unfractionated cell suspensions from IPF-derived lungs also resulted in a higher number of organoids, suggesting a dysregulated communication between epithelial and stroma cells in IPF, which may lead to distal lung alveolar impairment (Wisman et al.).

Another important model is the precision cut lung slice (PCLS) model, where thin slices of lung tissue are cultured *in vitro* for studies into disease mechanisms (6, 7). In this Research Topic, Cervantes et al. established PCLS from donors without a history of disease and exposed them to particulate matter from Afghanistan (PMa) (8) or particulate matter from California as a control (PMc) to investigate the mechanisms related to unique military deployment airway symptoms. Interestingly, PCLS was used to show that PMa increased airway hyperresponsiveness (AHR), but PMc had no effect (Cervantes et al.). Additionally, PMa co-stimulated with IL-13 resulted in significantly amplified AHR compared to PMc co-stimulations (Cervantes et al.).

Another important mechanism underlying respiratory disease pathogenesis is the disruption of the epithelial barrier integrity (9). Hsieh et al. used the Electric Cell-substrate Impedance Sensing (ECIS) system to assess the effect of different ECM substrates on the barrier integrity and attachment of basal airway epithelial cells. It was shown that airway epithelial cells attached faster on fibronectin, collagen I, and collagen III than on collagen IV and laminin. Further, fibronectin and collagen I enabled the fastest epithelial barrier formation compared to the other ECM proteins. This study demonstrated a potential protective role of these ECM proteins in pathological lung conditions (Hsieh et al.).

Respiratory cancers are a prominent source of cancer incidence and mortality worldwide, therefore investigations into their mechanisms of drug resistance are essential to identify novel treatment targets (10, 11). Tuffour et al. used CRISPER-Cas-9 gene editing to knockout the *CASD1* and *SIAE* genes, which are an important part of the breast cancer resistance protein (BCRP), a main ATP-binding cassette (ABC) transporter protein involved in multidrug resistant (MDR) pathways. Here, using CRISPR-gene editing and drug sensitivity analysis, it was shown that deacetylated Sias are utilized by cancer cells to overexpress BCRP as a pathway of MDR, which can be used to further advance the effectiveness of chemotherapies.

Ex vivo models have also been utilized to study the biological methods of disease and potentially identify mechanisms for therapeutics due to their ability to mimic the *in vivo* physiology. Ievlev et al. created a ferret tracheal model for injury and cell engraftment using tracheal explants and found a semblance to surface airway epithelium (SAE) and submucosal glands (SMGs). Consistent results in line with published data on *in vivo* injury systems were found after injury experiments. A 3D-printed culture chamber that allows imaging of ferret tissue explants was set up, which aided ferret cell ALI establishment.

In this Research Topic, various studies utilized a breadth of tools including CAD modeling, pulmonary sampling devices, ALIs, PCLS, ECIS, CRISPR, and *ex vivo* systems to study different mechanisms of pulmonary diseases as well as diagnostics and to perform drug studies. These prove the utility and adaptability of these systems for future studies and the advancement of the pulmonary field.

Author contributions

FT: Writing – original draft, Writing – review & editing. AF: Conceptualization, Writing – review & editing. SP: Conceptualization, Writing – review & editing. EO: Conceptualization, Writing – original draft, Writing – review & editing.

Funding

The author(s) declare that no financial support was received for the research, authorship, and/or publication of this article.

Conflict of interest

The authors declare that the research was conducted in the absence of any commercial or financial relationships that could be construed as a potential conflict of interest.

Publisher's note

All claims expressed in this article are solely those of the authors and do not necessarily represent those of their affiliated organizations, or those of the publisher, the editors and the reviewers. Any product that may be evaluated in this article, or claim that may be made by its manufacturer, is not guaranteed or endorsed by the publisher.

References

1. Lortet-Tieulent J, Soerjomataram I, López-Campos JL, Ancochea J, Coebergh JW, Soriano JB. International trends in COPD mortality, 1995-2017. *Eur Respir J*. (2019) 54. doi: 10.1183/13993003.01791-2019

2. Maher TM, Bendstrup E, Dron L, Langley J, Smith G, Khalid JM, et al. Global incidence and prevalence of idiopathic pulmonary fibrosis. *Respir Res*. (2021) 22:197. doi: 10.1186/s12931-021-01791-z

3. MacNeil A, Glaziou P, Sismanidis C, Date A, Maloney S, Floyd, K. Global epidemiology of tuberculosis and progress toward meeting global targets - worldwide, 2018. *MMWR Morb Mortal Wkly Rep*. (2020) 69:281–5. doi: 10.15585/mmwr.mm6911a2

4. Barkauskas CE, Chung MI, Fioret B, Gao X, Katsura H, Hogan BL. Lung organoids: current uses and future promise. *Development*. (2017) 144:986–97. doi: 10.1242/dev.140103

5. Matkovic Leko I, Schneider RT, Thimraj TA, Schrode N, Beitler D, Liu HY, et al. A distal lung organoid model to study interstitial lung disease, viral infection and human lung development. *Nat Protoc*. (2023) 18:2283–312. doi: 10.1038/s41596-023-00827-6

6. Alsafadi HN, Uhl FE, Pineda RH, Bailey KE, Rojas M, Wagner DE, et al. Applications and approaches for three-dimensional precision-cut lung slices. disease modeling and drug discovery. *Am J Respir Cell Mol Biol*. (2020) 62:681–91. doi: 10.1165/rcmb.2019-0276TR

7. Liu G, Betts C, Cunoosamy DM, Åberg PM, Hornberg JJ, Sivars KB, et al. Use of precision cut lung slices as a translational model for the study of lung biology. *Respir Res*. (2019) 20:162. doi: 10.1186/s12931-019-1131-x

8. Berman R, Rose CS, Downey GP, Day BJ, Chu HW. Role of particulate matter from Afghanistan and Iraq in deployment-related lung disease. *Chem Res Toxicol*. (2021) 34:2408–23. doi: 10.1021/acs.chemrestox.1c00090

9. Carlier FM, de Fays C, Pilette C. Epithelial barrier dysfunction in chronic respiratory diseases. *Front Physiol*. (2021) 12:691227. doi: 10.3389/fphys.2021.691227

10. Shanker M, Willcutts D, Roth JA, Ramesh R. Drug resistance in lung cancer. *Lung Cancer*. (2010) 1:23–36. doi: 10.2147/LCTT.S6861

11. Thandra KC, Barsouk A, Saginala K, Aluru JS. Epidemiology of lung cancer. *Contemp Oncol*. (2021) 25:45–52. doi: 10.5114/wo.2021.103829

frontiers in Medicine

SYSTEMATIC REVIEW
published: 10 March 2022
doi: 10.3389/fmed.2022.830515

A Systematic Review of Deep Learning Techniques for Tuberculosis Detection From Chest Radiograph

*Mustapha Oloko-Oba and Serestina Viriri**

Computer Science Discipline, School of Mathematics, Statistics and Computer Science, University of KwaZulu-Natal, Durban, South Africa

The high mortality rate in Tuberculosis (TB) burden regions has increased significantly in the last decades. Despite the possibility of treatment for TB, high burden regions still suffer inadequate screening tools, which result in diagnostic delay and misdiagnosis. These challenges have led to the development of Computer-Aided Diagnostic (CAD) system to detect TB automatically. There are several ways of screening for TB, but Chest X-Ray (CXR) is more prominent and recommended due to its high sensitivity in detecting lung abnormalities. This paper presents the results of a systematic review based on PRISMA procedures that investigate state-of-the-art Deep Learning techniques for screening pulmonary abnormalities related to TB. The systematic review was conducted using an extensive selection of scientific databases as reference sources that grant access to distinctive articles in the field. Four scientific databases were searched to retrieve related articles. Inclusion and exclusion criteria were defined and applied to each article to determine those included in the study. Out of the 489 articles retrieved, 62 were included. Based on the findings in this review, we conclude that CAD systems are promising in tackling the challenges of the TB epidemic and made recommendations for improvement in future studies.

Keywords: tuberculosis, chest radiograph, computer-aided diagnosis, deep learning, systematic review

OPEN ACCESS

Edited by:
Emmanuel Twumasi Osei, University of British Columbia Okanagan, Canada

Reviewed by:
Anjali Agrawal, Teleradiology Solutions, India
Muhammad Usman Akram, National University of Sciences and Technology (NUST), Pakistan

****Correspondence:***
Serestina Viriri
viriris@ukzn.ac.za

Specialty section:
This article was submitted to Pulmonary Medicine, a section of the journal Frontiers in Medicine

Received: *07 December 2021*
Accepted: *14 February 2022*
Published: *10 March 2022*

Citation:
Oloko-Oba M and Viriri S (2022) A Systematic Review of Deep Learning Techniques for Tuberculosis Detection From Chest Radiograph. Front. Med. 9:830515. doi: 10.3389/fmed.2022.830515

INTRODUCTION

Tuberculosis (TB) is ranked among the leading causes of death. About 10 million persons fell ill globally from TB infections in 2019 (1). TB is triggered by the Mycobacterium bacteria that usually affect the lungs (pulmonary) but sometimes affect other parts of the body (extrapulmonary) (2). Many TB patients lose their lives yearly due to diagnostic delay, misdiagnosis, and lack of appropriate treatments (3, 4). Although TB is a global challenge, the mortality rate is more prevalent in low and middle-income nations (5).

TB is certainly treatable if diagnosed early for appropriate treatment. Early diagnosis is essential for successful treatment, preventing further spread, and significantly reducing the mortality rate in line with the World Health Organization (WHO) End TB Strategy (1). The gold standard for TB screening is Sputum culture. However, posterior-anterior chest radiographs (CXR) are an effective technique with low-cost and moderately low radiation doses for screening lung abnormalities to achieve prompt results (6). CXR has been adequately employed in developed countries to analyze individuals exhibiting active TB symptoms. At the same time, its application is limited in developing countries where TB is most prevalent (7, 8). High TB burden regions lack the skilled and radiological expertise required to interpret CXR images adequately (9, 10).

In the last decades, several efforts have been made using Artificial Intelligence (AI) to develop a Computer-Aided Detection (CAD) system to advance automatic object/image recognition tasks and overcome the challenges of a skilled workforce. Machine Learning (ML) and Deep Learning (DL) are the predominant AI techniques employed to develop CAD systems for analyzing CXR images. Both techniques have had a significant impact, but the DL approach, such as Convolutional Neural Network (CNN), has become more prominent for analyzing different pulmonary abnormalities in the medical domain, most importantly in diagnosing TB. The application of an efficient classification tool is vital for improving the quality of diagnosis while reducing the time taken to analyze a large volume of CXRs (11). This endeavor is to achieve the global decline in TB incidence to about 5% annually compared to the current 2% yearly as part of the World Health Organization strategy to end TB (1).

The contribution of this systematic review is to present an extensive summary of the various state-of-the-art CAD system proposed in the literature for the classification of TB. Ultimately, only the CAD system developed using Deep Learning models is considered in this study detailing the diagnostic accuracy between 2017 and 2021. The rest of the paper is structured as follows: section Methodology presents the study methodology. The results are presented in section Results. Section Discussion presents the discussion, while the conclusion is expressed in section Conclusion and Recommendations.

METHODOLOGY

This systematic review aims to establish various CAD systems related to Tuberculosis diagnosis from CXR using DL techniques. The study followed the Preferred Reporting Items for Systematic Reviews and Meta-Analyses (PRISMA) procedures (12) to identify the standards for inclusion and exclusion, as shown in **Figure 1**. These standards were formulated based on the present study objectives and the research questions. All articles that satisfied the following conditions were included and excluded if otherwise:

- Articles that considered only pulmonary tuberculosis disease.
- Employed at least one deep learning technique as a classifier
- CXR is the only medical imagine for screening tuberculosis.
- Articles published between January 2017 and September 2021.
- Articles are entirely written in English.
- Articles must be full text. All others, such as abstract, preprints are excluded.

Search Strategy

The search strategy was developed to identify relevant published articles in Scopus (https://www.scopus.com/), IEEEXplore (https://ieeexplore.ieee.org/), Web of Science (www.webofscience.com), and PubMed (https://www.ncbi.nlm.nih.gov/pubmed/). Searches were performed across the four databases using the following search keywords: "tuberculosis," "chest x-ray," "classification," "artificial intelligence," "computer-aided diagnosis," "deep learning." These keywords were used to

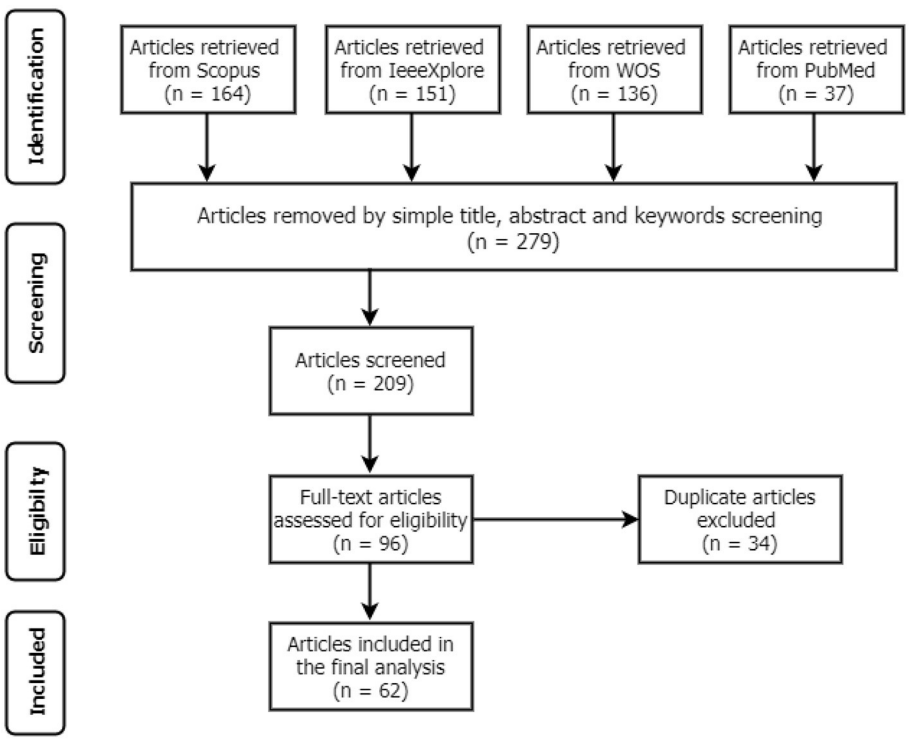

FIGURE 1 | The PRISMA structure for the study selection process.

TABLE 1 | Construction of search keywords.

Databases	Search keywords
Scopus	(TITLE-ABS-KEY ("Tuberculosis" AND "Chest X-Ray") AND TITLE-ABS-KEY ("Deep learning" OR "Machine learning" OR "Artificial Intelligence" OR "Classification")
IEEEXplore	(Tuberculosis) AND ("Chest X-Ray") AND ("Deep learning" OR "Machine learning" OR "classification" OR "artificial intelligence") AND ("CAD" OR "computer-aided detection")
Web of Science	((Tuberculosis AND Chest x-ray) AND ("Machine learning" OR "Deep learning" OR "Artificial intelligence") AND ("classification" OR "classify") AND ("computer-aided diagnosis" OR "CAD"))
PubMed	("Tuberculosis") AND ("chest x-ray") AND ("deep learning" OR "convolutional neural network") AND ("classify" or "classification") OR ("computer-aided diagnosis" OR "computer-aided detection" OR "CAD")

form Boolean search strings according to searching standards on different databases. The configuration of keywords used to retrieve all relevant articles from each database search engine is presented in **Table 1**.

Study Selection

A total of 488 articles were retrieved from the initial search on all the databases. The next step then scans the article topics and keywords to identify highly related papers from the irrelevant ones. This step is followed by the overview reading of the abstract, methods, and Conclusion to further screen for relevant papers for full-text reading and better understanding. Thus, 209 articles were considered for the title and abstract screening, out of which 96 papers were found suitable for full-text reading, and a total of 62 were finally included in the analysis after removing 34 duplicates. The detailed structure for the study selection is presented in **Figures 1**, **2** shows the numbers of articles included per year and databases. It is necessary to note that some relevant articles might have been unintentionally omitted.

Data Extraction

The details extracted from each article are presented in **Tables 2**–**5**. Each table represents the search results from the Scopus, IEEE Xplore, PubMed, and Web of Science databases. Data extracted include study aim and scope, computational techniques (DL models), CXR datasets, evaluation metrics/results achieved, and publication year. The database search shows that most IEEEXplore articles are conference proceedings and included in this systematic review, along with a few conference articles from springer and ACM. This is due to the articles' quality and contribution to the subject matter.

RESULTS

This study reviewed computer-aided diagnosis systems articles to detect pulmonary TB from January 2017 until September 2021. It was observed from the articles that the development of CAD follows a standard framework involving four steps as follows: "pre-processing" is the first step which deals with cleaning up the CXR images by eliminating noise and enhancing for clarity. The second step is "segmentation" of a region of interest from the entire image, which is the lung field region in the case of CXR. The third step is the "Feature extraction," where discriminative features are identified and selected for further analysis in the "classification" step, where the various images are categorized as normal or abnormal (infected) with TB. Several techniques such as handcraft, machine learning, and deep learning have been employed to diagnose TB, but DL has recorded more success in this regard; hence our interest was to analyze the CAD system based on one or more DL techniques as the classifier for TB detection.

The descriptive analysis of the results is presented in **Tables 2**–**5**. These tables show the computational technique, study scope, datasets, evaluation criteria, and results. Articles that utilized CXR as the only imaging modality and employed DL as the only computational technique for developing CAD are considered.

Imaging Modalities

Different screening procedures are used to confirm the presence of TB. Still, Chest Radiograph, otherwise referred to as Chest X-ray (CXR), is a radiograph tool used to detect abnormalities in the lungs and nearby structures. In recent years, CXR has remained a vital method for screening TB and other lung diseases and hence recommended by WHO due to its high sensitivity, wide availability, and relatively less expensive (70, 71).

Deep Learning Techniques

Many DL techniques have been used for screening, predicting, and diagnosing TB. In most classification algorithms, a dataset is required for training and testing with many samples of inputs and outputs to learn from. Model is developed using the training set to calculate how best to map examples of input data to a specific class label; then, the model validation is accomplished using the test set (72).

In **Tables 2**–**5**, only the results obtained from the test set are extracted. Some studies employed more the one DL technique to find the optimal results for diagnosing TB diseases. Only the best results are documented in this study if more than one accuracy is reported in an article.

Datasets

Data is crucial for developing CAD required to solve life-threatening diseases, including TB, as one of the leading causes of worldwide death. The various popular datasets that have been used in developing TB detection algorithms contain de-identified CXR images to protect the privacy of the patients. In other words, the identity of the patients is not disclosed. Most of the datasets are accompanied by radiological interpretation of the observed manifestation that can serve as groundtruth. These datasets are made available to the research communities to foster state-of-the-art research into finding lasting solutions to the early diagnosis of TB manifestations. Some of these public datasets include Montgomery County (73), Shenzhen (73), Peruvian (49), KIT (74), MIMIC-CXR (75), Belarus, NIH (chest x-ray 8, 14) (76), JSRT. **Figure 3** shows the datasets frequency of use.

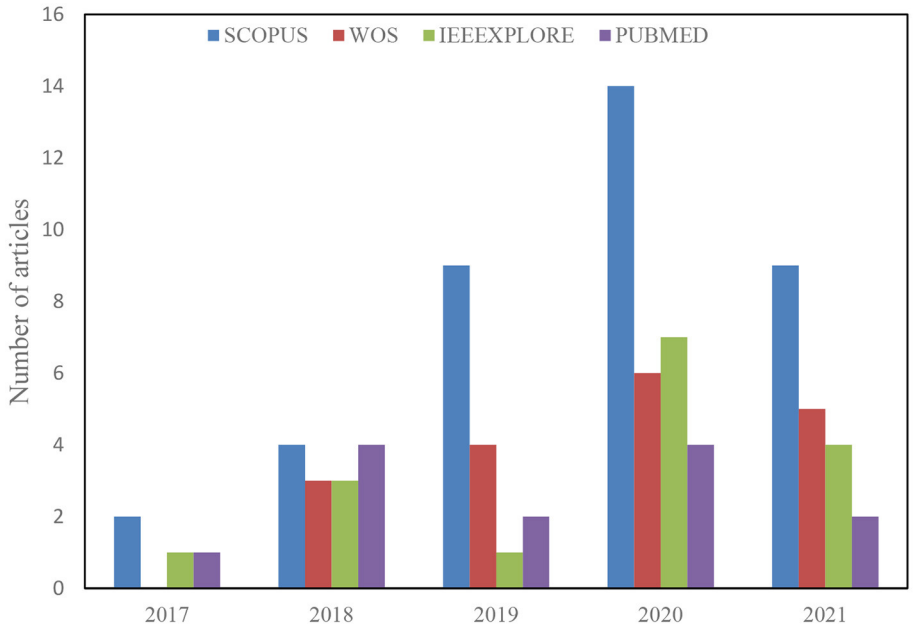

FIGURE 2 | Articles selection by database and year.

Evaluation Metrics

Once a model is trained using some training images, the test dataset is then employed to assess the quality of the model. It is evident from the data extraction process that different evaluation metrics exist for assessing model performance. Most of the popular evaluation metrics applied to the development of CAD system includes accuracy, sensitivity, specificity, and AUC. These evaluation metrics are briefly explained as follows:

Accuracy is the rate of the correct samples from the total number of samples examined (77). The equation gives the accuracy:

$$Accuracy = \frac{TP + TN}{TP + FP + TN + FN}$$

Sensitivity is the proportion of the actual positive samples that are correctly identified as positive (78). This metric is given as:

$$Sensitivity = \frac{TP}{TP + FN}$$

Specificity is the ratio of the actual negative samples that are correctly identified as negative (78). This metric is given as:

$$Specificity = \frac{TN}{TN + FP}$$

Precision, otherwise known as a positive predictive value, is the ratio of positive samples that are accurately predicted (77). This is given as:

$$Precision = \frac{TP}{TP + FP}$$

AUC-ROC Curve: sometimes written as AUROC, specify the rate at which a model distinguishes between classes [84]. It tells the probability of separating negative samples from positive samples. Thresholds are set to determine the ROC curve, which is the plot of True Positive Rate (TPR) against False Positive Rate (FPR) given as:

$$TPR = Sensitivity = \frac{TP}{TP + FN}$$

$$FPR = 1 - Specificity = \frac{FP}{FP + TN}$$

Where TP, TN, FP, FN, TPR, and FPR are true positive, true negative, false positive, false negative, true positive rate, and false positive rate.

DISCUSSION

This systematic review extensively searched the various Deep Learning classifiers for diagnosing TB from CXR. Automatic detection of TB has received mammoth attention in the last decades resulting in many publications with state-of-the-art techniques. **Figure 4** presents a hierarchical chart of computational techniques categorized according to the frequency of usage in CAD systems for TB based on the included articles. Despite some good accuracies reported in some studies, we found some limitations in the existing studies concerning methods and reported accuracy, which should be a point of consideration for developing CAD systems in the future. Many studies measured diagnostic accuracy without evaluating the risk of bias emerging from the datasets that were used. It is essential that the accuracy

TABLE 2 | Scopus search results.

References	Computational techniques	Study aim/scope	Datasets	Results	Year
Duong et al. (13)	EfficientNet, Vision Transformer	Classification of CXR as normal, pneumonia and TB	Montgomery, Shenzhen, Belarus, RSNA, A COVID-19 CXR	Acc = 97.72%, Auc = 100%	2021
Norval et al. (14)	AlexNet, VGG16, and VGG19	Improve accuracy and Classification of CXR as Has TB and No TB	Montgomery, Shenzhen, NIH	Acc = 89.99%	2021
Rahman et al. (15)	ResNet101, VGG19, and DenseNet201 XGBoost	The study utilizes three Deep CNN models as features extractor then classify using eXtreme Gradient Boosting	Montgomery, Shenzhen, Belarus, RSNA, Private	Acc = 99.92% Auc = 99.93% Pre = 99.85% Sen = 100% Spe = 99.85% F1 = 99.92%	2021
Govindarajan and Swaminathan (16)	ELM, OSELM	Identify and classify TB conditions from healthy subjects in chest radiographs using integrated local feature descriptors and variants of extreme learning machine	Montgomery	Acc = 99.2% Sen = 99.3% Spe = 99.3% Pre = 99.0% F1 = 99.20%	2021
Alawi et al. (17)	CNN	Study proposed automated technique to diagnose TB from CXR	NLM, Belarus, NIAID TB and RSNA	Acc = 98.71% Sen = 98.86% Spe = 98.57%	2021
Khatibi et al. (18)	Complex networks and stacked ensemble (CCNSE), CNN	A multi –instance classification model to detect TB from CXR is proposed	Shenzhen, Montgomery	Acc = 99.26%, Auc = 99.00%	2021
Ayaz et al. (19)	Deep CNN	Present a hybrid method for TB detection	Montgomery, Shenzhen	Auc = 0.99%	2021
Priya and Vimina (20)	VGG-19, RestNet50, DenseNet121, InceptionV3	The study employs transfer learning for TB diagnosis.	Montgomery, Shenzhen	Auc = 0.95%	2021
Dasanayaka and Dissanayake (21)	DC-GAN, VGG16 and InceptionV3	generate, segment, and classify CXR for TB using three deep architectures	Montgomery, Shenzhen	Acc = 97.10% Sen = 97.90% Spe = 96.20%	2021
Msonda et al. (22)	AlexNet, GoogLeNet, ResNet50 and Spatial Pyramid Pooling (SPP)	Integrate SPP with Deep CNN to improve performance for TB detection	Montgomery, Shenzhen, Private (KERH)	Acc = 0.98% Pre = 1.00% Spe = 1.00% F1 = 1.00%	2020
Owais et al. (23)	Fusion-based deep classification network	The study proposes a CAD system for the effective diagnosis of TB and provides visual with descriptive information that is useful to the radiologist	Montgomery, Shenzhen	Acc = 0.928% Auc = 0.965% Pre = 0.937% Recall = 0.921% F1 = 0.929%	2020
Yoo et al. (24)	ResNet18	Classify CXR into Normal, TB and Non-TB	Montgomery, Shenzhen, NIH	Acc = 0.98% Sen = 0.98% Spe = 0.97% Auc = 0.965% Pre = 0.97%	2020
Sathitratanacheewin et al. (25)	DCNN	To examine the generalization of deep CNN models for classification of CXR as normal or abnormal with different manifestations	Shenzhen, NIH (ChestX-ray8)	Acc = 0.985% Sen = 72% Spe = 82%	2020
Sahlol et al. (26)	MobileNet Artificial Ecosystem-based Optimization (AEO)	Classification of CXR to detect TB	Shenzhen, Private	Acc = 94.1%	2020
Das et al. (27)	InceptionV3	Screening CXR for TB abnormalities	Montgomery, Shenzhen	Acc = 91.7% Auc = 0.96% Sen = 0.89% Spe = 0.93% Pre = 0.93%	2020
Rahman et al. (28)	ResNet, ChexNet, InceptionV3, Vgg19, DenseNet201, SqueezeNet, MobileNet, and Ensemble	Automatic detection of TB from the CXR.	NLM, Belarus, NIAID TB, and RSNA	Acc = 98.6% F1 = 98.56% Sen = 98.56% Spe = 98.54% Pre = 98.57%	2020

(Continued)

TABLE 2 | Continued

References	Computational techniques	Study aim/scope	Datasets	Results	Year
Munadi et al. (29)	ResNet and EfficientNet	Enhances CXR images for improving TB detection accuracy	Shenzhen	Acc = 91.7% Auc = 0.96%	2020
Oloko-Oba and Viriri (30)	CNN	Detection of TB from CXR and classification as normal and abnormal	Shenzhen	Acc = 87.8%	2020
Xie et al. (31)	Faster RCNN	Detection of multiple categories of TB lesions in CXR	Montgomery, Shenzhen	Acc = 0.926% Auc = 0.977%	2020
Verma et al. (32)	InceptionV3, faster RCNN	Classify CXR as pulmonary TB and Pneumonia	Shenzhen	Acc = 99.01%	2020
Tasci (33)	AlexNet, VGGNet	classifying CXR ROI for TB detection	Montgomery, Shenzhen	Acc = 88.32% Auc = 0.92%	2020
Rajaraman and Antani (34)	Inception-V3, ResNet-V2, VGG-16, Xception, DenseNet-121, Ensemble	Improve state-of-the-art architecture for TB detection from CXR	Shenzhen, RSNA, Indiana	Acc = 0.941% F1 = 0.941% Sen = 0.926% Spe = 1.00% Auc = 0.990%	2020
Abideen et al. (35)	B-CNN	Identification and classification of CXR as TB and Non-TB	Montgomery, Shenzhen	Acc = 96.42%	2020
Hijazi et al. (36)	Ensemble of VGG16 InceptionV3	Detection of TB from CXR	Montgomery, Shenzhen	Acc = 89.77% Sen = 90.91% Spe = 88.64%	2019
Pasa et al. (37)	CNN	Developed a faster TB detection algorithm	Montgomery, Shenzhen, Belarus	Acc = 84.4% Auc = 0.900%	2019
Meraj et al. (38)	VGGNet, RestNet50, GoogLeNet	Detection of TB abnormalities from CXR	Montgomery, Shenzhen	Acc = 86.74% Auc = 92.0%	2019
Ahsan et al. (39)	VGG16	Screening of CXR to identify the presence of TB	Montgomery, Shenzhen	Acc = 81.25%	2019
Nguyen et al. (40)	ResNet-50, VGGNet, DenseNet-121, Inception, ResNet.	Improving detection rate of TB	Montgomery, Shenzhen, NIH-14	Auc = 0.99%	2019
Ho et al. (41)	InceptionResNetV2, ResNet150, DenseNet-121	Classification of CXR as pulmonary TB or healthy.	ChestX-ray14, Shenzhen, Montgomery	Auc = 0.95%	2019
Heo et al. (42)	VGG19, InceptionV3, ResNet-50, DenseNet-121, InceptionResNetV2.	Detection of TB from CXR	Privete (Yonsei University)	Auc = 0.9213% Sen = 0.815% Spe = 0.962%	2019
Hernández et al. (43)	Ensemble of VGG19, InceptionV3, ResNet-50	Automatic classification of CXR for TB detection.	Private	Acc = 0.8642.%	2019
Hijazi et al. (44)	Ensemble of InceptionV3, VGG16	Detection of TB from CXR without segmentation	Shenzhen, Montgomery	Acc = 91.0% Sen = 89.6% Spe = 90.7%	2019
Abbas and Abdelsamea (45)	AlexNet	Classification of CXR as healthy or having TB manifestation	Montgomery	Auc = 0.998% Sen = 0.997% Spe = 0.999%	2018
Karnkawinpong and Limpiyakorn (46)	AlexNet, VGG16, CapsNet	CAD for early diagnosis of TB	Private (Thai), Shenzhen, Montgomery	Acc = 90.79% Sen = 89.07% Spe = 92.50%	2018
Stirenko et al. (47)	DCNN	Prediction of the presence of TB from CXR	Shenzhen	———	2018
Becker et al. (48)	CNN	Detection and classification of different TB pathologies from CXR	Private	Auc = 0.98%	2018
Liu et al. (49)	AlexNet, GoogLeNet	Detection and classification of TB manifestations in CXR images	Peruvian	Acc = 85.68%	2017
Hooda et al. (3)	DCNN	Detect and classify TB from CXR as normal and abnormal	Shenzhen, Montgomery	Acc = 82.09%	2017

of CAD systems is evaluated using a different set of datasets (CXR images) from the set used for training. In other words, avoid

- Using the same set of CXR images for training and testing.
- Testing with CXR images that were not used for training but originated from the same image subset.
- Using images with class imbalance, and
- Using unannotated CXR images.

Otherwise, the diagnostic accuracy evaluation is likely to be exaggerated and could impact the overall generalization of the system. In general, about 80% of the studies used the

TABLE 3 | PubMed search results.

References	Computational techniques	Study aim/scope	Datasets	Results	Year
Oloko-Oba and Viriri (50)	Ensemble of VGG-16, ResNet50, Inception V3	Automatic detection of TB from CXR	Shenzhen, Montgomery	Acc = 96.14% Sen = 90.03% Spe = 92.41%	2021
Lee et al. (51)	DLAD	Detection of active TB and classification of relevant abnormalities on CXR	Private	Auc = 0.967% Sen = 0.821% Spe = 0.997%	2021
Zhang et al. (52)	Convolutional Block Attention Module (CBAM)	Classification of TB from CXR	Private	Acc = 87.7% Auc = 94.3% Recall = 89.7% Spe = 85.9.7%	2020
Hwang et al. (53)	DLAD	Developed a Deep Learning-based automatic detection algorithm (DLAD) for active Pulmonary TB on CXR and validate its performance using various datasets compared to physicians' results.	Shenzhen, Montgomery, Private (SNUH)	Auc = 0.977% Sen = 94.3% Spe = 91.1%	2019
Rajpurkar et al. (54)	CNN (CheXNeXt)	To evaluate the effectiveness of CheXNeXt in detecting TB and other abnormalities from CXR	ChestX-ray14	Auc = 0.862% Sen = 0.594% Spe = 0.927%	2018
Lakhani and Sundaram (55)	Ensemble of AlexNet, GoogLeNet	Evaluates the efficacy of deep models for detecting TB on CXR	Belarus, Shenzhen, Montgomery	Auc = 0.99% Sen = 97.3% Spe = 94.7%	2017

TABLE 4 | IEEE Xplore search results.

References	Computational techniques	Study aim/scope	Datasets	Results	Year
Cao et al. (56)	DenseNet121 VGGNet16, VGGNet19, ResNet152	Evaluates the performance of deep learning for classification of CXR for TB	Shenzhen, Montgomery	Acc = 90.38% F1 = 90.36% Pre = 90.33% Recall = 90.53%	2021
Karaca et al. (57)	VGG16, VGG19, DenseNet121, MobileNet, InceptionV3	Development of a TB detection system	Montgomery	Acc = 98.9% Auc = 1.00%	2021
Saif et al. (58)	DenseNet169, ResNet-50, InceptionV3	Detection of TB from CXR	Shenzhen, Montgomery	Acc = 99.7% Sen = 97.5% Spe = 98.4%	2021
Das et al. (27)	InceptionV3	Screening TB from CXR to eliminate patents diagnosis delay	Shenzhen, Montgomery	Acc = 91.7% Auc = 0.96%	2021
Imam et al. (59)	Modified Inception	They analyzed patients' CXR to determine those infected with TB or not.	Shenzhen, Montgomery	Acc = 91%	2020
Griffin et al. (60)	R-CNN	Location of TB manifestations on CXR	Peruvian	Auc = 0.753% Sen = 0.922% Spe = 0.666%	2020
Rashid et al. (61)	Ensemble of ResNet, Inception-ResNet, DenseNet	Development of a CAD system to classify CXR as normal and infected with TB	Shenzhen	Acc = 90.5%	2018
Abbas and Abdelsamea (45)	AlexNet	Classification of CXR as healthy and unhealthy with TB manifestation	Shenzhen, Montgomery	Auc = 0.998% Sen = 0.999% Spe = 0.997%	2018

same CXR images for training and testing or did not report on it.

CONCLUSION AND RECOMMENDATIONS

This systematic review intends to inform researchers of the existing Deep Learning classifiers and assist them in developing a CAD system for the efficient diagnosis of TB. Different state-of-the-art Deep Learning techniques that have been used to detect TB have been explored and presented in **Tables 2**–**5**. Generally, it is challenging to compare the methods with each other extensively. Factors like the types of datasets used for evaluation, number of image samples used, evaluation metrics approach, and model parameters tunning make the comparison complex.

TABLE 5 | Web of Science search results.

References	Computational techniques	Study aim/scope	Datasets	Results	Year
Fehr et al. (62)	CAD4TBv5	Implement CAD4TB to screen for TB on CXR	Private	Sen = 82.8% Spe = 68.0%	2021
Vats et al. (63)	CNN (iDoc-X)	Diagnosis of TB manifestations from CXR and classify images as TB and Non-TB	Private	Acc = 91.10%	2021
Khatibi et al. (18)	CNNs, complex networks and stacked ensemble	TB recognition from CXR images	Shenzhen, Montgomery	Acc = 99.26% Auc = 99.00%	2021
Rajpurkar et al. (64)	DenseNet121	Development of CheXaid for diagnosing TB	Private	Acc = 0.78% Auc = 0.83%	2020
Grivkov and Smirnov (65)	InceptionV3	Screening of CXR to detect TB pathologist	Shenzhen, Montgomery	Acc = 0.868%	2020
Msonda et al. (22)	AlexNet, GooLeNet, ResNet50, SPP	Integrate SPP with DCNN for the diagnosis of TB on CXR.	Shenzhen, Montgomery, Private (KERH)	Auc = 0.98% Spe = 1.0% Pre = 1.0% F1 = 1.0% Recall = 0.99%	2020
Gozes and Greenspan (66)	DenseNet121	Learned specific features from CXR to detect TB	Chest X-ray14	Auc = 0.965%	2019
Karnkawinpong and Limpiyakorn (67)	AlexNet, VGG-16, CapsNet	Classification of TB from CXR	NLM, Private	Acc = 94.56% Sen = 92.83% Spe = 96.06%	2019
Sivaramakrishnan et al. (68)	AlexNet, VGG16, VGG19, Xception, ResNet-50	evaluate the performance of Deep models toward improving the accuracy of TB screening from CXR	Shenzhen, Montgomery, Private	Acc = 0.855% Auc = 0.956%	2018
Vajda et al. (69)	CNN	Screening CXR to determine which CXR images are normal or abnormal with TB.	Shenzhen, Montgomery	Acc = 97.03% Auc = 0.99%	2018

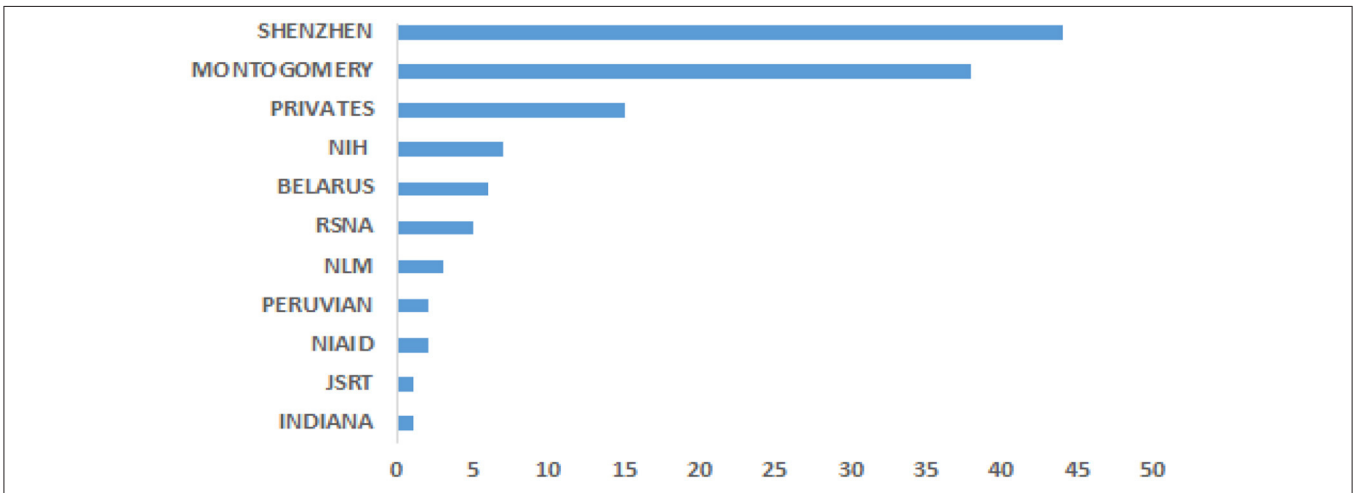

FIGURE 3 | Dataset frequency of usage.

As evident from the literature, these pre-trained models (VggNet, ResNet, AlexNet, DenseNet, and Inception) are the most popular and have been extensively explored for the classification of TB, as shown in **Figure 4**. Despite the effectiveness of Deep Learning models in detection and classification tasks, CAD systems for clinical diagnosis are still challenging in a real-world scenario. The physicians and radiologists see CAD intervention as a threat to their jobs rather

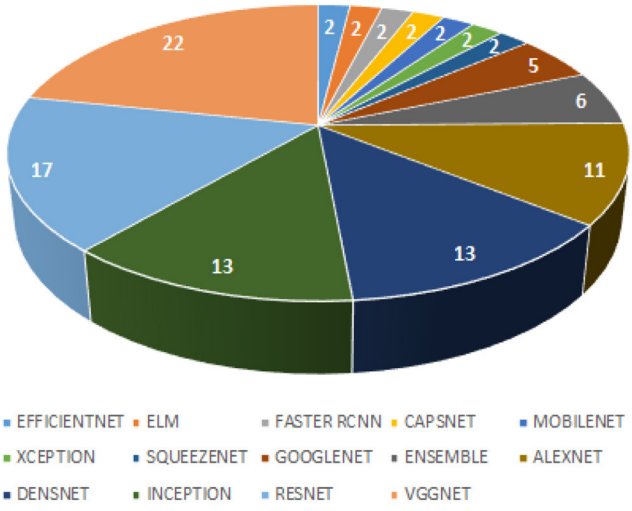

FIGURE 4 | Hierarchical chart of computational techniques according to the frequency of usage.

than a supporting system to improve physicians' performance in terms of time, effort, efficiency, and affordability, especially in developing countries. This review found that most existing works focused on development studies rather than clinical studies.

One of the likely weaknesses of this review is that it is limited to only the studies written in English because there might be other high-quality studies written in other languages. Also, we restricted the computational techniques to only Deep Learning classifiers, which could increase the risk of classifiers bias where studies that employed a hybrid of both Machine Learning and Deep Learning could have achieved better performance. Furthermore, this study did not undertake meta-analyses due to variations of algorithms used. Also, the raw data required to meta-analyze the diagnostic accuracy for most studies were unavailable.

However, it is recommended that studies be carried out using standardized public datasets that contain additional masks of the images that can be used as groundtruth to detect the infected aspect of the pulmonary images. It is highly recommended that models are trained with a set of images and evaluated on a different set of images. For instance, training a model with the Shenzhen datasets and evaluating it on the Montgomery dataset will validate better generalization. It is also recommended that future CAD systems focus more on clinical evaluation and should be able to identify foreign objects such as buttons and rings that look like a nodule on the CXR images, which may lead to misclassification.

DATA AVAILABILITY STATEMENT

The original contributions presented in the study are included in the article/supplementary material, further inquiries can be directed to the corresponding author/s.

AUTHOR CONTRIBUTIONS

All authors listed have made a substantial, direct, and intellectual contribution to the work and approved it for publication.

REFERENCES

1. *World Health Organization. Global Tuberculosis Report 2020: Executive Summary*. Available online at: https://apps.who.int/iris/handle/10665/337538 (accessed November 29, 2021). License: CC BY-NC-SA 3.0 IGO.
2. Baral SC, Karki DK, Newell JN. Causes of stigma and discrimination associated with tuberculosis in Nepal: a qualitative study. *BMC Public Health.* (2007) 7:1–0. doi: 10.1186/1471-2458-7-211
3. Hooda R, Sofat S, Kaur S, Mittal A, Meriaudeau F. Deep-learning: a potential method for tuberculosis detection using chest radiography. In: *2017 IEEE International Conference on Signal and Image Processing Applications (ICSIPA)* (IEEE) (2017), 497–502.
4. Zumla A, George A, Sharma V, Herbert RH, Oxley A, Oliver M. The WHO 2014 global tuberculosis report—further to go. *Lancet Global Health.* (2015) 3:e10–2. doi: 10.1016/S2214-109X(14)70361-4
5. Sathitratanacheewin S, Pongpirul K. Deep learning for automated classification of tuberculosis-related chest x-ray: dataset specificity limits diagnostic performance generalizability. *arXiv[Prepint].arXiv:1811.07985*. (2018).
6. World Health Organization. *Chest Radiography in Tuberculosis Detection: Summary of Current WHO Recommendations and Guidance on Programmatic Approaches*. (2016). World Health Organization. Available online at: https://apps.who.int/iris/handle/10665/252424 (accessed November 29, 2021).
7. Williams FH. The use of X-ray examinations in pulmonary tuberculosis. *Boston Med Surg J.* (1907) 157:850–3. doi: 10.1056/NEJM190712261572602
8. Pande T, Pai M, Khan FA, Denkinger CM. Use of chest radiography in the 22 highest tuberculosis burden countries. *Eur Respir J.* (2015) 46:1816–9. doi: 10.1183/13993003.01064-2015
9. Noor NM, Rijal OM, Yunus A, Mahayiddin AA, Peng GC, Abu-Bakar SA. A statistical interpretation of the chest radiograph for the detection of pulmonary tuberculosis. In: *2010 IEEE EMBS Conference on Biomedical Engineering and Sciences (IECBES)* (IEEE). (2010), 47–51.
10. Pedrazzoli D, Lalli M, Boccia D, Houben R, Kranzer K. Can tuberculosis patients in resource-constrained settings afford chest radiography? *Eur Respir J.* (2017) 49:1601877. doi: 10.1183/13993003.01877-2016
11. Schmidhuber J. Deep learning in neural networks: an overview. *Neural Netw.* (2015) 61:85–117. doi: 10.1016/j.neunet.2014.09.003
12. Moher D, Liberati A, Tetzlaff J, Altman DG, Prisma Group. Preferred reporting items for systematic reviews and meta-analyses: the PRISMA statement. *PLoS Med.* (2009) 6:e1000097. doi: 10.1371/journal.pmed.1000097
13. Duong LT, Le NH, Tran TB, Ngo VM, Nguyen PT. Detection of tuberculosis from chest X-ray images: boosting the performance with vision transformer and transfer learning. *Expert Syst Appl.* (2021) 184:115519. doi: 10.1016/j.eswa.2021.115519
14. Norval M, Wang Z, Sun Y. Evaluation of image processing technologies for pulmonary tuberculosis detection based on deep learning convolutional neural networks. *J Adv Inform Technol.* (2019) 12:253–9. doi: 10.12720/jait.12.3.253-259
15. Rahman M, Cao Y, Sun X, Li B, Hao Y. Deep pre-trained networks as a feature extractor with XGBoost to detect tuberculosis from chest X-ray. *Comput Elect Eng.* (2021) 93:107252. doi: 10.1016/j.compeleceng.2021.107252
16. Govindarajan S, Swaminathan R. Extreme learning machine based differentiation of pulmonary tuberculosis in chest radiographs using integrated local feature descriptors. *Comput Methods Progr Biomed.* (2021) 204:106058. doi: 10.1016/j.cmpb.2021.106058

17. Alawi AE, Al-basser A, Sallam A, Al-sabaeei A, Al-khateeb H. Convolutional neural networks model for screening tuberculosis disease. In: *2021 International Conference of Technology, Science and Administration (ICTSA)* (IEEE). (2021), 1–5.
18. Khatibi T, Shahsavari A, Farahani A. Proposing a novel multi-instance learning model for tuberculosis recognition from chest X-ray images based on CNNs, complex networks and stacked ensemble. *Phys Eng Sci Med.* (2021) 44:291–311. doi: 10.1007/s13246-021-00980-w
19. Ayaz M, Shaukat F, Raja G. Ensemble learning based automatic detection of tuberculosis in chest X-ray images using hybrid feature descriptors. *Phys Eng Sci Med.* (2021) 44:183–94. doi: 10.1007/s13246-020-00966-0
20. Priya PA, Vimina ER. Tuberculosis detection from CXR: an approach using transfer learning with various CNN architectures. In: *International Conference on Communication, Computing and Electronics Systems: Proceedings of ICCCES 2020*. Vol. 733 (Springer Nature). (2021), 407p.
21. Dasanayaka C, Dissanayake MB. Deep learning methods for screening pulmonary tuberculosis using chest X-rays. *Comput Methods Biomech Biomed Eng Imaging Vis.* (2021) 9:39–49. doi: 10.1080/21681163.2020.1808532
22. Msonda P, Uymaz SA, Karaagaç SS. Spatial pyramid pooling in deep convolutional networks for automatic tuberculosis diagnosis. *Traitement du Signal.* (2020) 37:1075–1084. doi: 10.18280/ts.370620
23. Owais M, Arsalan M, Mahmood T, Kim YH, Park KR. Comprehensive computer-aided decision support framework to diagnose tuberculosis from chest X-ray images: data mining study. *JMIR Med Inform.* (2020) 8:e21790. doi: 10.2196/21790
24. Yoo SH, Geng H, Chiu TL, Yu SK, Cho DC, Heo J, et al. Study on the TB and non-TB diagnosis using two-step deep learning-based binary classifier. *J Instrument.* (2020) 15:P10011. doi: 10.1088/1748-0221/15/10/P10011
25. Sathitratanacheewin S, Sunanta P, Pongpirul K. Deep learning for automated classification of tuberculosis-related chest X-Ray: dataset distribution shift limits diagnostic performance generalizability. *Heliyon.* (2020) 6:e04614. doi: 10.1016/j.heliyon.2020.e04614
26. Sahlol AT, Abd Elaziz M, Tariq Jamal A, Damaševičius R, Farouk Hassan O. A novel method for detection of tuberculosis in chest radiographs using artificial ecosystem-based optimization of deep neural network features. *Symmetry.* (2020) 12:1146. doi: 10.3390/sym12071146
27. Das D, Santosh KC, Pal U. Inception-based deep learning architecture for tuberculosis screening using chest X-rays. In: *2020 25th International Conference on Pattern Recognition (ICPR)*. Vol. 10 (IEEE) (2021), 3612–9.
28. Rahman T, Khandakar A, Kadir MA, Islam KR, Islam KF, Mazhar R, et al. Reliable tuberculosis detection using chest X-ray with deep learning, segmentation and visualization. *IEEE Access.* (2020) 8:191586–601. doi: 10.1109/ACCESS.2020.3031384
29. Munadi K, Muchtar K, Maulina N, Pradhan B. Image enhancement for tuberculosis detection using deep learning. *IEEE Access.* (2020) 8:217897–907. doi: 10.1109/ACCESS.2020.3041867
30. Oloko-Oba M, Viriri S. Tuberculosis abnormality detection in chest X-rays: a deep learning approach. In: *International Conference on Computer Vision and Graphics*. Vol. 14 (Cham: Springer) (2020), 121–32.
31. Xie Y, Wu Z, Han X, Wang H, Wu Y, Cui L, et al. Computer-aided system for the detection of multicategory pulmonary tuberculosis in radiographs. *Journal of Healthcare Engineering.* (2020) 2020:1–12. doi: 10.1155/2020/9205082
32. Verma D, Bose C, Tufchi N, Pant K, Tripathi V, Thapliyal A. An efficient framework for identification of tuberculosis and pneumonia in chest X-ray images using Neural Network. *Procedia Computer Science.* (2020) 171:217–24. doi: 10.1016/j.procs.2020.04.023
33. Tasci E. Pre-processing effects of the tuberculosis chest x-ray images on pre-trained cnns: an investigation. *In The International Conference on Artificial Intelligence and Applied Mathematics in Engineering. Vol. 20 (Cham: Springer).* (2019), 589-596. doi: 10.1007/978-3-030-36178-5_48
34. Rajaraman S, Antani SK. Modality-specific deep learning model ensembles toward improving TB detection in chest radiographs. *IEEE Access.* (2020) 8:27318–26. doi: 10.1109/ACCESS.2020.2971257
35. Abideen ZU, Ghafoor M, Munir K, Saqib M, Ullah A, Zia T, et al. Uncertainty assisted robust tuberculosis identification with bayesian convolutional neural networks. *IEEE Access.* (2020) 8:22812–25. doi: 10.1109/ACCESS.2020.2970023
36. Hijazi MH, Hwa SK, Bade A, Yaakob R, Jeffree MS. Ensemble deep learning for tuberculosis detection using chest X-Ray and canny edge detected images. *IAES Int J Artif Intel.* (2019) 8:429. doi: 10.11591/ijai.v8.i4.pp429-435
37. Pasa F, Golkov V, Pfeiffer F, Cremers D, Pfeiffer D. Efficient deep network architectures for fast chest X-ray tuberculosis screening and visualization. *Sci Rep.* (2019) 9:1–9. doi: 10.1038/s41598-019-42557-4
38. Meraj SS, Yaakob R, Azman A, Rum SN, Shahrel A, Nazri A, et al. Detection of pulmonary tuberculosis manifestation in chest x-rays using different convolutional neural network (CNN) models. *Int J Eng Adv Technol.* (2019) 9:2270–5. doi: 10.35940/ijeat.A2632.109119
39. Ahsan M, Gomes R, Denton A. Application of a convolutional neural network using transfer learning for tuberculosis detection. In: *2019 IEEE International Conference on Electro Information Technology (EIT)* (IEEE) (2019), 427–33.
40. Nguyen QH, Nguyen BP, Dao SD, Unnikrishnan B, Dhingra R, Ravichandran SR, et al. Deep learning models for tuberculosis detection from chest x-ray images. In: *2019 26th International Conference on Telecommunications (ICT)* (IEEE) (2019), 381–5.
41. Ho TK, Gwak J, Prakash O, Song JI, Park CM. Utilizing pretrained deep learning models for automated pulmonary tuberculosis detection using chest radiography. In: *11th Asian Conference on Intelligent Information and Database Systems, ACIIDS* (Springer Verlag) (2019), 395–403.
42. Heo SJ, Kim Y, Yun S, Lim SS, Kim J, Nam CM, et al. Deep learning algorithms with demographic information help to detect tuberculosis in chest radiographs in annual workers' health examination data. *Int J Environ Res Public Health.* (2019) 16:250. doi: 10.3390/ijerph16020250
43. Hernández A, Panizo Á, Camacho D. An ensemble algorithm based on deep learning for tuberculosis classification. In: *International Conference on Intelligent Data Engineering and Automated Learning* (Cham: Springer). (2019), 145–54.
44. Hijazi M, Yang L, Alfred R, Mahdin H, Yaakob R. Ensemble deep learning for tuberculosis detection. *Indonesian J Elect Eng Comput Sci.* (2020) 8:429. doi: 10.11591/ijeecs.v17.i2.pp1014-1020
45. Abbas A, Abdelsamea MM. Learning transformations for automated classification of manifestation of tuberculosis using convolutional neural network. In: *2018 13th International Conference on Computer Engineering and Systems (ICCES)* (IEEE). (2018), 122–6.
46. Karnkawinpong T, Limpiyakorn Y. Chest X-ray analysis of tuberculosis by convolutional neural networks with affine transforms. In: *Proceedings of the 2018 2nd International Conference on Computer Science and Artificial Intelligence.* (2018), 90–3.
47. Stirenko S, Kochura Y, Alienin O, Rokovyi O, Gordienko Y, Gang P, et al. Chest X-ray analysis of tuberculosis by deep learning with segmentation and augmentation. In: *2018 IEEE 38th International Conference on Electronics and Nanotechnology (ELNANO)* (IEEE) (2018), 422–8.
48. Becker AS, Blüthgen C, Sekaggya-Wiltshire C, Castelnuovo B, Kambugu A, Fehr J, et al. Detection of tuberculosis patterns in digital photographs of chest X-ray images using deep learning: feasibility study. *Int J Tubercul Lung Dis.* (2018) 22:328–35. doi: 10.5588/ijtld.17.0520
49. Liu C, Cao Y, Alcantara M, Liu B, Brunette M, Peinado J, et al. TX-CNN: Detecting tuberculosis in chest X-ray images using convolutional neural network. In: *2017 IEEE International Conference on Image Processing (ICIP)* (IEEE). (2017), 2314–8.
50. Oloko-Oba M, Viriri S. Ensemble of convolution neural networks for automatic tuberculosis classification. In: *International Conference on Computational Collective Intelligence* (Cham: Springer) (2021), 549–59. doi: 10.1007/978-3-030-88081-1_41
51. Lee JH, Park S, Hwang EJ, Goo JM, Lee WY, Lee S, et al. Deep learning–based automated detection algorithm for active pulmonary tuberculosis on chest radiographs: diagnostic performance in systematic screening of asymptomatic individuals. *Eur Radiol.* (2021) 31:1069–80. doi: 10.1007/s00330-020-07219-4
52. Zhang R, Duan H, Cheng J, Zheng Y. A study on tuberculosis classification in chest X-ray using deep residual attention networks. In: *2020 42nd Annual International Conference of the IEEE Engineering in Medicine & Biology Society (EMBC)* (IEEE) (2020), 1552–5.
53. Hwang EJ, Park S, Jin KN, Kim JI, Choi SY, Lee JH, et al. Development and validation of a deep learning–based automatic detection algorithm for

active pulmonary tuberculosis on chest radiographs. *Clin Infect Dis.* (2019) 69:739–47. doi: 10.1093/cid/ciy967
54. Rajpurkar P, Irvin J, Ball RL, Zhu K, Yang B, Mehta H, et al. Deep learning for chest radiograph diagnosis: a retrospective comparison of the CheXNeXt algorithm to practicing radiologists. *PLoS Med.* (2018) 15:e1002686. doi: 10.1371/journal.pmed.1002686
55. Lakhani P, Sundaram B. Deep learning at chest radiography: automated classification of pulmonary tuberculosis by using convolutional neural networks. *Radiology.* (2017) 4:574–82. doi: 10.1148/radiol.2017162326
56. Cao K, Zhang J, Huang M, Deng T. X-ray classification of tuberculosis based on convolutional networks. In: *2021 IEEE International Conference on Artificial Intelligence and Industrial Design (AIID)* (IEEE). (2021), 125–9. doi: 10.1109/AIID51893.2021.9456476
57. Karaca BK, Güney S, Dengiz B, Agildere M. Comparative study for tuberculosis detection by using deep learning. In: *2021 44th International Conference on Telecommunications and Signal Processing (TSP)* (IEEE) (2021), 88–91.
58. Saif AF, Imtiaz T, Shahnaz C, Zhu WP, Ahmad MO. Exploiting cascaded ensemble of features for the detection of tuberculosis using chest radiographs. *IEEE Access.* (2021) 9:112388–99. doi: 10.1109/ACCESS.2021.3102077
59. Imam OT, Haque M, Shahnaz C, Imran SA, Islam MT, Islam MT. Detection of tuberculosis from chest X-ray images based on modified inception deep neural network model. In: *2020 IEEE International Women in Engineering (WIE) Conference on Electrical and Computer Engineering (WIECON-ECE)* (IEEE). (2020), 360–3.
60. Griffin T, Cao Y, Liu B, Brunette MJ. Object detection and segmentation in chest X-rays for tuberculosis screening. In: *2020 Second International Conference on Transdisciplinary AI (TransAI)* (IEEE) (2020), 34–42.
61. Rashid R, Khawaja SG, Akram MU, Khan AM. Hybrid RID network for efficient diagnosis of tuberculosis from chest X-rays. In: *2018 9th Cairo International Biomedical Engineering Conference (CIBEC)* (IEEE) (2018), 167–70.
62. Fehr J, Konigorski S, Olivier S, Gunda R, Surujdeen A, Gareta D, et al. Computer-aided interpretation of chest radiography reveals the spectrum of tuberculosis in rural South Africa. *NPJ Dig Med.* (2021) 4:1–10. doi: 10.1101/2020.09.04.20188045
63. Vats S, Singh S, Kala G, Tarar R, Dhawan S. iDoc-X: an artificial intelligence model for tuberculosis diagnosis and localization. *J Discrete Math Sci Cryptogr.* (2021) 24:1257–72. doi: 10.1080/09720529.2021.1932910
64. Rajpurkar P, O'Connell C, Schechter A, Asnani N, Li J, Kiani A, et al. CheXaid: deep learning assistance for physician diagnosis of tuberculosis using chest x-rays in patients with HIV. *NPJ Dig Med.* (2020) 3:1–8. doi: 10.1038/s41746-020-00322-2
65. Grivkov AV, Smirnov AA. Application of convolutional neural networks for diagnostics of tuberculosis. *AIP Conf Proc.* (2020) 2313:080011.
66. Gozes O, Greenspan H. Deep feature learning from a hospital-scale chest x-ray dataset with application to TB detection on a small-scale dataset. In: *2019 41st Annual International Conference of the IEEE Engineering in Medicine and Biology Society (EMBC)* (IEEE) (2019), 4076–9.
67. Karnkawinpong T, Limpiyakorn Y. Classification of pulmonary tuberculosis lesion with convolutional neural networks. *J Phys Conf Series.* (2019) 1195:012007. doi: 10.1088/1742-6596/1195/1/012007
68. Sivaramakrishnan R, Antani S, Candemir S, Xue Z, Abuya J, Kohli M, et al. Comparing deep learning models for population screening using chest radiography. *Med Imaging 2018 Comput Aided Diag.* (2018) 10575:105751E. doi: 10.1117/12.2293140
69. Vajda S, Karargyris A, Jaeger S, Santosh KC, Candemir S, Xue Z, et al. Feature selection for automatic tuberculosis screening in frontal chest radiographs. *J Med Syst.* (2018) 42:1–11. doi: 10.1007/s10916-018-0991-9
70. Puddy E, Hill C. Interpretation of the chest radiograph. Continuing education in anaesthesia. *Crit Care Pain.* (2007) 7:71–5. doi: 10.1093/bjaceaccp/mkm014
71. Gilpin C, Korobitsyn A, Migliori GB, Raviglione MC, Weyer K. The world health organization standards for tuberculosis care and management. *Eur Respir J.* (2018) 51:1800098. doi: 10.1183/13993003.00098-2018
72. Brownlee J. *4 Types of Classification Tasks in Machine Learning.* Machine Learning Mastery, 4p. Available online at: https://machinelearningmastery.com/types-of-classification-in~machine-learning (accessed November 25, 2021).
73. Jaeger S, Candemir S, Antani S, Wáng YX, Lu PX, Thoma G. Two public chest X-ray datasets for computer-aided screening of pulmonary diseases. *Quant Imaging Med Surg.* (2014) 4:475. doi: 10.3978/j.issn.2223-4292.2014.11.20
74. Irvin J, Rajpurkar P, Ko M, Yu Y, Ciurea-Ilcus S, Chute C, et al. Chexpert: a large chest radiograph dataset with uncertainty labels and expert comparison. *Proc AAAI conf Artif Intell.* (2019) 33:590–7. doi: 10.1609/aaai.v33i01.3301590
75. Johnson AE, Pollard TJ, Greenbaum NR, Lungren MP, Deng CY, Peng Y, et al. MIMIC-CXR-JPG, a large publicly available database of labeled chest radiographs. *arXiv[Prepint].arXiv:1901.07042.* (2019).
76. Hwang S, Kim HE, Jeong J, Kim HJ. A novel approach for tuberculosis screening based on deep convolutional neural networks. *Med Imaging Comput Aided Diag.* (2016) 9785:97852W. doi: 10.1117/12.2216198
77. Lalkhen AG, McCluskey A. Clinical tests: sensitivity and specificity. *Continuing Educ Anesth Crit Care Pain.* (2008) 8:221–3. doi: 10.1093/bjaceaccp/mkn041
78. Davis J, Goadrich M. The relationship between precision-recall and ROC curves. In: *Proceedings of the 23rd International Conference on Machine Learning 2006 Jun 25*, 233–40.

Conflict of Interest: The authors declare that the research was conducted in the absence of any commercial or financial relationships that could be construed as a potential conflict of interest.

Publisher's Note: All claims expressed in this article are solely those of the authors and do not necessarily represent those of their affiliated organizations, or those of the publisher, the editors and the reviewers. Any product that may be evaluated in this article, or claim that may be made by its manufacturer, is not guaranteed or endorsed by the publisher.

Copyright © 2022 Oloko-Oba and Viriri. This is an open-access article distributed under the terms of the Creative Commons Attribution License (CC BY). The use, distribution or reproduction in other forums is permitted, provided the original author(s) and the copyright owner(s) are credited and that the original publication in this journal is cited, in accordance with accepted academic practice. No use, distribution or reproduction is permitted which does not comply with these terms.

frontiers | Frontiers in Medicine

TYPE Original Research
PUBLISHED 06 September 2022
DOI 10.3389/fmed.2022.897695

Check for updates

OPEN ACCESS

EDITED BY
Emmanuel Twumasi Osei,
University of British Columbia,
Okanagan Campus, Canada

REVIEWED BY
Mehra Haghi,
University of Technology
Sydney, Australia
Brady Rae,
University Medical Center
Groningen, Netherlands

*CORRESPONDENCE
Xinhua Yu
xinhuayu@fz-borstel.de
Frank Petersen
fpetersen@fz-borstel.de

SPECIALTY SECTION
This article was submitted to
Pulmonary Medicine,
a section of the journal
Frontiers in Medicine

RECEIVED 16 March 2022
ACCEPTED 15 August 2022
PUBLISHED 06 September 2022

CITATION
Kasper B, Yue X, Goldmann T,
Gülsen A, Kugler C, Yu X and
Petersen F (2022) Air exposure and cell
differentiation are essential for
investigation of SARS-CoV-2 entry
genes in human primary airway
epithelial cells *in vitro*.
Front. Med. 9:897695.
doi: 10.3389/fmed.2022.897695

COPYRIGHT
© 2022 Kasper, Yue, Goldmann,
Gülsen, Kugler, Yu and Petersen. This is
an open-access article distributed
under the terms of the Creative
Commons Attribution License (CC BY).
The use, distribution or reproduction
in other forums is permitted, provided
the original author(s) and the copyright
owner(s) are credited and that the
original publication in this journal is
cited, in accordance with accepted
academic practice. No use, distribution
or reproduction is permitted which
does not comply with these terms.

Air exposure and cell differentiation are essential for investigation of SARS-CoV-2 entry genes in human primary airway epithelial cells *in vitro*

Brigitte Kasper[1], Xiaoyang Yue[1], Torsten Goldmann[2], Askin Gülsen[1,3], Christian Kugler[1,3], Xinhua Yu[1]* and Frank Petersen[1]*

[1]Priority Area Chronic Lung Diseases, Research Center Borstel, Member of the German Center for Lung Research (DZL), Borstel, Germany, [2]Pathology, Research Center Borstel, Member of the German Center for Lung Research (DZL), Borstel, Germany, [3]Department of Surgery, LungenClinicGrosshansdorf, Grosshansdorf, Germany

Background: *In-vitro* models of differentiated primary human airway epithelial cells are a valuable tool to study severe acute respiratory syndrome coronavirus 2 (SARS-CoV-2) infection. Through the use of these models, it has been shown that the expression of SARS-CoV-2 entry genes in human airway epithelia is influenced by various factors such as age, sex, smoking status, and pathogenic conditions. In this study, we aimed to determine the effects of cell culture conditions and donor demographic and clinical characteristics on the expression of SARS-CoV-2 entry genes including angiotensin converting enzyme 2 (ACE2), transmembrane serine protease 2 (TMPRSS2), cathepsin L (CTSL), and tyrosine protein kinase receptor UFO (AXL) in primary airway epithelial cells.

Methods: Eleven lung cancer patients with or without chronic obstructive pulmonary disease (COPD) or asthma were recruited. Human bronchial epithelial cells (HBEC) or small airway epithelial cells (SAEC) isolated from submerged or air-liquid interface (ALI) cultures were analyzed by quantitative real-time PCR. We also tested for correlations with clinical data.

Results: In ALI cultures, the expression of AXL was significantly higher in HBEC than in SAEC. In addition, the expression of ACE2, TMPRSS2, and CTSL was significantly increased in both HBEC and SAEC differentiated under ALI conditions compared with the submerged culture. Negligible association was found between the expression of SARS-CoV-2 entry genes in SAEC and the age, sex, smoking status, and complication of COPD, asthma or hypertension of the cell donors.

Conclusion: These results demonstrate that the expression of SARS-CoV-2 entry genes in differentiated primary airway epithelial cells *in-vitro* is much more influenced by individual culture conditions than by specific characteristics of individual donors.

KEYWORDS

primary human airway epithelial cells, SARS-CoV-2 entry genes, submerged culture, ALI culture, COVID-19

Introduction

The interaction between the virus spike (S) protein and entry receptors on human respiratory epithelial cells is a critical step for infection with severe acute respiratory syndrome coronavirus 2 (SARS-CoV-2), the causative agent of 2019 coronavirus disease (COVID-19) (1). As the major cell entry receptor for SARS-CoV-2, angiotensin converting enzyme 2 (ACE2) recognizes the S1 receptor binding domain and mediates virus entry *via* two major pathways, cathepsin L-dependent endocytosis and transmembrane serine protease 2 (TMPRSS2)-dependent membrane fusion (1–3). Besides ACE2, the tyrosine protein kinase receptor UFO (AXL) was recently reported to be another entry receptor for SARS-CoV-2 (4). In contrast to ACE2, AXL promotes viral entry by interacting with the N-terminal domain of the SARS-CoV-2 S protein (4).

In-vitro modeling of SARS-CoV-2 infection in primary human airway epithelial cells is a valuable tool for understanding the molecular mechanisms underlying viral infection and for the search for potential COVID-19 drugs (5). In these *in-vitro* systems, primary human airway epithelial cells isolated from surgical resections of patients with various diseases are propagated in different cell culture systems, including submerged, air-liquid interface (ALI), and 3-dimensional cell cultures (3D; spheroids or bronchospheres) (6). Furthermore, age, sex, smoking status, and airway clinical complications have been reported to be associated with ACE2 expression in human airway epithelium (7–9). In addition, epithelial cells isolated from different parts of the airways, such as the nasal passages, bronchi, and small airways, also have different expression levels of ACE2 (10–12), which may further increase the complexity of modeling these differences with *in-vitro* systems.

In this study, we aimed to investigate the effects of different types of airway epithelial cells and cell culture conditions, as well as age, sex, smoking status, and clinical characteristics of the subjects on the expression of SARS-CoV-2 entry genes in differentiated cells *in-vitro*. For this purpose, human bronchial epithelial cells (HBEC) and small airway epithelial cells (SAEC) were isolated from surgical biopsies of the lungs of 11 patients with lung cancer and cultured *in vitro*. Our results show that the expression of SARS-CoV-2 entry genes was strongly influenced by cell culture systems, whereas it was not significantly related to patient age, sex, and smoking status or pulmonary co-morbidities such as chronic obstructive pulmonary disease (COPD) and asthma.

Abbreviations: ACE2, angiotensin converting enzyme 2; ALI, air-liquid interface; AXL, tyrosine protein kinase receptor UFO; CTSL, cathepsin L; COPD, chronic obstructive pulmonary disease; HBEC, human bronchial epithelial cells; SAEC, small airway epithelial cells; SM, submerged; TMPRSS2, transmembrane serine protease 2.

Materials and methods

Materials

Collagen I from human skin, Pronase, DNase I, SBTI, accutase, and IgG from human serum were purchased from Sigma-Aldrich; PneumaCult™-EX PLUS, PneumaCult™-ALI were from STEMCELL Technologies; EASYstrainer Cell Sieves (100 and 40 μm), transwell inserts and 96 well plates with cell-repellent surface were from Greiner Bio-One; High Pure RNA Isolation kit, Transcriptor First Strand cDNA synthesis kit, SYBR Green PCR Master Mix were from Roche Diagnostics.

Antibodies for flow cytometry staining were ACE2-AlexaFluor 647 (clone E-11), AXL-AlexaFluor647 (clone B-2), acetylated α-Tubulin-AlexaFluor 488 (clone 6-11B-1), MUC5AC-AlexaFluor 488 (clone 45M1), CC10-AlexaFluor 488 (clone E-11), Cytokeratin 5-AlexaFluor 488 (clone RCK103) were purchased from Santa Cruz Biotechnology; Mouse IgG1-AlexaFluor 488, Mouse IgG1-AlexaFluor 647 were from BioLegend, Mouse IgG2b-FITC was from DAKO; and Live/Dead™ Fixable Blue Dead Cell Stain was from Invitrogen.

Patients

Lung tissue and/or bronchus from 11 patients were provided by the Pathology Department (Research Center Borstel, Germany). All patients underwent lung resection and were characterized as lung cancer stages ranging from IA to IIB. These were samples from residual material without a declaration of consent (AZ 12-220) with defined accompanying data. Here, the regulations of the Bio Material Bank Nord are applied (AZ 14-225). The study was conducted in accordance with the Declaration of Helsinki. The use of biomaterial and data for this study was approved by the local ethics committee of the University Lübeck (AZ 17-131). Sex, age, and smoking behavior, and additional information for every individual are provided in Table 1 and Supplementary Table S1.

Isolation and submerged culture of primary human airway epithelial cells

Tissue was assembled during routine surgical intervention from lung cancer patients. Since it has been reported that there are significant difference in expression of SARS-CoV-2 entry genes between tumor and the adjacent tumor-free tissue (13), epithelial cells were isolated from tumor free tissues. Lung or bronchial tissue was placed in a 100 mm culture dish and rinsed in D-PBS. Tissue was cut in smaller pieces, excess surrounding tissue was dissected out, and bronchial tissue separated. A scalpel was used to cut open the bronchial pieces, and cut the tissue into 2–3 mm pieces, for better exposure

to enzyme solution. Bronchial tissue was then transferred to a tube containing 20 ml of RPMI1640, supplemented with 2 mM L-glutamin, 1.4 mg/ml pronase, 0.1 mg/ml DNAse I and placed at 4–8°C for overnight incubation. The next day, FCS was added to 10% to stop the action of the protease, and the tube was inverted several times to mix well and dislodge cells. Bronchial tissue was discarded, and the cell-containing supernatant was transferred through EASYstrainer Cell Sieves (100 and 40 μm) to new tubes and centrifuged 10 min at 600×g. Epithelial cells were then collected into a new tube and centrifuged after which pellet was resuspended in RPMI1640 to rinse cells and allow them to be counted. Cells were centrifuged again and the pellet was resuspended in expansion medium (PneumaCult EX PLUS™ Complete Medium), transferred to collagen I-coated (3.45 μg/cm^2) 100 mm culture plate (150.000–300.000 cells per culture plate), and incubated at 37°C, 5% CO_2. Medium was changed every 3–4 days until cells reached desired confluency. Cells isolated from lung tissue (secondary/tertiary bronchi and bronchioles) were named small airway epithelial cells (SAEC) and cells isolated from main (primary) bronchus were named human bronchial epithelial cells (HBEC) (Supplementary Figure S1). All cells could be expanded to passage 8–11. Most of the experiments were done with cells from passage 3–6.

Air-liquid interface (ALI) culture of primary human airway epithelial cells

Primary human airway epithelial cells were expanded and differentiated at ALI *in-vitro* following the protocol given by STEMCELL Technologies. Cells were expanded on collagen I-coated (3.45 μg/cm^2) dishes in expansion medium, and harvested by trypsinization with SBTI neutralization. The apical chambers of 6.5 mm transwell inserts were coated with 5 μg/cm^2 collagen I, and cells were seeded at 3 × 10^5 cells/insert in expansion medium, and the basolateral chambers received 500 μL of expansion medium alone. Once the epithelial cells reached confluence, the apical growth media was removed, and the basolateral medium was replaced with PneumaCult™-ALI Maintenance Medium (ALI-MM), initiating day 0 of the ALI mucociliary culture system. Epithelial cultures were allowed to differentiate at ALI *in-vitro* for 14–21 days at 37°C, 5% CO_2. In the basolateral chambers ALI-MM was changed every other day. Differentiation of the cells was confirmed by immunohistochemistry (Supplementary Figure S2).

3D culture of primary human airway epithelial cells

For the generation of spheroids 2–3 × 10^6 cells were resuspended in 10 ml ALI-MM and seeded onto 96 well plates with cell-repellent surface (100 μl cells/well). Plates were centrifuged for 1 min at 450×g and incubated at 37°C, 5% CO_2 for 4–7 days. The spheroids were featured by ciliated cells on the apical, outer side (Supplementary Figure S3).

Detection of ACE2 and AXL by flow cytometry

For flow cytometry ALI or 3D cultured cells were used. ALI cultured cells were detached from transwell membranes using accutase, and 3D cultured cells were carefully resuspended. The surface markers of cells were analyzed for the presence of ACE2, AXL, and acetylated α-Tubulin using AlexaFluor 488- or AlexaFluor 647 conjugated monoclonal antibodies (all diluted 1/100 in D-PBS/Live-Dead stain (1:1000), supplemented with 60 μg/ml human IgG (Sigma Aldrich) at 8°C for 30 min. After that, cells were washed in FACS buffer (D-PBS/0.1% BSA), fixed in 4% PFA at room temperature (RT) for 15 min and permeabilized in 0.2% Triton X-100 at RT for 20 min. Intracellular markers MUC5AC, CC10 and cytokeratin 5 were analyzed using AlexaFluor 488 conjugated monoclonal antibodies (all diluted 1/100 in FACS buffer, supplemented with 60 μg/ml human IgG) at 8°C for overnight. The cells were washed and analyzed by flow cytometry (LSRII, BD Biosciences), and post-acquisition analysis was carried out using FCSExpress 7 (De Novo Software).

RNA extraction, cDNA synthesis and quantitative PCR

RNA was extracted from cell lysates of primary airway epithelial cells (either expanded in submerged cultures or differentiated in ALI cultures), by using the High Pure RNA Isolation kit, and reverse transcription of 0.5–1 μg of total RNA was performed using the Transcriptor First Strand cDNA synthesis kit. Amplifications of target and HPRT genes were performed using SYBR Green PCR Master Mix, following the manufacturer's instructions, in a LightCycler 480 System (Roche Diagnostics). Data analyses were done using the LightCycler 480 relative quantification software with data normalized to the mRNA level of HPRT housekeeping gene. The sequences of the primer used were synthetized by Metabion and include: *ACE2* forward: AACTACCCGGAG GGCATAG and reverse: CTGGGATGTCCGGTCATATT; *AXL* forward: AACCAGGACGACTCCATCC and reverse: AGC TCTGACCTCGTGCAGAT; *CTSL* forward: GGGAGGGCAGT TGAGGAC and reverse: GCAAGGATGAGTGTAGGATTCA; *TMPRSS2* forward: CGCTGGCCTACTCTGGAA and reverse: CTGAGGAGTCGCACTCTATCC; *HPRT* forward: TGACCTT GATTTATTTTGCATACC and reverse: CGAGCAAGACG TTCAGTCCT.

TABLE 1 Demographic and clinical features of patients recruited for the isolation of airway epithelial cells.

	Lung cancer	Lung cancer + asthma	Lung cancer + COPD
Number of patients (total = 11)	4	4	3
Male/female	3/1	2/2	2/1
Age [years] (range)	74.0 (68–83)	69.3 (57–81)	71.7 (70–75)
Smoking status (current/ex-smoker)	3/1	2/2	0/3
Hypertension, *n* (4/11)	2	2	0

Statistical analysis

For all statistical analyses, the GraphPad Prism 5 software package was used (GraphPad Software). For quantitative data, statistical significance between groups was determined by paired *t* test, unpaired *t* test, one-way ANOVA followed by Tukey's Multiple Comparison Test, or Kruskal-Wallis test followed by Dunn's Multiple Comparison Test. Pearson's correlation was used to measures the statistical relationship between two continuous variables. For patients whose SAEC were used in multiple cultures, mean values of gene expression levels were used for the correlation analysis. A p values of 0.05 or lower were considered statistically significant.

Results

Patients and cells

As summarized in Table 1, tumor free lung tissues from 11 patients with lung cancer was studied, including 2 with squamous cell carcinoma, 8 with adenocarcinoma and 1 with non-small cell lung cancer (NSCLC; not otherwise specified). The 11 patients were 8 former smokers and 3 current smokers, 7 men and 4 women. The mean age of the patients was 72 years and ranged from 57 to 83 years. SAEC were isolated from all 11 patients, whereas HBEC were isolated from 4 of them. The isolated primary airway epithelial cells were passaged and then cultured in submerged or ALI cultures to examine the expression of SARS-CoV-2 entry genes.

HBEC and SAEC express comparable levels of SARS-CoV-2 entry genes with exception of AXL

First, we compared HBEC and SAEC with respect to the expression of SARS-CoV-2 entry genes. HBEC and SAEC isolated from same donors were cultured under both, submerged and ALI conditions, and the expression levels of *ACE2*, *TMPRSS2*, *CSTL,* and *AXL* were determined and normalized to the expression of housekeeping gene *HPRT*. As shown in Figure 1A, none of the four genes were significant differentially expressed when compared between submerged cultured HBEC and SAEC. When cells were differentiated under in ALI conditions, no significant difference was observed between HBEC and SAEC in expression levels of *ACE2*, *TMPRSS2,* and *CTSL*. However, expression of *AXL* was significantly higher in HBEC than in SAEC (0.98 ± 0.28 vs. 0.54 ± 0.23, $p = 0.0168$) (Figure 1B). Therefore, with the exception of *AXL* expression under ALI culture conditions, *in-vitro* differentiated HBEC and SAEC expressed comparable levels of SARS-CoV-2 entry genes.

SARS-CoV-2 entry gene expression is strongly associated with cell culture conditions

The above experiments provide preliminary evidence for a possible influence of cell culture conditions on the expression of SARS-CoV-2 entry genes. Therefore, HBEC cells derived from submerged and ALI cultures were examined for the expression of SARS-CoV-2 entry genes (Figure 2A). Notably, expression of *ACE2* in HBEC differentiated under ALI condition was significantly higher than those grown in submerged culture (0.094 ± 0.032 vs. 0.011 ± 0.004, $p = 0.0353$). In addition, the expression of the other two genes involved in ACE2-mediated viral entry, *TMPRSS2* (4.99 ± 1.10 vs. 1.81 ± 0.79, $p = 0.0313$) and *CTSL* (0.0082 ± 0.0012 vs. 0.0046 ± 0.0016, $p = 0.0018$), was also significantly increased in HBEC grown under ALI conditions compared to those grown in submerged culture. Similar findings were observed in SAEC cells, where differentiation under ALI conditions significantly increased the expression of *ACE2* (0.118 ± 0.052 vs. 0.010 ± 0.004, $p = 0.0313$), *TMPRSS2* (4.16 ± 0.95 vs. 0.99 ± 0.32, $p = 0.0121$) and *CTSL* (0.0061 ± 0.0009 vs. 0.0024 ± 0.0009, $p = 0.0349$) compared with submerged culture (Figure 2B). In contrast, the expression of *AXL* was not significantly different between the two cell culture conditions in both HBEC and SAEC.

SARS-CoV-2 entry gene expression is not associated with COPD or asthma

Because ALI culture is closer to physiological conditions than submerged culture, we focused on the expression of these

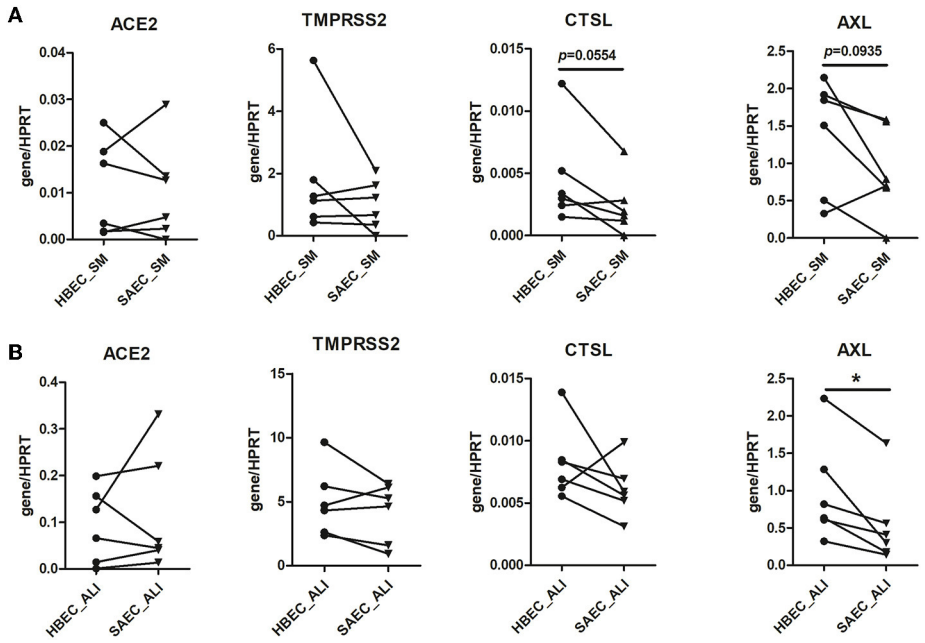

FIGURE 1
Comparison of expression of SARS-CoV-2 entry genes between human bronchial epithelial cells (HBEC) and small airway epithelial cells (SAEC). HBEC and SAEC derived from the same donors were submerged cultured (SM) **(A)** or differentiated under air-liquid interface (ALI) conditions (4 patients, 6 cultures) **(B)**. Gene expression of SARS-CoV-2 entry genes including ACE2, TMPRSS2, CTSL and AXL was determined by LightCycler PCR and normalized to HRPT expression. Comparisons on expression of the four SARS-CoV-2 genes between HBEC and SAEC from same donors are performed for cells cultured in submerged culture and ALI culture. Statistical significance was determined by paired *t* test ($n = 6$). *$p < 0.05$.

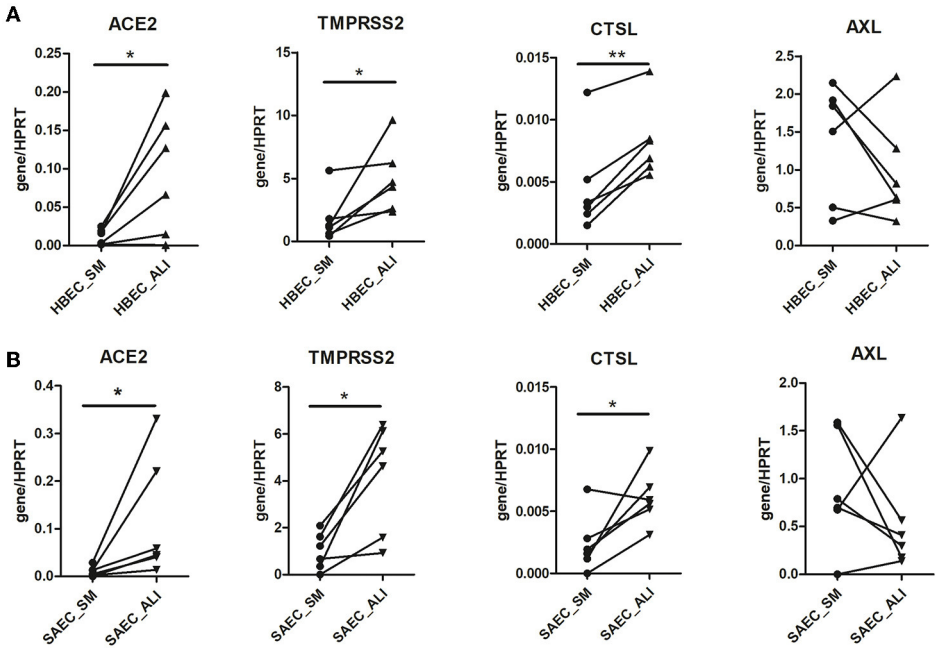

FIGURE 2
Effect of cell culture systems on the expression of SARS-CoV-2 entry genes in primary human airway epithelial cells. Human bronchial epithelial cells (HBEC) **(A)** and small airway epithelial cells (SAEC) **(B)** derived from the same donors were submerged cultured (SM) or differentiated under air-liquid interface (ALI) conditions (4 patients, 6 cultures). Gene expression of SARS-CoV-2 entry genes including ACE2, TMPRSS2, CTSL and AXL was determined by LightCycler PCR and normalized to HRPT expression. Expression of the four SARS-CoV-2 genes in HBEC and SAEC cultured in submerged culture was compared with those in ALI culture. Statistical significance was determined by paired *t* test ($n = 6$). *$p < 0.05$ and **$p < 0.01$.

genes in SAEC differentiated under the former conditions in the following experiments. Because there is evidence that respiratory diseases such as COPD and asthma may affect the expression of SARS-CoV-2 entry genes (14–16), we next examined whether SAEC derived from patients with COPD or asthma differed in gene expression from that of donors without asthma or COPD. As shown in Figure 3, the expression of *ACE2* in SAEC isolated from lung cancer patients without respiratory co-morbidities, lung cancer patients with asthma, and lung cancer patients with COPD was 0.041 ± 0.017, 0.057 ± 0.012, and 0.035 ± 0.011, respectively, with no significant differences between groups. No significant difference was also observed in the expression levels of *TMPRSS2*, *CTSL*, and *AXL* among SAEC isolated from the three patient groups, although there was a tendency for higher expression of *CTSL* and *AXL* in SAEC isolated from patients with co-morbidity of COPD, but this was not statistically significant.

Minimal effect of smoking status, sex, and age of cell donors or hypertension on the expression of SARS-CoV-2 entry genes in SAEC

Given that no significant difference in expression of SARS-CoV-2 entry genes was observed between SAEC from lung cancer patients with or without respiratory complications, we next combined all samples for further analysis. We first determined the effect of smoking by comparing data sets of current smokers and ex-smokers. Expression of *ACE2* in SAEC of current smokers (0.038 ± 0.0085) was not significantly different to that of former smokers (0.046 ± 0.010). Furthermore, levels expression of *TMPRSS2*, *CTSL,* and *AXL* in SAEC of current smokers were also comparable to those of former smokers (Figure 4A). When these SAEC were divided into two groups according to sex of the cell donors, only a significant difference was observed between the two subgroups in the expression of *TMPRSS2*, with female SAEC showing significantly higher expression than male SAEC (Figure 4B), while comparing of the four genes in patients with or without hypertension no significant differences could be observed (Figure 4C). To evaluate the effect of age of cell donors, a correlation analysis was performed. As shown in Figure 4D, only a marginally significant inverse correlation was detected between cell donor age and *TMPRSS2* expression, with a Pearson's correlation coefficient of−0.58 ($p = 0.0622$). Also, no significant correlation was found between the age of cell donors and expression of and the expression of *ACE2*, *CTSL* and *AXL*.

Surface expression of ACE2 and AXL on *in-vitro* differentiated SAEC

High expression of *ACE2*, *TMPRSS2* and *CTSL* in SAEC cultured under ALI condition implies that expression SARS-CoV-2 entry genes is dependent on the differentiation of SAEC. SAEC could either be differentiated under ALI conditions, or in 3D culture. Using flow cytometry, we next determined the surface protein expression of ACE2 and AXL on *in-vitro* differentiated SAEC. As shown in Supplementary Figure S4A, SAEC differentiated under ALI condition consisted of 27.00 ± 3.77% ciliated cells, 5.17 ± 1.26% goblet cells, 29.26 ± 3.28% club cells, and 24.97 ± 2.33% basal cells. Notably, majority of all four types of cell express ACE2 and AXL (Supplementary Figure S4B). Regarding the levels of surface expression of ACE2 and AXL, goblet cells showed highest expression of both ACE2 and AXL, while the expression levels of the other three types of cells were comparable (Supplementary Figure S4C). Further, flow cytometry analysis revealed that the cell composition in the 3D cultured spheroids is comparable to that in SAEC differentiated under ALI condition, with 19.00 ± 2.92% ciliated cells, 3.40 ± 0.43% goblet cells, 14.51 ± 1.59% club cells, and 19.11 ± 2.38% basal cells (Supplementary Figure S4D). Furthermore, similar to SAEC differentiated under ALI condition, majority of all above of four types of cells express both ACE2 and AXL, and goblet cells express higher levels of ACE2 and AXL than other three cells types (Supplementary Figures S4E,F).

Discussion

In-vitro differentiated human primary airway epithelial cells are a valuable tool for studying the interaction between SARS-CoV-2 and host cells. However, to generate a physiologically relevant *in-vitro* modeling system, several factors must be considered, including epithelial cell type, cell donor, and cell culture conditions. In the present study, we examined the expression of SARS-CoV-2 entry genes, including *ACE2*, *TMPRSS2*, *CTSL,* and *AXL* in primary human airway epithelial cells isolated from 11 lung cancer patients. Our results show that (i) the expression of SARS-CoV-2 entry genes is comparable between SAEC and HBEC, except for higher expression of *AXL* in HBEC than in SAEC, (ii) ALI culture leads to higher expression of *ACE2*, *TMPRSS2* and *CTSL* in both HBEC and SAEC than submerged culture, (iii) a negligible association was found between the expression of SARS-CoV-2 entry genes and donor-related parameters such as age, smoking status, and disease co-morbidities, (iv) *in-vitro* differentiated SAEC, either differentiated under ALI conditions or differentiated in 3D cultures express comparable levels of ACE2 and AXL on ciliated cells, goblet cells, club cells, and basal cells.

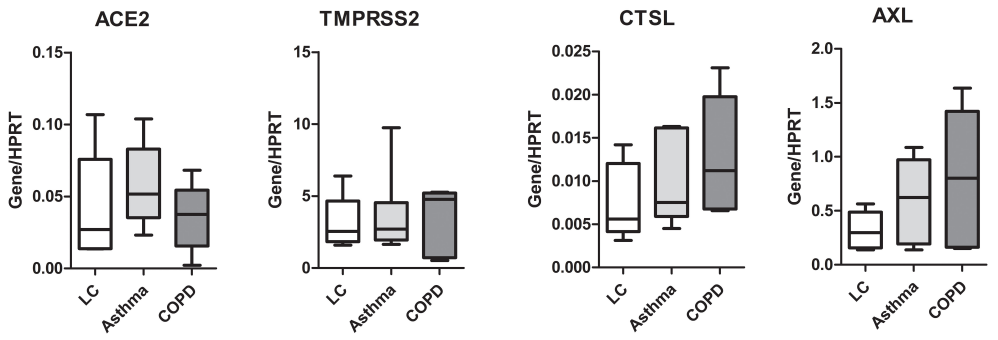

FIGURE 3
Expression of SARS-CoV-2 entry genes is not associated with asthma or COPD. SAEC isolated from patients with lung cancer (LC; 4 patients, 5 cultures), LC with asthma (4 patients, 6 cultures), and LC with COPD (3 patients, 5 cultures) were ALI cultured. Gene expression was analyzed by LightCycler PCR and normalized to HRPT expression. Data are presented as Box and Whiskers (min to max) and statistical significance was tested by one-way ANOVA followed by Tukey's Multiple Comparison Test, or Kruskal-Wallis test followed by Dunn's Multiple Comparison Test.

Using HBEC and SAEC isolated from the same donors, we were able to compare the expression of SARS-CoV-2 entry genes in the two cell types. To our knowledge, this is the first report describing differences in SARS-CoV-2 entry gene expression between donor-matched two types of *in-vitro* differentiated primary airway epithelial cells. Unexpectedly, no significant difference was found between HBEC and SAEC with respect to the expression of *ACE2*, *TMPRSS2*, or *CTSL*. This finding suggests that both HBEC and SACE are suitable for the *in-vitro* modeling system for investigating SARS-CoV-2. Previously, Aguiar and colleagues compared the expression of SARS-CoV-2 entry genes, including *ACE2*, *TMPRSS2*, and *CTSL*, in airway epithelial cells collected from bronchial brushings of the trachea, large airways, and small airways (10). Their results show that the expression of *ACE2* is highest in the trachea and lowest in the small airways, the expression of *TMPRSS2* is not significantly different among the three groups, and the expression of *CTSL* is highest in the small airways and lowest in the trachea. There are two possible reasons for the discrepancy between our results and the results of Aguiar's study. First, we examined gene expression from *in-vitro* differentiated primary human airway epithelial cells, whereas Aguiar focused on samples from bronchial brushings. The *in-vitro* differentiation process could alter the expression profile of SARS-CoV-2 entry genes. In contrast to our study, in which HBEC and SAEC were from the same donors, in Aguiar's study bronchial brushes were collected from different parts of the airways from different donors.

In addition to *ACE2*, it was recently suggested by Wang et al. (4) that *AXL* is another entry receptor for SARS-CoV-2. In their study, Wang et al. show that the expression of *ACE2* in lung and epithelial cells is much lower than that of *AXL*, suggesting that virus entry mediated by *AXL* plays an important role in promoting SARS-CoV-2 infection. Our observations on *in-vitro* differentiated primary SAEC confirmed that the expression of *AXL* at the mRNA level is indeed much higher than that of *ACE2*. Furthermore, the current study shows that *in-vitro* differentiated HBEC express more *AXL* than SAEC under ALI conditions, whereas such difference was not observed between the two cell types in submerged cultures. This finding suggests that the two types of primary epithelial cells show different expression of *AXL* under different *in-vitro* cell differentiation status.

In particular, the expression of *ACE2*, *TMPRSS2*, and *CTSL* is significantly increased in cells differentiated under ALI conditions compared with submerged culture, and this effect is observed in both HBEC and SAEC. Compared with submerged culture, ALI conditions correspond much more closely to the physiological situation of the lung epithelium *in-vivo*, so that the biological effects observed here appear to be more relevant than those observed under the former conditions (17). For example, primary airway epithelial cells differentiated under ALI conditions are able to reproduce the transcriptional profile of human airway epithelium (18) and recapitulate *in-vivo* responses to cigarette smoke (19). Because ACE2, TMPRSS2, and CTSL are all involved in ACE2-mediated SARS-CoV-2 entry (20), the current study suggests that the expression of genes involved in ACE2-mediated virus entry is related to the state of cell differentiation and that *in-vivo*-like differentiation conditions increase the expression of these genes. Based on these results, it is conceivable that primary airway epithelial cells differentiated under ALI conditions are better *in-vitro* modeling systems than submerged cultures for studying SARS-CoV-2 infection. Of note, while this paper was under review, a study by Guo et al. (12) has been published that clearly shows (i) ACE2 and TMPRSS2 expression is significantly increased in bronchial epithelial cells differentiated under ALI conditions compared to submerged cultured cells, (ii) differentiated ALI cultures are a suitable model to investigate SARS-CoV-2 infection in the presence or absence of therapeutic drugs. Therefore, findings from both the current study and Guo's study suggest that cells differentiated under ALI

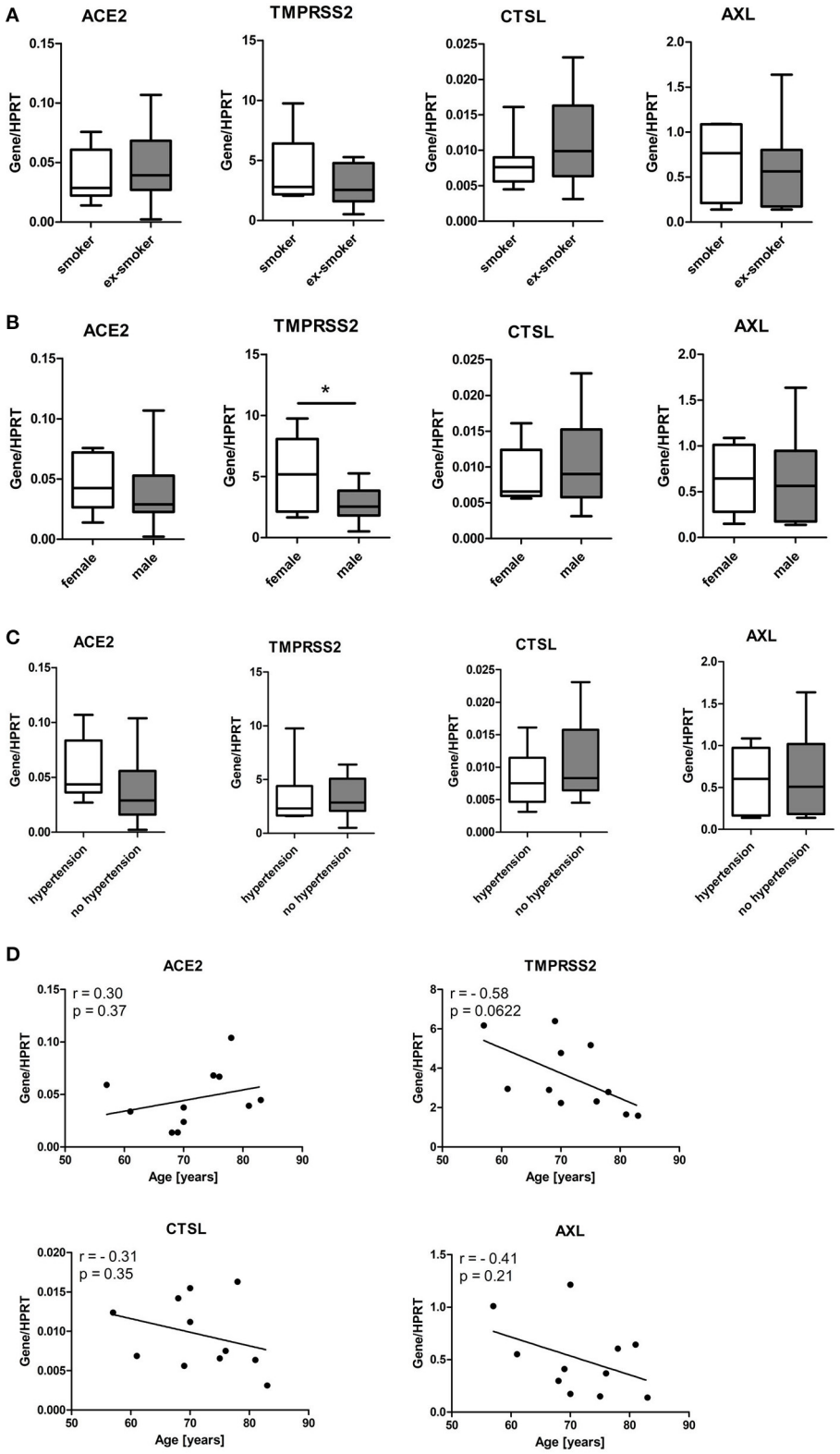

FIGURE 4
Influence of smoking status, gender, age and hypertension of patients on expression of SARS-CoV-2 entry genes in SAEC. SAEC isolated from 11 lung cancer patients were ALI cultured. Gene expression was analyzed by LightCycler PCR and normalized to HRPT expression. **(A)** Comparison of gene expression of SARS-CoV-2 entry genes between current smokers (3 patients, 7 cultures) and ex-smokers (8 patients, 11 cultures).

(Continued)

FIGURE 4 (Continued)
(B) Comparison of gene expression of SARS-CoV-2 entry genes between males (7 patients, 13 cultures) and females (4 patients, 5 cultures). **(C)** Comparison of gene expression of SARS-CoV-2 entry genes between patients with or without hypertension (4 patients, 6 cultures or 7 patients, 12 cultures, respectively). Data were presented as Box and Whiskers (min to max) and statistical significance was determined by unpaired *t* test. $*p < 0.05$. **(D)** Correlation between levels of gene expression and age of 11 patients. For patients whose SAEC were used in multiple cultures, mean values of gene expression levels were used for the correlation analysis. Pearson correlation coefficient (r) and *p* values are indicated.

conditions are physiologically relevant models for investigating SARS-CoV-2 infection.

The expression of SARS-CoV-2 entry genes, particularly *ACE2*, in human airway epithelium has been shown to be related to demographic and clinical characteristics. For example, a recent study reported that increased gene expression of *ACE2* was associated with male sex (16), while Watson et al. (11) reported that *ACE2* expression did not correlate with age and was not different dependent on gender. It has been suggested that COPD and asthma, two pathogenic respiratory diseases, are associated with increased and decreased expression of *ACE2*, respectively (9, 15, 16). In addition, current smokers have been shown to be associated with increased expression of *ACE2* compared with ex-smokers and never smokers (9, 15, 21). Unexpectedly, our results show that the above clinical and demographic characteristics are not associated with the expression of *ACE2* and *AXL* in *in-vitro* differentiated SAEC. This discrepancy suggests that the effects of these characteristics on the expression of SARS-CoV-2 entry genes *in-vivo* are not transmitted during *in-vitro* cell differentiation in this modeling system. Therefore, the differences between *in-vitro* and patient sampled cells may be of note to *in-vitro* investigations in the future. The current study has two major limitations. First, although tumor-free, all airway epithelial cells used in this study were isolated from patients with lung cancer, which could have an impact on the results. Second, the number of samples used in this study is relatively small. Only 11 patients were recruited for the study, which could affect the results. For example, correlation analysis showed an inverse but non-significant correlation between age and expression of *TMPRSS2*. In addition, a tendency for higher expression of *AXL* was observed in SAEC from COPD patients than in the other two groups. It is not clear whether the lack of statistical significance was due to the lack of effect or the limitation due to the small sample size.

In summary, the present study demonstrates that *in-vitro* model selection, but not cell donor characteristics, is the main factor affecting SARS-CoV-2 entry gene expression in primary airway epithelial cells differentiated *in-vitro*. This finding suggests that culture conditions drowns out the patient characteristics in the regulation of expression of SARS-CoV-2 entry genes. Therefore, airway epithelial cells differentiated under ALI conditions are superior to those grown submerged as *in-vitro* model systems for studying SARS-CoV-2 infection.

Data availability statement

The original contributions presented in the study are included in the article/Supplementary material, further inquiries can be directed to the corresponding author/s.

Ethics statement

The studies involving human participants were reviewed and approved by Local Ethics Committee of the University Lübeck. Written informed consent for participation was not required for this study in accordance with the national legislation and the institutional requirements.

Author contributions

BK, XYu, and FP were involved in the conception and design of the study. BK and XYue performed the experimental work. BK analyzed the data and generated figures. TG, AG, and CK contributed by providing essential materials (Lung biopsy and clinical information). XYu and BK were involved in drafting the manuscript. All authors were involved in revising the manuscript. All authors contributed to the article and approved the submitted version.

Funding

This study was supported by the German Federal Ministry of Education and Research (BMBF) *via* German Center for Lung Research (DZL) and Airway Research Center North (ARCN).

Acknowledgments

We thank Karoline Gaede from the Bio Material Bank Nord for providing help with ethical approval and access to the samples of the patients. We would like to thank Christine Engellenner and Diana Heinrich for technical assistance.

Conflict of interest

The authors declare that the research was conducted in the absence of any commercial or financial relationships that could be construed as a potential conflict of interest.

Publisher's note

All claims expressed in this article are solely those of the authors and do not necessarily represent those of their affiliated organizations, or those of the publisher, the editors and the reviewers. Any product that may be evaluated in this article, or claim that may be made by its manufacturer, is not guaranteed or endorsed by the publisher.

Supplementary material

The Supplementary Material for this article can be found online at: https://www.frontiersin.org/articles/10.3389/fmed.2022.897695/full#supplementary-material

References

1. Hoffmann M, Kleine-Weber H, Schroeder S, Kruger N, Herrler T, Erichsen S, et al. SARS-CoV-2 cell entry depends on ACE2 and TMPRSS2 and is blocked by a clinically proven protease inhibitor. *Cell.* (2020) 181:271–80. doi: 10.1016/j.cell.2020.02.052

2. Ou X, Liu Y, Lei X, Li P, Mi D, Ren L, et al. Characterization of spike glycoprotein of SARS-CoV-2 on virus entry and its immune cross-reactivity with SARS-CoV. *Nat Commun.* (2020) 11:1620. doi: 10.1038/s41467-020-15562-9

3. Zhou P, Yang XL, Wang XG, Hu B, Zhang L, Zhang W, et al. A pneumonia outbreak associated with a new coronavirus of probable bat origin. *Nature.* (2020) 579:270–3. doi: 10.1038/s41586-020-2012-7

4. Wang S, Qiu Z, Hou Y, Deng X, Xu W, Zheng T, et al. AXL is a candidate receptor for SARS-CoV-2 that promotes infection of pulmonary and bronchial epithelial cells. *Cell Res.* (2021) 31:126–40. doi: 10.1038/s41422-020-00460-y

5. Rijsbergen LC, van Dijk LLA, Engel MFM, de Vries RD, de Swart RL. *In vitro* modelling of respiratory virus infections in human airway epithelial cells: a systematic review. *Front Immunol.* (2021) 12:683002. doi: 10.3389/fimmu.2021.683002

6. Aydin M, Naumova EA, Bellm A, Behrendt AK, Giachero F, Bahlmann N, et al. From submerged cultures to 3D cell culture models: evolution of nasal epithelial cells in asthma research and virus infection. *Viruses.* (2021) 13:387. doi: 10.3390/v13030387

7. Baker SA, Kwok S, Berry GJ, Montine TJ. Angiotensin-converting enzyme 2 (ACE2) expression increases with age in patients requiring mechanical ventilation. *PLoS ONE.* (2021) 16:e0247060. doi: 10.1371/journal.pone.0247060

8. Gu J, Yin J, Zhang M, Li J, Wu Y, Chen J, et al. Study on the clinical significance of ACE2 and its age-related expression. *J Inflamm Res.* (2021) 14:2873–82. doi: 10.2147/JIR.S315981

9. Yin J, Kasper B, Petersen F, Yu X. Association of cigarette smoking, COPD, and lung cancer with expression of SARS-CoV-2 entry genes in human airway epithelial cells. *Front Med.* (2020) 7:619453. doi: 10.3389/fmed.2020.619453

10. Aguiar JA, Tremblay BJ, Mansfield MJ, Woody O, Lobb B, Banerjee A, et al. Gene expression and in situ protein profiling of candidate SARS-CoV-2 receptors in human airway epithelial cells and lung tissue. *Eur Respir J.* (2020) 56:2001123. doi: 10.1183/13993003.01123-2020

11. Watson A, Oberg L, Angermann B, Spalluto CM, Huhn M, Burke H, et al. Dysregulation of COVID-19 related gene expression in the COPD lung. *Respir Res.* (2021) 22:164. doi: 10.1186/s12931-021-01755-3

12. Guo W, Porter LM, Crozier TW, Coates M, Jha A, McKie M, et al. Topical TMPRSS2 inhibition prevents SARS-CoV-2 infection in differentiated human airway cultures. *Life Sci Alliance.* (2022) 5:e202101116. doi: 10.26508/lsa.202101116

13. Khamko R, Wasenang W, Daduang J, Settasatian C, Limpaiboon T. Combined OPCML and AXL expression as a prognostic marker and OPCML enhances AXL inhibitor in cholangiocarcinoma. *In Vivo.* (2022) 36:1168–77. doi: 10.21873/invivo.12816

14. Jackson DJ, Busse WW, Bacharier LB, Kattan M, O'Connor GT, Wood RA, et al. Association of respiratory allergy, asthma, and expression of the SARS-CoV-2 receptor ACE2. *J Allergy Clin Immunol.* (2020) 146:203–6. doi: 10.1016/j.jaci.2020.04.009

15. Jacobs M, Van Eeckhoutte HP, Wijnant SRA, Janssens W, Joos GF, Brusselle GG, et al. Increased expression of ACE2, the SARS-CoV-2 entry receptor, in alveolar and bronchial epithelium of smokers and COPD subjects. *Eur Respir J.* (2020) 56:2002378. doi: 10.1183/13993003.02378-2020

16. Wark PAB, Pathinayake PS, Kaiko G, Nichol K, Ali A, Chen L, et al. ACE2 expression is elevated in airway epithelial cells from older and male healthy individuals but reduced in asthma. *Respirology.* (2021) 26:442–51. doi: 10.1111/resp.14003

17. Wu R, Sato GH, Whitcutt MJ. Developing differentiated epithelial cell cultures: airway epithelial cells. *Fundam Appl Toxicol.* (1986) 6:580–90.

18. Pezzulo AA, Starner TD, Scheetz TE, Traver GL, Tilley AE, Harvey BG, et al. The air-liquid interface and use of primary cell cultures are important to recapitulate the transcriptional profile of *in vivo* airway epithelia. *Am J Physiol Lung Cell Mol Physiol.* (2011) 300:L25–31. doi: 10.1152/ajplung.00256.2010

19. Brekman A, Walters MS, Tilley AE, Crystal RG. FOXJ1 prevents cilia growth inhibition by cigarette smoke in human airway epithelium *in vitro*. *Am J Respir Cell Mol Biol.* (2014) 51:688–700. doi: 10.1165/rcmb.2013-0363OC

20. Hoffmann M, Pohlmann S. How SARS-CoV-2 makes the cut. *Nat Microbiol.* (2021) 6:828–9. doi: 10.1038/s41564-021-00931-x

21. Cai G, Bosse Y, Xiao F, Kheradmand F, Amos CI. Tobacco smoking increases the lung gene expression of ACE2, the receptor of SARS-CoV-2. *Am J Respir Crit Care Med.* (2020) 201:1557–9. doi: 10.1164/rccm.202003-0693LE

frontiers | Frontiers in Medicine

TYPE Original Research
PUBLISHED 14 March 2023
DOI 10.3389/fmed.2023.1144050

Check for updates

OPEN ACCESS

EDITED BY
Simon D. Pouwels,
University Medical Center Groningen,
Netherlands

REVIEWED BY
Claire Mary Smith,
University College London,
United Kingdom
Gimano Amatngalim,
University Medical Center Utrecht,
Netherlands
Brian F. Niemeyer,
University of Colorado,
United States

*CORRESPONDENCE
Kazuhiro Ito
✉ k.ito@imperial.ac.uk

SPECIALTY SECTION
This article was submitted to
Pulmonary Medicine,
a section of the journal
Frontiers in Medicine

RECEIVED 13 January 2023
ACCEPTED 20 February 2023
PUBLISHED 14 March 2023

CITATION
Ito K, Daly L and Coates M (2023) An impact of age on respiratory syncytial virus infection in air-liquid-interface culture bronchial epithelium.
Front. Med. 10:1144050.
doi: 10.3389/fmed.2023.1144050

COPYRIGHT
© 2023 Ito, Daly and Coates. This is an open-access article distributed under the terms of the Creative Commons Attribution License (CC BY). The use, distribution or reproduction in other forums is permitted, provided the original author(s) and the copyright owner(s) are credited and that the original publication in this journal is cited, in accordance with accepted academic practice. No use, distribution or reproduction is permitted which does not comply with these terms.

An impact of age on respiratory syncytial virus infection in air-liquid-interface culture bronchial epithelium

Kazuhiro Ito*, Leah Daly and Matthew Coates

National Heart and Lung Institute, Imperial College, London, United Kingdom

Background: Elderly people are known to be vulnerable to virus infection. However, this has not been appropriately tested in *in vitro* studies due to a lack of appropriate virus infection models. In this report, we investigated the impact of age on respiratory syncytial virus (RSV) in pseudostratified air-liquid-interface (ALI) culture bronchial epithelium, which more closely mimic human airway epithelium morphologically and physiologically, than submerged cancer cell line cultures.

Methods: RSV A2 was inoculated apically to the bronchial epithelium obtained from 8 donors with different ages (28–72years old), and time-profiles of viral load and inflammatory cytokines were analyzed.

Results: RSV A2 replicated well in ALI-culture bronchial epithelium. The viral peak day and peak viral load were similar between donors at ≤60years old (n=4) and >65years old (n=4; elderly group), but virus clearance was impaired in the elderly group. Furthermore, area under the curve (AUC) analysis, calculated from viral load peak to the end of sample collection (from Day 3 to 10 post inoculation), revealed statistically higher live viral load (PFU assay) and viral genome copies (PCR assay) in the elderly group, and a positive correlation between viral load and age was observed. In addition, the AUCs of RANTES, LDH, and dsDNA (cell damage marker) were statistically higher in the elderly group, and the elderly group showed a trend of higher AUC of CXCL8, CXCL10 and mucin production. The gene expression of $p21^{CDKN1A}$ (cellular senescence marker) at baseline was also higher in the elderly group, and there was a good positive correlation between basal p21 expression and viral load or RANTES (AUC).

Conclusion: Age was found to be a key factor affecting viral kinetics and biomarkers post virus infection in an ALI-culture model. Currently, novel or innovative *in vitro* cell models are introduced for virus research, but when virus studies are conducted, similarly to working with other clinical samples, the age balance is important to obtain more accurate results.

KEYWORDS

age, respiratory syncytial virus, air-liquid-interface culture, CXCL8, IL-6, RANTES (regulated upon activation), mucin, dsDNA

Introduction

Historically, virus infection research was conducted using submerged cancer cell line monolayer cultures (2D), which are susceptible to specific virus species. For example, MDCK cells were used for influenza, HEp-2 cells were used for respiratory syncytial virus (RSV), and HeLa cells were used for human rhinovirus (HRV). However, especially during the COVID-19 pandemic, we realized that the outcomes from cancer cell line research were not often translational to the clinic, as those are limited to a single cell type originally from a single donor (or sometimes from animals) having defect of host defense at molecular level, and submerged, thus, do not mimic 3D human tissue architecture and lack biochemical and biomechanical cues. These models are low cost and suitable for high throughput systems, but consequently, routinely require *in vivo* animal model validation. However, animal models are expensive, rarely accurately mimic human biological responses due to obvious differences in physiology, pathology and other genetic factors, as well as having ethical issues. Air-liquid interface (ALI)-culture airway epithelium are being increasingly recognized for their ability to overcome many of the disadvantages of submerged cell culture models (1–3). They consist of pseudostratified fully differentiated cells, cultured in transwell inserts, wherein the apical cells are exposed to the air and the basolateral cells fed by culture medium from below, and thus are a more structurally and biologically accurate representation of the human respiratory microenvironment. Attempts to repurpose existing drugs to SARS-CoV-2 treatment identified the anti-malaria drug chloroquine, which demonstrated potent antiviral activity against SARS-CoV-2 in a submerged cancer cell culture model (Vero E6 cells) (4). However, it was later proved to have limited efficacy in clinical trials and was confirmed to be unsuccessful in reducing SARS-CoV-2 infection in ALI tissue culture models (5–7). Nirmatrelvir and remdesivir were weak but showed good efficacy in ALI-culture as well as clinical trials (8, 9), perhaps indicating that these ALI models more accurately simulate human airway tissue responses. In fact, the kinetics of virus replication seen in ALI-culture was similar to human virus challenge or clinical studies. For example, viral peak and the level of nasal virus shedding seen in ALI-culture was similar to viral kinetics observed in SARS-CoV-2 or RSV human challenge studies (10–13). Thus, RSV is known to replicate well in this *in vitro* model and the infection system have been well established as previously published (12, 14–16).

Thus, it indicates that these ALI models more accurately simulate human airway tissue responses. In addition, ALI-culture, therefore, contributes to the 3Rs strategy (Replacement, Reduction and Refinement) of animal experiments. Furthermore, this is a useful model to evaluate new types of inhaled or intranasal antiviral agents *via* treatment of the exposed apical surface (17).

A major downside of the use of ALI-culture cells is the difference in responses to viruses by different batches of cells. As the primary cells are obtained from different donors to prepare ALI epithelium, this is an obvious and well acknowledged outcome. Consequently, donors from different diseases such as asthma, cystic fibrosis and chronic obstructive pulmonary disease, or having smoking history are usually carefully selected and studied separately. However, other factors such as age and gender are often ignored, or occasionally epithelial cells from only one donor were used as a representative for research or publication. Elderly people are known to be vulnerable to virus infection (18). However, the impact of cellular senescence on virus infection is controversial (19, 20). This has not been appropriately tested in the *in vitro* setting due to lack of proper virus infection models. At least, virus infection was reported to induce cellular senescence (21, 22), but this is not proof that virus is susceptible to senescent cells. Vom Steeg and Kelin (23) have described that, during viral infections, females have greater inflammatory, antiviral, and humoral immune responses compared with males, although males are more susceptible to virus infection, but again this has not been considered when conducting respiratory virus infection studies using ALI-culture epithelium.

Human RSV is a single-stranded, negative-sense RNA virus and a member of the family of Pneumoviridae of the Mononegavirales order. RSV infection is increasingly implicated as a cause of exacerbations in patients suffering from chronic obstructive pulmonary disease (COPD) (24), asthma (25) and cystic fibrosis (26). In immuno-compromised adults, approximately 50% of upper respiratory tract infections with RSV progress to pneumonia. In addition, RSV infection is the most common cause of childhood acute lower respiratory infection (27), and can produce severe disease in patients of any age. Even more importantly, the elderly population are reported to be particularly vulnerable (28), which is the reason why we selected RSV for the current study. Therefore, the aim of this report is to investigate the impact of age on RSV infection in pseudostratified ALI-culture bronchial epithelium.

Materials and methods

Cells and virus

Human larynx epithelial (HEp-2) cells (HeLa cell contaminant) (ATCC® CCL-23™) were purchased from the American Tissue Culture Collection (ATCC, Manassas, VA, United States) and maintained in 10% foetal bovine serum (FBS) supplemented DMEM with phenol red (# 4190–094: Life Technologies Ltd., Paisley, United Kingdom) at 37°C/5% CO_2. MucilAir™ bronchial epithelium was provided fully differentiated as 24-well plate sized inserts by Epithelix Sàrl (Geneva, Switzerland). Cells were isolated from the lung tissue without any characteristics of cancer cells based on pathological analysis (Supplementary Table S1). Twice weekly, MucilAir™ inserts were transferred to a new 24-well plate containing 780 µL of MucilAir™ culture medium (EP04MM), and the apical surface was washed weekly with 400 µL PBS (once). MucilAir™ cultures were incubated at 37°C, 5% CO_2. RSV A2 strain was obtained from the National Collection of Pathogenic Viruses (Public Health England) and passaged in HEp-2 cells containing DMEM supplemented with 2% (v/v) FBS to generate a virus stock solution ($1.3 \sim 1.7 \times 10^5$ PFU/mL). Fifty percent (w/v) sucrose in PBS was added to clarified culture supernatants to a final volume of 12.5% (v/v) sucrose solution.

Abbreviations: ALI, air liquid interface; PFU, plaque forming unit; RSV, respiratory syncytial virus; LOQ, limit of quantification.

Infection and treatment of MucilAir™ culture

Prior to infection, MucilAir™ cultures were washed once with PBS and transferred to a new 24-well plate containing MucilAir™ culture medium. Virus was inoculated by adding 2000 PFU (an approximate multiplicity of infection of 0.01) of RSV stock solution to the apical surface of each well for 1 h. We previously tested with inoculum at 0.00001 to 1 MOI and found 0.01 is the minimum inoculum to achieve high peak viral load without acute cell toxicity (data not shown). Virus inoculum was then removed, and the apical surface washed twice with PBS. A third apical wash using 300 µL of PBS was collected and added to 100 µL PBS containing 50% (w/v) sucrose to generate a baseline (Day 0) for viral load and cytokine assessment. On subsequent days (Day 1–10), 300 µL of PBS was applied to the apical surface, and this wash was collected daily for viral load and cytokine assessment. On Day 5 post inoculation, the basolateral medium was removed from all wells and replenished with fresh MucilAir™ culture medium as a necessary maintenance step for MucilAir™ inserts.

Determination of viral load by plaque assay

HEp-2 cells were seeded into 24-well plates (Corning, NY) at a density of $5 \sim 10 \times 10^4$ cells/well and grown for 48-h prior to infection in 10% FBS DMEM until they attained 100% confluency. Collected apical wash samples were thawed at room temperature and 10-fold serial dilutions were prepared in serum-free DMEM. The growth medium from HEp-2 cells was aspirated and replaced with 300 µL of serially diluted virus collections and left to infect at 37°C/5% CO_2 for 4 h. The infectious media was aspirated and replaced with 1 mL of Plaque Assay Overlay [0.3% Avicel RC-591 (FMC Biopolymer United Kingdom, Girvan, Scotland)] in MEM, supplemented to a final concentration of 2% FBS), and incubated for 7 days at 37°C/5% CO_2. Cells were fixed with ice-cold methanol for 10 min before methanol was removed and cells washed twice with sterile PBS. Cells were then stained with 200 µL of 0.1% crystal violet solution (in distilled water) for 1 h. Crystal violet solution was removed, and cells were rinsed with water before plaques were counted and viral load enumerated.

Viral RNA extraction and quantitative reverse transcriptase polymerase chain reaction for respiratory syncytial virus a nucleoprotein

Viral RNA was extracted from collected samples and the RSV A2 inoculation stock solution using a MagMAX™-96 Viral RNA isolation kit (Ambion by Life technologies) as per the manufacturer's instructions before being subjected to quantitative PCR analysis using the One-Step qRT-PCR system (Primer Design, Southampton, United Kingdom). Briefly, 5 µL of extracted viral RNA was mixed with 10 µL OneStep qRT-PCR master mix, 4 µL RNase/DNase free water and 1 µL of the RSV A primer/probe mix (Cat # Path-RSV-A-standard, Primer Design, Southampton, United Kingdom) per reaction, with reactions being performed in duplicate. PCR plates were sealed with MicroAmp™ optical adhesive film (Cat # 4311971, life technologies) and briefly centrifuged at 1200 RPM. The One-Step PCR reaction and subsequent amplification analysis was carried out using an Applied Biosystems StepOnePlus™ Real-Time PCR System (Cat # 4376598, Life Technologies) using the following condition; 55°C for 10 min and 95°C for 8 min, followed by 50 cycles of qPCR at 10 s at 95°C and 60 s at 60°C. Reactions containing 10-fold serial dilutions of RNA extracted from the stock RSV A2 virus solution were used to generate a standard curve against which the RSV RNA content measured from test samples was quantified.

Cytokine analysis

Collected apical washes were subjected to cytokine analysis using standard Ultra-Sensitive Meso Scale Diagnostics (MSD) assays for RANTES, V-Plex IL-8 MSD assays for IL-8, Human IP-10 Tissue Culture Kit for CXCL10, and Human proinflammatory 9-plex TC assay or Human IL-6 Tissue Culture Kit for IL-6 (all: MSD, Rockville, MA). Measurement of RANTES, CXCL10, and CXCL8/IL-6 required dilution of samples 1:2, 1:5 and 1:10, respectively, in Reagent Diluent. The electrochemiluminescence signal of serially-diluted standard samples, provided with each assay kit, was measured using a MESO QuickPlex plate reader and used to generate a standard curve using Discovery Workbench 4.0 software for each analyte. Each apical wash sample was quantified using these standard curves.

Mucin quantification

Mucin concentrations were quantified using an enzyme-linked lectin assay (ELLA) based on the protocol previously described (29). Briefly, samples were sonicated for 10 min and added to high-bind ELISA plates coated in lectin from *Triculum vulgaris*. A standard curve was prepared using serially diluted mucin of known concentration from bovine submaxillary gland. Following incubation at 37°C for 30 min, the plates were washed three times with a wash buffer before the addition of detection reagent (containing HRP-conjugated Glycine max soybean lectin) for a further 30 min at 37°C. Following a further wash cycle, a substrate solution containing H_2O_2 and tetramethylbenzidine (R&D Systems, Minneapolis, MN) was added and allowed to develop for 5 min. The reaction was terminated using 2 M H_2SO_4, absorbance was read immediately at 450 nm with 570 nm as reference. Standard curves were created using GraphPad Prism and these were used to calculate the concentration of mucin in all samples.

Double stranded DNA quantification

The concentration of dsDNA in apical washes was quantified using a Quant-iT PicoGreen dsDNA Assay Kit (Life technologies) as per manufacturer's instructions. A standard curve was prepared by serially-dilution of a 2 µg/ml stock of dsDNA (Phage lambda DNA), and then incubated in the presence of the Quant-iT™ PicoGreen® dsDNA reagent for 3 min. Samples were added to the plates at a 1:2 dilution in TE buffer and incubated for 3 min in the presence of Quant-iT™ PicoGreen® dsDNA reagent, and the fluorescence of each well [545 nm (excitation) / 590 nm (emission)] was determined using

a monochromator microplate reader (CLARIOstar®: BMG Labtech, Buckinghamshire, United Kingdom). A standard curve was created using MARS data analysis software (BMG Labtech, Buckinghamshire, United Kingdom) and the equation used to calculate concentration levels including the dilution factor used.

Lactate dehydrogenase assay

LDH in apical washes was quantified using a CyQuant LDH Cytotoxicity assay kit (Thermo Fisher Scientific Inc. Basingstoke, United Kingdom) as per manufacturer's instructions. Samples were added to the plates at a 1:2 dilution and incubated with Reaction Mixture for 30 min at room temperature, and the reaction was stopped by adding Stop Solution. The absorbance of each well at 490 nm and 680 nm was determined using a monochromator microplate reader (CLARIOstar®: BMG Labtech, Buckinghamshire, United Kingdom). The LDH activity was provided as OD, by subtracting the 680 nm OD from the 490 nm OD.

p21/CDKN1A RT-qPCR

RNA extraction was performed using the RNeasy plant mini kit (Qiagen Ltd., Manchester, United Kingdom) in accordance with manufacturer's instructions. RNA was stored at −80°C if not used immediately for RT-qPCR. TaqMan® RNA-to-CT ™ 1-Step Kit (Thermo Fisher Scientific, Basingstoke, United Kingdom) was used for gene expression analysis according to manufacturer's instruction. Briefly, kit components and the primers pair (p21/CDKN1A:#Hs01121172_m1,GAPDH:#Hs99999905_m1, Thermo Fisher Scientific) were combined in a MicroAmp™ Fast Optical 96-Well Reaction Plate, 0.1 mL (10μLTaqMan® RT-PCR Mix (2x), 1 μL TaqMan® gene expression assay (20X), 0.5 μL TaqMan® RT Enzyme Mix (40x), 5 μL RNA template [up to 1 μg), 3.5 μL RNase-free H2O (up to Σ20μL)] was covered with MicroAmp optical adhesive film, briefly centrifuged. The PCR reaction was carried out using the Applied Biosystems StepOnePlus™ Real-Time PCR System with the run cycle (x1 reverse transcription, 30 min at 48°C, x1 cycle enzyme activation, 10 min at 95°C, x40 cycles (Denaturation 15 s at 95°C and Data collection, 1 min at 60°C). Fold change in gene expression vs. GAPDH was calculated as ΔCT.

Statistical analysis

Results were represented as mean ± standard error of the mean or standard error as indicated. AUC (DAY 3–10) was calculated using GraphPad Prism (GraphPad Software, Inc., La Jolla, CA), and min-max with median was shown for grouping analysis. The comparison between two groups was performed by unpaired non-parametric Mann–Whitney test or *t*-test with Welch's correction using GraphPad Prism. Correlation analysis between indicated parameters was also conducted by non-parametric Spearman test with statistical significance defined as $p < 0.05$.

Results

An impact of age on respiratory syncytial virus A2 viral load

RSV A2 was inoculated apically to the ALI-culture bronchial epithelium, and apical washed collected daily. Time-profiles of viral load (live virus by plaque assay, virus genome by RT-PCR) in apical washes were analyzed in donors from two different age groups, ≤60 years old donors ($n = 4$, 46.8 ± 13.7) and > 65 years old donors ($n = 4$, 68.5 ± 3.51; Table 1; Supplementary Table S1).

In the younger group (≤60 years old), following inoculation with a low level of RSV A2 (0.01 MOI), virus replicated well, and the virus load (plaque assay) peaked on Day 3, and then gradually reduced up to Day 10 (Figure 1A). In contrast, in the elderly group (>65 years old), although the peak day and peak viral load were similar to those in younger group, RSV viral load did not reduce substantially up to Day 10 post inoculation, suggesting impaired virus clearance (Figure 1A; Table 2). This was also proven as significantly lower slope of viral load reduction in elderly group compared with that of younger group (Table 2). Consequently, viral load AUC in the elderly group was significantly higher than that in younger group (Figure 1B). There was no correlation between the peak viral load and virus clearance (either slope of virus reduction at Day 3–6 or at Day 3–10), [Spearman

TABLE 1 Comparison of basal biomarker levels between younger (≤60years old) and elderly (>65years old) donors.

	≤60years old donors	>65years old donors	Statistical analysis
n	4	4	
Age	46.8 ± 13.7	68.5 ± 3.51	$p < 0.05$
Gender male/female	3/1	2/2	N/A
Basal CXL8 (pg/mL)	376 ± 507	73.1 ± 141	NS
Basal IL-6 (pg/mL)	15.4 ± 16.4	0.858 ± 0.495	NS
Basal RANTES (pg/mL)	1.01 ± 0.975	0.667 ± 0.996	NS
Basal CXCL10 (pg/mL)	88.2 ± 67.4	15.8 ± 18.7	NS
Basal mucin (AU)	348 ± 218	499 ± 474	NS
Basal dsDNA (ng/mL)	15.4 ± 81.2	43.6 ± 49.5	NS
Basal $p21^{CDKN1A}$ (vs. GAPDH, RT-PCR)	0.313 ± 0.181	0.781 ± 0.220	$p < 0.05$

Mean ± SD is shown. Basal biomarker levels were determined in intact bronchial epithelium. PFU, plaque forming units. AU: absorbance units, NS: not significant.

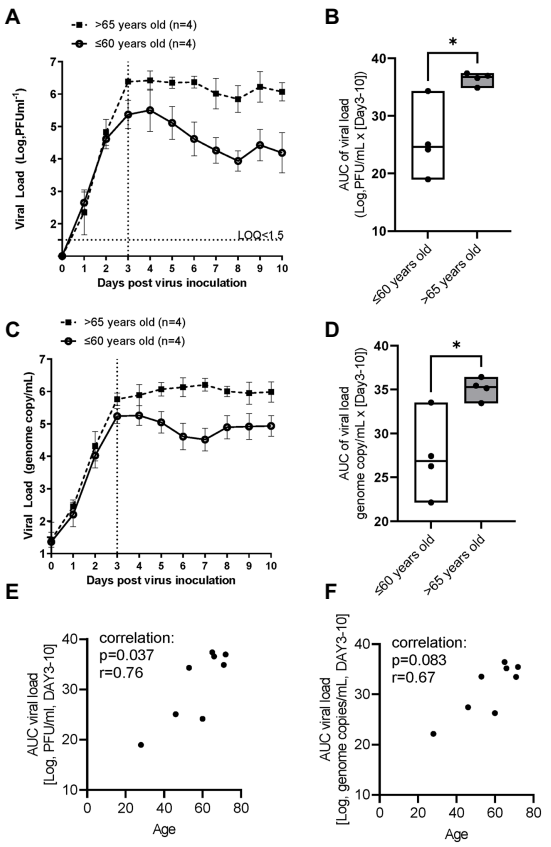

FIGURE1
The comparison of RSV A2 viral load in apical washes collected from ALI-bronchial epithelium post RSV A2 inoculation in younger (≤60years old) and elderly (>65years old) groups. **(A)** Time-profile of viral load determined by plaque assay, mean±SEM. **(B)** AUC (Day 3–10) of viral load determined by plaque assay, min-max with median. **(C)** Time-profile of viral load determined by qRT-PCR. **(D)** AUC (Day 3–10) of viral load determined by qRT-PCR. A correlation between age and viral load by plaque assay **(E)** and qRT-PCR **(F)**. *p<0.05, the LOQ is 1.5 log, PFU/mL for a plaque assay, and virus load lower than LOQ was shown as <1.5.

r = −0.60 p = 0.13 and r = −0.59 p = 0.13, respectively], and therefore, the peak viral load will not be a driving factor for virus clearance. This was also confirmed by the viral load determined as the genome copies of RSV by RT-PCR (Figures 1C,D). In addition, there was a statistically significant and a trend of positive correlation between age and viral load determined by plaque assay or and RT-PCR, respectively (Figures 1E,F).

An impact of age on respiratory syncytial virus A2 induced cytokine production

RSV A2 replication stimulated CXCL8 production in apical washes, which peaked on Day 3 post virus inoculation and then reduced over times, in parallel with viral load shown in Figure 1A in the younger group (Figure 2A). In contrast, the reduction rate of CXCL8 after peak was lower in the elderly group (Figure 2A), and AUC of CXCL8 (Day 3–10) trended towards being higher in elderly group than in younger group (Figure 2B; Table 2). There was a trend of positive correlation between CXCL8 and age, but not statistically significant (Supplementary Table S2). We did not observe any significant difference in basal CXCL8 levels (Table 1). RSV A2 replication also stimulated IL-6 production in apical washes, but the AUC of IL-6 was slightly higher in younger group although it was not statistically significant (Figure 2C; Table 2; Supplementary Figure S1A).

RSV A2 replication strongly and continuously stimulated RANTES production in apical washes, from Day 3 post virus inoculation, when virus load peaked, in the elderly group although there was limited induction in RANTES in the younger group (Figure 2D). Consequently, the AUC of RANTES was significantly higher in the elderly group than the younger group (Figure 2E; Table 2). We also observed a similar trend in virus induced CXCL10 induction (Figure 2F; Table 2; Supplementary Figure S1B).

An impact of age on respiratory syncytial virus A2 induced mucin, dsDNA and LDH release

RSV A2 replication stimulated mucin production in apical washes after Day 4 post virus inoculation (Figure 3A) and the AUC trended to being higher in the elderly group than the younger group (Figure 3B). dsDNA, as a marker of cell damage at the apical site, was also increased after virus inoculation, peaked at Day 6 post virus inoculation in elderly group, but the dsDNA release was less in the younger group, which was confirmed by significantly higher AUC of dsDNA in the elderly group (Figures 3C,D; Table 2). There was no difference of baseline mucin and dsDNA between the elderly and younger groups (Table 1). LDH, as another marker of cell damage at the apical site, was also increased after virus inoculation, peaked at Day 6 post virus inoculation in elderly group, but the LDH release was less in the younger group, which was confirmed by significantly higher AUC of dsDNA in the elderly group (Figures 3E,F; Table 2). There were statistically significant positive correlations of dsDNA or LDH with age (Supplementary Table S2).

Basal p21 gene expression

To investigate whether cells were senescent before infection, the basal level of gene expression of $p21^{CDKNA1}$ was determined by RT-PCR in epithelium (non-infection) as a cellular senescent marker. The p21 gene expression was significantly higher in elderly group (Figure 4A). There were significant positive correlations between p21 gene expression and age, viral load AUC and RANTES AUC (Figures 4B–D).

Discussion

In this paper, we demonstrated for the first time that airway epithelium obtained from an older population showed an impaired virus clearance with increased chemokines, cell damage and mucin production, which were correlated with the level of cellular senescence before infection. Although respiratory viruses are reported to induce cellular senescence in airway epithelial cells upon infection, this is important findings that RSV A2 was susceptible to aged cells,

TABLE 2 Comparison of viral infection parameters and biomarker levels between younger (≤60years old) and elderly (>65years old) donors.

	≤60years old donors	>65years old donors	Statistical analysis
n	4	4	
Viral peak (day)	3.75 ± 0.500	3.50 ± 0.577	NS
Viral peak (Log, PFU/mL)	5.63 ± 1.08	6.50 ± 0.197	NS
Viral load (slope Day 3–6)	0.251 ± 0.116	0.005 ± 0.061	$p < 0.05$
Viral load (slope Day 3–10)	0.169 ± 0.107	0.0446 ± 0.0450	NS
Viral load (AUC [log, PFU/mL] Day 3–10)	25.6 ± 6.38	36.5 ± 1.09	$p < 0.05$
PCR Viral load (AUC [log, copy/mL] Day 3–10)	27.3 ± 4.70	35.1 ± 1.23	$p < 0.05$
AUC CXCL8 (pg/mL) Day 3–10	7,590 ± 3,440	13,000 ± 6,350	NS
AUC IL-6 (pg/mL) Day 3–10	246 ± 266	137 ± 160	NS
AUC RANTES (pg/mL) Day 3–10	87.2 ± 41.0	622 ± 416	$p < 0.05$
AUC CXCL10 (pg/mL) Day 3–10*	6,020 ± 2,670	133,000 ± 191,000	NS
AUC mucin (AU) Day 3–10	8,660 ± 6,580	156,000 ± 201,000	NS
AUC dsDNA (ng/mL) Day 3–10	1,920 ± 1,610	5,650 ± 1,280	$p < 0.05$
AUC LDH (OD) Day 3–10*	4.54 ± 0.540	5.61 ± 0.408	$p < 0.05$

Mean ± SD is shown. PFU, plaque forming unit, *$n = 3$ of ≤60 years old donors. AU: absorbance units, OD: optical density, NS: not significant.

providing a potential reason why older populations are vulnerable to respiratory virus infections.

Toapanta and Ross (30) demonstrated that older mice showed impaired virus clearance due to delayed immune response, however, in contrast, several reports showed that aging was protective to virus infection (31, 32). For aging research, 18 month old mice are usually used, which is roughly equivalent to the end of human middle age or the beginning of old age, according to the information provided by the Jackson Laboratory (33). In humans, generally 65 years is used as the fixed threshold at which old age and economic dependency begins based on the old social security act, which might be redefined as the life expectancy becomes longer in current times. Thus, aged mouse studies might not translate to the events in elderly people. In fact, in this study, although we had limited donors, analysis revealed that a threshold of 65 years is still the best to demonstrate differences between elderly and younger donors compared with thresholds of 55 and 70 years old (data not shown). However, the fact remains that the low sample number severely limits the meaningful interpretation of the data regarding the age threshold, and further studies should be necessary. It should be noted that patients are usually admitted to hospital after being symptomatic, meaning after virus infection is well established or after peak, therefore, an accurate time-course cannot be measured. In this study, we did not find much difference in peak viral load or peak day post inoculation, however, clear differences between groups were seen in clearance of virus at later timepoints. Apoptosis of virus infected cells is known to be one of the mechanisms for host cells to tackle virus infection (34). However, senescence cells are known to be anti-apoptotic (35), and therefore, virus could potentially continuously replicate in the senescent cells, thereby acting as a kind of reservoir for viruses. This has not been reported or confirmed yet, and further studies using senescent cells are required.

Thus, we found the viral clearance was impaired in elder population without any statistical difference in peak viral load (Figures 1A,B; Table 2). There was no correlation between the peak viral load and the virus clearance determined as the slope of virus reduction as described in Results section. Thus, the peak viral load will not be a driving factor of poor viral clearance. Further studies with different inoculum size will help to understand the difference in the future.

ALI-cultures were also characterized by increases in the concentrations of several biomarkers. RANTES has been shown to correlate with RSV disease severity (36) and with RSV load in humans (37). CXCL8 and IL-6 were also reported to increase in nasal aspirate after infection and show a strong correlation with symptoms (36). RSV is known to be a strong mucus producer. In this report, we also found an increase in CXCL8, IL-6, RANTES, CXCL10, mucin, LDH as well as dsDNA, a potential marker of cell damage. Interestingly, RANTES, dsDNA and LDH release were significantly (but mucin, CXCL10 and CXCL8 not significantly) higher in the elderly population. However, IL-6 tended to be higher in younger and female populations (Table 2; Supplementary Table S3). Despite serving as a high-fidelity model of the human airway and observation of the difference between ages, there were some limitations that hindered data interpretation in this study. Firstly, the study was not appropriately powered to detect differences in some biomarkers. Although we observed significant difference on viral load, RANTES and dsDNA, more donors were required to demonstrate differences in CXCL8, mucin and others. In our previous studies, power calculations indicated that $n = 3$ per group is required for viral load but a larger sample size is needed to compare biomarkers due to greater variation between donors (12). In fact, we were able to show significant difference in viral load AUC between younger and elderly groups in this study with the sample size of $n = 4$ per group. Surprisingly, we also showed statistical differences in RANTES, dsDNA and LDH in limited sample size, but we need to increase donor number in future to obtain conclusive data. In addition, we observed cells from a 28-year-old donor showed the lowest viral load (peak and AUC) as well as lowest dsDNA level (cell damage) and lower levels in other biomarkers (data not shown). Therefore, it would be beneficial to

10.3389/fmed.2023.1144050

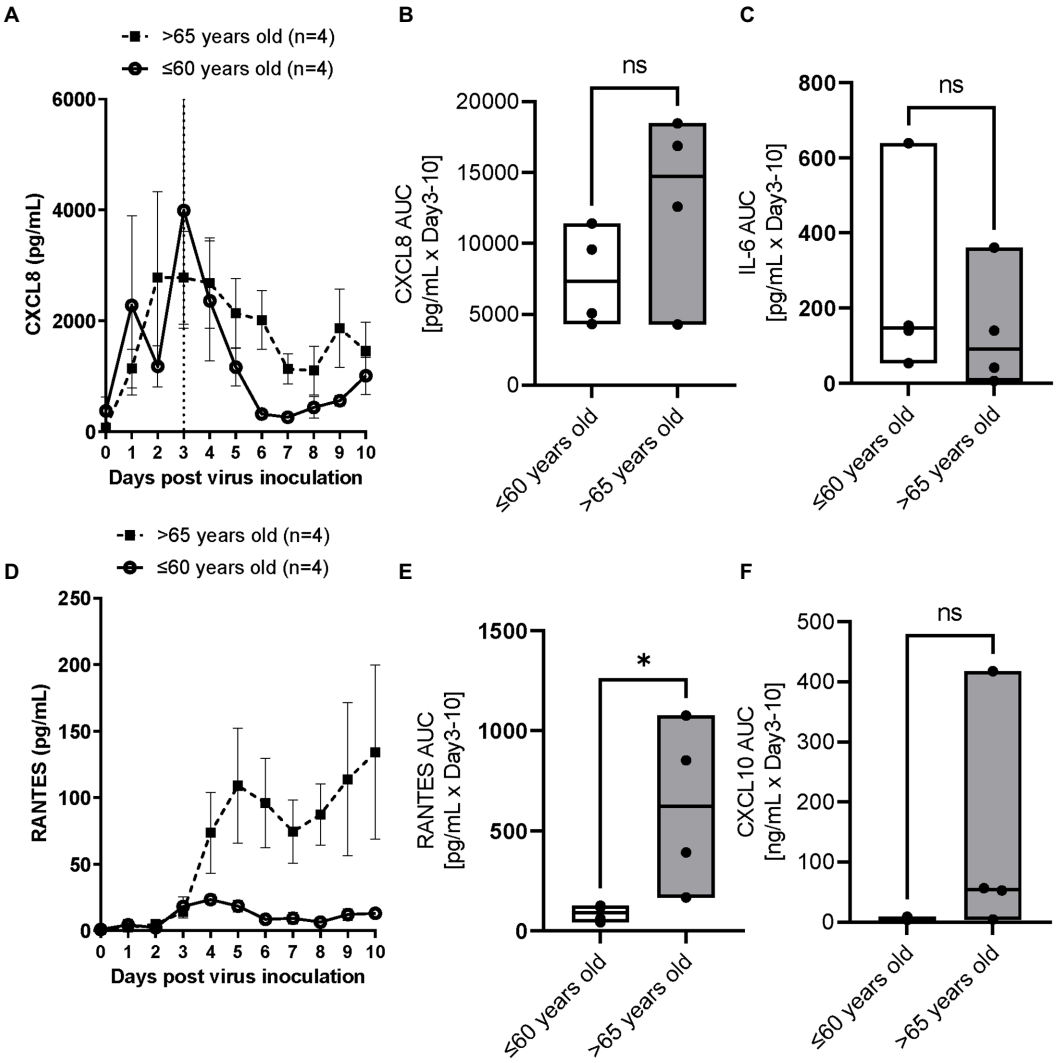

FIGURE 2
The comparison of RSV A2 induced cytokine biomarkers in apical washes collected from ALI-bronchial epithelium post RSV A2 inoculation in younger (≤60years old) and elderly (>65years old) groups. **(A)** Time-profile of CXCL8, **(B)** AUC (Day 3–10) of CXCL8, **(C)** AUC (Day 3–10) of IL-6, **(D)** Time-profile of RANTES, **(E)** AUC (Day 3–10) of RANTES, **(F)** AUC (Day 3–10) of CXCL10, mean±SEM or min-max with median *p<0.05. NS: not significant.

divide the <60 years group into two groups of younger donors (20–40 years old) and middle age group (40–60 years old) to further investigate this. Secondly, gender balance of samples was not often considered when selecting donors of ALI epithelium. Vom Steeg and Kelin (23) have described that, during viral infections, females have greater inflammatory, antiviral, and humoral immune responses compared with males, although males are more susceptible to virus infection. For example, in an influenza challenge test, females were more likely to be symptomatic (38), and also Robinson et al. demonstrated that females suffer worse outcomes from influenza A infection than males (39). Conversely, a male bias in COVID19 mortality and inflammation was reported (40). In this study, the viral load and biomarkers AUC were compared between male and female donors (Supplementary Table S3) and no significant differences in peak day, peak viral load, slope of virus reduction after peak, CXCL8, RANTES and dsDNA were observed. IL-6 showed a trend of higher levels in females, and mucin production appeared to be higher in males, but these were not statistically significant. Thus, an impact of gender on RSV infection in ALI epithelium was inconclusive in this study due to lack of power. More studies are required, but the gender balance should be considered when conducting respiratory virus infection studies using ALI-culture epithelium. Thirdly, we measured gene expression of p21 (cellular senescence markers) in cell lysate of whole epithelium sheet at baseline (before infection) to understand the senescent level of cells before infection. Although we observed a good positive correlation between basal p21 expression and viral load, it is not clear whether the virus replicated more in senescent cells or not. As we do not believe that all cells were senescent, cell specific observations using imaging with virus and cellular senescent markers would help to understand this. In addition, the level of cellular senescence should be confirmed by other senescent markers such asp16, phosphorylated p53 and 402 Lamin B1.

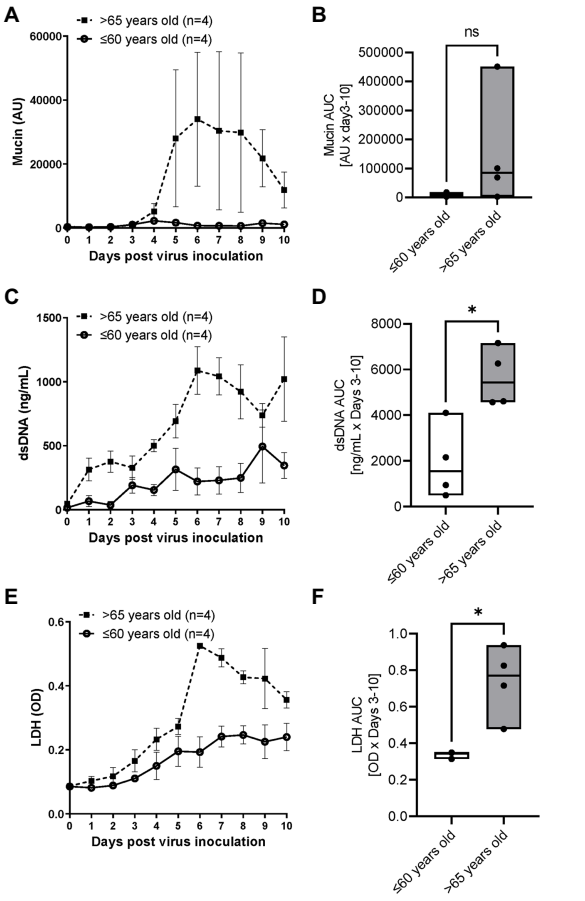

FIGURE 3
The comparison of RSV A2 induced mucin production and dsDNA/LDH release in apical washes collected from ALI-bronchial epithelium post RSV A2 inoculation in younger (≤60years old) and elderly (>65years old) groups. **(A)** Time-profile of mucin production, **(B)** AUC (Day 3–10) of mucin, **(C)** Time-profile of dsDNA, **(D)** AUC (Day 3–10) of dsDNA. **(E)** Time-profile of LDH, and **(F)** AUC (Day 3–10) of LDH. Mean±SEM, *p<0.05. AU: absorbance units, OD: optical density, NS: not significant.

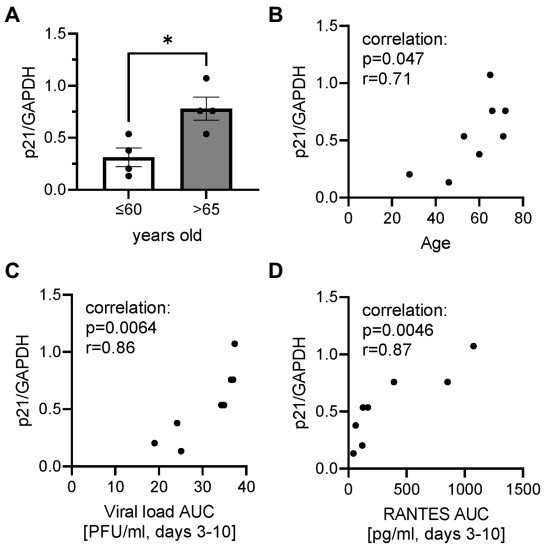

FIGURE 4
Basal p21 gene expression normalized by housekeeping gene GAPDH. **(A)** The comparison of basal p21 gene expression in cells collected from ALI-bronchial epithelium in younger (≤60years old) and elderly (>65years old) groups. A correlation between p21 gene expression and age **(B)**, plaque assay-viral load (Log, PFU/ml) AUC **(C),** or RANTES AUC **(D)**. *p<0.05.

Fourthly, unlike these cultures, in the whole body, adaptive immune cells participate in virus elimination. In fact, although the peak virus load was similar to that observed in nasal wash samples collected from healthy subjects challenged with RSV Memphis 37 strain (41) or from RSV-infected infants (42), the viral load was sustained for more than 10 days in ALI epithelium whereas the virus infection resolved in 10 days in healthy subjects *in vivo*. Particularly, the vulnerability of aged population to respiratory virus infection is known to be caused by immune-senescence (43). Therefore, to obtain a more accurate picture, we need a co-culture system with immune cells from an aged population. Finally, ALI-culture itself still has some limitations. It is limited by the absence of a nutrient and waste transport system as well as by a lack of certain biomechanical pressures (to more accurately simulate breathing). However, a new pre-clinical model which takes into account both of these aforementioned limitations whilst maintaining the advantageous features of ALI-cultures, is coming to the fore of respiratory research; the airway-on-chip. This model consists of an advanced microfluidic cell culture device that also simulates *in vivo* vascular perfusion and biomechanical forces implicated in breathing, to provide the most accurate *in vitro* representation of the respiratory microenvironment to date (44). The system still has some problems such as lack of standardized protocols as well as its high cost and complexity to operate, but it will help to overcome the problems of ALI-culture for studying virus infections in the future.

In summary, we found aging was an important factor affecting respiratory virus infection and its clearance as well as virus associated biomarkers. Novel or innovative *in vitro* cell models are vital for researching respiratory virus infection or virus-associated exacerbations in chronic inflammatory pulmonary diseases, but as in clinical studies, the age (and potentially gender) balance of cell donors should be considered to obtain more translational results.

Data availability statement

The raw data supporting the conclusions of this article will be made available by the authors, without undue reservation.

Author contributions

KI conceived and designed the experiments. LD, MC, and KI performed the experiments and analyzed and interpreted the data. All authors contributed to the article and approved the submitted version.

Funding

This study was partially funded by Pulmocide Ltd.

Conflict of interest

KI was a co-founder and shareholder of Pulmocide Ltd., and currently serves as a consultant. MC was an employee and shareholder of Pulmocide Ltd. LD was an employee of Pulmocide Ltd.

Publisher's note

All claims expressed in this article are solely those of the authors and do not necessarily represent those of their affiliated organizations, or those of the publisher, the editors and the reviewers. Any product that may be evaluated in this article, or claim that may be made by its manufacturer, is not guaranteed or endorsed by the publisher.

Supplementary material

The Supplementary material for this article can be found online at: https://www.frontiersin.org/articles/10.3389/fmed.2023.1144050/full#supplementary-material

References

1. Zarkoob H, Allue-Guardia A, Chen YC, Jung O, Garcia-Vilanova A, Song MJ, et al. Modeling SARS-CoV-2 and influenza infections and antiviral treatments in human lung epithelial tissue equivalents. *Commun Biol*. (2021) 5:810. doi: 10.1038/s42003-022-03753-7

2. Baldassi D, Gabold B, Merkel O. Air-liquid interface cultures of the healthy and diseased human respiratory tract: promises, challenges and future directions. *Adv Nanobiomed Res*. (2021) 1:2000111. doi: 10.1002/anbr.202000111

3. Michi AN, Proud D. A toolbox for studying respiratory viral infections using air-liquid interface cultures of human airway epithelial cells. *Am J Physiol Lung Cell Mol Physiol*. (2021) 321:L263–79. doi: 10.1152/ajplung.00141.2021

4. Liu J, Cao R, Xu M, Wang X, Zhang H, Hu H, et al. Hydroxychloroquine, a less toxic derivative of chloroquine, is effective in inhibiting SARS-CoV-2 infection in vitro. *Cell Discov*. (2020) 6:16. doi: 10.1038/s41421-020-0156-0

5. Cochin M, Touret F, Driouich JS, Moureau G, Petit PR, Laprie C, et al. Hydroxychloroquine and azithromycin used alone or combined are not effective against SARS-CoV-2 ex vivo and in a hamster model. *Antivir Res*. (2022) 197:105212. doi: 10.1016/j.antiviral.2021.105212

6. Deng J, Zhou F, Heybati K, Ali S, Zuo QK, Hou W, et al. Efficacy of chloroquine and hydroxychloroquine for the treatment of hospitalized COVID-19 patients: a meta-analysis. *Future Virol*. (2021) 17:95–118. doi: 10.2217/fvl-2021-0119

7. Maisonnasse P, Guedj J, Contreras V, Behillil S, Solas C, Marlin R, et al. Hydroxychloroquine use against SARS-CoV-2 infection in non-human primates. *Nature*. (2020) 585:584–7. doi: 10.1038/s41586-020-2558-4

8. Chen W, Shao Y, Peng X, Liang B, Xu J, Xing D. Review of preclinical data of PF-07304814 and its active metabolite derivatives against SARS-CoV-2 infection. *Front Pharmacol*. (2022) 13:1035969. doi: 10.3389/fphar.2022.1035969

9. Do TND, Donckers K, Vangeel L, Chatterjee AK, Gallay PA, Bobardt MD, et al. A robust SARS-CoV-2 replication model in primary human epithelial cells at the air liquid interface to assess antiviral agents. *Antivir Res*. (2021) 192:105122. doi: 10.1016/j.antiviral.2021.105122

10. Killingley B, Mann AJ, Kalinova M, Boyers A, Goonawardane N, Zhou J, et al. Safety, tolerability and viral kinetics during SARS-CoV-2 human challenge in young adults. *Nat Med*. (2022) 28:1031–41. doi: 10.1038/s41591-022-01780-9

11. Pizzorno A, Padey B, Julien T, Trouillet-Assant S, Traversier A, Errazuriz-Cerda E, et al. Characterization and treatment of SARS-CoV-2 in nasal and bronchial human airway epithelia. *Cell Rep Med*. (2020) 1:100059. doi: 10.1016/j.xcrm.2020.100059

12. Brookes DW, Coates M, Allen H, Daly L, Constant S, Huang S, et al. Late therapeutic intervention with a respiratory syncytial virus L-protein polymerase inhibitor, PC786, on respiratory syncytial virus infection in human airway epithelium. *Br J Pharmacol*. (2018) 175:2520–34. doi: 10.1111/bph.14221

13. DeVincenzo J, Cass L, Murray A, Woodward K, Meals E, Coates M, et al. Safety and antiviral effects of nebulized PC786 in a respiratory syncytial virus challenge study. *J Infect Dis*. (2022) 225:2087–96. doi: 10.1093/infdis/jiaa716

14. Mirabelli C, Jaspers M, Boon M, Jorissen M, Koukni M, Bardiot D, et al. Differential antiviral activities of respiratory syncytial virus (RSV) inhibitors in human airway epithelium. *J Antimicrob Chemother*. (2018) 73:1823–9. doi: 10.1093/jac/dky089

15. Mellow TE, Murphy PC, Carson JL, Noah TL, Zhang L, Pickles RJ. The effect of respiratory synctial virus on chemokine release by differentiated airway epithelium. *Exp Lung Res*. (2004) 30:43–57. doi: 10.1080/01902140490252812

16. Villenave R, Shields MD, Power UF. Respiratory syncytial virus interaction with human airway epithelium. *Trends Microbiol*. (2013) 21:238–44. doi: 10.1016/j.tim.2013.02.004

17. Strong P, Ito K, Murray J, Rapeport G. Current approaches to the discovery of novel inhaled medicines. *Drug Discov Today*. (2018) 23:1705–17. doi: 10.1016/j.drudis.2018.05.017

18. Greenberg SB. Viral respiratory infections in elderly patients and patients with chronic obstructive pulmonary disease. *Am J Med*. (2002) 112:28S–32S.

19. Baz-Martinez M, Da Silva-Alvarez S, Rodriguez E, Guerra J, El Motiam A, Vidal A, et al. Cell senescence is an antiviral defense mechanism. *Sci Rep*. (2016) 6:37007. doi: 10.1038/srep37007

20. Kim JA, Seong RK, Shin OS. Enhanced viral replication by cellular replicative senescence. *Immune Netw*. (2016) 16:286–95. doi: 10.4110/in.2016.16.5.286

21. Seoane R, Vidal S, Bouzaher YH, El Motiam A, Rivas C. The interaction of viruses with the cellular senescence response. *Biology* (2020);9:455455, doi: 10.3390/biology9120455.

22. Evangelou K, Veroutis D, Paschalaki K, Foukas PG, Lagopati N, Dimitriou M, et al. Pulmonary infection by SARS-CoV-2 induces senescence accompanied by an inflammatory phenotype in severe COVID-19: possible implications for viral mutagenesis. *Eur Respir J*. (2022) 60:2951. doi: 10.1183/13993003.02951-2021

23. vom Steeg LG, Klein SL. SeXX matters in infectious disease pathogenesis. *PLoS Pathog*. (2016) 12:e1005374. doi: 10.1371/journal.ppat.1005374

24. Mehta J, Walsh EE, Mahadevia PJ, Falsey AR. Risk factors for respiratory syncytial virus illness among patients with chronic obstructive pulmonary disease. *COPD*. (2013) 10:293–9. doi: 10.3109/15412555.2012.744741

25. Darveaux JI, Lemanske RF Jr. Infection-related asthma. *J Allergy Clin Immunol Pract*. (2014) 2:658–63. doi: 10.1016/j.jaip.2014.09.011

26. Abman SH, Ogle JW, Butler-Simon N, Rumack CM, Accurso FJ. Role of respiratory syncytial virus in early hospitalizations for respiratory distress of young infants with cystic fibrosis. *J Pediatr*. (1988) 113:826–30. doi: 10.1016/S0022-3476(88)80008-8

27. Nair H, Nokes DJ, Gessner BD, Dherani M, Madhi SA, Singleton RJ, et al. Global burden of acute lower respiratory infections due to respiratory syncytial virus in young children: a systematic review and meta-analysis. *Lancet*. (2010) 375:1545–55. doi: 10.1016/S0140-6736(10)60206-1

28. Walsh EE, Falsey AR. Respiratory syncytial virus infection in adult populations. *Infect Disord Drug Targets*. (2012) 12:98–102. doi: 10.2174/187152612800100116

29. McCoy JP Jr, Varani J, Goldstein IJ. Enzyme-linked lectin assay (ELLA). II. Detection of carbohydrate groups on the surface of unfixed cells. *Exp Cell Res*. (1984) 151:96–103. doi: 10.1016/0014-4827(84)90359-8

30. Toapanta FR, Ross TM. Impaired immune responses in the lungs of aged mice following influenza infection. *Respir Res*. (2009) 10:112. doi: 10.1186/1465-9921-10-112

31. Hernandez-Vargas EA, Wilk E, Canini L, Toapanta FR, Binder SC, Uvarovskii A, et al. Effects of aging on influenza virus infection dynamics. *J Virol*. (2014) 88:4123–31. doi: 10.1128/JVI.03644-13

32. Lu J, Duan X, Zhao W, Wang J, Wang H, Zhou K, et al. Aged mice are more resistant to influenza virus infection due to reduced inflammation and lung pathology. *Aging Dis*. (2018) 9:358–73. doi: 10.14336/AD.2017.0701

33. Hagan C. *When are mice considered old?* The Jackson Laboratory (2017). Available online at: https://www.jax.org/news-and-insights/jax-blog/2017/november/when-are-mice-considered-old.

34. Herold S, Ludwig S, Pleschka S, Wolff T. Apoptosis signaling in influenza virus propagation, innate host defense, and lung injury. *J Leukoc Biol*. (2012) 92:75–82. doi: 10.1189/jlb.1011530

35. Hu L, Li H, Zi M, Li W, Liu J, Yang Y, et al. Why senescent cells are resistant to apoptosis: an insight for Senolytic development. *Front Cell Dev Biol*. (2022) 10:822816. doi: 10.3389/fcell.2022.822816

36. DeVincenzo JP, Wilkinson T, Vaishnaw A, Cehelsky J, Meyers R, Nochur S, et al. Viral load drives disease in humans experimentally infected with respiratory syncytial virus. *Am J Respir Crit Care Med*. (2010) 182:1305–14. doi: 10.1164/rccm.201002-0221OC

37. Thompson TM, Roddam PL, Harrison LM, Aitken JA, DeVincenzo JP. Viral specific factors contribute to clinical respiratory syncytial virus disease severity differences in infants. *Clin Microbiol*. (2015) 04:206. doi: 10.4172/2327-5073.1000206

38. Giurgea LT, Cervantes-Medina A, Walters KA, Scherler K, Han A, Czajkowski LM, et al. Sex differences in influenza: the challenge study experience. *J Infect Dis*. (2022) 225:715–22. doi: 10.1093/infdis/jiab422

39. Robinson DP, Lorenzo ME, Jian W, Klein SL. Elevated 17beta-estradiol protects females from influenza a virus pathogenesis by suppressing inflammatory responses. *PLoS Pathog*. (2011) 7:e1002149. doi: 10.1371/journal.ppat.1002149

40. Scully EP, Haverfield J, Ursin RL, Tannenbaum C, Klein SL. Considering how biological sex impacts immune responses and COVID-19 outcomes. *Nat Rev Immunol*. (2020) 20:442–7. doi: 10.1038/s41577-020-0348-8

41. Kelly G, Laxton C, Garelnabi M, Alton B, Addan F, Catchpole A, et al. Use of qualitative integrative cycler PCR (qicPCR) to identify optimal therapeutic dosing time-points in a respiratory syncytial virus human viral challenge model (hVCM). *J Virol Methods*. (2015) 224:83–90. doi: 10.1016/j.jviromet.2015.08.019

42. DeVincenzo JP, El Saleeby CM, Bush AJ. Respiratory syncytial virus load predicts disease severity in previously healthy infants. *J Infect Dis*. (2005) 191:1861–8. doi: 10.1086/430008

43. Allen JC, Toapanta FR, Chen W, Tennant SM. Understanding immunosenescence and its impact on vaccination of older adults. *Vaccine*. (2020) 38:8264–72. doi: 10.1016/j.vaccine.2020.11.002

44. Francis I, Shrestha J, Paudel KR, Hansbro PM, Warkiani ME, Saha SC. Recent advances in lung-on-a-chip models. *Drug Discov Today*. (2022) 27:2593–602. doi: 10.1016/j.drudis.2022.06.004

frontiers | Frontiers in Medicine

TYPE Original Research
PUBLISHED 11 April 2023
DOI 10.3389/fmed.2023.1144754

Check for updates

OPEN ACCESS

EDITED BY
Emmanuel Twumasi Osei,
University of British Columbia,
Okanagan Campus,
Canada

REVIEWED BY
Dawei Yang,
Fudan University,
China
Jazmin Calyeca,
The Ohio State University,
United States

*CORRESPONDENCE
John F. Engelhardt
✉ john-engelhardt@uiowa.edu
Kalpaj R. Parekh
✉ kalpaj-parekh@uiowa.edu

SPECIALTY SECTION
This article was submitted to Pulmonary Medicine, a section of the journal Frontiers in Medicine

RECEIVED 15 January 2023
ACCEPTED 15 March 2023
PUBLISHED 11 April 2023

CITATION
Ievlev V, Pai AC, Dillon DS Jr, Kuhl S, Lynch TJ, Freischlag KW, Gries CB, Engelhardt JF and Parekh KR (2023) Development and characterization of ferret *ex vivo* tracheal injury and cell engraftment model. *Front. Med.* 10:1144754. doi: 10.3389/fmed.2023.1144754

COPYRIGHT
© 2023 Ievlev, Pai, Dillon, Kuhl, Lynch, Freischlag, Gries, Engelhardt and Parekh. This is an open-access article distributed under the terms of the Creative Commons Attribution License (CC BY). The use, distribution or reproduction in other forums is permitted, provided the original author(s) and the copyright owner(s) are credited and that the original publication in this journal is cited, in accordance with accepted academic practice. No use, distribution or reproduction is permitted which does not comply with these terms.

Development and characterization of ferret *ex vivo* tracheal injury and cell engraftment model

Vitaly Ievlev[1], Albert C. Pai[2], Drew S. Dillon Jr[3], Spencer Kuhl[3], Thomas J. Lynch[2], Kyle W. Freischlag[2], Caitlyn B. Gries[2], John F. Engelhardt[1]*and Kalpaj R. Parekh[2]*

[1]Department of Anatomy and Cell Biology, Carver College of Medicine, University of Iowa, Iowa City, IA, United States, [2]Department of Cardiothoracic Surgery, Carver College of Medicine, University of Iowa Hospitals and Clinics, Iowa City, IA, United States, [3]Protostudios, Carver College of Medicine, University of Iowa, Iowa City, IA, United States

The field of airway biology research relies primarily on *in vitro* and *in vivo* models of disease and injury. The use of *ex vivo* models to study airway injury and cell-based therapies remains largely unexplored although such models have the potential to overcome certain limitations of working with live animals and may more closely replicate *in vivo* processes than *in vitro* models can. Here, we characterized a ferret *ex vivo* tracheal injury and cell engraftment model. We describe a protocol for whole-mount staining of cleared tracheal explants, and showed that it provides a more comprehensive structural overview of the surface airway epithelium (SAE) and submucosal glands (SMGs) than 2D sections, revealing previously underappreciated structural anatomy of tracheal innervation and vascularization. Using an *ex vivo* model of tracheal injury, we evaluated the injury responses in the SAE and SMGs that turned out to be consistent with published *in vivo* work. We used this model to assess factors that influence engraftment of transgenic cells, providing a system for optimizing cell-based therapies. Finally, we developed a novel 3D-printed reusable culture chamber that enables live imaging of tracheal explants and differentiation of engrafted cells at an air-liquid interface. These approaches promise to be useful for modeling pulmonary diseases and testing therapies.

KEYWORDS

explant, engraftment, tissue-transwell, trachea, ferret, injury model, regeneration, airway

Introduction

In recent years the field of airway biology has seen a surge in new imaging and culture methods. Novel techniques such as precision-cut lung slices (1) and lung-on-a-chip models (2, 3) are gaining popularity among researchers because they account for 3-D complexity and cell-type heterogeneity of the airways. In addition, *in vitro* monocultures of airway epithelial progenitors enable researchers to precisely manipulate and image cells. However, these methods cannot account for the complex cellular crosstalk that drives non-cell autonomous effects originating from cells in the airway mesenchyme, cartilage, submucosal glands (SMGs), and elsewhere. Airway tissue complexity is reflected by the plethora of cell types discovered by recent single-cell RNA sequencing studies (4–7). Although *in vivo* experimentation remains the gold standard in terms of biological relevance of the findings, many of the precise manipulations and

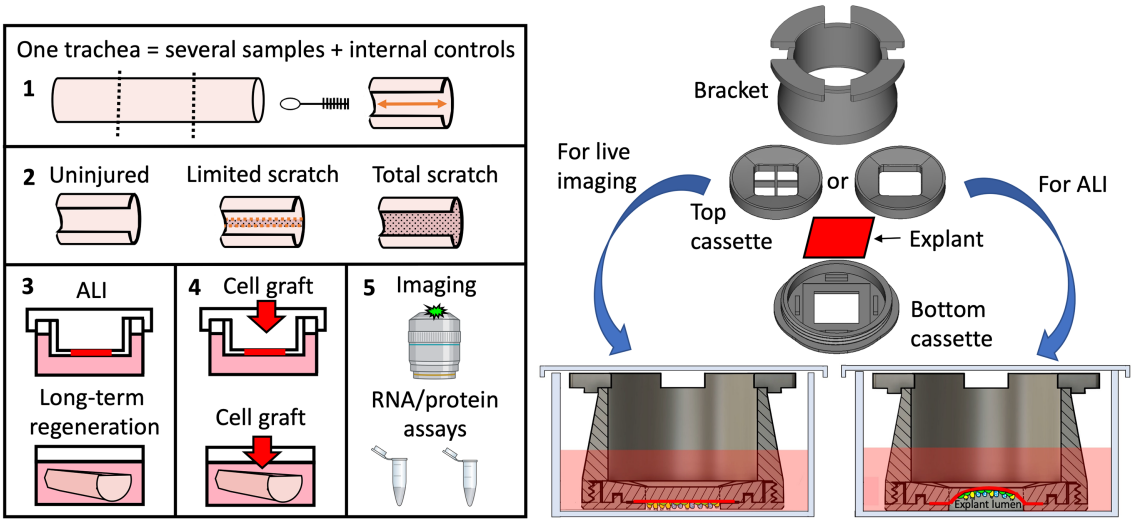

GRAPHICAL ABSTRACT
1,**2**. We describe here a method for differential mechanical injury of ferret tracheal explants that can be used to evaluate airway injury responses ex vivo. **3**. Injured explants can be cultured at ALI (using the novel tissue-transwell device on the right) and submerged long-term to evaluate tissue-autonomous regeneration responses. **4**. Tracheal explants can also be used for low throughput screens of compounds to improve cell engraftment efficiency or can be seeded with particular cells to model a disease phenotype. **5**. Lastly, we demonstrate that ex vivo-cultured tracheal explants can be evaluated by various molecular assays and by immunofluorescent imaging that can be performed live using our custom-designed tissue-transwell.

imaging methods are costly and either challenging or impossible to carry out in living animals. *Ex vivo* tissue culture approaches overcome some of the limitations of *in vivo* and *in vitro* models and also provide an independent means of validating the experimental results.

In the current study, we characterized a ferret tracheal explant model of injury and cell engraftment. As opposed to mice, rats, and rabbits, for which tracheal explants were described previously (8–10), ferrets are useful, because they have extensively developed submucosal glands (SMG) throughout cartilaginous airways, which is also the case in humans. This is critical because these structures contribute significantly to airway regeneration (11, 12). Even though some other species (i.e., pigs and sheep) also have well developed SMGs, ferrets are exceptionally useful as a model organism due to relatively low costs for raising and housing them. Additionally, existing transgenic ferret lines can be used for lineage tracing (e.g., a fluorescent reporter ROSA26-Tomato/EGFP and several Cre^{ERT2} driver lines are available) (13).

In this work we developed protocols for *ex vivo* culture, injury, cell engraftment, and imaging of ferret tracheal explants. In addition, we designed and tested a tissue culture chamber for explants that enables separation of the luminal and adventitial sides of the explant to create an air-liquid interface (ALI). We optimized *ex vivo* culture conditions to stimulate regeneration of the surface airway epithelia by both the surface basal cells and the glandular progenitors such as myoepithelial cells (MECs). Our *ex vivo* model of ferret trachea allows us to screen for optimal engraftment conditions at a much lower cost than that associated with *in vivo* methods. As a proof of principle, we show that both partial and complete removal of the tracheal explant epithelium stimulates engraftment of Tomato+ primary ferret airway basal cells. These findings are important because patients with tracheal stenosis or genetic airway diseases such as cystic fibrosis (*CF*) could potentially be treated by engraftment of gene-corrected, autologous cells either directly into the patient or into a tracheal scaffold. We additionally show that this *ex vivo* model can be used to study transcriptional changes in the tracheal epithelium, both after injury and after transgenic cell engraftment, and that it can be used to generate air-liquid interphase cultures that are compatible with live imaging.

Materials and methods

Ex vivo tracheal brush injury

We used adult wild-type (WT) ferret tracheas for scratch injury assays *ex vivo*. Shortly after the animal was euthanized, the trachea was dissected and cut open longitudinally on the membranous side while the cartilaginous side was brushed with a stiff nylon brush (Justman Brush Company, cat#415140, d = 2 mm). Specifically, injury was performed either by making 3 overlapping streaks along the proximal-distal axis (limited injury) or by extensively brushing in all directions (total injury). The explants were then cultured in F-medium [3:1 (v/v) DMEM (Invitrogen): F-12 Nutrient Mixture (Gibco), 7.5% FBS, 1% Penicillin/Streptomycin, 125 ng/ml epidermal growth factor (Invitrogen), 25 µg/mL hydrocortisone (Sigma-Aldrich), 5 µg/mL insulin (Sigma-Aldrich), 0.01 mg/mL Gentamicin, 0.1% amphotericin B, 11.7 µM cholera toxin (Sigma-Aldrich) and 10 µmol/L Y-27632 (Tocris)] and pulsed with a nucleotide analog – 10 µM EdU (5-ethynyl-2′-deoxyuridine, Thermo Fisher Scientific C10340) on specified days after injury.

Whole-mount ferret trachea staining

At various experimental timepoints the explants were fixed in 4% paraformaldehyde or 10% neutral buffered formalin for 2 h at room

temperature on a rocker, then washed three times in PBS for 20 min each. For staining of proteins that require antigen retrieval, samples were additionally incubated in citrate buffer (10 mM sodium citrate, 0.05% Tween 20, pH = 6.0) at 55°C overnight. The samples were then washed in PBS three times and incubated in blocking buffer (20% donkey serum, 0.3% Triton X-100, and 1 mM $CaCl_2$ dissolved in PBS, pH 7.6), either overnight at 37°C or for 24–72 h at 4°C. Tissues were rinsed in PBS, after which EdU was detected using the Click-iT™ EdU Cell Proliferation Kit for Imaging (Thermo Fisher Scientific), in accordance with the supplied protocol. The tissues were then washed three times for 20 min each in PBS and incubated with primary antibodies (dissolved in diluent buffer: 1% donkey serum, 0.3% Triton X-100, and 1 mM $CaCl_2$ in PBS, pH 7.6) for 18–24 h at 37°C with agitation (see Table 1). The tracheas were then washed three times for 20 min in PBS and incubated with secondary antibodies (dissolved in diluent buffer) for 24 h at 37°C, with agitation. Next, the tissues were washed three times for 20 min in PBS and submerged in Ce3D tissue clearing solution (Biolegend cat# 427704) for 2 h at RT or overnight at 4°C. Samples were mounted under 0.33 mm coverslips or under 1 mm glass slides and the edges were sealed with Gorilla Glue™ and clamped with binder clips for about 20 min to ensure glue fixation. Tile scan and Z-projection modules of a Zeiss LSM 880 or 980 line-scanning confocal microscope (Carl Zeiss, Germany) were used for imaging of the entire explant.

Isolation, culture, and engraftment of primary airway basal cells

Isolation of primary cells

Primary surface epithelial cells were isolated from ferret trachea and/or extra-lobar bronchi by a previously described enzymatic digestion method (14). Tissues were digested for 1 h at 37°C with agitation, in 5 mg/ml pronase (Roche) dissolved in F-12 medium (Gibco), to dissociate surface airway epithelial (SAE) cells. Epithelium from the luminal surface of the airways was further detached with a cell scraper. Detached sheets of SAE cells were then passed through a 100 µm strainer to separate cell aggregates and to filter out the debris. Next, we washed the cells twice in an excess of complete DMEM (DMEM with 10% FBS, 1% Penicillin/Streptomycin) to remove all traces of pronase. The SAE cells were then plated on 804G-coated plastic plates. The remaining tissue, which contained SMG cells was minced and incubated for 45 min at 37°C on a rocker in 1X Collagenase/Hyaluronidase (STEMCELL Technologies, Inc.; diluted from 2x in F-12 medium). For every 3 ml of 1x Collagenase/Hyaluronidase solution, 1 ml of Trypsin/EDTA (0.025% Trypsin, 0.01% EDTA: Thermo Fisher Scientific) was added and samples were incubated for an additional 10 min at 37°C. After the digestion, SMG cells were liberated by pipetting using a 10 ml serological pipette tip. The detached SMG cells were then passed through a 100 µm cell strainer and washed twice in an excess of complete DMEM, and finally plated on 804G-coated tissue culture dishes.

TABLE 1 Primary antibodies.

Antibody target	Company	Catalog #	Concentration
KRT5	BioLegend	905,901	1:500
KRT15	BioLegend	833,901	1:200
AC-TUB	Cell Signaling Technology	5,335	1:500
CCSP	Millipore Sigma	ABS1673	1:4000
KRT14	Labvision	RB-9020-P1	1:500
KRT14	Thermo Fisher Scientific	MA5-11599	1:300
α-SMA	Abcam	ab7817	1:500
SOX9	Millipore Sigma	AB5535	1:500
KRT8	Origene	BP5007	1:500

Primary cell culture

Primary cells were cultured under the conditions used to propagate airway basal cells (BCs) and SMG progenitors as described previously (14). Ferret primary airway basal stem cells were cultured in PneumacultEX+ with 1% Penicillin/Streptomycin. 2-D cell cultures were grown on tissue-culture plastic pre-coated with filter-sterilized, extracellular matrix (ECM)-enriched 804G-conditioned medium for ≥1 h as described previously (14). Accutase (STEMCELL Technologies, Inc.) was used to detach the cells from the culture plates. During the washes, the cells were centrifuged for 5 min at 500 g force.

Quantitative PCR analysis

RNA was isolated from brushed off cells using Trizol regent (Ambion) following the manufacturer's protocol. A High-Capacity cDNA Synthesis Kit (Applied Biosystems) was used to synthesize cDNA following the protocol provided by the manufacturer. qPCR reactions were set up using 10 nM primers, the POWER SYBR master mix (Applied Biosystems), cDNA, and H_2O. Reactions were run on a CFX Connect Real-Time PCR Detection System (Bio-Rad). The Delta–Delta-CT method was used to normalize the expression data. Primers are listed in Table 2.

TABLE 2 Ferret qPCR primers.

ITGB1 qPCR primers	Fwd: TGTATACAAGCAGGGCCAAAT Rev.: TCTCTGCTGTTCCTTTGCTAC
ITGA6 qPCR primers	Fwd: CGACCCTTCATCAGAAAGCA Rev.: CTCCATCCATGTCATCCTCAATC
ITGA3 qPCR primers	Fwd: CCGATTCCTGGTGGTGAAG Rev.: GCTCACAGTCGTCCTTGTC
CD44 qPCR primers	Fwd: GTGGAGAAGAATGGTCGTTACA Rev.: GGTGTTGGATGTGAGGATGT
Tomato qPCR primers	Fwd GTATCGGACAGCGCAAAGAACG Rev. CTGGTAGGTACAGCAGCTCATC
LAMA3 qPCR primers	Fwd: CTCAGGCACACAGTACAACA Rev.: GAGTAGGTGCTTCCAAAGTCTAC
MMP9 qPCR primers	Fwd: GAAGCCGACATCGTCATTCA Rev.: CAGGGACCACAACTCTTCATC
SOX9 qPCR primers	Fwd: GTCAACGAGTTCGACCAGTA Rev.: CAGCTGCTCCGTCTTGAT
ACTN-B qPCR primers	Fwd: TGGGACGACATGGAGAAGAT Rev.: CCTGGATGGCCACATACAT

Image analysis

Merged tile scans were quantified using ImageJ. Epithelial coverage of the explants was scored in ImageJ by dividing the area stained with epithelial markers (KRT5, KRT14, KRT15 or Tomato) over the total area of the explant. The % fraction of actively proliferating SMGs was calculated by dividing the selected areas with discretely high EdU+ cell density by the total area of all the SMGs as defined morphologically by staining with Krt14/5 and/or αSMA and Sox9.

Statistical analysis

Unless stated otherwise in a figure legend, results are reported as mean +/− SEM, individual dots on the graphs represent biological replicates, and statistical analysis was conducted using Prism version 9 (GraphPad Software) where N equaled the number of independent animals. The statistical tests used are stated in each figure legend. Data were considered significant at $p < 0.05$.

Results

Whole-mount staining reveals fine details of anatomy of the ferret trachea

Whole-mount tissue staining provides opportunities to capture aspects of the cellular architecture and organization that are often lost in 2D tissue sections. Furthermore, because a greater surface area is covered in such preparations than in tissue sections, this approach makes it possible to capture cellular events at the whole organ level. This approach is also well suited for capturing rare cell types and structures in the organ of choice, for example, the ionocytes in the airway epithelium. We developed an accessible and cost-effective method for whole-mount staining, clearing, and embedding of the ferret trachea (Figures 1A–C) that enables clear visualization of SMGs (Figures 1D–F). Specifically, we found that between each cartilage ring, ferrets have two rows of SMG acini, each perfused with blood vessels (20–25 μm in diameter) that branch laterally to the acini bundles (Figure 1D). Additionally, SMGs appear to be the most innervated structure in the trachea, with a dense network of thick Ac-Tubulin+ nerve bundles surrounding the acini (Figures 1E,F). This whole-mount staining approach can be used to evaluate anatomical structures over a large tissue area. For example, we imaged tracheal fragments 7–7.5 cm in length, from four animals, covering 100% of the width and about 90% of the length of an adult ferret trachea, to evaluate the SMG distribution. Our examination of ROSA-TG transgenic ferrets revealed that SMGs are located only on the ventral side of the trachea, between the cartilage rings, and that their abundance declines slightly along the distal axis (Figures 1G,H). In summary, our whole-mount staining and confocal microscopy experiments reveal the complexities of the structure, innervation, and vascularization of the trachea.

F-medium stimulates induction of KRT14 at the wound edges and proliferation of the SAE and SMGs during regeneration after tracheal injury *ex vivo*

Next, we determined the culture conditions conducive to robust SAE repair and to proliferation of SMG progenitors after injury. We initially tested two media: DMEM containing antibiotics and antifungal agents; and F-medium, which contains DMEM, F12, 7.5% FBS, and other additives (see the methods for details). DMEM was chosen for its simplicity because we hypothesized that tracheal explants can produce everything that they require for prolonged survival and repair after injury. F-medium was chosen because it is permissive for the survival of both epithelial and mesenchymal cells when used in colony formation efficiency (CFE) assays of airway basal cells that are grown on 3 T3-J2 fibroblasts (15, 16).

The tracheal lumen of ferrets was subjected to mechanical injury using a stiff 2-mm-wide nylon brush. This left a gap in the SAE that was partially repaired by basal progenitor cells over the course of 15 days (Figure 2A). We observed that in basal cells KRT14 was upregulated at the leading edges of the scratch (orange dashed lines in Figures 2B–H). This is consistent with the observations that KRT14 is upregulated in different animal models of airway injury, for example with SO_2, Cl_2, naphthalene, and polidocanol as well as in human airway diseases, such as idiopathic pulmonary fibrosis (IPF), restrictive allograft syndrome (RAS), and bronchiolitis obliterans syndrome (BOS) (17–21). KRT14 is not the only airway injury response marker, but it has been one of the more robust and consistent injury-induced gene markers that our laboratory has focused on in the past (16–18). Cellular changes such as upregulation of KRT14 and cell proliferation, as well as altered cell morphology at the wound edges, were more pronounced in F-medium than in DMEM on days 2, 5 and 15 (Figures 2B–G). These findings suggest a more robust injury response in F-medium. Additionally, in the explants cultured in F-medium but not in those cultured in DMEM, a wide band of cells along the scratch boundary incorporated EdU, indicating that they were actively proliferating. Explants cultured in F-medium covered most of the denuded scratch by day 15, whereas those cultured in DMEM showed no signs of scratch re-epithelization by day 21 (Figures 2F,G). After 15 days of recovery while submerged in F-medium, the regenerated epithelium had not differentiated into ciliated cells; however, ciliated cells were retained at the uninjured periphery of the scratch (Figure 2H). We conclude that in the ferret *ex vivo* tracheal injury model F-medium is better suited than DMEM for regeneration studies.

The Rho Kinase inhibitor Y-27632 is a standard component of F-medium and is frequently used in culturing airway stem cells. We evaluated the effects of Y-27632 on SAE wound closure and SMG proliferation in our *ex vivo* tracheal injury model. When examining the SMGs following complete removal of the SAE by brushing, we noticed three distinct glandular phenotypes: "passive", "active", and "compromised" (Figure 3A). When explants were pulsed with EdU for 24 h on day-3 post injury (DPI3) and fixed on DPI5, "passive" glands contained few EdU+ cells whereas "active" glands contained many and this often coincided with increased KRT5 staining (Figures 3C,D). On DPI5 after total injury (extensive luminal brushing), "active" glands were typically found below KRT5+/EdU+ epithelium on the tracheal surface, suggesting that SAE regeneration involves migration of progenitors from these glands to the airway surface (Figure 3B).

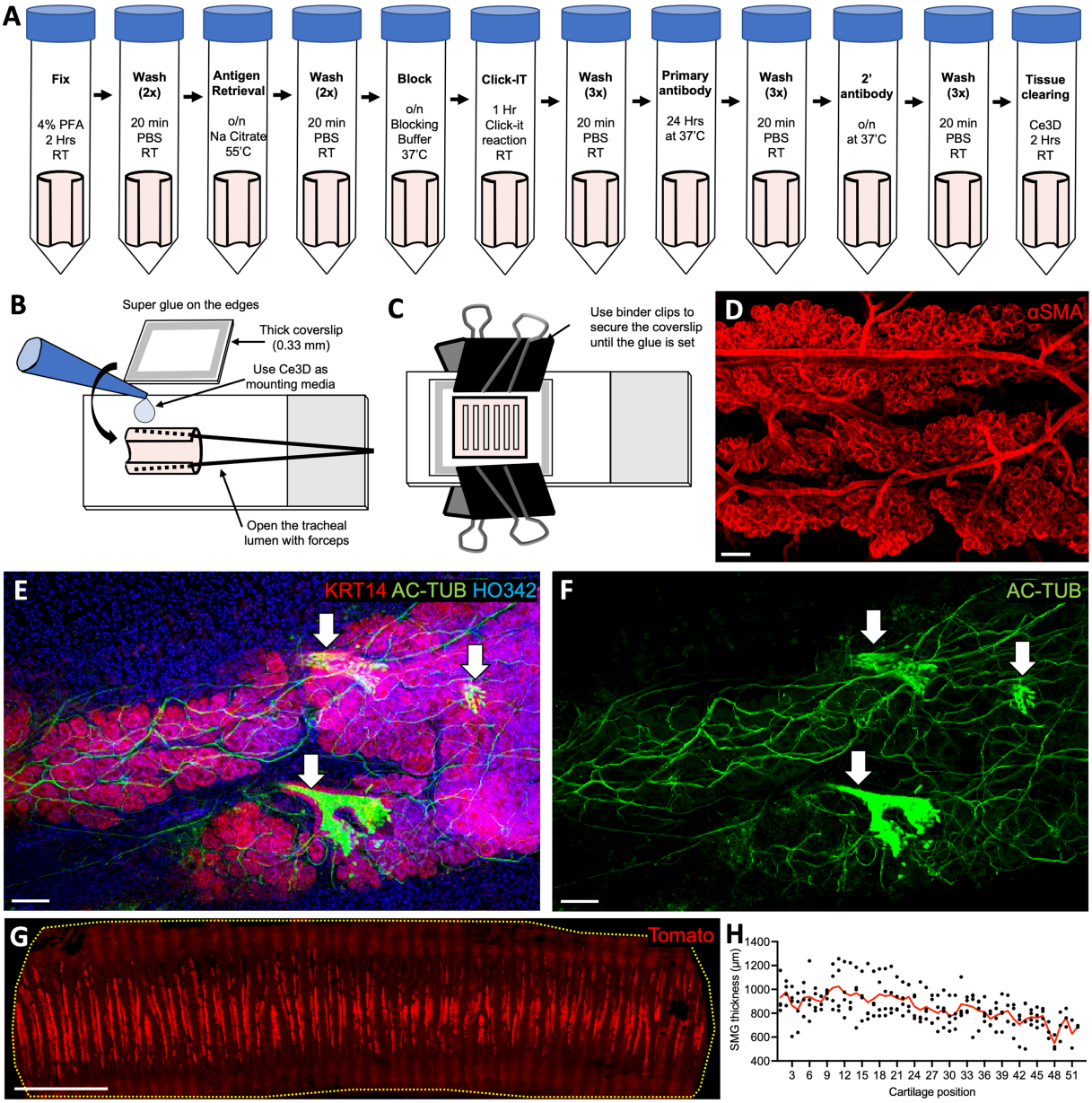

FIGURE 1
Whole-mount staining of ferret tracheal explants reveals SMG structure and distribution. **(A)** Protocol for whole-mount staining of ferret tracheal explants (open pink cylinders on the schematic). **(B,C)** Steps in mounting ferret tracheal explants. **(D–F)** Confocal maximum intensity projections of the SMGs from ferret tracheas stained on whole-mount. **(D)** αSMA staining, showing vascularization and SMG structure. **(E,F)** AC-TUB staining, showing glandular innervation and ciliated ducts (arrows). **(G)** Confocal maximum intensity projection of an adult ROSA-TG ferret trachea where Tomato expression is enriched in SMGs. **(H)** Quantification of the SMG thickness in relation to cartilage position. Red line represents an average value for *N*=4 ferrets. All scale bars are 100μm, except in **(G)** the scale bar is 1cm.

Glands of the "compromised" category were relatively rare, comprising <5% of the total gland volume; they incorporated no EdU and were negative for SOX9 (SMG marker, Figure 3E). This gland type most likely represents the SMGs that are no longer viable but retain keratin remnants, and thus also the distinct glandular morphology. We observed that the injured explants cultured in F-medium with Y-27632 contained higher percentages of 'active' glands (24.6% +/− 3.3% vs. 9.2% +/− 1.1%) and had more extensive SAE re-epithelialization (15.7% +/− 1.1% vs. 3.5% +/− 1.9% on DPI5 and 54.1% +/−3.0% vs. 22.5% +/− 7.3% on DPI9) than those cultured in F-medium without Y-27632 (Figures 3F–I). We conclude that Y-27632 stimulates SAE regeneration by glandular progenitors, and therefore selected F-medium with Y-27632 as the main culture method for subsequent experiments. Interestingly, most of the SMGs did not actively proliferate even when the explants were continuously cultured in the presence of EdU for 9 days after a total surface brushing. Only 37.3% +/−3.7% of the glands were actively proliferating (Figures 3I,K,L). If this phenomenon holds true *in vivo*, this has interesting implications as a natural mechanism to prevent replicative exhaustion of the glandular SC niche.

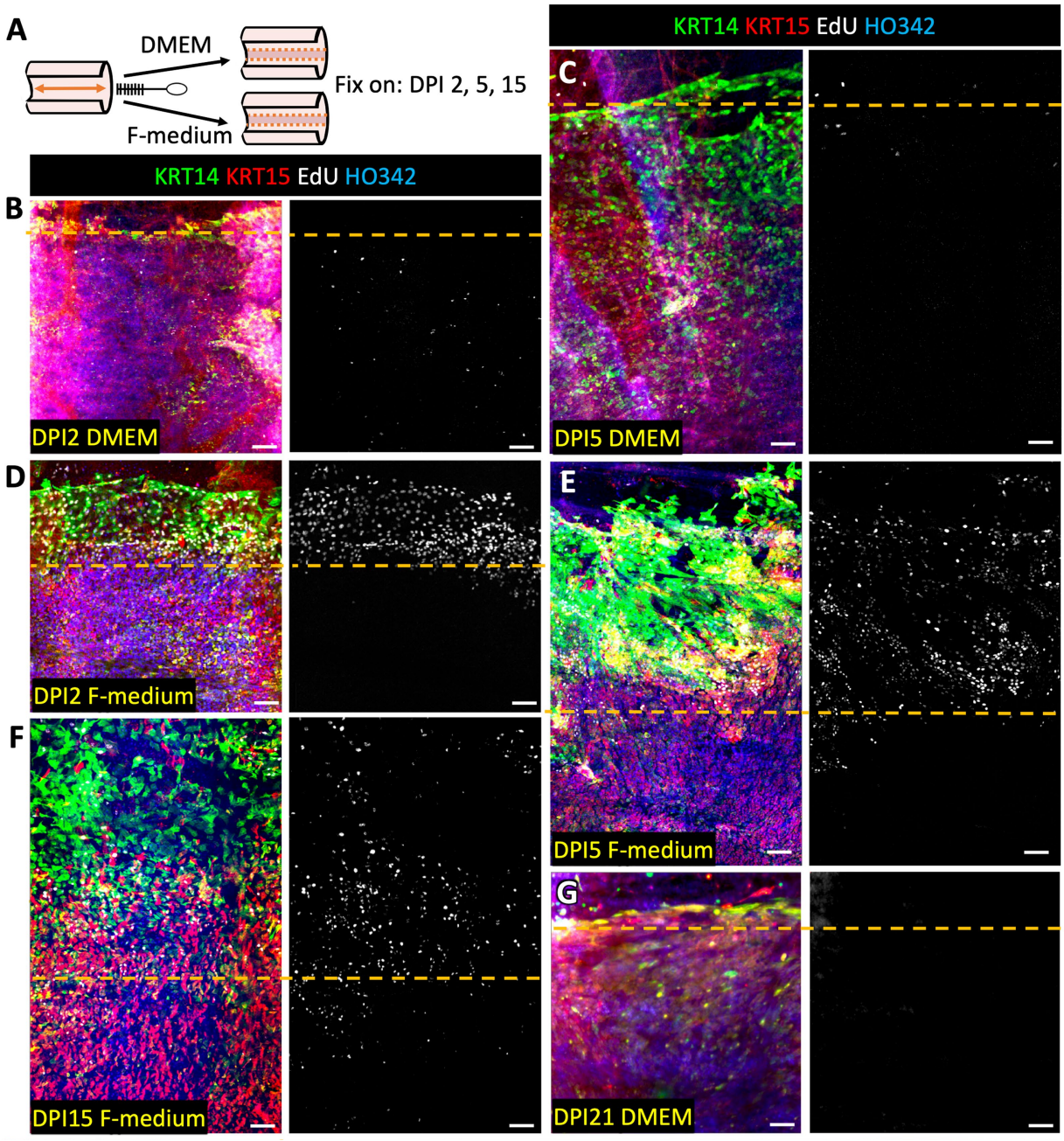

FIGURE 2
F-medium with Rock-inhibitor stimulates SAE regeneration, upregulation of KRT14 and proliferation at the wound edges in injured tracheal explants. **(A)** Experimental design: The SAE of WT ferret tracheal explants was injured by limited brushing and cultured in DMEM or in F-medium. Samples were fixed and stained on the specified days post injury (DPI). DPI2 samples were cultured with EdU for during the entirety of the experiment, whereas all other samples were pulsed with EdU for 24h on DPI3. **(B,C,G)** Representative confocal micrographs of the explants cultured in DMEM. **(D–F,H)** Representative confocal micrographs of the explants cultured in F-medium. Results were reproduced using $N \geq 3$ ferrets. Orange dashed lines indicate the approximate boundaries of the initial scratch. Scale bars are 100μm.

Cell engraftment onto a ferret tracheal explant is facilitated by airway epithelial injury

An important area of interest for cell therapy applications is the efficiency of transgenic cell engraftment (22, 23). With this in mind, we tested the ability of Tomato+ primary basal cells from ferrets to engraft onto intact, partially scratched, and fully scratched WT ferret tracheal explants. We hypothesized that reduced competition with endogenous airway epithelium would facilitate the engraftment of transgenic cells and therefore the efficiency will be higher in the context of total and partial injury versus uninjured explants. We tested this by seeding tracheal explants with $2*10^6$ Tomato+ passage-6 (p6) ferret surface airway basal cells immediately after partial or complete brush injury or onto uninjured control explants (Figure 4A). After the lumen was seeded with Tomato+ cells, the tissues were cultured for 2 or 15 days in F-medium containing Y-27632. We observed that infrequent patches of Tomato+ cells, that engrafted onto uninjured explants on DPI2, stained for KRT14 more intensely than the surrounding Tomato-native SAE (Figure 4B). This

10.3389/fmed.2023.1144754

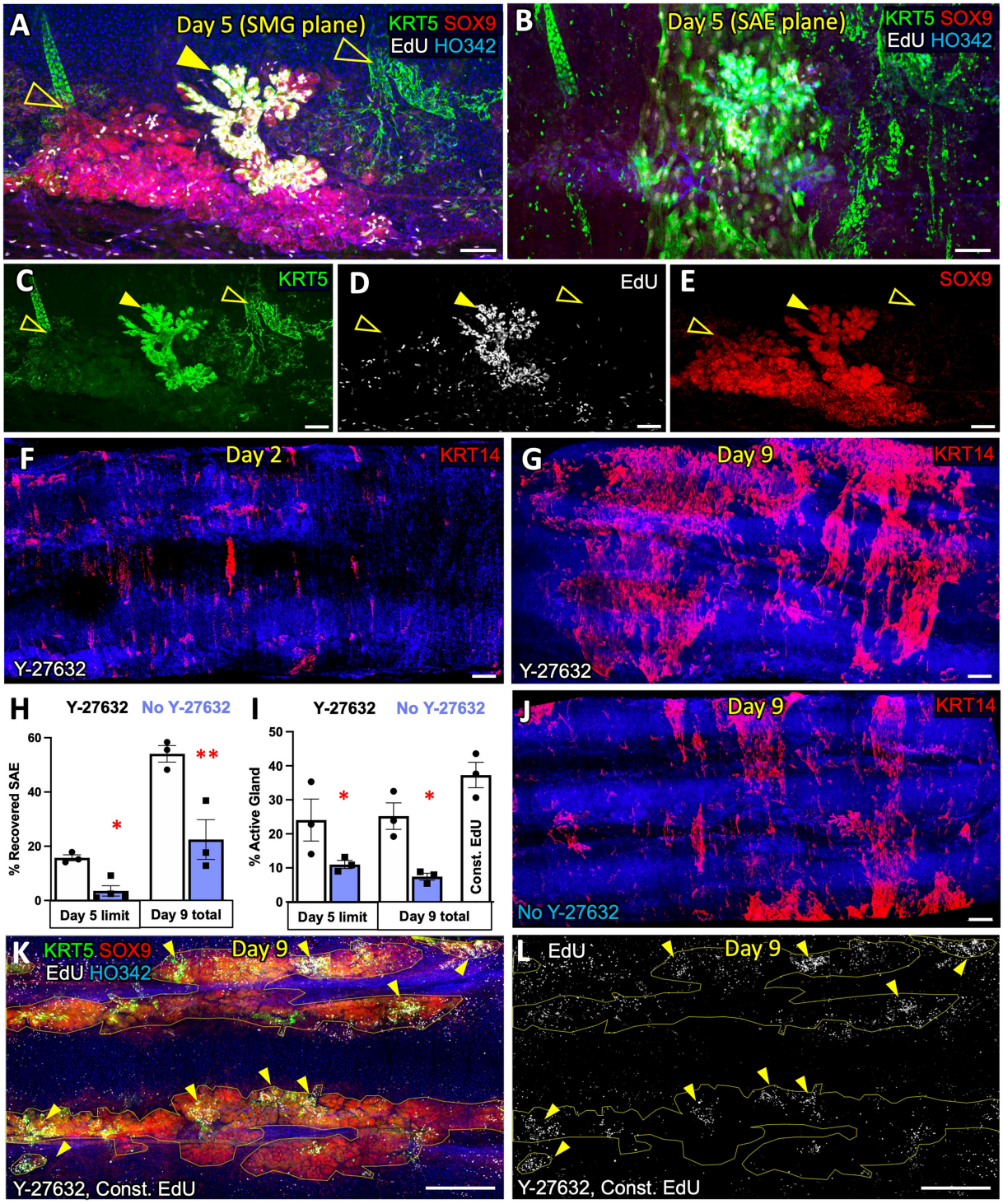

FIGURE 3
F-medium with ROCK-inhibitor stimulates SAE regeneration by glandular progenitors in ferret trachea *ex vivo*. **(A)** Confocal micrograph of a ferret tracheal explant cultured in F-medium with the ROCK-inhibitor Y-27632, after total brush injury and a 24-h EdU pulse on DPI3. The image shows the diversity of SMG phenotypes providing examples of an actively proliferating gland (solid arrow) and two glands with fewer proliferating cells (unfilled arrows). **(B)** Confocal micrograph focused on the z-plane at the SAE, superficial to the SMGs in panel **(A)**. **(C–E)**, Individual channels of the micrograph in panel **A**, showing **(C)** KRT5, **(D)** EdU, and **(E)** SOX9 expression. **(F,G)** Confocal micrographs of explants subjected to total brush injury, imaged on **(F)** DPI2 and **(G)** DPI9. **(H)** Quantification of SAE recovery, shown as a percentage of the surface area covered with KRT14+ SAE. **(I)** Quantification of the % of SMG area assigned to actively proliferating glands (with high EdU+ cell density). **(J)** Representative micrograph of an explant imaged on DPI9 when cultured in F-medium without Y-27632. **(K,L)** Representative max intensity projections of the SMG plane of the explants that were fully brushed and cultured in constant presence of EdU for 9days. Graphs show mean +/− SEM, $N \geq 3$ explants from independent ferrets. Significance was determined by 2-way-ANOVA, Holm-Sidak multiple comparison test. *$p<0.05$, **$p<0.01$. Scale bars in **(A–E)** are 100μm; all other scale bars are 500μm.

10.3389/fmed.2023.1144754

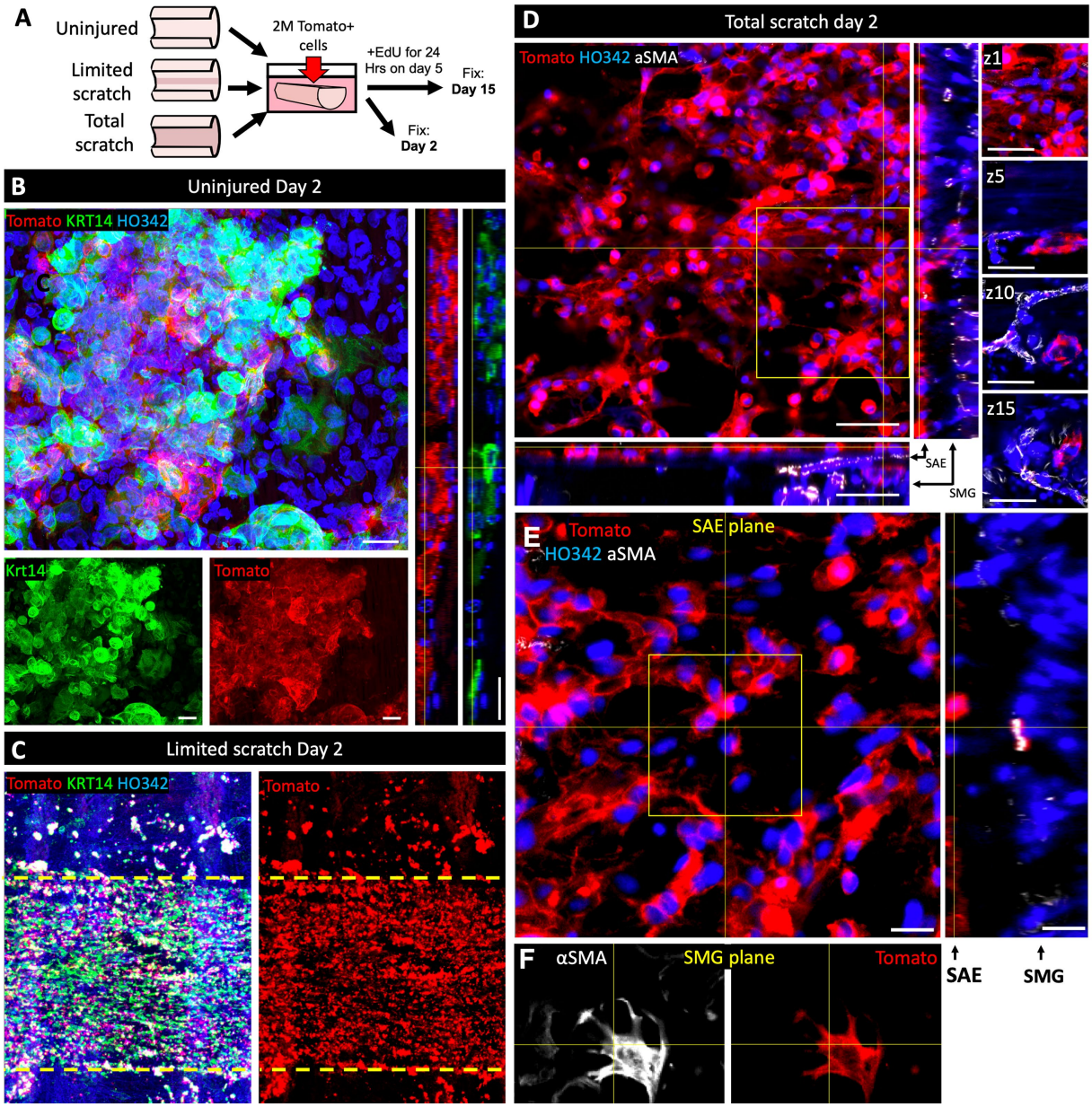

FIGURE 4
Cell engraftment on ferret tracheal explants is facilitated by epithelial injury. **(A)** Experimental design: Ferret tracheal explants, ~7mm in length, were either left uninju-red, partially or completely de-epithelialized by scratching the lumen with a stiff 2-mm nylon brush. Explants were then submerged in F-medium and seeded with $2*10^6$ p6 Tomato+ primary ferret airway basal cells. Samples were fixed on day 2 or day 15 after engraftment of Tomato+ cells. For the day 15 explants, a 24-h pulse of EdU was administered on day 5. **(B–E)** Confocal micrographs of **(B)** uninjured, **(C)** partially brushed, or **(D,E)** fully brushed explants on day 2 after cell engraftment. Insets in panels **(B–E)** show split channels or orthogonal views and different *z*-planes of the boxed regions. Images are representative of *N*=3 independent experiments. Scale bars in all panels other than **(D)** are 20μm; in **(D)** they are 50μm.

outcome was expected because KRT14 is rapidly induced in cultured SAE basal cells (16). In the explants with partially injured SAE, Tomato+ cells were incorporated primarily into the injured regions on day 2 (Figure 4C). In the explants with fully brushed surface after a total injury, SAE Tomato+ cells were incorporated throughout the surface as well as into the SMG ducts on day 2 (Figure 4D); Tomato+ cells were also incorporation into the SMG acini and their differentiation into αSMA+ MECs was observed, but this was very rare (Figure 4E). On day 15, Tomato+ SAE coverage was similar to that on day 2, and it was the highest in the explants subjected to a total injury, where engrafted cells covered 34.0% +/− 4.3% of the explant lumen (Figure 5A). In explants that received a limited scratch injury before cell engraftment, Tomato+ cells were incorporated mostly into the brushed region covering 29.6% +/− 5.1% of the scratch and 13.8% +/− 0.9% of the total explant. Uninjured explants incorporated the fewest Tomato+ cells in the SAE, covering 1.7% +/− 0.6% of the lumen (Figures 5A–C). These findings demonstrate that an injury that creates space for stem cells to attach prior to engraftment can improve their attachment efficiency. Staining of the explants with KRT5 and EdU click chemistry revealed that at least some of the engrafted cells were EdU+/KRT5+ (Figures 5D–G), suggesting that they were able to divide after engraftment which was evident by their incorporation of EdU that was pulsed for 24h on DPI5.

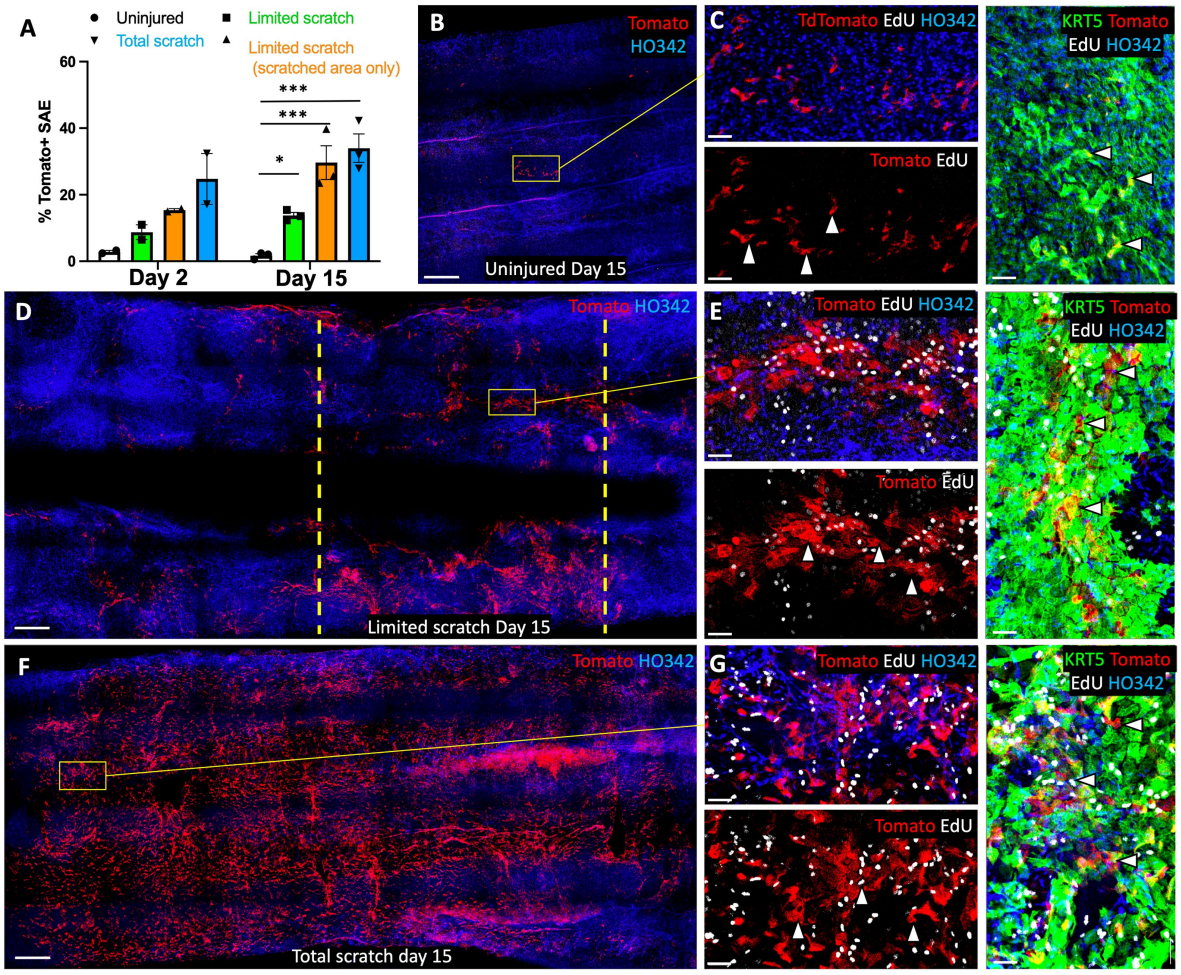

FIGURE 5
Retention of engrafted cells on ferret tracheal explants is facilitated by epithelial injury on. This experiment was performed as outlined in Figure 4, and all images show the samples on day 15 post engraftment. **(A)** Quantification of explant lumen coverage with Tomato+ SAE on day 2 and day 15 after engraftment. **(B–G)** Confocal micrographs of explants that were **(B,C)** uninjured, or underwent **(D,E)** partial injury or **(F,G)** complete injury, on day 15 after cell engraftment. Composite panels showing KRT5 staining in **(C,E,G)** are rotated 90° clockwise. Dashed lines indicate the boundaries of the scratch. Graph shows Mean +/− SEM, *N*=3 independent experiments. Significance was determined by one-way ANOVA, Tukey multiple comparison test (*** p<0.001, ns - not significant). Scale bars in **(B,D,E)** are 500μm; in **(C,E,G)** scale bars are 50μm.

Mechanical injury and cell engraftment *ex vivo* results in transcriptional changes to the surface airway basal cells

To better understand the factors that influence the efficiency of cell engraftment, we assessed the differences in the transcription of cell adhesion related genes between Tomato+ cells seeded on a denuded tracheal graft and an ECM-coated cell culture dish. To this end, we removed the SAE from freshly excised tracheas using a series of SDS-containing detergent washes as described previously (24). Then, we engrafted 10^7 p6 Tomato+ primary surface airway basal cells into a 3-cm ferret tracheal segment using a rotating bioreactor method developed by our group previously for ferret tracheal explant cultures (24). After 18 h, the explants were rigorously washed with PBS to remove any cells that did not fully engraft, and then the luminal surface of the tracheas was brushed to collect Tomato+ cells. RNA from these cells was compared to that of Tomato+ primary basal cells that had been seeded on 804G-coated culture dishes for 18 h (Figure 6A). Subsequent qPCR analysis revealed that expression of ITGB1, ITGA6 and ITGA3 was lower in the cells seeded on tracheal grafts than in those seeded on culture plates (Figure 6B). Expression of CD44, a surface receptor that binds the ECM and promotes cell adhesion was unchanged as was the expression of Tomato, which served as a control to ensure that we had primarily collected the newly engrafted Tomato+ cells and not the native cells of the Tomato-explant (Figure 6B). These data suggest that downregulated integrin expression could account for the decreased efficiency of engraftment of cells on the basal lamina of the tracheal explants versus ECM-coated culture dishes.

Efficient cell engraftment in injured airways is dependent not only on the donor cells but also the injury response of native epithelium that remains present. Therefore, we evaluated how different degrees of explant injury impact the native SAE during regeneration. To this end, we evaluated the cells on the explant

surface after 14 days of regeneration following either partial or complete removal of the original SAE by luminal brushings. In the case of partial brush injury, regeneration of the SAE involved both the remaining surface basal cells and SMG progenitors, whereas in the case of total injury, regeneration was attributed primarily to the glandular progenitors. On DPI14 we collected the SAE cells from regenerating explants by brushing the lumen and isolated RNA from them for evaluation by qPCR (Figure 6C). Given that this was a proof-of-principle experiment, we focused on gene targets that we expected to be upregulated in regenerating airway epithelia. Although this method can be used for unbiased screens of transcriptional changes associated with regeneration using single-cell or bulk RNA-sequencing, in this experiment we focused on the expression of three genes. Two of them were MMP9 and LAMA3 that are both associated with ECM deposition and remodeling and are upregulated in epidermal wound healing (25, 26). We also assessed the expression of SOX9, a marker of airway SMG progenitors that have been previously shown to participate in SAE regeneration (15, 27, 28). As expected, all three of these targets were upregulated in both severely injured

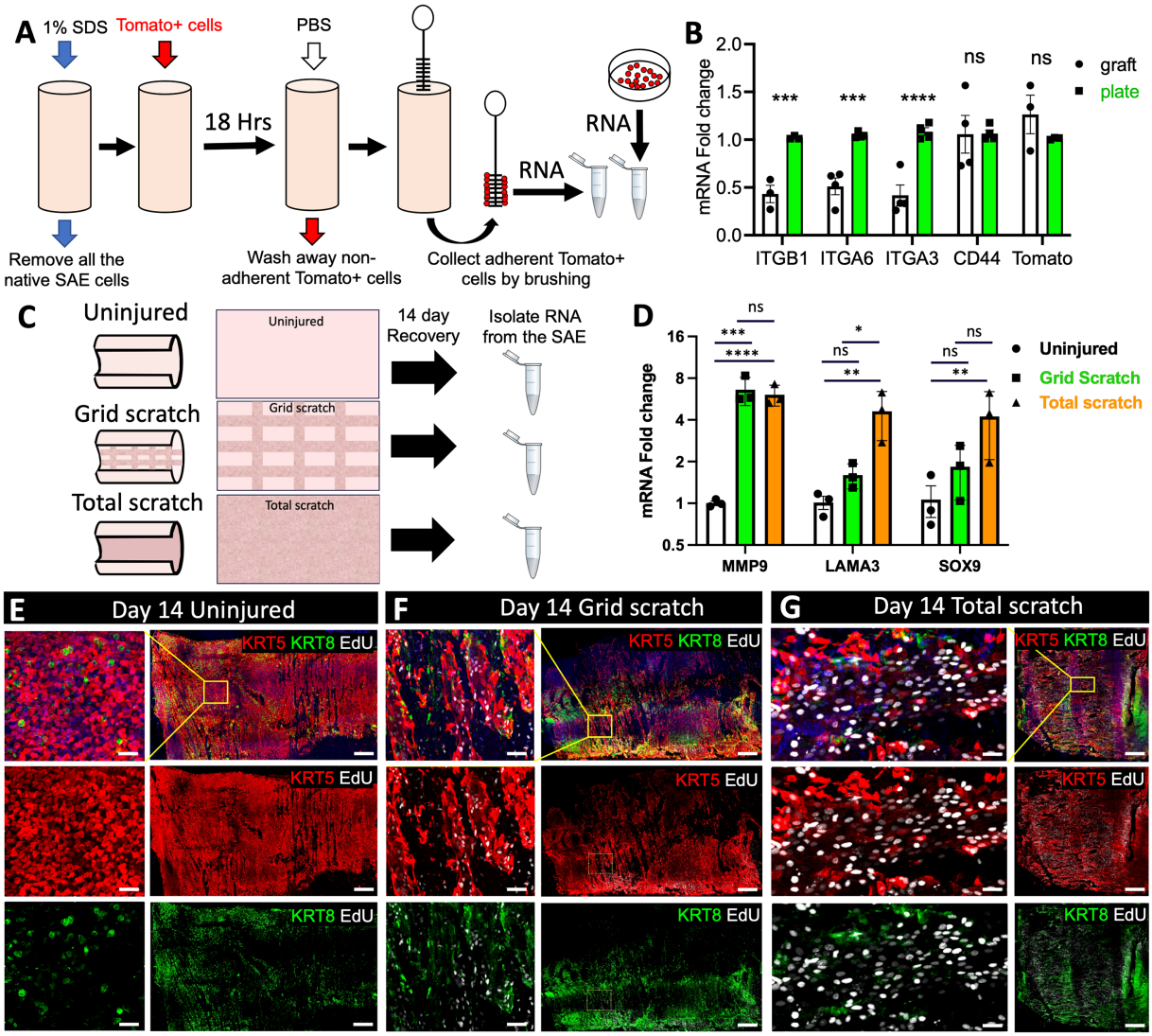

FIGURE 6
Transcriptional changes in the SAE after mechanical injury and cell engraftment *ex vivo*. **(A)** Experimental design: freshly harvested WT tracheas from adult ferrets were stripped of the native SAE by washing the lumen with 1% SDS. The grafts were then seeded with 10^7 p6 primary Tomato+ ferret surface airway basal cells using rotating bioreactor as described previously (24). After 18h, the grafts were washed with PBS 3 times to remove non-adherent cells. The graft lumen was then brushed to collect Tomato+ SAE cells and RNA was isolated from them. Control Tomato+ cells were grown on 804G-coated plates. **(B)** qPCR analysis for the indicated genes in these samples. Graphs show mean +/− SEM, N≥3 independent experiments. **(C)** Experimental design: explants from adult WT ferrets were either left uninjured or differentially injured by total or partial brushing the lumen. The samples were then cultured for 14days to allow regeneration of the SAE and on day 3 they were pulsed with EdU for 24h. On day 14 all samples were lightly brushed to remove columnar cells, after which a small slice was cut off and fixed for staining. The rest of the explant was brushed thoroughly to collect basal cells from the lumen which were then processed for RNA isolation and **(D)** qPCR analysis. Graphs show mean +/− SEM. Data are representative of 3 independent experiments. **(E–G)** Representative confocal micrographs of the explant surface epithelium at the time of RNA collection. Significance was determined by 2-way-ANOVA, Tukey's multiple comparison test in **(D)** and by multiple two-tailed T-tests in **(B)**. ****$p<0.0001$, *** $p<0.001$, ** $p<0.01$, * $p<0.05$. Scale bars in **(E–G)** are 500μm and 50μm in the enlarged insets.

and moderately injured epithelia, with the level of upregulation corresponding to the level of injury (Figure 6D). We additionally verified that the proportion of basal cells (KRT5+) and non-basal cells (KRT8+) was similar between the treatment groups at the time of RNA collection by immunofluorescent staining (Figures 6E–G). Consistent with the published literature (29) and our prior observations (15, 16), we noted that epithelial cells on the airway surface were larger and incorporated EdU more frequently in explants that were injured versus uninjured (Figures 6E–G).

Design of the 3D-printed explant holding chamber for long-term culture and live imaging

One of the greatest limitations of mammalian *in vivo* systems is the difficulty of performing high-resolution live imaging (30). An *ex vivo* culture system has brought us a step closer to circumventing this limitation. Existing methods for live imaging of the tracheal explants involve pinning the tissue to the support stage and imaging it under a dissecting microscope. This method works well for terminal assays such as mucociliary clearance, but is unsuitable for long-term culture of the explants. Additionally, the resolution and magnification of a dissecting microscope is limited even though individual cells can be resolved. For these reasons we sought to develop an explant culture chamber in which tissue can be positioned for imaging with a confocal laser scanning microscope while sterility is maintained. We designed and 3D-printed a 3-piece device that can keep epithelial tissue explants such as tracheas at an ALI and position them for confocal imaging (Figures 7A–I). Conceptually, an assembled device loaded with an explant resembles a transwell™ (Corning). Therefore, we will refer to it as a "tissue-transwell" for simplicity. The key difference between our device and traditional transwells that are available for *in vitro* culture is that instead of the permeable support for cells at the bottom, the tracheal explant itself fills the opening at the bottom of tissue-transwell acting as a barrier between the two compartments (which can be filled with media or be exposed to air). During assembly of the tissue transwell, the tissue is placed between the top and bottom parts of the cassette and this "sandwich" is screwed into the bracket (Figure 7B). The loaded tissue-transwell can be cultured in a 6-well dish or in a special 3D-printed housing chamber. Different sizes of this device were designed for mouse/rat, ferret, and human explants and printed using biocompatible plastic Med 610 HQ (31). After autoclaving the devices, we loaded them with fully brushed WT ferret tracheas and seeded the lumen with $2*10^6$ Tomato+ ferret airway basal cells. Seven days later we performed live imaging of the explants, confirming that this system is compatible with live imaging and that the newly engrafted cells were viable and able to migrate on day 7 after seeding (Figure 7J).

Basal cells engrafted *ex vivo* in tissue-transwells can differentiate into ciliated and secretory cells within 21days of ALI culture

The main purpose of designing the tissue-transwell was to open the tracheal tube and position the airway lumen near the microscope objective for imaging. A secondary purpose was to compartmentalize the luminal and adventitial sides of the explant so that they can be treated with different media. We made two customizable versions of the top tissue cassette piece: one with a 1 cm^2 opening and another one with a thin cross-piece subdividing this opening into 4 smaller ones. In the version with the larger opening, the curvature caused by the tracheal cartilage is retained and an air bubble is trapped underneath, creating an ALI. In the version with a cross-piece, the tissue is held flat against the bottom of the dish for imaging. Tissue culture in the appropriate media at an ALI can stimulate differentiation of airway epithelia after basal cell engraftment or after an injury that removes differentiated luminal cells. As a proof of concept, we completely removed the native SAE by brushing and seeded it with Tomato+ SAE cells prior to transitioning the explant to an ALI. We used a version of the tissue-transwell with a 1 cm^2 opening without the cross piece in the middle (Figure 8A). Having a trapped air bubble ensures that the ALI forms even when the explant is loaded imperfectly or when the tissue is accidentally punctured. After 21 days of differentiation at an ALI, the engrafted Tomato+ ferret SAE cells differentiated into AC-TUB+ multi-ciliated cells and CCSP+ secretory cells, even without reaching 100% confluency (Figures 8B–D). On the other hand, loading the explants into the version of the tissue-transwell with a cross piece and flattening them for imaging made it possible to image cilia motility live after adding Sir Tubulin (a reagent for viable labeling of the cilia; Figures 8E,F). Finally, we evaluated how well the tracheal explants tolerate long-term culture at an ALI within the tissue-transwell. In these experiments, the explants were exposed to Pneumacult ALI medium on the adventitial side for 42 days (with media exchanges every 2–3 days). In this experiment, most of the SAE cells in the transwell opening were ciliated and secretory (Figures 8G,H), suggesting that the device can be used for *ex vivo* modeling of acute and chronic lung and airway diseases.

Discussion

The current study provides proof-of-principle evidence that *ex vivo* tracheal injury and culture can be effectively utilized to address biological questions regarding the dynamics of epithelial regeneration in the airway. The whole-mount staining and tissue clearing protocol that we describe here allowed us to rapidly evaluate large areas of the SAE and SMGs and can be used to efficiently capture low-frequency events. For example, we were able to assess the abundance of ionocytes on multiple whole ferret tracheas (manuscript is under review) and to survey transgenic cell engraftment. Additionally, this method of staining revealed a previously underappreciated complexity of airway SMG structure, vascularization, and innervation (Figure 4). This protocol can be adapted to other organs, as our colleagues have used it successfully for staining the pancreas, spleen, and adipose tissue (unpublished data).

The current study also provides information on suitable culture conditions for *ex vivo* injury experiments. Our discovery that acceptable regeneration was achieved in F-medium containing Y-27632 (Figures 1, 5) and that this was significantly more effective than simple DMEM (Figure 5), leads us to expect that one or more of the F-medium additives supports tracheal regeneration *ex vivo*. Our demonstration that Y-27632 stimulates robust repair of the explant airway surface after injury *ex vivo* (Figure 1) is interesting given that one of the well-described functions of Y-27632 is to prevent the

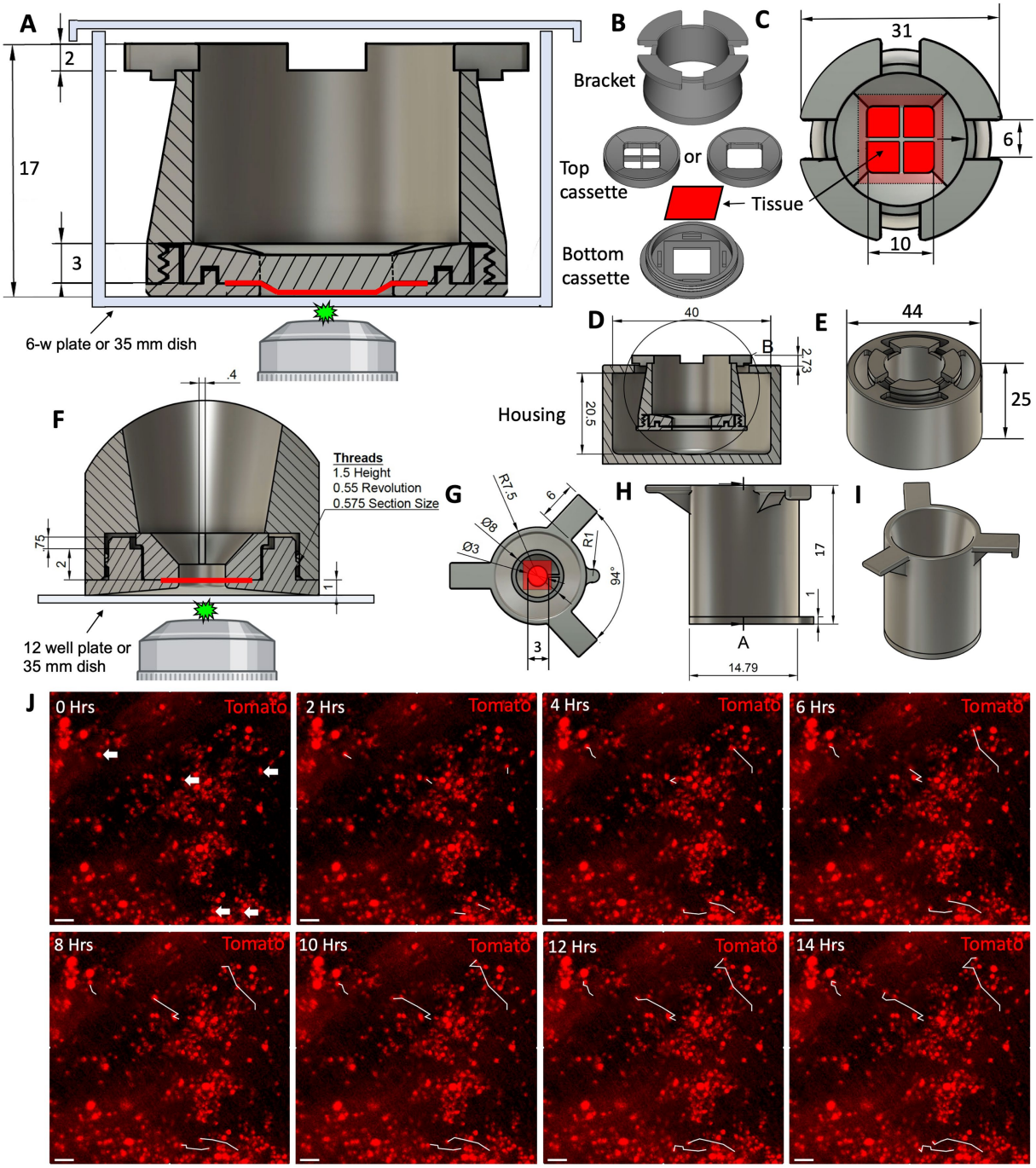

FIGURE 7
Design of the 3D-printed tissue culture chamber for live cell imaging. **(A)** Cross section of the tissue-transwell placed into a tissue culture plate for live imaging. The epithelial tissue sample is depicted in red. **(B)** Individual components of a disassembled tissue-transwell. **(C)** Top view of a loaded and assembled tissue-transwell. **(D)** Cross section of the tissue-transwell inside its external housing chamber. **(E)** 3D overview of the tissue-transwell inside the external housing chamber (loose-fitting lid is not shown). **(F–I)** A smaller version of the tissue-transwell designed for imaging samples from smaller animals (i.e., mice and rats). **(F)** Cross section of the insert with tissue positioned for live imaging. **(G)** Top view of the tissue-transwell insert. **(H)** Side view of the insert. **(I)** 3D view of the insert. **(J)** 14h time lapse of Tomato+ ferret SAE on day 7 after engraftment on WT non-fluorescent trachea, white tracks showing the path that the cell had completed at each timepoint. Scale bars are 50μm.

induction of stem cell death by dissociation (anoikis) (32). This leads us to speculate that Y-27632 protects the pioneer airway basal stem cells that detach from the main cell mass in their attempt to repair the injured regions. The effects of other components of F-medium on regeneration can be further tested by removing them individually in future studies. For the purposes of this study, we proceeded with F-medium given that it resulted in satisfactory regeneration of the tracheal epithelium by progenitors from both the SMGs and SAE. Our recent work indicates that under these media conditions fully brushed explants gradually re-epithelialize ~90% of the explant surface within

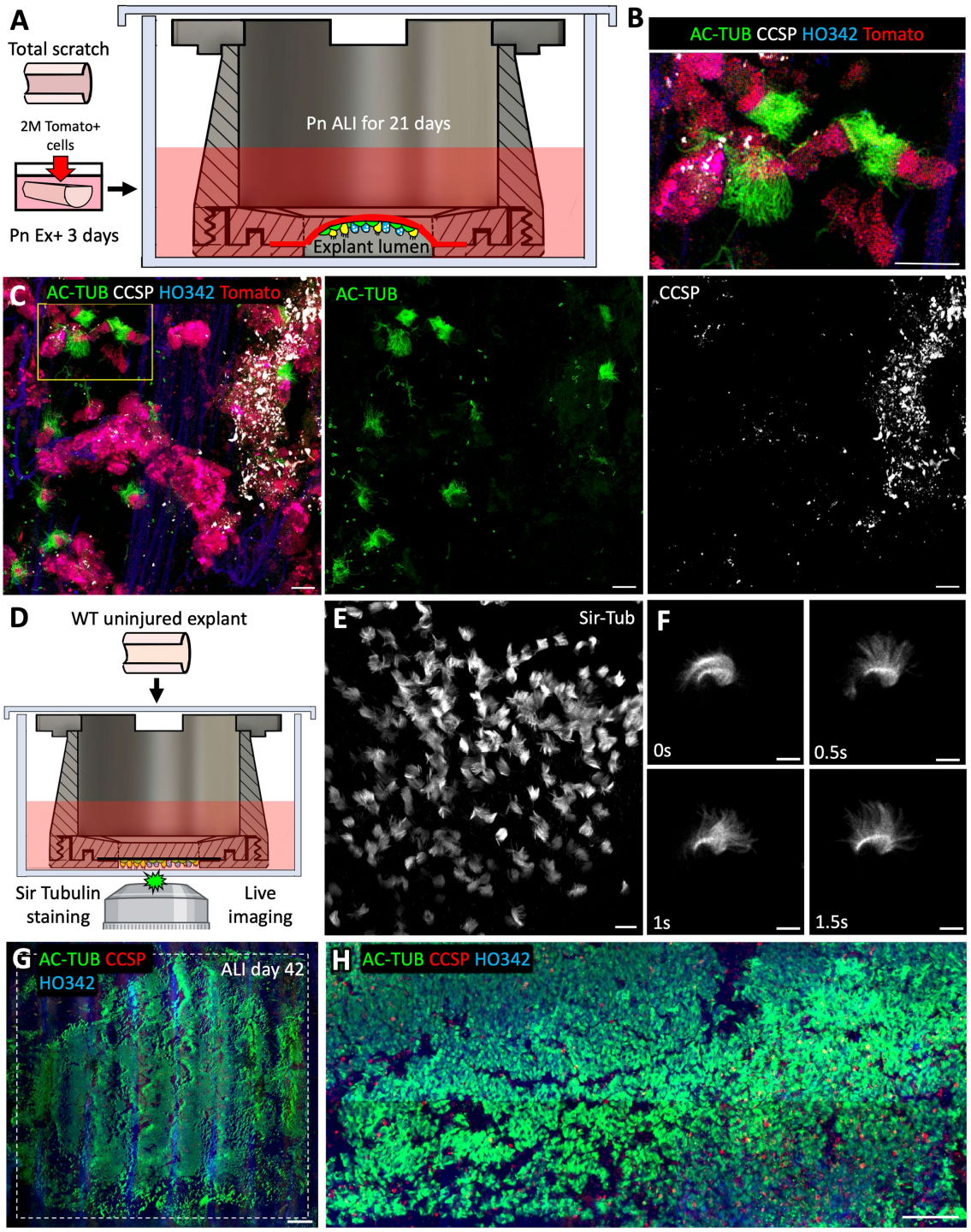

FIGURE 8
After 21days of ALI culture, *ex vivo* engrafted basal cells can differentiate into ciliated and secretory cells. **(A)** Experimental design: Freshly collected tracheal explants from adult WT ferrets were fully brushed to remove all the native SAE and then seeded with $2*10^6$ p6 Tomato+ ferret SAE cells. After engraftment, explants were cultured submerged in Pneumacult Ex+ medium for 3days prior to being loaded into tissue-transwells and cultured in Pneumacult ALI medium with an air bubble trapped in the explant lumen to ensure ALI. Samples were collected after 21days of differentiation at ALI. **(B,C)** Confocal micrographs of Tomato+ engrafted cells on ALI day 21 showing the presence of AC-TUB+ ciliated cells and CCSP+ secretory cells. **(D)** Experimental design: WT uninjured tracheal explant was placed into a tissue-transwell (with a cross-piece) and incubated in Pneumacult ALI medium containing Sir Tubulin reagent to stain the motile cilia. **(E,F)** Confocal micrographs of beating cilia. **(G,H)** Confocal micrographs of WT uninjured explants that were loaded into tissue-transwells (without the cross pieces) and cultured at an ALI for 42days. Scale bars are: 20μm in **(B,C,E)**; 10μm in **(F)**; 1,000μm in **(G)**; and 100μm in **(H)**.

15 days of the injury and majority of this regeneration is attributed to SMG progenitors (16).

Our study of EdU incorporation rates demonstrates that SMGs are non-uniform in their injury responses, with about 25% of the gland clusters abundantly incorporating EdU following injury, often concomitant with strong KRT5 expression in gland ducts (Figure 1). Our observation that EdU was more frequently incorporated into the gland ducts than in the acini is consistent with previous studies (15), and this could be due to their closer proximity to the injured airway surface. On day 5 after the total SAE removal, the airway surface overlying 'active' gland clusters was locally covered with EdU+ basal cells that were contiguous with the gland ducts suggesting that these glands are the first ones to start populating the airway surface after injury (Figure 1). It is interesting that when fully brushed explants were cultured in the continuous presence of EdU for 9 days (rather than being pulsed with it for 24 h on day 3), only about 37% of the gland acini contained a high abundance of EdU+ cells, the other 63% having a relatively sparse EdU+ cell density (Figure 1). In future, it will be important to determine whether the observed mosaic pattern of injury-induced SMG proliferation occurs *in vivo* and whether specific gland clusters are primed to respond to injury more intensively than others. Alternatively, the observed mosaic pattern of actively regenerating SMG clusters might reflect a mechanism whereby a gland that is first to engage in regeneration inhibits proliferation of progenitors in the neighboring glands. Functionally, this could prevent depletion of all the reserve gland progenitors at once. Indeed, gland progenitors are depleted in bronchiolitis obliterans syndrome (BOS) following lung transplantation (17, 18), which could reflect that this mechanism is broken in this form of chronic lung allograft dysfunction.

Investigation of airway injury resolution mechanisms is ultimately aimed at developing therapies for various lung diseases. Many cell-based therapies rely on delivering *in vitro*-expanded stem/progenitor cells that have been genetically modified. For example, cell therapies that lead to engraftment of gene-corrected autologous airway stem cells in the patient could benefit about 10% of *CF* patients with nonsense variants of CFTR. Similar cell therapeutic strategies can be applied to patients with other chronic lung diseases. For example, depleted airway epithelial stem cell niches can be reconstituted using patient-derived iPCSs which would mediate continuous large-scale tissue repair later on (33). Efficient cell engraftment remains challenging *in vivo* (13), and the tractable system we provide for optimizing engraftment conditions can help to overcome this barrier. As a testament to this expectation, we demonstrate that only limited engraftment occurred in intact airway epithelia, but the efficiency was greatly improved when the cells were seeded onto a partially of fully denuded tracheal grafts rather than onto intact explants (Figures 2, 3). Similar observations were made in a mouse nasal cell transplant model previously (34). The reason for it might be a better access of the engrafted cells to the ECM of the basement membrane where they can attach. This is encouraging, considering that the airways of patients who would most benefit from cell therapies are often in a chronically injured state. Another possibility is that intact airway epithelium has too much locomotion for exogenous cell to engraft due to ciliary beating. In the future, low-throughput *ex vivo* screens can be used after high-throughput *in vitro* screens to validate the potential of candidate compounds to enhance engraftment of airway stem cells. Good potential targets for such screens could be the drugs that temporarily stall ciliary beating, mucolytics, and tight junction modulators.

In optimizing cell engraftment, it is important to understand what changes cells undergo when they are moved from tissue culture plastic to a complex scaffold such as a partially denuded trachea. Specifically, the observed changes in cell adhesion markers provide insights into which pathways to target to improve the efficiency of cell engraftment. In this work we compared the expression of several cell adhesion markers between the cells engrafted onto tracheal scaffolds and the cells seeded on ECM-coated plastic. Overall, we observed a decline in the expression of various integrins (ITGB1, ITGA6 and ITGA3), but not in CD44 (Figures 6A,B). We speculate that that this downregulation of integrin expression led to a diminished attachment of engrafted cells to the explants compared to the tissue culture plates. If this speculation is experimentally validated, it is possible that the airway stem cell engraftment *ex vivo* and *in vivo* might be improved by stimulating integrin expression.

Enhancement of our general understanding of airway epithelial regeneration holds promise for the advancement of cell therapies. Multiple studies have evaluated global transcriptional changes that are associated with wound healing in the epidermis and airways *in vivo* (25, 35, 36). In this work, we validated some of these observations in our *ex vivo* system on day 14 after a tracheal brush injury. We detected an upregulation of genes involved in ECM deposition and remodeling in regenerating SAE, specifically transcription of MMP9 and LAMA3 was significantly increased in injured conditions (Figure 6D). This had been previously observed at the leading edges of regenerating mouse epidermis after a punch biopsy *in vivo* (25). Additionally, MMP9 is elevated in the airway epithelial cells of human patients who develop BOS after lung transplantation (26, 37, 38). Also, our group and others had previously shown that SOX9+ glandular progenitors participate in SAE repair after severe injury *in vivo* and *ex vivo* (14, 15, 27). Our observation that SOX9 mRNA expression is elevated in regenerated SAE on DPI14 is consistent with those findings (Figure 6D). Thus, our *ex vivo* tracheal injury model can reliably capture transcriptional changes in the airway epithelium during wound healing. In the future, the field would benefit from unbiased surveys of global changes at the transcriptional and protein levels within the airway epithelium following injury *ex vivo* and *in vivo*.

Lastly, we designed and 3D-printed a reusable tissue-transwell (Figure 7) that can be used for a variety of applications. For example, it can be used to culture airway explants at an ALI, where the airway lumen is exposed to air while the adventitia is in contact with medium (Figure 8). These culture conditions can be used to model airway diseases, because they reflect the physiological airway environment more accurately than submerged explant cultures do. Moreover, the ability to mount whole tissues for live imaging is expected to be helpful in numerous other applications, notably for recording the motility of cilia (Figure 7), clearance of the mucus, tracing cell lineages and evaluating migration during wound healing (Figure 6). Although this *ex vivo* model has advantages over *in vitro* culture, it is important to recognize its limitations relative to *in vivo* systems, for example the lack of innervation and vascular perfusion, as well as hypoxia, a condition that is unavoidable in the absence of constant air flow for gas exchange. Researchers need to be aware that *ex vivo* conditions might alter injury responses, and thus there may be discrepancies between *ex vivo* and *in vivo* systems, which emphasizes the importance of cross-system validation of biological findings.

Conclusion

In this work we demonstrate that *ex vivo* ferret tracheal cultures can be useful to answer certain biological questions that are challenging to address *in vivo* or *in vitro*. We also characterize the tools and approaches needed in order to take full advantage of this tracheal explant model, namely whole-mount tissue staining, *ex vivo* mechanical injury, stem-cell engraftment, and tissue-transwells for live imaging and ALI culture. In the future, this explant model can be used to explore changes associated with wound healing in airway epithelia and optimize cell engraftment conditions. The tissue-transwells that we introduce here are cost-effective and reusable, and they can be applied to a variety of membrane-containing organs including airways, esophagus, stomach, intestine, bladder, and skin. We encourage investigators to contact us for details on where to acquire tissue-transwells for their research applications.

Data availability statement

The raw data supporting the conclusions of this article will be made available by the authors, without undue reservation.

Ethics statement

The animal study was reviewed and approved by The University of Iowa Institutional Animal Care and Use Committee (IACUC).

Author contributions

VI, AP, JE, and KP designed the research studies. VI and AP conducted experiments and acquired data. VI, AP DD, SK, and KP designed the tissue-transwell. VI, JE, and KP analyzed data. VI wrote the manuscript. VI, JE, KP, KF, TL, and CG edited the manuscript. All authors contributed to the article and approved the submitted version.

Funding

This work was funded by the following grants: R01 HL136370 (to KP); P01 HL152960 (to JE), NHLBI Contract 75N92019R0014 (to JE); P30 DK054759 (to JE), R01 HL165404 (to JE); T32 HL007638 (to TL), K99HL155843 (to TL).

Acknowledgments

The authors would like to thank the members of Parekh and Engelhardt labs for discussion of the data presented in this paper.

Conflict of interest

The authors declare that the research was conducted in the absence of any commercial or financial relationships that could be construed as a potential conflict of interest.

Publisher's note

All claims expressed in this article are solely those of the authors and do not necessarily represent those of their affiliated organizations, or those of the publisher, the editors and the reviewers. Any product that may be evaluated in this article, or claim that may be made by its manufacturer, is not guaranteed or endorsed by the publisher.

References

1. Liu QZ, Liu K, Cui GZ, Huang XZ, Yao S, Guo WK, et al. Lung regeneration by multipotent stem cells residing at the bronchioalveolar-duct junction. *Nat Genet*. (2019) 51:766–8. doi: 10.1038/s41588-019-0388-9

2. Stucki AO, Stucki JD, Hall SRR, Felder M, Mermoud Y, Schmid RA, et al. A lung-on-a-chip array with an integrated bio-inspired respiration mechanism. *Lab Chip*. (2015) 15:1302–10. doi: 10.1039/C4LC01252F

3. Huh D, Mammoto A, Montoya-Zavala M, Ingber DE. A human breathing lung-on-a-chip. *FASEB J*. (2010) 24:1065–22. doi: 10.1096/fasebj.24.1_supplement.1065.22

4. Garcia SR, Deprez M, Lebrigand K, Cavard A, Paquet A, Arguel MJ, et al. Novel dynamics of human mucociliary differentiation revealed by single-cell RNA sequencing of nasal epithelial cultures. *Development*. (2019) 146:1–17. doi: 10.1242/dev.174318

5. Wang GQ, Lou HH, Salit J, Leopold PL, Driscoll S, Schymeinsky J, et al. Characterization of an immortalized human small airway basal stem/progenitor cell line with airway region-specific differentiation capacity. *Resp Res*. (2019) 20:1–14. doi: 10.1186/s12931-019-1140-9

6. Carraro G, Langerman J, Sabri S, Lorenzana Z, Purkayastha A, Zhang GZ, et al. Transcriptional analysis of cystic fibrosis airways at single-cell resolution reveals altered epithelial cell states and composition. *Nat Med*. (2021) 27:806. doi: 10.1038/s41591-021-01332-7

7. Deprez M, Zaragosi LE, Truchi M, Becavin C, Garcia SR, Arguel MJ, et al. A single-cell atlas of the human healthy airways. *Am J Resp Crit Care*. (2020) 202:1636–45. doi: 10.1164/rccm.201911-2199OC

8. Francis R, Lo C. Ex vivo method for high resolution imaging of cilia motility in rodent airway epithelia. *Jove-J Vis Exp*. (2013) 78:1–6. doi: 10.3791/50343

9. Batioglu-Karaaltin A, Karaaltin MV, Ovali E, Yigit O, Kongur M, Inan O, et al. *In vivo* tissue-engineered Allogenic trachea transplantation in rabbits: a preliminary report. *Stem Cell Rev Rep*. (2015) 11:347–6. doi: 10.1007/s12015-014-9570-8

10. Mir SM, Chen JW, Pinezich MR, O'Neill JD, Huang SXL, Vunjak-Novakovic G, et al. Imaging-guided bioreactor for de-epithelialization and long-term cultivation of ex vivo rat trachea. *Lab Chip*. (2022) 22:1018–31. doi: 10.1039/D1LC01105G

11. Lynch TJ, Ievlev V, Parekh KR. Heterogeneity of pulmonary stem cells. *Adv Exp Med Biol*. (2019) 1169:95–7. doi: 10.1007/978-3-030-24108-7_6

12. Lynch TJ, Ahlers BA, Swatek AM, Ievlev V, Pai AC, Brooks L, et al. Ferret lung transplantation models differential lymphoid aggregate morphology between restrictive and obstructive forms of chronic lung allograft dysfunction. *Transplantation*. (2022) 106:1974–89. doi: 10.1097/TP.0000000000004148

13. Tang Y, Yan Z, Engelhardt JF. Viral vectors, animal models, and cellular targets for gene therapy of cystic fibrosis lung disease. *Hum Gene Ther*. (2020) 31:524–7. doi: 10.1089/hum.2020.013

14. Lynch TJ, Anderson PJ, Rotti PG, Tyler SR, Crooke AK, Choi SH, et al. Submucosal gland Myoepithelial cells are reserve stem cells that can regenerate mouse tracheal epithelium. *Cell Stem Cell*. (2018) 22:653–9. doi: 10.1016/j.stem.2018.03.017

15. Ievlev V, Jensen-Cody CC, Lynch TJ, Pai AC, Park S, Shahin W, et al. Sox9 and Lef1 regulate the fate and behavior of airway glandular progenitors in response to injury. *Stem Cells*. (2022) 40:778–0. doi: 10.1093/stmcls/sxac038

16. Ievlev V, Lynch TJ, Freischlag KW, Gries CB, Shah A, Pai AC, et al. Krt14 and Krt15 differentially regulate regenerative properties and differentiation potential of airway basal cells. *JCI Insight*. (2022) doi: 10.1172/jci.insight.162041

17. Swatek AM, Lynch TJ, Crooke AK, Anderson PJ, Tyler SR, Brooks L, et al. Depletion of airway submucosal glands and TP63(+)KRT5(+) basal cells in Obliterative bronchiolitis. *Am J Resp Crit Care*. (2018) 197:1045–57. doi: 10.1164/rccm.201707-1368OC

18. Swatek A, Crooke A, Anderson P, Lynch T, Ivanovic M, Klesney-Tait J, et al. Obliterative bronchiolitis following lung transplantation is preceded by

depletion of airway submucosal glands and basal stem cells. *Am J Transplant*. (2016) 16:237.

19. Ghosh M, Brechbuhl HM, Smith RW, Li BL, Hicks DA, Titchner T, et al. Context-dependent differentiation of multipotential keratin 14-expressing tracheal basal cells. *Am J Resp Cell Mol*. (2011) 45:403–0. doi: 10.1165/rcmb.2010-0283OC

20. Musah S, Chen J, Hoyle GW. Repair of tracheal epithelium by basal cells after chlorine-induced injury. *Resp Res*. (2012):13. doi: 10.1186/1465-9921-13-107

21. Smirnova NF, Schamberger AC, Nayakanti S, Hatz R, Behr J, Eickelberg O. Detection and quantification of epithelial progenitor cell populations in human healthy and IPF lungs. *Resp Res*. (2016):17. doi: 10.1186/s12931-016-0404-x

22. Yan ZY, McCray PB, Engelhardt JF. Advances in gene therapy for cystic fibrosis lung disease. *Hum Mol Genet*. (2019) 28:R88–94. doi: 10.1093/hmg/ddz139

23. Yan ZY, Stewart ZA, Sinn PL, Olsen JC, Hu J, McCray PB, et al. Ferret and pig models of cystic fibrosis: prospects and promise for gene therapy. *Hum Gene Ther Cl Dev*. (2015) 26:38–49. doi: 10.1089/humc.2014.154

24. Pai AC, Lynch TJ, Ahlers BA, Ievlev V, Engelhardt JF, Parekh KR. A novel bioreactor for reconstitution of the epithelium and submucosal glands in Decellularized ferret tracheas. *Cells-Basel*. (2022) 11:1027–1044. doi: 10.3390/cells11061027

25. Aragona M, Dekoninck S, Rulands S, Lenglez S, Mascre G, Simons BD, et al. Defining stem cell dynamics and migration during wound healing in mouse skin epidermis. *Nat Commun*. (2017):8. doi: 10.1038/ncomms14684

26. Hubner RH, Meffert S, Mundt U, Bottcher H, Freitag S, El Mokhtari NE, et al. Matrix metalloproteinase-9 in bronchiolitis obliterans syndrome after lung transplantation. *Eur Respir J*. (2005) 25:494–1. doi: 10.1183/09031936.05.00091804

27. Tata A, Kobayashi Y, Chow RD, Tran J, Desai A, Massri AJ, et al. Myoepithelial cells of submucosal glands can function as reserve stem cells to regenerate airways after injury. *Cell Stem Cell*. (2018) 22:668. doi: 10.1016/j.stem.2018.03.018

28. Anderson PJ, Lynch TJ, Engelhardt JF. Multipotent Myoepithelial progenitor cells are born early during airway submucosal gland development. *Am J Resp Cell Mol*. (2017) 56:716–6. doi: 10.1165/rcmb.2016-0304OC

29. Erjefalt JS, Sundler F, Persson CGA. Epithelial barrier formation by airway basal cells. *Thorax*. (1997) 52:213–7. doi: 10.1136/thx.52.3.213

30. Kim JK, Vinarsky V, Wain J, Zhao R, Jung K, Choi J, et al. *In vivo* imaging of tracheal epithelial cells in mice during airway regeneration. *Am J Resp Cell Mol*. (2012) 47:864–8. doi: 10.1165/rcmb.2012-0164OC

31. Kozior T, Bochnia J, Gogolewski D, Zmarzly P, Rudnik M, Szot W, et al. Analysis of metrological quality and mechanical properties of models manufactured with photo-curing PolyJet matrix Technology for Medical Applications. *Polymers-Basel*. (2022) 14.:408–436.doi: 10.3390/polym14030408

32. Gauthaman K, Fong CY, Bongso A. Effect of ROCK inhibitor Y-27632 on Normal and variant human embryonic stem cells (hESCs) *in vitro*: its benefits in hESC expansion. *Stem Cell Rev Rep*. (2010) 6:86–95. doi: 10.1007/s12015-009-9107-8

33. Calvert BA, Ryan AL. Application of iPSC to modelling of respiratory diseases. Cell biology and translational medicine. *Stem Cells Ther Emerg Approach*. (2020) 7:1–16. doi: 10.1007/978-3-030-37845-5_442

34. Farrow N, Cmielewski P, Donnelley M, Rout-Pitt N, Moodley Y, Bertoncello I, et al. Epithelial disruption: a new paradigm enabling human airway stem cell transplantation. *Stem Cell Res Ther*. (2018):9:1–8. doi: 10.1186/s13287-018-0911-4

35. Haensel D, Jin SQ, Sun P, Cinco R, Dragan M, Nguyen Q, et al. Defining epidermal basal cell states during skin homeostasis and wound healing using single-cell Transcriptomics. *Cell Rep*. (2020) 30:3932–3947.e6. doi: 10.1016/j.celrep.2020.02.091

36. Siriwach R, Ngo AQ, Higuchi M, Arima K, Sakamoto S, Watanabe A, et al. Single-cell RNA sequencing identifies a migratory keratinocyte subpopulation expressing THBS1 in epidermal wound healing. *Iscience*. (2022) 25. doi: 10.1016/j.isci.2022.104130

37. Banerjee B, Ling KM, Sutanto EN, Musk M, Yerkovich ST, Hopkins PMA, et al. The airway epithelium is a direct source of matrix degrading enzymes in bronchiolitis obliterans syndrome. *J Heart Lung Transpl*. (2011) 30:1175–85. doi: 10.1016/j.healun.2011.06.007

38. Riise GC, Linden A. Phenotyping BOS could improve understanding of mechanisms involved reply. *J Heart Lung Transpl*. (2011) 30:113. doi: 10.1016/j.healun.2010.08.018

frontiers | Frontiers in Oncology

TYPE Original Research
PUBLISHED 12 June 2023
DOI 10.3389/fonc.2023.1145333

Check for updates

OPEN ACCESS

EDITED BY
Francoise Degoul,
Institut National de la Santé et de la Recherche Médicale (INSERM), France

REVIEWED BY
Laurent Morel,
Université Clermont Auvergne, France
Somanath Kundu,
Upstate Medical University, United States
Agnès Germot,
University of Limoges, France

*CORRESPONDENCE
Rachel Willand-Charnley
rachel.willand@sdstate.edu

RECEIVED 02 February 2023
ACCEPTED 30 May 2023
PUBLISHED 12 June 2023

CITATION
Tuffour I, Amuzu S, Bayoumi H, Surtaj I, Parrish C and Willand-Charnley R (2023) Early *in vitro* evidence indicates that deacetylated sialic acids modulate multi-drug resistance in colon and lung cancers *via* breast cancer resistance protein. *Front. Oncol.* 13:1145333. doi: 10.3389/fonc.2023.1145333

COPYRIGHT
© 2023 Tuffour, Amuzu, Bayoumi, Surtaj, Parrish and Willand-Charnley. This is an open-access article distributed under the terms of the Creative Commons Attribution License (CC BY). The use, distribution or reproduction in other forums is permitted, provided the original author(s) and the copyright owner(s) are credited and that the original publication in this journal is cited, in accordance with accepted academic practice. No use, distribution or reproduction is permitted which does not comply with these terms.

Early *in vitro* evidence indicates that deacetylated sialic acids modulate multi-drug resistance in colon and lung cancers *via* breast cancer resistance protein

Isaac Tuffour[1], Setor Amuzu[2], Hala Bayoumi[1], Iram Surtaj[3], Colin Parrish[4] and Rachel Willand-Charnley[1]*

[1]Department of Chemistry and Biochemistry, South Dakota State University, Brookings, SD, United States, [2]Department of Human Genetics, McGill University, Montreal, QC, Canada, [3]Department of Medical Sciences, American University of Iraq, Sulaimani, Iraq, [4]Baker Institute for Animal Health, Department of Microbiology and Immunology College of Veterinary Medicine, Cornell University, Ithaca, NY, United States

Cancers utilize sugar residues to engage in multidrug resistance. The underlying mechanism of action involving glycans, specifically the glycan sialic acid (Sia) and its various functional group alterations, has not been explored. ATP-binding cassette (ABC) transporter proteins, key proteins utilized by cancers to engage in multidrug resistant (MDR) pathways, contain Sias in their extracellular domains. The core structure of Sia can contain a variety of functional groups, including O-acetylation on the C6 tail. Modulating the expression of acetylated-Sias on Breast Cancer Resistance Protein (BCRP), a significant ABC transporter implicated in MDR, in lung and colon cancer cells directly impacted the ability of cancer cells to either retain or efflux chemotherapeutics. *Via* CRISPR-Cas-9 gene editing, acetylation was modulated by the removal of CAS1 Domain-containing protein (CASD1) and Sialate O-Acetyl esterase (SIAE) genes. Using western blot, immunofluorescence, gene expression, and drug sensitivity analysis, we confirmed that deacetylated Sias regulated a MDR pathway in colon and lung cancer in early *in vitro* models. When deacetylated Sias were expressed on BCRP, colon and lung cancer cells were able to export high levels of BCRP to the cell's surface, resulting in an increased BCRP efflux activity, reduced sensitivity to the anticancer drug Mitoxantrone, and high proliferation relative to control cells. These observations correlated with increased levels of cell survival proteins, BcL-2 and PARP1. Further studies also implicated the lysosomal pathway for the observed variation in BCRP levels among the cell variants. *RNASeq* data analysis of clinical samples revealed higher *CASD1* expression as a favorable marker of survival in lung adenocarcinoma. Collectively, our findings indicate that deacetylated Sia is utilized by colon and lung cancers to engage in MDR *via* overexpression and efflux action of BCRP.

KEYWORDS

breast cancer resistance protein, sialic acid, O-acetyl sialic acid, cancer, multidrug resistance

Introduction

A variety of current chemotherapeutic treatments are compromised by multidrug resistance (MDR), a refractory mechanism, resulting in therapeutic failure and extended treatments with second or third-line therapies. Strikingly, MDR is responsible for 90% of deaths in cancer patients receiving conventional or novel-targeted therapeutics (1). It is therefore imperative to intensify research efforts to prevent and understand MDR pathways. Cancers employ MDR pathways *via* a multitude of mechanisms including mutations in drug targets, altered drug metabolism, diminished apoptosis (cell death) signaling, and reduced drug accumulation (2), with reduced drug accumulation accounting for the majority of chemotherapy resistance (3–5). This particular MDR mechanism occurs through the overexpression of a group of heavily glycosylated transmembrane proteins referred to as ATP-binding cassette (ABC) transporters. ABC transporters, known as efflux pumps, belong to a large protein superfamily comprising of 48 members that facilitate the energy-dependent extrusion of a broad range of compounds against a concentration gradient (6). The major ABC transporters implicated in clinical MDR include permeability-glycoprotein (P-gp), the multidrug resistance protein 1 (MRP1), and the breast cancer resistance protein (BCRP) (7, 8).

In this study, attention was given to BCRP due to its broad substrate specificity. Human BCRP is the second member of the ATP binding cassette sub-family G (ABCG2), encoded by the *ABCG2* gene that is located on chromosome 4q22 (9). Physiologically, it is highly expressed in placenta, brain micro-vessel endothelium, mammary gland, colon, liver, small intestine, biliary tract, ovary, testis, kidney, and hematopoietic stem cells; contributing to the pharmacokinetics of drugs and endogenous compounds as well as protecting tissues from toxic xenobiotics (10–12). It actively transports a broad spectrum of conventional anticancer agents, including doxorubicin, mitoxantrone, topotecan, methotrexate, and daunorubicin as well as novel targeted molecules such as the tyrosine kinase inhibitors, imatinib and gefitinib (13, 14). BCRP is overexpressed in many malignancies and contributes to poor chemotherapeutic response in acute myelogenous leukemia (AML), chronic myeloid leukemia (CML), pancreatic ductal adenocarcinomas, non-small lung cancer cells (NSCLC), and other solid tumors (10). Existing therapeutic strategies aimed at overcoming BCRP mediated MDR include various pharmacological classes of inhibitors such as tyrosine kinase inhibitors (TKIs), HCV protease inhibitors, antifungal azoles, and immune suppressants (15–18). Although these inhibitors have shown MDR reversal activity in pre-clinical studies, they have yielded limited clinical success due to toxicity and off-target drug interactions when co-administered with additional anticancer drugs, prompting the need for alternative clinically relevant therapeutics (19–21). Several mechanisms including transcriptional (promoter activation by cis-acting elements and miRNAs targeting BCRP/ABCG2), epigenetic (CpG island hypomethylation and histone hypermethylation), post-translational (e.g., BCRP phosphorylation by Pim-1 kinase) and glycans have been reported to modulate BCRP expression (22–25). The role of sialic acid and its associated functional group alterations in MDR remained unexplored.

Glycans are present on asparagine residues (N-linked recognition sites) in specific extracellular loops connecting the transmembrane helices of the transporter proteins (9, 26, 27). Although prior studies have reported a positive correlation between glycosylation status of BCRP and drug resistance (poor therapeutic outcomes) in cancers, for instance (28) reported significant reversal of MDR phenotypes in ovarian and colorectal cancers following chemical inhibition of BCRP glycosylation, Sia remained uninvestigated. Furthermore, the functional checkpoints of BCRP revealed that mutagenic substitution of asparagine 596, the crucial glycosylation site on BCRP, with glutamine disrupted N-linked glycosylation, interfered with localization, function of BCRP, and sensitized hitherto MDR cancer cells to chemotherapeutics (29). Lastly, lectin binding experiments revealed branched oligosaccharide chains capped with either α-2,6 or α-2,3 linkage of sialic acids (30–32).

Sialic acids (Sia e.g., N-acetylneuraminic acid [Neu5Ac]) are a family of 9-carbon sugars found as terminal residues on cell surface glycoproteins, glycolipids, and gangliosides (33–35). Aberrant expression of sialic acids on death receptors TNFR1 and FasR has been widely reported to inhibit cell death and promote drug resistant phenotypes in ovarian, pancreatic and colon cancer cells (36, 37). Ma et al. (38) also reported increased levels of ST3GAL5 and ST8SIA4 sialyltransferases in drug resistant human acute myeloid leukemia (AML). They further identified that these alterations regulated the activity of PI3K/Akt signaling and correlated with the overexpression of ABC transport proteins, suggesting a strong correlation between glycan sialylation and MDR thus warranted further exploration. The hydroxyl groups associated with Sia may be further chemically modified with various functional groups including acetyl, lactyl, methyl, sulfate, or phosphate groups (34). Acetylated Sias are the most clinically studied modification. Of specific interest are the modifications to the C6 hydroxylated tail. Modulation of the acetyl functional group C6 tail are mediated by two enzymes, CAS 1 Domain-containing protein (CASD1) and Sialic acid acetyl esterase (SIAE) respectively (35). Driven by our recent discovery that the overexpression of deacetylated-Sia on colon and lung cancers results in immune evasion, of Natural Killer (NK) mediated cytotoxicity *via* the Siglec-Sia pathway (35), we began turning our attention to additional mechanistic pathways undermining the effective prevention of cancers involving glycosylation, specifically deacetyl-Sias. Although Sias have been implicated in several cancer hallmarks including metastasis and invasion (39) (Figure 1A), the role acetyl functional group modulation on Sia play in MDR remained unexplored. As a result, and based on our prior work, we hypothesized that increasing the expression of deacetylated Sias on BCRP would modulate MDR *via* BCRP expression on the cell's surface. As such, we investigated BCRP expression and function as well as survival in control, CASD1 knockout cells that lack acetylated Sia, and SIAE knockout cells that over-express acetylated Sia in lung and colon cancer cell line.

Abbreviations: MDR, Multidrug resistance; BCRP, Breast Cancer Resistance; CASD1, CAS 1 domain containing 1; Sia, Sialic acid; O Acetyl Sia, O-Acetyl Sialic acid; PARP; Poly-ADP Ribose Polymerase; BcL-2, B cell lymphoma 2; Siglecs, Sialic acid-binding immunoglobulin-like lectins.

10.3389/fonc.2023.1145333

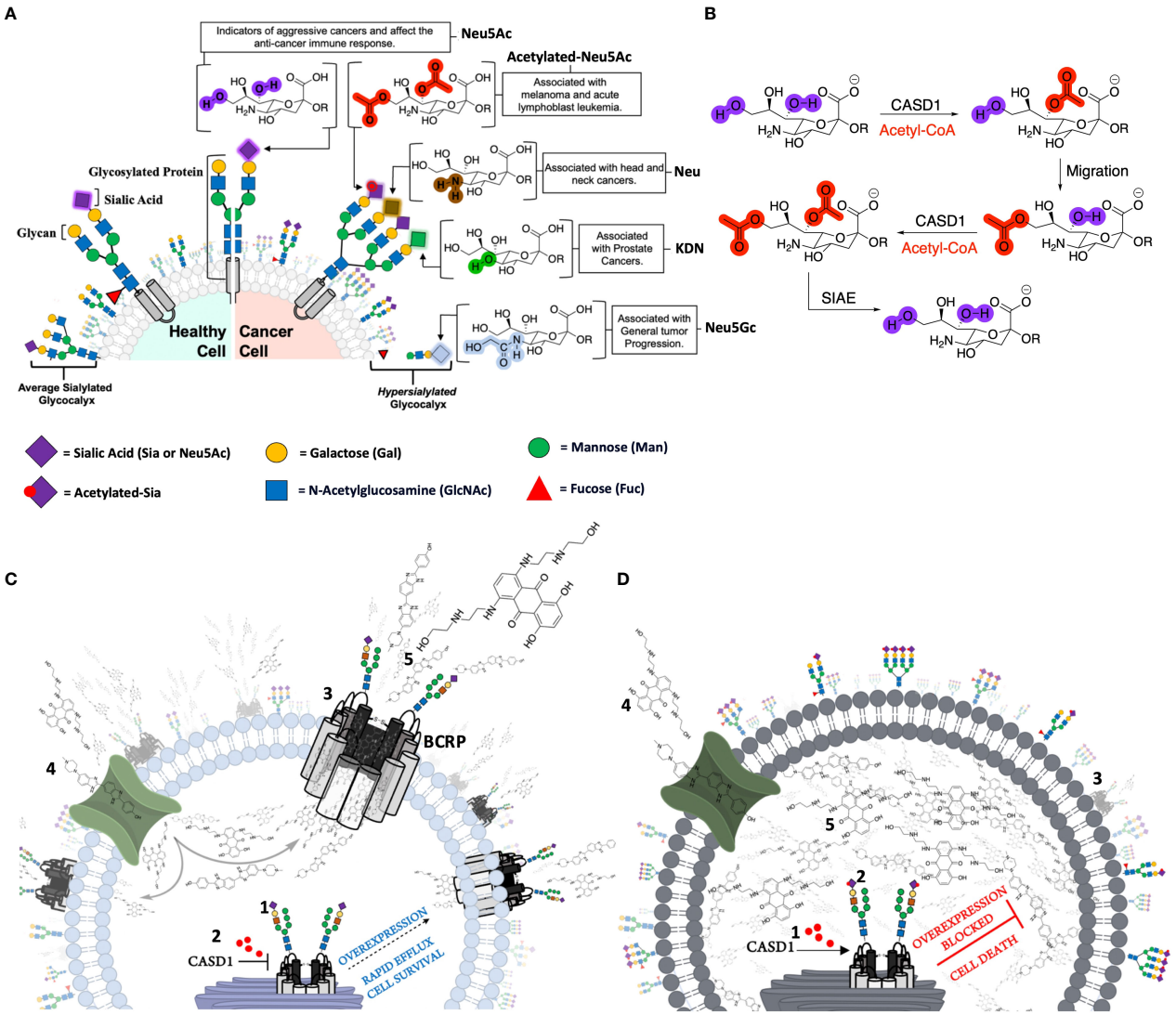

FIGURE 1
The contribution of canonical and non-canonical forms of Sialic acids in cancer and cancer related pathways. **(A)** Healthy cells are covered with an averagely sialylated glycocalyx and present moderate levels of Sialic acids (Sia or Neu 5Ac) on glycosylated proteins. Malignant or cancer cells on the other hand have an altered Sialome, expressing high levels of both canonical (unmodified) and non-canonical forms of Sia as a mechanism for survival. Overexpression of Neu 5Ac enables cancer cells to evade immune-mediated death and serves as an indicator of aggressiveness. Neu5Gc overexpression is also associated with general tumor progression. Non-canonical Sias including the Deacetylated (Neu) and Deaminated (KDN) forms are associated with Head/Neck and Prostate cancers respectively. Melanomas and Acute Lymphoblast Leukemias (ALL) distinctly express high levels of Acetylated Neu5Ac. **(B)** CASD1 and SIAE enzymes modulate 9-O and 7,9-O acetylation of Sia (Neu 5Ac). CASD1 adds acetyl functional groups, via an Acetyl CoA donor, to the seventh carbon of Sia, from which it migrates to the ninth carbon (Neu 5,9Ac2) under physiological conditions. This facilitates the addition of new acetyl group to the seventh carbon by CASD1 yielding Neu 5,7,9Ac3. SIAE can remove acetyl functional groups, regenerating the canonical form of Sia (Neu 5Ac) **(C)** Sia (purple diamonds) is added to the glycan chain on BCRP in the golgi by Sialyltransferases (2) In the absence of CASD1 (i.e., CASD1 Knockout), no acetyl groups (red circles) are added to the sialylated transporter (3) Majority of deacetylated transporters are successfully trafficked to the cell surface (4) Chemotherapeutics and BCRP substrates targeted at cells, permeate into the cytoplasm (5) The high expression levels of BCRP at the cell surface confers a multidrug resistance phenotype as large amounts of chemotherapeutics are rapidly pumped out enabling the cell to survive. **(D)** CASD1 adds acetyl groups (red circles) to (2) sialylated glycan chain on transporter (3) The majority of the transporter with acetyl group modification is transported to the lysosome for degradation (4) Chemotherapeutics and BCRP substrates targeted at cells, permeate into the cytoplasm (5) Due to the low expression levels of BCRP at the cell surface, only a small fraction of chemotherapeutics is pumped out of the cell with high amount accumulated in the cytoplasm exerting prolonged pharmacological effect leading to cell death (apoptosis). *For simplicity, the authors have deliberately excluded sialylated O-glycans and gangliosides.

Materials and methods

Scientific rigor

All reagents/antibodies/cell lines have been selected based on published figures and purchased from companies that provide validation. Experiments were performed in technical triplicates and then biological triplicates. We used t-tests or ANOVA followed by Tukey post-tests for multiple comparisons using GraphPad Prism 8 (San Diego, CA). Data, as seen below, is always presented as mean ± standard deviation with $P < 0.05$ indicating significance.

Reagents

Fetal bovine serum (FBS) and penicillin/streptomycin (P/S) were obtained from Corning Incorporated (Corning, NY). The GAPDH loading control monoclonal antibody (ref AM4300, lot #: 00939504), Alexa Fluor 488 conjugated goat anti-mouse IgG cross-adsorbed secondary antibody (2 mg/mL, Cat #A32723), PowerUp SYBR green PCR master mix (Cat # A25741) and paraformaldehyde were obtained from Thermo Fisher Scientific Inc (Rockford, IL). Anti-ABCG2 antibodies, BCRP/ABCG2 (Cat #EPR20080, lot #: 3026758) and clone BXP-21 (Cat #MAB4146) were obtained from Abcam (Waltham, MA) and Millipore (Billerica, MA) respectively. IRDye Goat anti-mouse and anti-rabbit IgG secondary antibody (lot#: C90130-02) were obtained from LI-COR (Lincoln, NE). Mitoxantrone, dimethyl sulfoxide (DMSO), 3-(4,5-dimethylthiazolyl)-2,5-diphenyltetrazolium bromide (MTT), 4′,6-diamidino-2-phenylindole (DAPI), Ko143, Bafilomycin A1, and Triton X-100 were purchased from Sigma Chemical Co (St. Louis, MO). All other chemicals used were of analytical grade.

Cell lines and cell culture

A549 cells were cultured in Dulbecco modified Eagle medium (Corning) supplemented with 10% FBS and 1% P/S (Corning). HCT 116 cells were cultured in RPMI 1640 medium (Corning) supplemented with 10% FBS and 1% P/S. All cell lines were originally purchased from American Type Culture Collection (Rockville, MD). Cell Dissociation Buffer (Gibco, Waltham, MA) was exclusively used for passaging cells.

CASD1 and SIAE knockout A549 cell lines were obtained from Dr. Colin Parrish (Cornell University, Ithaca, NY). CRISPR-Cas9 stably expressing cells and the third-generation lentiviral system were gifted from Dr. Michael Bassik (Stanford University, Stanford, CA). HEK 293/PcDNA 3.1 cells were a generous gift from Dr. Surtaj Iram (American University of Iraq, Sulaimani, Iraq). CRISPR-Cas9 editing of CASD1 and SIAE in HCT 116 and A549 cells was previously published (35, 40). Briefly, paired Cas9 plasmids targeting adjacent sites in early exons of *CASD1* and *SIAE* were transfected using TransIT-X2 (Mirus Bio LLC, Madison, WI). Transfected cells were selected with puromycin, and single cell clones screened with a specific virolectin recognizing 9-O-acetyl Sia (PToV-P4 HE-Fc) (35, 40, 41). Full sequencing was used to confirm loss of *CASD1* and *SIAE* function in both alleles. qPCR and western blot analysis were also performed to confirm knockout efficiencies.

Generation of BCRP overexpressing HEK 293 cell line

A BCRP (ABCG2)-overexpressing cell line was developed and used as a positive control for efflux studies. Briefly, HEK 293 Wildtype cells were plated in 6 well plate (Corning, NY) at a density of $5x10^5$ cells/ml and cultured until 80% confluency was attained. Cells were then transiently transfected with 2 µg PcDNA 3.1 plasmid containing Human ABCG2 cDNA ORF clone (GenScript Biotech, NJ). Transfection was carried out with Lipofectamine 3000 (Invitrogen, MA) in Opti-MEM medium (Gibco, MD), according to manufacturer's protocol (42). ABCG2-expressing stable cells were selected by treating cells with 0.8mg/ml G418 for up to a week. A G418 (Geneticin) (Gibco, MA) kill curve was performed prior to transfection on HEK 293 Wildtype cells to select appropriate G418 concentration for stable cell line generation. Western blot analysis was used to confirm stable transfection.

Western blot analysis

Cell lysates were prepared in RIPA buffer (Thermo-Fisher Scientific, MA) supplemented with Protease and Phosphatase Inhibitor (ThermoFisher Scientific, MA). Protein concentration was determined using Pierce BCA Protein Assay (ThermoFisher Scientific, MA). Cell lysates (20-30 µg protein) were electrophoresed on 4-12% Criterion TGX Precast gels (BioRad, CA) and transferred onto Trans-Blot turbo nitrocellulose membranes (BioRad, CA). Membranes were blocked with Intercept blocking buffer (LI-COR, NE) for 1 h at room temperature and incubated overnight at 4°C with monoclonal anti-BCRP antibody (Abcam, MA), anti-GAPDH antibody (Thermo Fisher Scientific, IL), anti-Bcl2 antibody (Thermo Fisher Scientific, IL) and anti-PARP1 antibody (Thermo Fisher Scientific, IL) at 1:500, 1:2000, 1:1000 and 1:1000 dilutions in blocking buffer respectively. Secondary antibody incubation (1:1000 dilution in PBS containing 0.1%Tween 20) was performed using goat anti-mouse IRDye secondary antibody (LiCOR, NE) and goat anti-rabbit IRDye secondary (Li-COR, NE) for 1 h at room temperature. Target proteins were detected using the Odyssey CLx Imager (LiCOR, NE). For protein expression comparison, protein band density was analyzed using Image StudioLite (LI-COR, NE) software and corrected for uneven sample loading and transfer using GAPDH as the loading control. For expression levels of Cleaved PARP1 determination, cells were challenged with 0.5µg/ml Mitoxantrone for 48h prior to lysate preparation. This same approach was used to investigate the effect of the lysosomal enzyme inhibitor, Bafilomycin A1 (BMA), on BCRP protein expression levels. Cells (4×10^5 cell/ml) were challenged with 100nM BMA for

2h prior to lysate preparation using a previously established protocol (29).

Immunofluorescence assay

Cellular expression of BCRP was determined by immunofluorescence microscopy as previously described (43). In brief, HCT 116, A549 and HEK/BCRP cells (2×10^4 cells per well) were grown on glass coverslip. Cells were then fixed in 4% paraformaldehyde and permeabilized with 0.5% Triton X-100. Slides were blocked in a buffer containing 0.01% goat serum, 0.01% saponin, and 0.05% glycine in PBS for 1 h. After incubation with 1:20 dilution of human ABCG2 antibody BXP-21 (Millipore, MA) in PBS (containing 0.1% BSA) overnight at 4°C, cells were incubated with 1:200 dilution Alexa Fluor 488 conjugated goat anti-mouse IgG cross-adsorbed secondary antibody (Thermo Fischer, IL) in PBS (containing 0.1% BSA) in the dark for 1 h. DAPI (Sigma, MO) (1μg/mL final concentration) was used to stain nuclei of cells. BioTek Cytation Live Cell imager (BioTek, WA) was used to collect immunofluorescence images.

Hoechst 33342 accumulation assay

Intracellular fluorescence of Hoechst 33342 was analyzed with a fluorescence microscope (Carl Zeiss, Goettingen, Germany) as described previously (44). Briefly, cells were cultured in a 6-well plate (Corning, NY) containing poly-L lysine coated glass cover slips overnight at a density of $5x10^5$ cells/ml. Cells were exposed to 1μM Hoechst 33342 in the presence or absence of 1μM Ko143. Cells were then washed twice with ice-cold PBS, covered with HEPES buffer and fluorescence images were measured. Image StudioLite (LI-COR, NE) software was used to quantify fluorescence intensity (Hoechst 33342 accumulation).

Cell viability assay

Differential sensitivity of cells to Mitoxantrone was measured using the MTT (3-(4,5-dimethylthiazolyl)-2,5-diphenyltetrazolium bromide) colorimetric assay as described previously (45). Briefly, cells were plated at a density of $2x10^5$ cells/ml in a 96 well plate (Corning, NY) and challenged with varying concentrations (0-5 μg/ml) of Mitoxantrone for 48 h in the presence or absence of the BCRP inhibitor, Ko143 (1μM). MTT solution (5 mg/ml) was then added to each well and cells further incubated for 4 h at 37°C. The amount of formazan produced was measured at a wavelength of 570 nm with a microplate reader (BioTek Cytation 3, WA). Absorbance values were recorded and used to evaluate the percentage cell viability. GraphPad Prism 8 software was used to evaluate the individual IC_{50} values, following which fold resistance (ratio of IC_{50} value for each cell line to IC_{50} of its corresponding Wildtype cell line) was estimated.

Cell proliferation assay

Growth rate of cells was measured and compared *via* the method described by Barnard et al. (40). Briefly, cells were plated $2x10^5$ cells/ml in a 96 well plate (Corning, NY) overnight. The cells were subsequently harvested, stained with trypan blue and counted every day for up to 4 days with an automated cell counter (BioRad, CA). Culture medium was replaced with fresh culture medium after the second day for days 3 and 4 of the experiments.

mRNA expression analysis

Total RNA was extracted from each cell variant using Direct-zol RNA mini-prep kit (Zymo Research Corporation, Irvine, CA), according to the manufacturer's instructions. First-strand cDNA was prepared from the extracted RNA in a reverse transcriptase reaction with a High-Capacity cDNA Archive Kit (Applied Biosystems, Foster City, CA) and random hexamers as a primer, according to the manufacturer's protocol in an iCycler™ thermal cycler (Bio-Rad Laboratories Inc., Hercules, CA). cDNA concentration and purity were measured with a Nanodrop 2000 spectrophotometer (Thermo Scientific, USA). Using the primer sets (Integrated DNA Technologies, Coralville, IA) shown below, relative BCRP gene expression was further investigated by quantitative real-time PCR.

ABCG2: 5'-GATCTCTACCCTGGGGCTTGTGGA-3'; 5'-TGTGCAACAGTGTGATGGCAAGGGA-3'

GAPDH: 5'-ACTGCCAACGTGTCAGTGGTGGACCTGA-3'; 5'-GGCTGGTGGTCCAGGGGTCTTACTCCTT-3′.

Briefly, each cDNA sample (1 μl) was amplified with 10 μl of Thermo Scientific PowerUp SYBR Green qPCR Master Mix and 1 μM of each primer. Amplification was performed in a Quant Studio 3 Real Time PCR system (Applied Biosystems, Foster City, USA) with the following parameters: UDG activation at 50°C, Activation (Dual-Lock DNA polymerase) at 95°C for 2 min followed by 40 cycles of denaturation at 95 °C for 15 s, annealing/extension at 60°C for 1 min. The relative expression levels of ABCG2 in each sample (normalized to that of GAPDH) were determined using $2^{-\Delta\Delta Ct}$ method. RT-qPCR experiments were repeated three times.

Expression of *CASD1* and *SIAE* in clinical samples

To investigate the potential prognostic value of *CASD1* and *SIAE*, we performed survival analysis of *CASD1* and *SIAE* mRNA expression and overall survival in clinical lung adenocarcinoma (LUAD) samples (n=501) and clinical colon adenocarcinoma (COAD) samples (n=374) from the TCGA PanCancer Atlas study (46). Survival data and gene expression data were downloaded *via* cBioPortal (https://www.cbioportal.org/) (47, 48). Gene expression data downloaded for our analysis were *mRNA Expression, RSEM (Batch normalized from Illumina HiSeq_RNASeqV2)*. Survival

analysis and visualization were performed with R programming language using *ggsurvfit* and *survival* (49) packages. Kaplan-Meier plots were generated to visually compare survival across gene expression groups and cancer types. Samples were split into two groups, high and low, based on the median expression per gene (high: >=median, low: <median). Overall survival status was coded 1 for deceased and 0 for censored, overall survival time was expressed in months, and gene (*CASD1* or *SIAE*) expression status was coded 1 for low and 2 for high. Univariable Cox proportional hazard regression models were fit using survival outcome (based on overall survival status and overall survival time) as response variable and gene expression status as explanatory variable. The Cox proportional hazard regression hazard ratio (HR), 95% confidence intervals (CI) and log-rank p value were reported in each Kaplan-Meier plot. Statistical significance was set at log-rank p value < 0.05.

Results

Generation of BCRP/ABCG2 overexpressing HEK 293 cells

To develop a stable BCRP-overexpressing cell line to serve as a positive control for functional studies, we first constructed a Geneticin (G418) kill curve to determine appropriate G418 concentration for stable cell line selection. The results revealed that 0.8mg/ml G418 inhibited 99% cell growth (Figure S1A). HEK 293 Wildtype were then transiently transfected with a PcDNA 3.1 vector containing Human ABCG2 cDNA ORF clone and selected for stably transfected cells by applying 0.8mg/ml G418 pressure for a week. Results of transfection revealed high BCRP/ABCG2 protein expression in transfected cells (HEK 293/BCRP) compared to the Wildtype cell line (HEK 293 WT) and cell transfected with an empty vector (HEK 293/PcDNA3.1) (Figure S1B). Also, the generated HEK 293/BCRP cell line was functionally characterized by comparing it to HEK 293 WT in terms of their response or sensitivity to the chemotherapeutic drug, Mitoxantrone. Our results showed significantly increased cell viability (Figure S1C) and 5-fold increased resistance (Supplementary Table 1) in transfected cell compared to wildtype cells.

Sialate O-acetyltansferase knockout upregulates BCRP/ABCG2 expression

To determine the effect of O-acetyl modification of Sia on BCRP, western blot analysis and immunofluorescence assay were performed to compare BCRP protein expression in Wildtype HCT 116 and A549 cell lines to those without O-acetyl Sia (CASD1 knockout) and those that express high levels of O-acetyl Sia (SIAE knockout). The results indicate that knockout cells showed high expression of BCRP (ABCG2) in both HCT 116 (Figures 2A, 3A, C) and A549 (Figures 2B, 3B, D) cell lines as compared to wild type

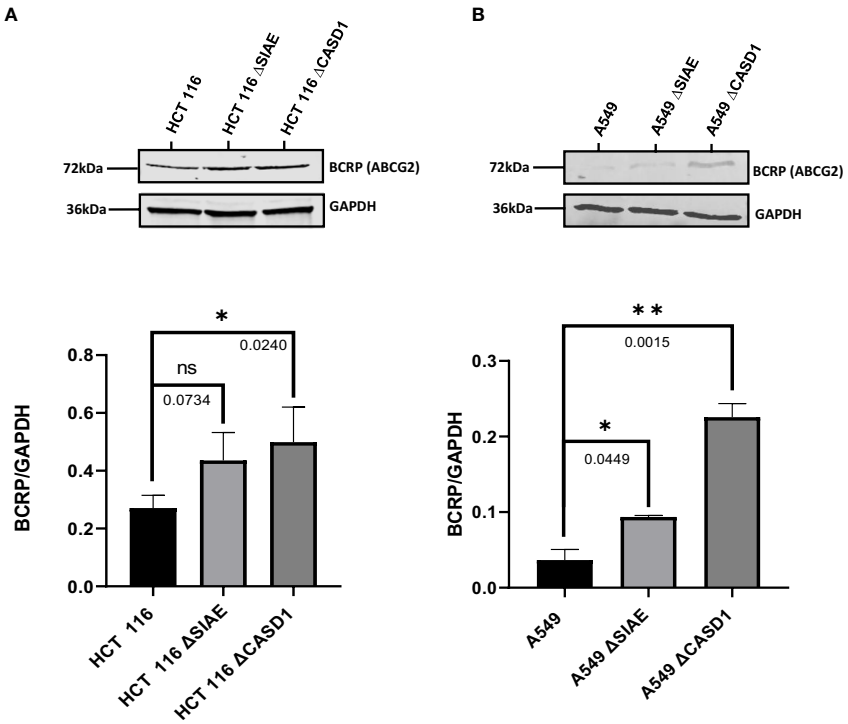

FIGURE 2
BCRP (ABCG2) expression in Wild type, Knockout (CASD1 and SIAE) cell lines. Western blot analysis was performed on whole cell lysate using BCRP-specific antibodies. GAPDH was used as loading control **(A)** Immunoblot analysis of whole cell lysates prepared from HCT 116 cell lines. Below is normalized Protein band density. **(B)** Immunoblot analysis of whole cell lysates prepared from A549 cell lines. Below is normalized Protein band density. One-way ANOVA with Tukey's posttest for multiple comparison, *P < 0.05, **P < 0.01.

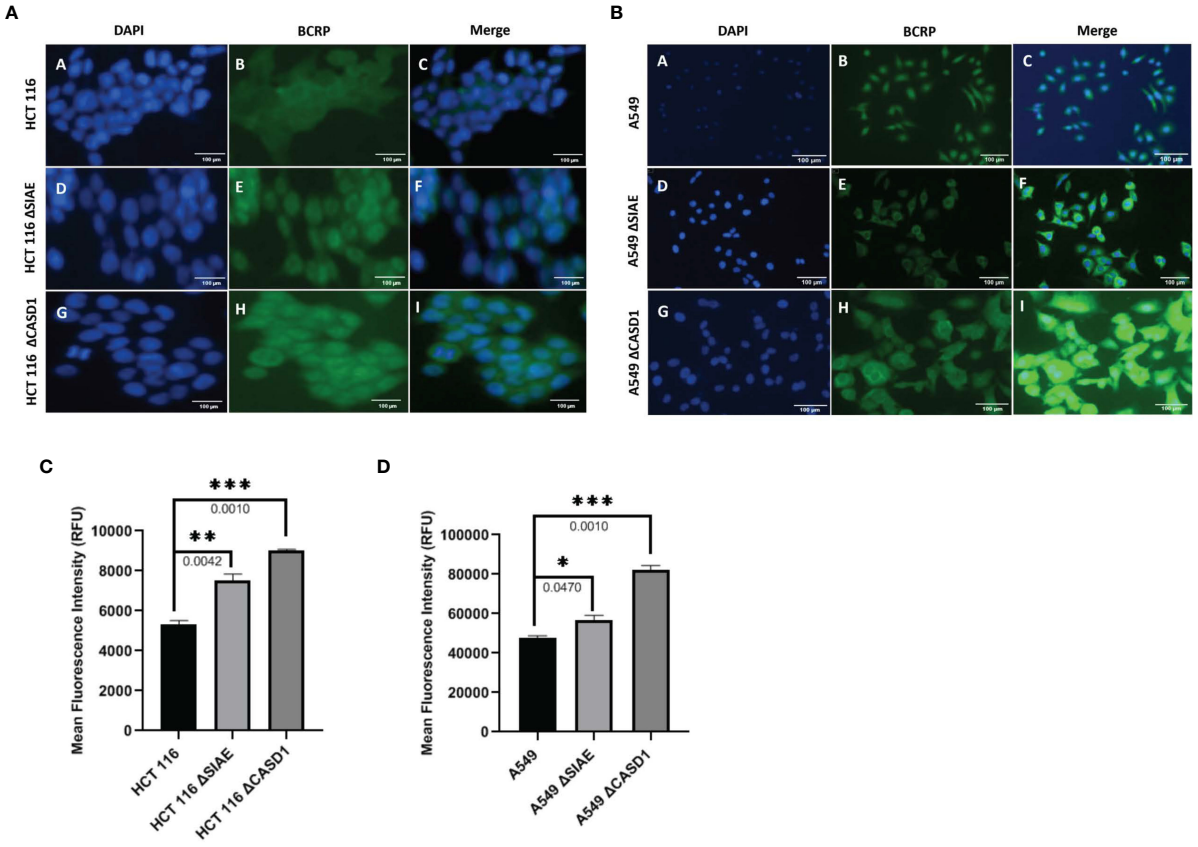

FIGURE 3
BCRP (ABCG2) expression in Wild type, Knockout (CASD1 and SIAE) cell lines. Cells were fixed, permeabilized, treated with BCRP-specific primary antibody and Alexa-Fluor 488 conjugated secondary antibody. DAPI was used for counter staining **(A)** Immunofluorescent localization of BCRP in HCT 116 cell lines. **(B)** Immunofluorescent localization of BCRP in A549 cell lines. **(C)** BCRP Fluorescence Intensity plot for HCT 116 cell lines. **(D)** BCRP Fluorescence Intensity plot for A549 cell lines. One-way ANOVA with Tukey's posttest for multiple comparison, *P < 0.05, **P < 0.01 and ***P ≤ 0.001.

cells. CASD1 knockout cells recorded the most significant overexpression of BCRP (p-values =0.0240 and 0.015 for HCT 116 and A549 cell lines respectively) followed by SIAE knockout cells (p-value = 0.0449 for A549 cell line). Also, CASD1 knockout A549 cells comparatively appeared cytologically transformed (i.e., increase in size) (Figure 3B).

CASD1 knockout decreases intracellular accumulation of Hoechst 33342

To investigate the effect of O-acetylated Sia modifications on BCRP (ABCG2) function, BCRP fluorescent substrate, Hoechst 33342 was used to assess transport (efflux) competence of wild type and knockout cell lines. To further prove BCRP's involvement in this efflux phenomenon, potent BCRP inhibitor, Ko143 was used to block efflux function. Our data shows generally high fluorescent intensities for Ko143-inhibited cell lines compared to control (vehicle-treated) cell lines (Figures 4B, D). Also, we observed reduced accumulation of Hoechst 33342 (i.e., high efflux) in knockout cell lines compared to wild type cell lines (Figure 4B), and (Figure 4D). Comparatively, CASD1 knockout cells recorded the most significant reduction in Hoechst fluorescence intensity in HCT 116 cell lines (i.e., Panel A of Figures 4A, B (p-value = 0.0344) and A549 cell lines (i.e., Panel A of Figures 4C, D (p-value = 0.0022)

CASD1 knockout confers resistance to mitoxantrone

To investigate the effect of O-acetyl Sia on cancer cell response to the chemotherapeutic drug, Mitoxantrone, the MTT (tetrazolium-based) cell viability assay was performed. Following exposure to varying concentrations (0-5μg/ml) of Mitoxantrone for 48h in the presence or absence of BCRP inhibitor (Ko143), the result revealed reduced cell viability in all cancer lines in the presence of Ko143 inhibitor as compared to vehicle treated (uninhibited) cells (Figures 5A–C, 5E–G). The results further showed a reduced sensitivity/response in CASD1 knockout cell lines of both cancer cells as compared to the Wild types and SIAE knockout cells. This is inferred from the IC_{50} values of 0.512, 0.658 and 1.009 μg/ml recorded for HCT 116 Wildtype, HCT 116 SIAE knockout and HCT 116 CASD1 knockout cell lines respectively (Table 1; Figure 5D). A549 Wildtype, A549 SIAE knockout and

10.3389/fonc.2023.1145333

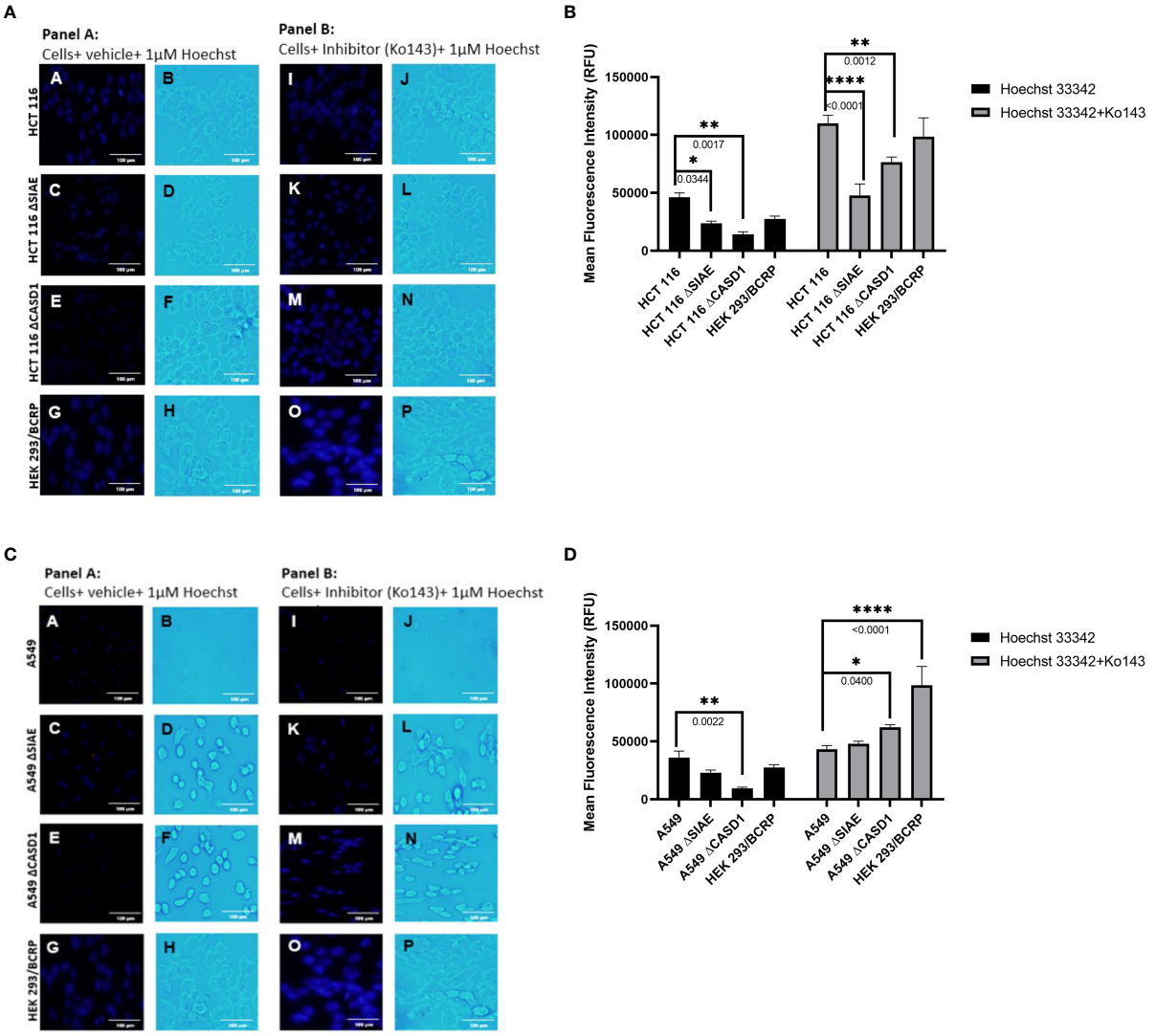

FIGURE 4
Intracellular accumulation of Hoechst 33342 in HEK and A549 Cells. Cells were treated with Hoechst 33342 in the presence or absence of Ko143 and stained with Hoechst 33342. **(A)** Fluorescent and Bright field images of HCT 116 cells. **(B)** Fold change in Hoechst 33342 accumulation in HCT 116 cells. **(C)** Fluorescent and Bright field images of A549 cells. **(D)** Fold change in Hoechst 33342 accumulation in A549 cells. One-way ANOVA with post hoc Tukey's test. *P < 0.05, **P < 0.01, and ****P <0.0001.

A549 CASD1 knockout cell lines also recorded IC_{50} values of 0.423, 0.710 and 1.226 µg/ml respectively (Table 1; Figure 5H). In effect, CASD1 knockouts of both cancer cells exhibited significantly higher resistance towards Mitoxantrone (i.e., ~2-fold resistance and 3-fold resistance for HCT 116 and A549 cell lines respectively when compared to their Wildtype cells) (Table 1)

CASD1 knockout enhances cell proliferation

To examine the association of O-acetyl Sia as well as BCRP expression in phenotypic drug resistant (aggressive) characteristics, we monitored the growth rate/cell proliferation of the wild type and knockout cells over a period of 4 days. Our results revealed significantly increased cell proliferation in the knockout cells compared to the wild type for the A549 cells (Figure 6B). The CASD1 knockout cell line demonstrated the highest growth rate over the 4-day period of examination followed by the SIAE knockout cell line (Figure 6B). A similar cell proliferation pattern was observed for HCT 116 cell lines (Figure 6A), however, there was no significant difference between growth rate of wild type and knockout cells.

CASD1 knockout increases expression of cell survival proteins

To better understand the mechanism of CASD1 knockout-mediated cell proliferation as well the role O-acetyl Sia play in cell survival, we investigated the levels of cell survival proteins Bcl-2 and PARP 1 in the wild type and knockout cell lines. Our results

10.3389/fonc.2023.1145333

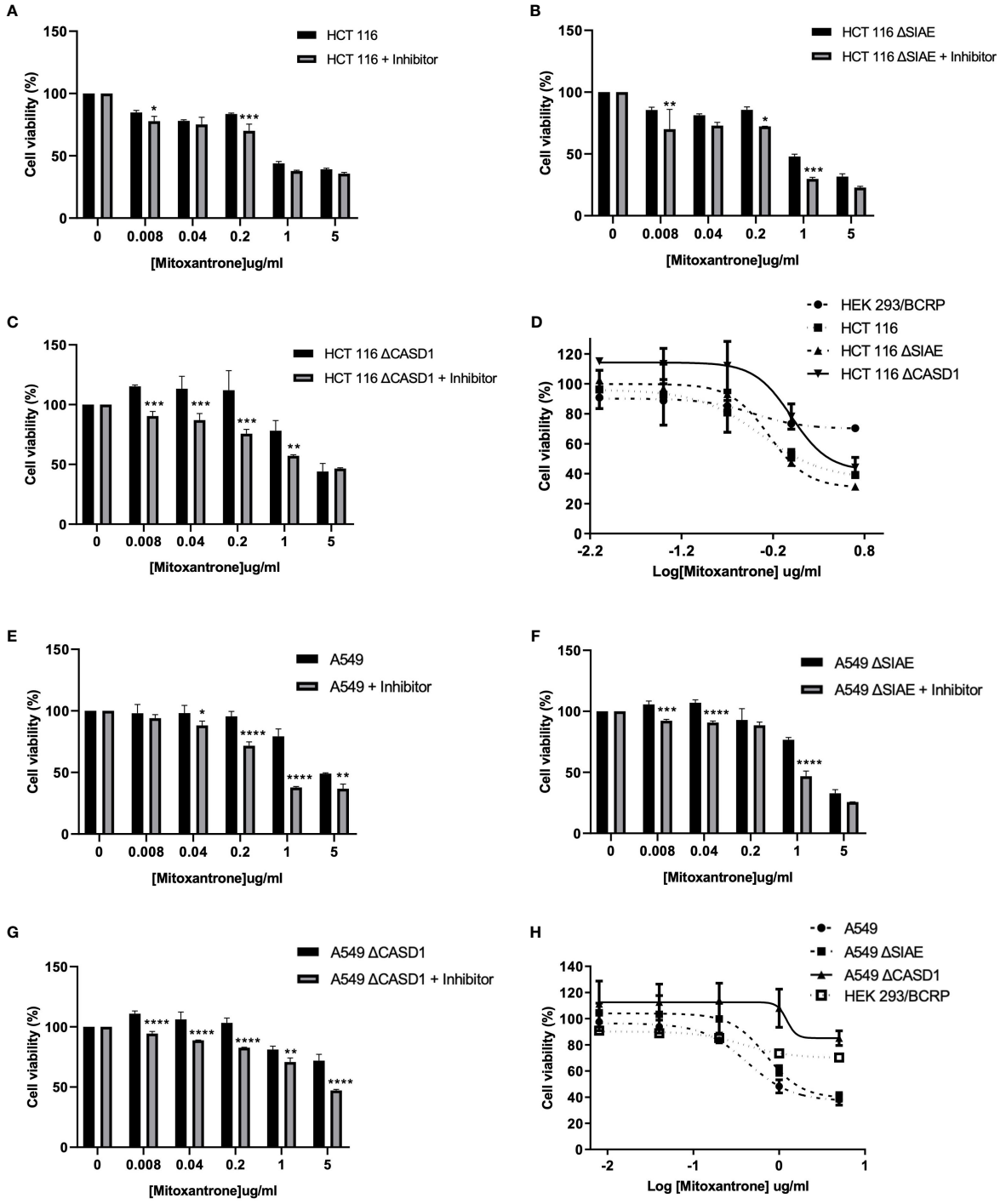

FIGURE 5
Cytotoxic effect of Mitoxantrone on HCT 116 and A549 cells. Cells were treated with Mitoxantrone (0-5ug/ml) in the presence or absence of 1uM Ko143. Dose-response of the effect of Mitoxantrone on **(A)** HCT 116 Wildtype cells **(B)** HCT 116 SIAE knockout cells **(C)** HCT 116 CASD1 knockout cells **(D)** Comparative cell viability profiles. Data reported as mean + sd of three independent experiments. Two-way ANOVA with Tukey's posttest for multiple comparison, *P ˂ 0.05. Cytotoxic effect of Mitoxantrone on A549 cells. Cells were treated with Mitoxantrone (0-5ug/ml) in the presence or absence of 1uM Ko143. Doseresponse of the effect of Mitoxantrone on **(E)** A549 Wildtype cells **(F)** A549 SIAE knockout cells **(G)** A549 CASD1 knockout cells **(H)** Comparative cell viability profiles. Data reported as mean + sd of three independent experiments. Two-way ANOVA with Tukey's posttest for multiple comparison, *P < 0.05, **P < 0.01, ***P < 0.001 and ****P < 0.0001.

showed significantly higher levels (~2 fold) of Bcl-2 expression in SIAE and CASD1 knockout HCT 116 cell lines relative to their counterpart wild type cell line (Figure 7A). In comparison to the wildtype cell line, the CASD1 and SIAE knockouts of A549 cell lines also recorded higher Bcl-2 protein expression; however, between the two, CASD1 knockout cell showed a much higher and significant (~2 fold) Bcl-2 protein expression (Figure 7B). To elucidate the protein expression levels of the 25 kDa PARP1 fragment (cleaved

TABLE 1 Effect of Acetyl Sia on Cellular response to Mitoxantrone.

Cell line	IC_{50} (μg/ml)	
	Mitoxantrone	Fold Resistance
HCT 116	0.512 + 0.070	1.00
HCT 116 SIAE Knockout	0.658 + 0.012	1.28
HCT 116 CASD1 Knockout	1.009 + 0.017*	1.97
HEK 293/BCRP	1.013 + 0.012*	1.96
A549	0.423 + 0.132	1.00
A549 SIAE Knockout	0.710 + 0.177	1.68
A549 CASD1 Knockout	1.226 + 0.479**	2.90
HEK 293/BCRP	1.013 + 0.012**	2.39

Mean + SD of three independent experiments performed in triplicate. Fold resistance determined by dividing the IC_{50} value for each cell line by the IC50 value of Wild type.
*P < 0.05 and
**P < 0.01 significantly different from the Wild type cell line

PARP 1) cells were incubated in the presence or absence of the apoptosis inducer, Mitoxantrone. Generally low levels of cleaved PARP1 were observed in the absence of Mitoxantrone, however, levels increased significantly in treated Wild type and SIAE knockout cell lines (Figures 8A, B). On the other hand, increase in Cleaved PARP 1 levels in Mitoxantrone-treated CASD1 knockouts for both HCT 116 and A549 cell lines were not significant compared its untreated counterpart. Also, CASD1 knockout cell lines expressed the lowest levels (~2 fold less) cleaved PARP1 compared wild type and SIAE knockout cell lines (Figures 8A, B).

CASD1 Knockout upregulates BCRP/ABCG2 mRNA expression levels

We explored gene expression events as a possible factor linking deacetylated Sia and BCRP protein expression by analyzing the relative expression levels of BCRP mRNA. Our results showed statistically comparable BCRP mRNA levels in Wild type and SIAE Knockout variants of both HCT 116 and A549 cells. However, significantly high expression levels were observed in CASD1 knock out cells (i.e., ~2.5-fold and ~ 6-fold increase in HCT 116 and A549 cells lines respectively) (Figures 9A, B),

Lysosomal pathway is involved in decreased BCRP protein stability and levels

Protein degradation occurs in two major sites, namely lysosomes and proteasomes. To elucidate the role of the lysosomal pathway in the observed differences in BCRP protein level across the various cell lines (i.e., Wildtype and knockouts), cells were cultured in the presence or absence of 100 nM of potent lysosomal enzyme inhibitor, Bafilomycin A1 (BMA), and levels of BCRP in cell lysate determined *via* western blot. Whereas BCRP levels in CASD1 knockout cells remained significantly unchanged following BMA treatment in both cell lines, our results show significant increases in BCRP level for wild type and SIAE knockout cells of HCT 116 cells (p-values= 0.0121 and 0.0119 respectively) (Figure 10A). A significant increase in BCRP levels was also recorded for wild type of A549 cells (p-value= 0.0010), however no significant increase was seen in the SIAE knockout cells (p-value= 0.9879) (Figure 10B).

CASD1 expression favors survival in lung adenocarcinoma

After observing that CASD1 knockout promotes cell survival and proliferation in cancer cell lines, we investigated the clinical relevance of *CASD1* and *SIAE* expression in clinical samples by examining the relationship between overall patient survival and *CASD1* and *SIAE* mRNA expression in lung adenocarcinoma (LUAD) and colon adenocarcinoma (COAD) clinical samples from The Cancer Genome Atlas (TCGA). LUAD samples with high expression levels of *CASD1* (red line) were significantly associated with high patient survival rates (HR = 0.73, 95% CI: 0.54 – 0.98, log-rank p value = 0.034) compared to those with low expression (blue line) (Figure 11A). Median survival in the high and low *CASD1* expression groups are 53 months and 40 months respectively. This

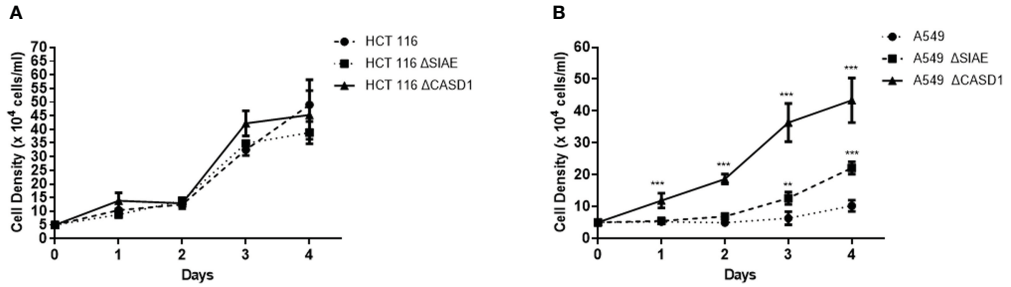

FIGURE 6
Comparative cell proliferation/growth assessment. 5X104 cells/ml was seeded and cell density was measured every 24h for 4 days **(A)** Cell growth profile for HCT 116 cell lines **(B)** Cell growth profile for A549 cell lines. Data reported as mean + sd of three independent experiments performed in triplicates. *P < 0.05, **P < 0.01 and ***P < 0.001.

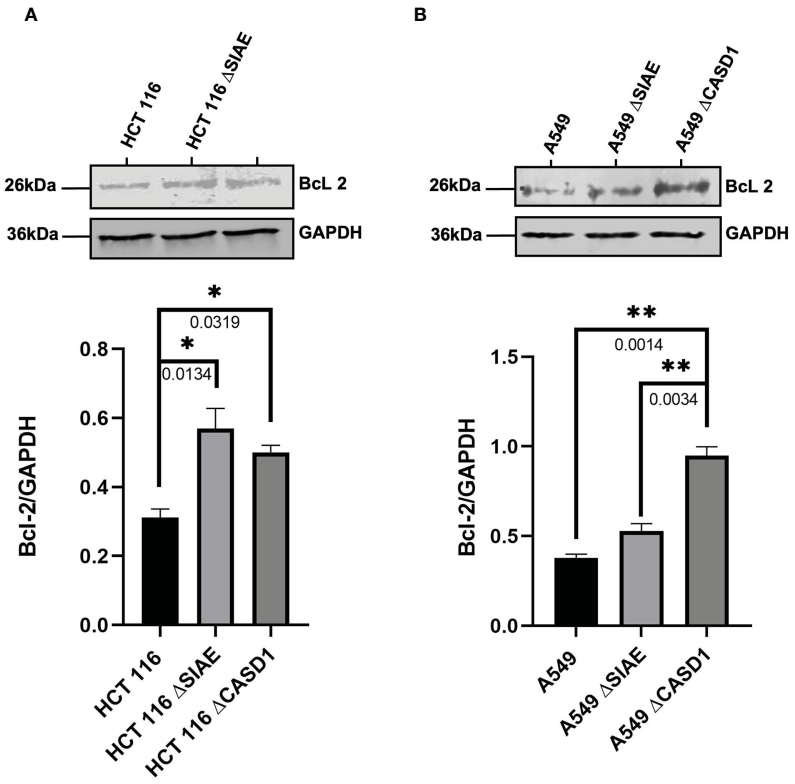

FIGURE 7
Bcl-2 Protein Expression in Wild type, Knockout (CASD1 and SIAE) cell lines. Western blot analysis was performed on whole cell lysate using BcL2-specific antibodies. GAPDH was used as loading control **(A)** Immunoblot analysis of whole cell lysates prepared from HCT 116 cell lines. Below is the normalized Protein band density **(B)** Immunoblot analysis of whole cell lysates prepared from A549 cell lines. Below is Protein band density. One-way ANOVA with Tukey's posttest for multiple comparison, *P < 0.05 and **P < 0.01.

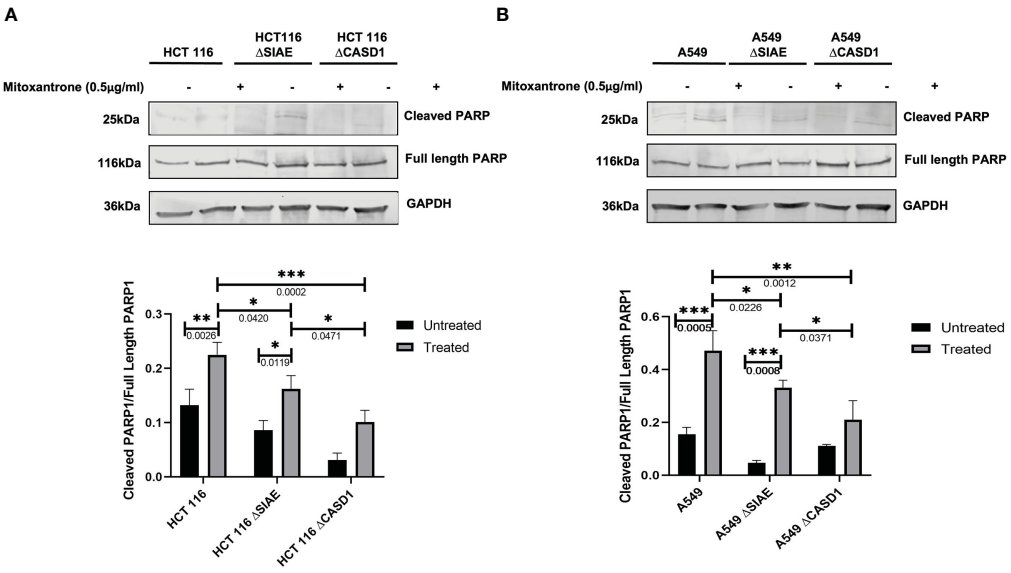

FIGURE 8
Cleaved PARP levels in Wild type, Knockout (CASD1 and SIAE) cell lines. Western blot analysis was performed on whole cell lysate using Cleaved PARP-specific antibodies. GAPDH was used as loading control **(A)** Immunoblot analysis of whole cell lysates prepared from HCT 116 cell lines. Below is the normalized Protein band density. **(B)** Immunoblot analysis of whole cell lysates prepared from A549 cell lines. Below is the normalized Protein band density. One-way ANOVA with Tukey's posttest for multiple comparison, *P < 0.05, **P < 0.01 and ***P < 0.001.

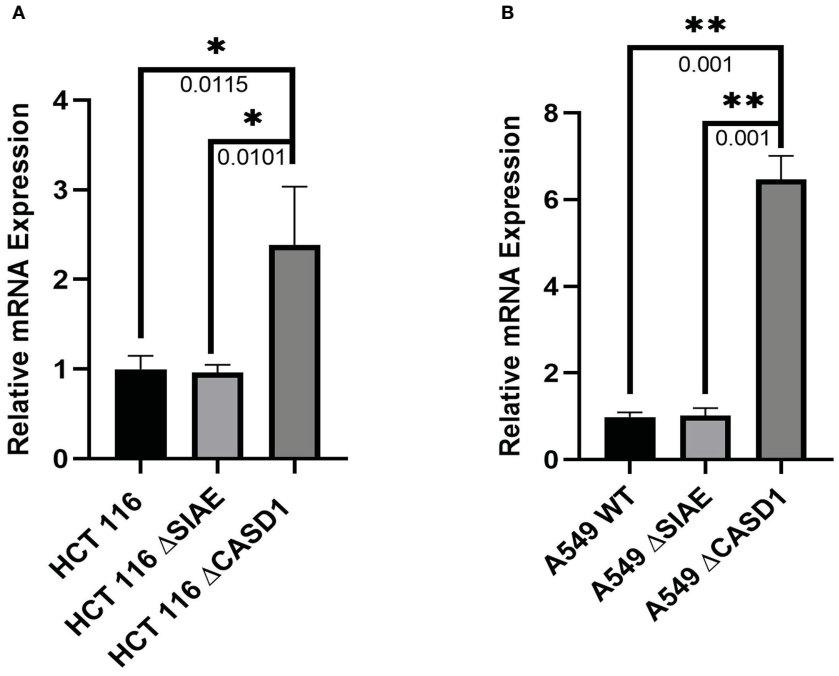

FIGURE 9
BCRP (ABCG2) mRNA expression in Wild type, Knockout (SIAE and CASD1) cell lines via qPCR. **(A)** BCRP mRNA expression profile from HCT 116 cell lines. **(B)** BCRP mRNA expression profile of A549 cell lines. One-way ANOVA with Tukey's posttest for multiple comparison. *P < 0.05, **P < 0.01.

finding suggests that higher *CASD1* expression is a favorable marker of survival in LUAD. No significant association was observed in survival rates for (COAD) samples with high expression levels of *CASD1* compared to those with low expression (HR = 1.15, 95% CI: 0.74 – 1.77, log-rank p value = 0.500) (Figure 11C). Similarly, no significant associations were observed in *SIAE* expression and survival rates for patients with LUAD and COAD (log-rank p-value = 0.922 and 0.130 respectively) (Figures 11B, D).

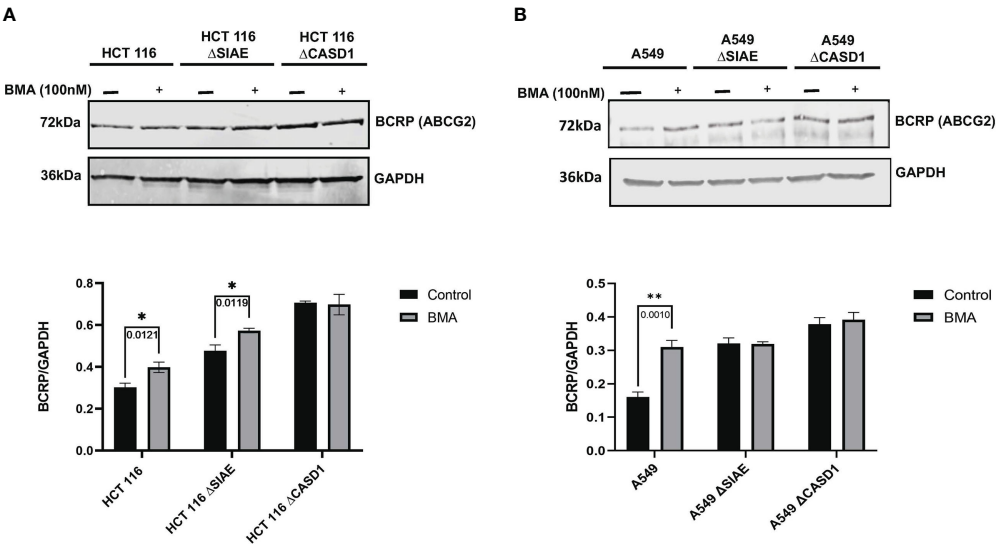

FIGURE 10
BCRP (ABCG2) expression in Wild type, Knockout (CASD1 and SIAE) cell lines following Bafilomycin A1 treatment (grey bars). Cells were treated with 100nM BMA, lysed and Immunoblot analysis was performed on whole cell lysate using BCRP-specific antibodies. GAPDH was used as loading control **(A)** Immunoblot analysis of whole cell lysates prepared from HCT 116 cell lines. Below is normalized Protein band density. **(B)** Immunoblot analysis of whole cell lysates prepared from A549 cell lines. Below is normalized Protein band density. Two-way ANOVA with Tukey's posttest for multiple comparison, *P < 0.05 and **P < 0.01.

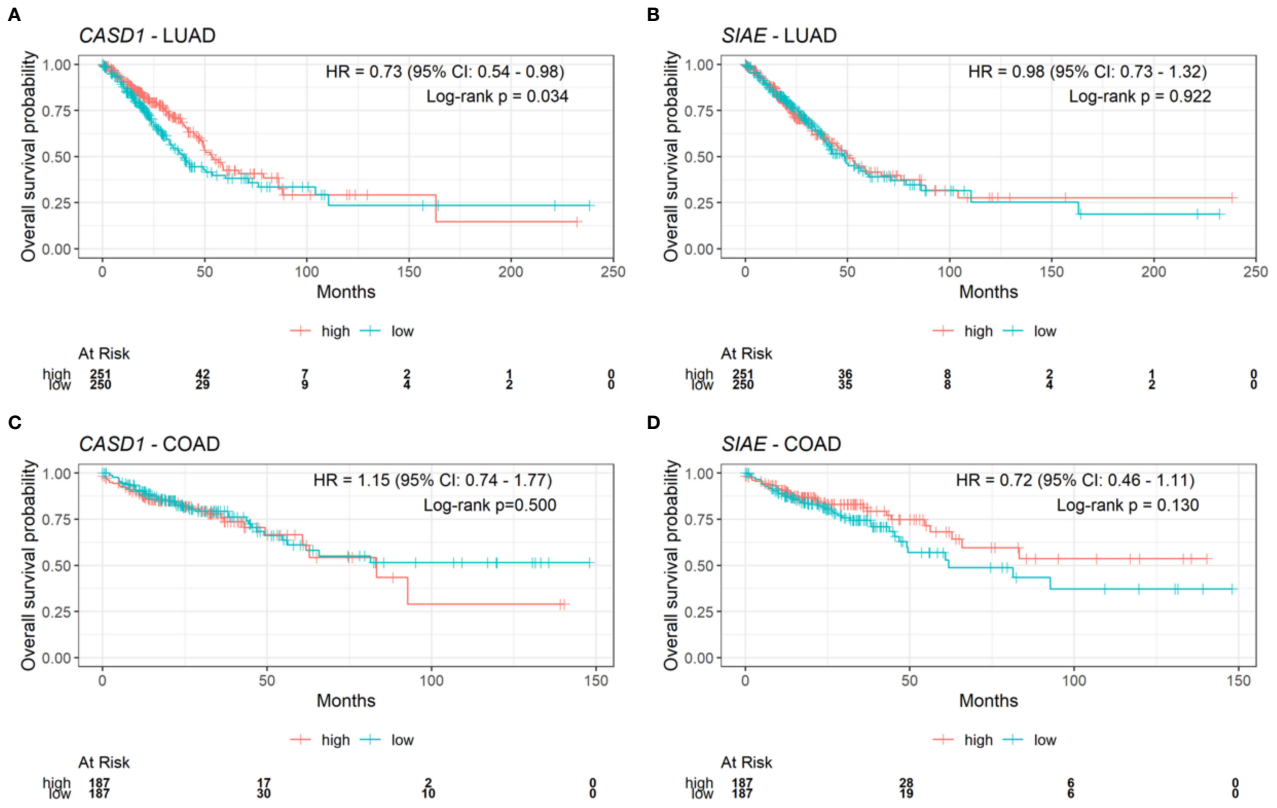

FIGURE 11
Kaplan-Meier plots for CASD1 and SIAE mRNA expression and overall survival in clinical lung adenocarcinoma (LUAD) and colon adenocarcinoma (COAD) samples. **(A)** CASD1 mRNA expression in LUAD samples. **(B)** CASD1 mRNA expression in COAD samples. **(C)** SIAE mRNA expression in LUAD samples. **(D)** SIAE mRNA expression in COAD samples. Cox proportional hazard regression hazard ratio, HR, (with 95% confidence interval, CI), and log-rank p value are annotated on each plot. Risk table is shown beneath each Kaplan-Meier plot. Samples were split into high (red) and low (blue) expression groups per gene using the median (high: >=median, low: <median).

Discussion

The contribution of Sias in the process of multidrug resistance has remained unexplored despite the various roles Sias play in cancer progression and as viable targets for glycan related therapeutics. Sias have been implicated in the pathogenesis of a myriad of diseases including autoimmune disorders, inflammation, coronary artery disease, influenza infections, SARS-COV2 infections, cancer among others (40, 50–52). In cancers, Sia has been shown to mediate communication and interaction with receptors on immune cells *via* the sialic acid-Siglec pathway (35, 53).

Physiologically, more than 50 chemically distinct functional group modifications of Sia have been identified, among which the acetyl modification/variant is the most clinically studied (34). Cancer cells may differentially exploit these O-acetyl modifications in perpetuation of unique survival hallmarks such as immune cell evasion and aggressive phenotype development (39). For instance, Grabenstein et al. (35) in an extensive study, reported that Sia acetylation reduces engagement of cancer associated Siglecs and increases NK mediated cytotoxicity in colon and lung cancer cells. Comparative studies on colon-derived mucins have revealed over 50% acetylation of Sia in healthy tissues and predominantly high deacetylated Sia in cancerous tissues. Research has also shown that hypoacetylation of Sia on the tumor associated antigen, Sialyl Lewis X motifs, is the key alteration associated with metastatic colorectal cancers (54). Furthermore, high levels of 9-O acetyl sialylation of sialoglycoproteins have been shown to be distinctly expressed in human acute lymphoblastic leukemia (ALL) and used as diagnostic biomarker for the detection of pediatric ALL (55). It has also been touted to contribute to the survival and drug resistance characteristics observed in mouse and *in vitro* models of pre-B ALL (56). One of the ways in which cancer cells develop resistance toward chemotherapeutics is overexpression of sialyltransferases. ST6Gal-I sialyltransferase, an enzyme upregulated in numerous cancers has been reported to promote survival and resistance in ovarian, pancreatic, and colorectal cancers *via* hypersialylation of tumor necrosis factor receptor 1 (TNFR1) and Fas Receptor (FasR) death receptor (36, 37). Hypersialylation blocks receptor internalization and the formation of the death-inducing signaling complex (DISC), thereby disabling apoptotic signaling thus leading to cell survival (36, 37). Also, Ma et al. (38) reported overexpression of ST3GAL5 and ST8SIA4 sialyltransferases in drug resistant human acute myeloid leukemia (AML) cells relative to parental cancer cells in both *in vitro* and *in vivo* experimental models. Further studies revealed that altered levels of ST3GAL5 and ST8SIA4 correlated with high expression levels of P-gp and

MRP1, suggesting a strong association between glycan sialylation and MDR.

In the current study, we explored the role of O-acetyl Sia modification in BCRP-mediated MDR. We employed lung cancer (A549) and colon cancer (HCT 116) cells whose sialate O-acetyl transferase (*CASD1*) gene and sialate O-acetyl esterase (*SIAE*) gene have been removed *via* CRISPR Cas 9 gene editing. The *CASD1* and *SIAE* genes encode key enzymes that respectively catalyze the addition and removal of acetyl groups to C-9 and/or C-7 positions of Sia (57, 58) (Figure 1B). The cells had been genotypically and phenotypically characterized in earlier studies (35, 40). For the purposes of this study, we further developed and characterized BCRP overexpressing HEK 293 cell to serve as positive control.

We first examined how these gene knockouts affected BCRP protein expression. Our results revealed high BCRP expression levels in the knockouts compared to the wild types of both cancer cells (Figures 1C, D). The CASD1 knockout cell lines (i.e., cells that lack O-acetyl Sia) in particular, demonstrated significantly higher levels of BCRP expression (Figures 1C). With respect to Sia modifications, prior studies have reported a positive correlation between Sialyl transferases, ST3Gal5 and ST8Sia4 expression and efflux proteins, PgP and MRP1 expression in human acute myeloid leukemia (38). Our data suggests that there is a strong correlation between dysregulation of O-acetylation in cells, particularly loss of CASD1, and BCRP expression. Colocalization experiments with membrane protein-specific probes are however needed to effectively establish whether altered Sialic acid acetylation disrupts BCRP trafficking (addressing) to the plasma membrane. Although all cells were imaged under same magnification (scale bar: 100um), a key observation made during microscopic analysis worth mentioning, is the cytological transformation (i.e., increase in size) of CASD1 knockout cells relative to the other cell variants. This may be attributed to its comparatively high expression of the BCRP efflux pump. Studies have shown that overexpression of membrane proteins reshapes membrane domain and induces elongation of the membrane, ultimately increasing cell size (59) Overexpression of BCRP confers resistance to several novel targeted molecules such as tyrosine kinase inhibitors as well as wide range of chemotherapeutic drugs including mitoxantrone, methotrexate and flavopiridol (60). In addition to its role of conferring resistance towards chemotherapeutic agents, BCRP also actively transports structurally diverse fluorescent compounds such as Hoechst 33342, BODIPY-prazosin, and pheophorbide A (9). Having identified the modulatory effects of O-acetyl Sia on BCRP expression, we next sought to probe how O-acetyl Sia modification affected efflux function of BCRP. Specifically, we elucidated Hoechst 33342 accumulation and cell sensitivity to Mitoxantrone in the wild type and knockout cells. Hoechst 33342(2'-[4-ethoxyphenyl]-5-[4-methyl-1-piperazinyl]-2,5'-bi-1H-benzimidazole trihydrochloride trihydrate) is a cell permeable dye that emits blue fluorescence when bound to double stranded DNA (61). Mitoxantrone on the other hand, is a chemotherapeutic agent that is clinically used to treat solid tumors, leukemias, and as an immune system modulator in multiple sclerosis. It functions as an anticancer agent by inhibiting topoisomerase II, an enzyme involved in DNA replication, chromosome condensation and segregation (62). This leads to increase in the incidence of double strand breaks and ultimately resulting in cell death. Our results showed significantly high levels of Hoechst 33342 accumulated in the nuclei of wildtype cell lines as compared to the knockout cell lines. The CASD1 knockout cell lines accumulated the least amount in their nuclei, hence recording the lowest fluorescent intensity. This may be attributed to the earlier reported variation in BCRP expression levels across the individual cell types. Generally, there is a positive correlation between efflux activity and levels of efflux proteins (i.e., BCRP) present in the cell. The wildtype cells extrude small amounts of Hoechst 33342 due to its low BCRP expression levels hence more of this fluorescent substrate accumulates in its nuclei. The knockout cells on the other hand, express high levels of BCRP hence they extrude large amounts of Hoechst 33342, ultimately resulting in the observed low intracellular (nuclei) levels, especially in CASD1 knockout cells. These variations in BCRP efflux activity also accounts for the observed responses of the various cell types towards the chemotherapeutic drug, mitoxantrone. Wildtype of both experimented cancer cells were observed to be more sensitive to mitoxantrone. This may be due to their inability to extrude high amounts of mitoxantrone because of their inherently low BCRP levels. Thus, high amount of this cytotoxic agent is retained intracellularly, leading to a reduction in cell viability. Conversely, the CASD1 knockout cells were observed to be more refractory (2- and 3-fold resistance for colon and lung cancer cells respectively) to mitoxantrone. The high efflux activity culminating from high BCRP levels in CASD1 knockout cells may account for this observation. These cells minimize intracellular levels of mitoxantrone and its associated cytotoxic effect by actively pumping out relatively high amounts of mitoxantrone out of the cells. Our data therefore suggests that the absence of O-acetyl Sia (Deacetylated Sia) confers drug resistance characteristics in lung and colon cancer cells. This observation is in contrast with earlier studies conducted by Parameswaran et al. (56) who reported a strong correlation between the presence of 9-O acetyl Sia and vincristine or nilotinib drug-resistant ALL cells. These contradictory observations suggest that the relationship between O-acetyl Sia modification and MDR may be cell or cancer specific. Also, since vincristine is not a substrate of BCRP, it suggests BCRP may not be involved in the earlier studies involving ALL cells but rather P-glycoprotein (PgP) efflux pump. Both nilotinib and vincristine are substrates of PgP (63) thus, we speculate that the role of O-acetyl Sia modification in MDR may also be efflux protein specific.

We further investigated whether O-acetyl Sia mediated-BCRP modulation, promotes phenotypic cell survival characteristics such as enhanced cell proliferation. Our results showed significantly high growth rate in CASD1 knockout lung cancer cells compared to wildtype and SIAE knockout cell lines. A similar pattern was recorded for the colon cancer cells albeit differences in growth rate were not significant. This observation is consistent with earlier reports that implicate Sia hypo/deacetylation as key alteration associated with aggressive and metastatic colorectal cancers (54). BCRP is also known to be a stem cell marker, whose expression in cancer cells is driven by metabolic and signaling pathways that confer multiple mechanisms of drug resistance, invasiveness (aggressiveness), and self-renewal (64)

hence confirming the observed high proliferative ability of the BCRP-overexpressing CASD1 knockout cells.

We further elucidated the expression levels of BcL-2 and Poly-ADP Ribose Polymerase (PARP), two proteins that have been shown to be key drivers of cell proliferation and cell survival. BcL-2 family of proteins are key regulator of apoptosis that primarily function by either inhibiting or promoting cell death. The fate of a cell is dependent on the balance between pro-apoptotic and pro-survival members of the BcL-2 family. Pro-apoptotic members of this family such as Bax and Bak promote cell death by direct binding interaction that disrupts mitochondrial outer membrane potential leading to irreversible release of intermembrane space-bound protein cytochrome C, subsequent caspase activation and apoptosis (65). Pro-survival BcL-2 family members such as BcL-2 and Bcl-xL on the other hand, prevent apoptosis by inhibiting mitochondrial outer membrane depolarization and promoting cell survival and proliferation (66). Our results revealed consistently significant high levels of the pro-survival protein BcL-2 in CASD1 knockout cells compared to the wild type and SIAE knockout cell lines for the lung cancers and wild type for the colon cancers. This once again corroborates the significantly high proliferation observed earlier in the CASD1 knockout cells. PARP 1, a 116kDa protein, belonging to the PARP superfamily, is a crucial protein involved in ensuring cell survival. Physiologically, full or active PARP 1 is known for its involvement in DNA repair processes (67). Enzymatic cleavage of PARP 1 by active Caspase 3 results in 2 inactive fragments that are unable to facilitate DNA repair leading to genomic instability and ultimately cell death. Evidence from several studies have reported upregulation of PARP activity in some cancer types. For instance, a study conducted on hepatocellular carcinoma patients showed significantly increased levels of PARP in tumor tissues than adjacent non-tumorous tissues (68). Also, strikingly high PARP 1 mRNA levels have been reported in triple negative breast cancer tumors and tumors of the endometrium, lung, ovary, and skin (69). In comparison to the wild type and SIAE knockout cells, our results showed significantly low levels of 25kDa cleaved/inactive PARP1 fragments in the CASD1 knockout lung and colon cancer cells when challenged with mitoxantrone. This observation may be attributed to the rapid efflux of mitoxantrone by CASD1 cells resulting in significant reduction of the cytotoxic concentration required to stimulate the protein mediators of the apoptosis cascade which includes Cleaved PARP1 (44). This data also confirms and corroborates our earlier findings that sialic acid deacetylation promotes cell survival in lung and colon cancer cells.

Gene expression modulatory factors and post-translational modification check points at the endoplasmic reticulum (ER) and endosome-lysosome govern the relative expression levels and stability of most proteins (70). Thus, to better understand the factor responsible for the varied protein expression levels and function of BCRP, we determined the levels of BCRP mRNA in each of the cell variants. CASD1 knockout cells significantly expressed high levels of BCRP mRNA relative to wild type and SIAE knockouts of all cell types. This finding support/confirm the BCRP protein expression data, suggesting that deacetylation of sialic acid acids alters (increases) BCRP mRNA transcript levels and consequently upregulates level of expressed proteins. We also probed for the involvement of the Lysosomal Protein degradation pathway in this phenomenon. CASD1 is localized at the trans Golgi membrane where it modifies terminal sialic acids on glycoproteins before they are trafficked to the plasma membrane. An earlier study reported that majority of plasma-membrane bound glycoproteins with O-acetyl functional group modifications are retained in the Golgi compartment (i.e., 7,9-O- and 9-O-Ac) whereas only some (9-O-Ac) are transported to the cell surface (40, 71). After remaining in the plasma membrane domain for a short period, these unstable modified glycoproteins are recycled and degraded *via* the endosome-lysosome pathway. We therefore blocked protein degradation *via* the lysosome by treating all cell variants with Bafilomycin A1 (BMA). BMA is a macrolide antibiotic that prevents maturation of autophagic vacuoles by inhibiting fusion between autophagosomes and lysosomes (72). It also serves as a specific inhibitor of vacuolar H^+ ATPase (V-ATPase) causing alkalinization of the lysosome lumen, impairing lysosomal enzyme function and subsequently leading to cellular accumulation of lysosome-bound proteins (73). We observed significantly increased levels of BCRP in BMA-treated cells in the wildtype and SIAE knockout cells in both lung and colon cancer cell lines. However, no significant increase was recorded in BCRP level for BMA-treated CASD1 knockout cancer cells suggesting that lysosomal degradation pathway may also be responsible for modulating levels of acetyl modified glycoproteins including BCRP. Consistent with our experimental findings that CASD1 knockout confers resistance to mitoxantrone and promotes cell survival, we also found that CASD1 expression favors survival in clinical lung Adenocarcinoma (LUAD) samples. This implies that CASD1-mediated sialic acid acetylation may represent a potential therapeutic target in LUAD requiring further studies to understand how the mechanism and modifiers of this process counteracts BCRP-mediated drug resistance.

Taken together, our results highlight the crucial role O-acetyl Sia modification play in cancer related MDR. Specifically, this study provides empirical evidence that modulation of acetyl Sia (specifically deacetylated Sia) upregulates BCRP expression and promote survival in lung and colon cancer cell lines. Clinical data also validated that in patients with LUAD, lower levels of CASD1 and thus less O-acetyl Sia expression had lower survival rates than those patients with high CASD1 expression. Findings from this study may have relevance to a broader spectrum of malignancies and provide a promising avenue for future MDR-circumventing therapeutics. Further studies are however warranted to explore the effect of acetyl Sia modulation on other cancers as well as other relevant MDR efflux proteins such as Pgp and MRP1.

Data availability statement

The datasets presented in this study can be found in online repositories. The names of the repository/repositories and accession number(s) can be found in the Supplementary Material.

Ethics statement

This study used *CASD1* and *SIAE* mRNA expression and overall survival data from de-identified clinical lung adenocarcinoma and clinical colon adenocarcinoma samples publicly available online (https://www.cbioportal.org/). These data were derived from previously approved human cancer genomics study The Cancer Genome Atlas (TCGA, accession numbers: PRJNA74949, PRJNA41443).

Author contributions

RW-C ad IS contributed to conception and design of the study. IT performed experiments, data analysis and wrote the first draft of the manuscript. SA performed clinical data analysis and wrote sections of the manuscript. HB performed experiment and data analysis. CP generated A549 Lung cancer knockout cell lines. All authors contributed to manuscript revision, read, and approved the submitted version. All authors contributed to the article and approved the submitted version.

Acknowledgments

We thank Dr. Michael Bassik for providing us with the CRISPR-Cas9 stably expressing cells and the third-generation lentiviral system. Special thanks also go to Dr. Colin Parish and Dr. Iram Surtaj for generously providing CASD1 and SIAE knockout A549 cell lines and HEK 293/PcDNA 3.1 cells.

Conflict of interest

The authors declare that the research was conducted in the absence of any commercial or financial relationships that could be construed as a potential conflict of interest.

Publisher's note

All claims expressed in this article are solely those of the authors and do not necessarily represent those of their affiliated organizations, or those of the publisher, the editors and the reviewers. Any product that may be evaluated in this article, or claim that may be made by its manufacturer, is not guaranteed or endorsed by the publisher.

Supplementary material

The Supplementary Material for this article can be found online at: https://www.frontiersin.org/articles/10.3389/fonc.2023.1145333/full#supplementary-material

References

1. Bukowski K, Kciuk M, Kontek R. Mechanisms of multidrug resistance in cancer chemotherapy. *Int J Mol Sci* (2020) 21. doi: 10.3390/ijms21093233

2. Gottesman MM. Mechanisms of cancer drug resistance. *Annu Rev Med* (2002) 53:615–27. doi: 10.1146/annurev.med.53.082901.103929

3. Wu CP, Calcagno AM, Ambudkar SV. Reversal of ABC drug transporter-mediated multidrug resistance in cancer cells: evaluation of current strategies. *Curr Mol Pharmacol* (2008) 1:93–105. doi: 10.2174/1874467210801020093

4. Vadlapatla RK, Vadlapudi AD, Pal D, Mitra AK. Mechanisms of drug resistance in cancer chemotherapy: coordinated role and regulation of efflux transporters and metabolizing enzymes. *Curr Pharm Des* (2013) 19:7126–40. doi: 10.2174/13816128113199990493

5. Alfarouk KO, Stock CM, Taylor S, Walsh M, Muddathir AK, Verduzco D, et al. Resistance to cancer chemotherapy: failure in drug response from ADME to p-gp. *Cancer Cell Int* (2015) 15:71. doi: 10.1186/s12935-015-0221-1

6. Hall MD, Handley MD, Gottesman MM. Is resistance useless? multidrug resistance and collateral sensitivity. *Trends Pharmacol Sci* (2009) 30:546–56. doi: 10.1016/j.tips.2009.07.003

7. Germann UA, Chambers TC. Molecular analysis of the multidrug transporter, p-glycoprotein. *Cytotechnology* (1998) 27:31–60. doi: 10.1023/A:1008023629269

8. Deeley RG, Cole SP. Substrate recognition and transport by multidrug resistance protein 1 (ABCC1). *FEBS Lett* (2006) 580:1103–11. doi: 10.1016/j.febslet.2005.12.036

9. Mao Q, Unadkat JD. Role of the breast cancer resistance protein (BCRP/ABCG2) in drug transport–an update. *AAPS J* (2015) 17:65–82. doi: 10.1208/s12248-014-9668-6

10. Maliepaard M, Scheffer GL, Faneyte IF, Van Gastelen MA, Pijnenborg AC, Schinkel AH, et al. Subcellular localization and distribution of the breast cancer resistance protein transporter in normal human tissues. *Cancer Res* (2001) 61:3458–64.

11. Huls M, Brown CD, Windass AS, Sayer R, Van Den Heuvel JJ, Heemskerk S, et al. The breast cancer resistance protein transporter ABCG2 is expressed in the human kidney proximal tubule apical membrane. *Kidney Int* (2008) 73:220–5. doi: 10.1038/sj.ki.5002645

12. Pollex E, Lubetsky A, Koren G. The role of placental breast cancer resistance protein in the efflux of glyburide across the human placenta. *Placenta* (2008) 29:743–7. doi: 10.1016/j.placenta.2008.05.001

13. Maliepaard M, Van Gastelen MA, De Jong LA, Pluim D, Van Waardenburg RC, Ruevekamp-Helmers MC, et al. Overexpression of the BCRP/MXR/ABCP gene in a topotecan-selected ovarian tumor cell line. *Cancer Res* (1999) 59:4559–63.

14. Doyle L, Ross DD. Multidrug resistance mediated by the breast cancer resistance protein BCRP (ABCG2). *Oncogene* (2003) 22:7340–58. doi: 10.1038/sj.onc.1206938

15. Gupta A, Zhang Y, Unadkat JD, Mao Q. HIV Protease inhibitors are inhibitors but not substrates of the human breast cancer resistance protein (BCRP/ABCG2). *J Pharmacol Exp Ther* (2004) 310:334–41. doi: 10.1124/jpet.104.065342

16. Houghton PJ, Germain GS, Harwood FC, Schuetz JD, Stewart CF, Buchdunger E, et al. Imatinib mesylate is a potent inhibitor of the ABCG2 (BCRP) transporter and reverses resistance to topotecan and SN-38 *in vitro*. *Cancer Res* (2004) 64:2333–7. doi: 10.1158/0008-5472.CAN-03-3344

17. Ozvegy-Laczka C, Hegedus T, Varady G, Ujhelly O, Schuetz JD, Varadi A, et al. High-affinity interaction of tyrosine kinase inhibitors with the ABCG2 multidrug transporter. *Mol Pharmacol* (2004) 65:1485–95. doi: 10.1124/mol.65.6.1485

18. Shi Z, Peng XX, Kim IW, Shukla S, Si QS, Robey RW, et al. Erlotinib (Tarceva, OSI-774) antagonizes ATP-binding cassette subfamily b member 1 and ATP-binding cassette subfamily G member 2-mediated drug resistance. *Cancer Res* (2007) 67:11012–20. doi: 10.1158/0008-5472.CAN-07-2686

19. Palmeira A, Sousa E, Vasconcelos MH, Pinto MM. Three decades of p-gp inhibitors: skimming through several generations and scaffolds. *Curr Med Chem* (2012) 19:1946–2025. doi: 10.2174/092986712800167392

20. Binkhathlan Z, Lavasanifar A. P-glycoprotein inhibition as a therapeutic approach for overcoming multidrug resistance in cancer: current status and future perspectives. *Curr Cancer Drug Targets* (2013) 13:326–46. doi: 10.2174/15680096113139990076

21. Kathawala RJ, Gupta P, Ashby CRJr., Chen ZS. The modulation of ABC transporter-mediated multidrug resistance in cancer: a review of the past decade. *Drug Resist Update* (2015) 18:1–17. doi: 10.1016/j.drup.2014.11.002

22. Turner JG, Gump JL, Zhang C, Cook JM, Marchion D, Hazlehurst L, et al. ABCG2 expression, function, and promoter methylation in human multiple myeloma. *Blood* (2006) 108:3881–9. doi: 10.1182/blood-2005-10-009084

23. Xie Y, Xu K, Linn DE, Yang X, Guo Z, Shimelis H, et al. The 44-kDa pim-1 kinase phosphorylates BCRP/ABCG2 and thereby promotes its multimerization and drug-resistant activity in human prostate cancer cells. *J Biol Chem* (2008) 283:3349–56. doi: 10.1074/jbc.M707773200

24. Li X, Pan Y-Z, Seigel GM, Hu Z-H, Huang M, Yu A-M. Breast cancer resistance protein BCRP/ABCG2 regulatory microRNAs (hsa-miR-328, -519c and -520h) and their differential expression in stem-like ABCG2+ cancer cells. *Biochem Pharmacol* (2011) 81:783–92. doi: 10.1016/j.bcp.2010.12.018

25. Saison C, Helias V, Ballif BA, Peyrard T, Puy H, Miyazaki T, et al. Null alleles of ABCG2 encoding the breast cancer resistance protein define the new blood group system junior. *Nat Genet* (2012) 44:174–7. doi: 10.1038/ng.1070

26. Ambudkar SV, Kimchi-Sarfaty C, Sauna ZE, Gottesman MM. P-glycoprotein: from genomics to mechanism. *Oncogene* (2003) 22:7468–85. doi: 10.1038/sj.onc.1206948

27. Cole SPC. Targeting multidrug resistance protein 1 (MRP1, ABCC1): past, present, and future. *Annu Rev Pharmacol Toxicol* (2014) 54:95–117. doi: 10.1146/annurev-pharmtox-011613-135959

28. Wojtowicz K, Januchowski R, Nowicki M, Zabel M. Inhibition of protein glycosylation reverses the MDR phenotype of cancer cell lines. *BioMed Pharmacother* (2015) 74:49–56. doi: 10.1016/j.biopha.2015.07.001

29. Nakagawa H, Wakabayashi-Nakao K, Tamura A, Toyoda Y, Koshiba S, Ishikawa T. Disruption of n-linked glycosylation enhances ubiquitin-mediated proteasomal degradation of the human ATP-binding cassette transporter ABCG2. *FEBS J* (2009) 276:7237–52. doi: 10.1111/j.1742-4658.2009.07423.x

30. Greer DA, Ivey S. Distinct n-glycan glycosylation of p-glycoprotein isolated from the human uterine sarcoma cell line MES-SA/Dx5. *Biochim Biophys Acta* (2007) 1770:1275–82. doi: 10.1016/j.bbagen.2007.07.005

31. Wesolowska O, Paprocka M, Kozlak J, Motohashi N, Dus D, Michalak K. Human sarcoma cell lines MES-SA and MES-SA/Dx5 as a model for multidrug resistance modulators screening. *Anticancer Res* (2005) 25:383–9.

32. Nakagawa H, Tamura A, Wakabayashi K, Hoshijima K, Komada M, Yoshida T, et al. Ubiquitin-mediated proteasomal degradation of non-synonymous SNP variants of human ABC transporter ABCG2. *Biochem J* (2008) 411:623–31. doi: 10.1042/BJ20071229

33. Varki NM, Varki A. Diversity in cell surface sialic acid presentations: implications for biology and disease. *Lab Invest* (2007) 87:851–7. doi: 10.1038/labinvest.3700656

34. Varki A, Schauer R. Sialic acids. In: Varki A, Cummings RD, Esko JD, Freeze HH, Stanley P, Bertozzi CR, Hart GW, Etzler ME, editors. *Essentials of glycobiology*. Cold Spring Harbor Press (NY (2009).

35. Grabenstein S, Barnard KN, Anim M, Armoo A, Weichert WS, Bertozzi CR, et al. Deacetylated sialic acids modulates immune mediated cytotoxicity *via* the sialic acid-siglec pathway. *Glycobiology* (2021) 31:1279–94. doi: 10.1093/glycob/cwab068

36. Swindall AF, Bellis SL. Sialylation of the fas death receptor by ST6Gal-I provides protection against fas-mediated apoptosis in colon carcinoma cells. *J Biol Chem* (2011) 286:22982–90. doi: 10.1074/jbc.M110.211375

37. Holdbrooks AT, Britain CM, Bellis SL. ST6Gal-I sialyltransferase promotes tumor necrosis factor (TNF)-mediated cancer cell survival *via* sialylation of the TNF receptor 1 (TNFR1) death receptor. *J Biol Chem* (2018) 293:1610–22. doi: 10.1074/jbc.M117.801480

38. Ma H, Zhou H, Song X, Shi S, Zhang J, Jia L. Modification of sialylation is associated with multidrug resistance in human acute myeloid leukemia. *Oncogene* (2015) 34:726–40. doi: 10.1038/onc.2014.7

39. Pearce OM, Laubli H. Sialic acids in cancer biology and immunity. *Glycobiology* (2016) 26:111–28. doi: 10.1093/glycob/cwv097

40. Barnard KN, Wasik BR, Laclair JR, Buchholz DW, Weichert WS, Alford-Lawrence BK, et al. Expression of 9-o- and 7,9-O-Acetyl modified sialic acid in cells and their effects on influenza viruses. *mBio* (2019) 10. doi: 10.1128/mBio.02490-19

41. Langereis MA, Rabouw HH, Holwerda M, Visser LJ, Van Kuppeveld FJ. Knockout of cGAS and STING rescues virus infection of plasmid DNA-transfected cells. *J Virol* (2015) 89:11169–73. doi: 10.1128/JVI.01781-15

42. Wang T, Larcher LM, Ma L, Veedu RN. Systematic screening of commonly used commercial transfection reagents towards efficient transfection of single-stranded oligonucleotides. *Molecules* (2018) 23. doi: 10.3390/molecules23102564

43. Wang JQ, Teng QX, Lei ZN, Ji N, Cui Q, Fu H, et al. Reversal of cancer multidrug resistance (MDR) mediated by ATP-binding cassette transporter G2 (ABCG2) by AZ-628, a RAF kinase inhibitor. *Front Cell Dev Biol* (2020) 8:601400. doi: 10.3389/fcell.2020.601400

44. Uto T, Tung NH, Appiah-Opong R, Aning A, Morinaga O, Edoh D, et al. Antiproliferative and pro-apoptotic activity of diarylheptanoids isolated from the bark of alnus japonica in human leukemia cell lines. *Am J Chin Med* (2015) 43:757–67. doi: 10.1142/S0192415X15500470

45. Osei-Safo D, Dziwornu GA, Appiah-Opong R, Chama MA, Tuffour I, Waibel R, et al. Constituents of the roots of dichapetalum pallidum and their anti-proliferative activity. *Molecules* (2017) 22. doi: 10.3390/molecules22040532

46. Liu J, Lichtenberg T, Hoadley KA, Poisson LM, Lazar AJ, Cherniack AD, et al. An integrated TCGA pan-cancer clinical data resource to drive high-quality survival outcome analytics. *Cell* (2018) 173:400–416.e11. doi: 10.1016/j.cell.2018.02.052

47. Cerami E, Gao J, Dogrusoz U, Gross BE, Sumer SO, Aksoy BA, et al. The cBio cancer genomics portal: an open platform for exploring multidimensional cancer genomics data. *Cancer Discovery* (2012) 2:401–4. doi: 10.1158/2159-8290.CD-12-0095

48. Gao J, Aksoy BA, Dogrusoz U, Dresdner G, Gross B, Sumer SO, et al. Integrative analysis of complex cancer genomics and clinical profiles using the cBioPortal. *Sci Signal* (2013) 6:p11. doi: 10.1126/scisignal.2004088

49. Therneau TM, Grambsch PM. The cox model. In: Therneau TM, Grambsch PM, editors. *Modeling survival data: extending the cox model*. New York, NY: Springer New York (2000).

50. Mahajan VS, Pillai S. Sialic acids and autoimmune disease. *Immunol Rev* (2016) 269:145–61. doi: 10.1111/imr.12344

51. Zhang C, Chen J, Liu Y, Xu D. Sialic acid metabolism as a potential therapeutic target of atherosclerosis. *Lipids Health Dis* (2019) 18:173. doi: 10.1186/s12944-019-1113-5

52. Baker AN, Richards SJ, Guy CS, Congdon TR, Hasan M, Zwetsloot AJ, et al. The SARS-COV-2 spike protein binds sialic acids and enables rapid detection in a lateral flow point of care diagnostic device. *ACS Cent Sci* (2020) 6:2046–52. doi: 10.1021/acscentsci.0c00855

53. Varki A, Kornfeld S. P-type lectins. In: Varki A, Cummings RD, Esko JD, Stanley P, Hart GW, Aebi M, Darvill AG, Kinoshita T, Packer NH, Prestegard JH, Schnaar RL, Seeberger PH, editors. *Essentials of glycobiology*. Cold Spring Harbor Press (NY (2015).

54. Shen Y, Kohla G, Lrhorfi AL, Sipos B, Kalthoff H, Gerwig GJ, et al. O-Acetylation and de-o-acetylation of sialic acids in human colorectal carcinoma. *Eur J Biochem* (2004) 271:281–90. doi: 10.1046/j.1432-1033.2003.03927.x

55. Pal S, Ghosh S, Mandal C, Kohla G, Brossmer R, Isecke R, et al. Purification and characterization of 9-o-acetylated sialoglycoproteins from leukemic cells and their potential as immunological tool for monitoring childhood acute lymphoblastic leukemia. *Glycobiology* (2004) 14:859–70. doi: 10.1093/glycob/cwh111

56. Parameswaran R, Lim M, Arutyunyan A, Abdel-Azim H, Hurtz C, Lau K, et al. O-Acetylated n-acetylneuraminic acid as a novel target for therapy in human pre-b acute lymphoblastic leukemia. *J Exp Med* (2013) 210:805–19. doi: 10.1084/jem.20121482

57. Baumann AM, Bakkers MJ, Buettner FF, Hartmann M, Grove M, Langereis MA, et al. 9-O-Acetylation of sialic acids is catalysed by CASD1 *via* a covalent acetyl-enzyme intermediate. *Nat Commun* (2015) 6:7673. doi: 10.1038/ncomms8673

58. Mather RL, Loveson KF, Fillmore HL. Human sialic acid O-acetyl esterase (SIAE) - mediated changes in sensitivity to etoposide in a medulloblastoma cell line. *Sci Rep* (2019) 9:8609. doi: 10.1038/s41598-019-44950-5

59. Cornet J, Preira P, Salomé L, Daumas F, Lagane B, Destainville N, et al. Protein overexpression can induce the elongation of cell membrane nanodomains. *Biophys J* (2022). doi: 10.1016/j.bpj.2022.12.009

60. Stacy AE, Jansson PJ, Richardson DR. Molecular pharmacology of ABCG2 and its role in chemoresistance. *Mol Pharmacol* (2013) 84:655–69. doi: 10.1124/mol.113.088609

61. Kim M, Turnquist H, Jackson J, Sgagias M, Yan Y, Gong M, et al. The multidrug resistance transporter ABCG2 (breast cancer resistance protein 1) effluxes hoechst 33342 and is overexpressed in hematopoietic stem cells. *Clin Cancer Res* (2002) 8:22–8.

62. Boland MP, Fitzgerald KA, O'neill LA. Topoisomerase II is required for mitoxantrone to signal nuclear factor kappa b activation in HL60 cells. *J Biol Chem* (2000) 275:25231–8. doi: 10.1074/jbc.275.33.25231

63. Dohse M, Scharenberg C, Shukla S, Robey RW, Volkmann T, Deeken JF, et al. Comparison of ATP-binding cassette transporter interactions with the tyrosine kinase inhibitors imatinib, nilotinib, and dasatinib. *Drug Metab Dispos* (2010) 38:1371–80. doi: 10.1124/dmd.109.031302

64. Nakanishi T, Ross DD. Breast cancer resistance protein (BCRP/ABCG2): its role in multidrug resistance and regulation of its gene expression. *Chin J Cancer* (2012) 31:73–99. doi: 10.5732/cjc.011.10320

65. Kale J, Osterlund EJ, Andrews DW. BCL-2 family proteins: changing partners in the dance towards death. *Cell Death Differ* (2018) 25:65–80. doi: 10.1038/cdd.2017.186

66. Tsujimoto Y. Role of bcl-2 family proteins in apoptosis: apoptosomes or mitochondria? *Genes Cells* (1998) 3:697–707. doi: 10.1046/j.1365-2443.1998.00223.x

67. Chaitanya GV, Steven AJ, Babu PP. PARP-1 cleavage fragments: signatures of cell-death proteases in neurodegeneration. *Cell Commun Signal* (2010) 8:31. doi: 10.1186/1478-811X-8-31

68. Nomura F, Yaguchi M, Togawa A, Miyazaki M, Isobe K, Miyake M, et al. Enhancement of poly-adenosine diphosphate-ribosylation in human hepatocellular carcinoma. *J Gastroenterol Hepatol* (2000) 15:529–35. doi: 10.1046/j.1440-1746.2000.02193.x

69. Ossovskaya V, Koo IC, Kaldjian EP, Alvares C, Sherman BM. Upregulation of poly (ADP-ribose) polymerase-1 (PARP1) in triple-negative breast cancer and other primary human tumor types. *Genes Cancer* (2010) 1:812–21. doi: 10.1177/1947601910383418

70. Furukawa T, Wakabayashi K, Tamura A, Nakagawa H, Morishima Y, Osawa Y, et al. Major SNP (Q141K) variant of human ABC transporter ABCG2 undergoes lysosomal and proteasomal degradations. *Pharm Res* (2009) 26:469–79. doi: 10.1007/s11095-008-9752-7

71. Visser EA, Moons SJ, Timmermans S, De Jong H, Boltje TJ, Büll C. Sialic acid O-acetylation: from biosynthesis to roles in health and disease. *J Biol Chem* (2021) 297:100906. doi: 10.1016/j.jbc.2021.100906

72. Yan Y, Jiang K, Liu P, Zhang X, Dong X, Gao J, et al. Bafilomycin A1 induces caspase-independent cell death in hepatocellular carcinoma cells *via* targeting of autophagy and MAPK pathways. *Sci Rep* (2016) 6:37052. doi: 10.1038/srep37052

73. Wang S, Liu F, Zeng Z, Yang H, Jiang H. The protective effect of bafilomycin A1 against cobalt nanoparticle-induced cytotoxicity and aseptic inflammation in macrophages *In vitro*. *Biol Trace Elem Res* (2016) 169:94–105. doi: 10.1007/s12011-015-0381-9

frontiers | Frontiers in Medicine

TYPE Original Research
PUBLISHED 28 June 2023
DOI 10.3389/fmed.2023.1177665

Check for updates

OPEN ACCESS

EDITED BY
Emmanuel Twumasi Osei,
University of British Columbia, Okanagan Campus, Canada

REVIEWED BY
Isabella Cavalieri,
Chapman University, United States
Maria Gabriella Verso,
University of Palermo, Italy

*CORRESPONDENCE
Hong Wei Chu
✉ chuh@njhealth.org
Brian J. Day
✉ dayb@njhealth.org

RECEIVED 01 March 2023
ACCEPTED 12 June 2023
PUBLISHED 28 June 2023

CITATION
Cervantes D, Schaunaman N, Downey GP, Chu HW and Day BJ (2023) Desert particulate matter from Afghanistan increases airway obstruction in human distal lungs exposed to type 2 cytokine IL-13.
Front. Med. 10:1177665.
doi: 10.3389/fmed.2023.1177665

COPYRIGHT
© 2023 Cervantes, Schaunaman, Downey, Chu and Day. This is an open-access article distributed under the terms of the Creative Commons Attribution License (CC BY). The use, distribution or reproduction in other forums is permitted, provided the original author(s) and the copyright owner(s) are credited and that the original publication in this journal is cited, in accordance with accepted academic practice. No use, distribution or reproduction is permitted which does not comply with these terms.

Desert particulate matter from Afghanistan increases airway obstruction in human distal lungs exposed to type 2 cytokine IL-13

Diana Cervantes, Niccolette Schaunaman, Gregory P. Downey, Hong Wei Chu* and Brian J. Day*

Department of Medicine, National Jewish Health, Denver, CO, United States

Introduction: Deployment related asthma-like symptoms including distal airway obstruction have been described in U.S. military personnel who served in Iraq and Afghanistan. The mechanisms responsible for the development of distal airway obstruction in deployers exposed to desert particulate matter (PM) is not well understood. We sought to determine if respiratory exposure to PM from Afghanistan (PMa) increases human distal airway hyperresponsiveness (AHR) with or without exposures to IL-13, a type 2 cytokine. We further tested whether mitochondrial dysfunction, such as ATP signaling and oxidative stress, may contribute to PMa- mediated AHR.

Methods: Precision-cut lung slices from donors without a history of lung disease, tobacco smoking, or vaping were pre-treated with IL-13 for 24 h. This was followed by exposure to PMa or PM from California (PMc, control for PMa) for up to 72 h. The role of hydrogen peroxide and ATP in AHR was assessed using the antioxidant enzyme catalase or an ATP receptor P2Y13 antagonist MRS2211. AHR in response to methacholine challenges as well as cytokine IL-8 production were measured.

Results: PMa alone, but not PMc alone, trended to increase AHR. Importantly, the combination of PMa and IL-13 significantly amplified AHR compared to control or PMc+IL-13. PMa alone and in combination with IL-13 increased IL-8 as compared to the control. PMa increased H2O2 and ATP. MRS211 and catalase reduced AHR in PCLS exposed to both PMa and IL-13.

Discussion: Our data suggests that PMa in a type 2 inflammation-high lung increased AHR in part through oxidative stress and ATP signaling.

KEYWORDS

particulate matter, human lung, IL-13, airway hyperresponsiveness, oxidative stress

Introduction

Nearly three million U.S. military personnel have served in Afghanistan and Iraq since 2001, of whom 14% reported deployment related asthma-like symptoms (1, 2). Environmental hazards from areas of deployment, such as sandstorms, burn bits, and combat dust, are linked to respiratory complications post deployment (2). Common respiratory reported include exertional dyspnea, cough, chest tightness, and wheezing (3). PM from each of these areas has a unique composition since there is variable exposure to diesel byproducts, metals, and other toxins (4). Regardless, parts of their surface composition, such as LPS, can act as Toll-like receptor ligands, which initiate an inflammatory response (5). Since PM is often coated with metals, PM exposures may lead

to production of reactive oxygen species (ROS) and subsequent mitochondrial dysfunction (5, 6). The mitochondria are important for many normal cellular functions and are responsible for biosynthetic reactions such as ATP synthesis via the electron transport chain, ion homeostasis, and particularly Ca^{2+} regulation (7, 8). Loss of this homeostasis, often initiated by upstream stimuli like inflammation, ultimately leads to mitochondrial damage and induces a stress response (9). Mitochondrial dysfunction originating from mitochondrial damage or stress is associated with disease pathobiology such as asthma and chronic obstructive pulmonary disease (COPD) (10). Mitochondrial function can be altered by mitochondrial damage and oxidative stress induced by an increase in ROS production that include superoxide and hydrogen peroxide. Inflammation and ROS production can alter normal mitochondrial function. This initiates the release of mitochondrial DNA (mtDNA) and ATP, which serve as damage associated molecular patterns (DAMPS) (10). These DAMPS are released into the cytosol or extracellularly and can activate intracellular signaling cascades (10). An abnormal increase in ATP production can lead to a Ca^{2+} flux, activation of the inflammasome, further mtDNA release, increased ROS, and ongoing mitochondrial dysfunction (6, 8, 10). PM exposure diminishes the epithelial cell integrity which can activate Toll-like receptor signaling and induce oxidative stress and other downstream effects such as the release of pro-inflammatory cytokines (6, 8, 9, 11, 12).

A key feature of allergic asthma is airway hyperresponsiveness, which is characterized as narrowing of the airway lumen (13). The type 2 cytokine IL-13 plays a direct role in the recruitment of eosinophils during allergic inflammation, as well as in epithelial remodeling (14, 15). Manson et al. (13) showed that IL-13 induces airway hyperresponsiveness, which may be associated with increased ROS production and therefore leading to ER stress and an increase in Ca^{2+} flux levels in airway smooth muscle (16).

In the current study, given the role of PM or IL-13 in airway inflammation and AHR, we hypothesized that exposure to PMa alone and particularly in combination with IL-13 worsens distal airway obstruction in part through ROS and ATP signaling. We utilized human precision-cut lung slices (PCLS) as a highly physiologically relevant model to test our hypothesis.

Methods

Processing of human lungs for PLCS, and measurement of AHR

The upper lobes of the right lung from healthy non-smoking donors with no history of lung disease were obtained from the International Institute for the Advancement of Medicine (Philadelphia, PA, United States) or the Donor Alliance of Colorado (Denver, CO, United States). All the donor lungs were selected based on the non-smoking status and no history of lung disease/infection. The causes of death of the donors are related to car accidents, head trauma/brain bleeds, stroke or complications with heart conditions. The detailed donor demographic information is given in Table 1. The Institutional Review Board (IRB) at National Jewish Health approved our studies as meeting requirements of exempt human subject research.

TABLE 1 Demographics of human lung donors n=5.

Subject	Age	Gender	Smoking status
1	30	Male	Non-smoker
2	27	Female	Non-smoker
3	20	Male	Non-smoker
4	75	Male	Former light smoker, quit 50 years ago
5	55	Male	Non-smoker

Human lungs were inflated with 1.5% low melting agarose (RPI, Mt. Prospect, IL) and cooled on ice. The tissue was cored and sliced using a Precisionary vibrating microtome at 300 µm thickness. The PCLS were incubated at 37°C in 24-well culture plates filled with 500 µL of DMEM containing penicillin/streptomycin, amphotericin B and fluconazole media with the addition of 0.2 M glutathione. Twenty-four hours after slicing, PCLS were pretreated with IL-13 (25 ng/mL). We chose IL-13 at 25 ng/mL because optimization on human PCLS showed greatest eotaxin 2 levels after 72 h. Previous studies have used IL-13 at 25 ng/mL in PCLS and IL-13 was able to induce AHR even after 5 days in culture (17). After 24 h of IL-13 treatment, PCLS were treated with particulate matter from Afghanistan (PMa) (95 ng/well) or particulate matter from California (PMc) (95 ng/well) in the presence or absence of an ATP receptor antagonist MRS2211 (1 µM) or catalase (500 U/mL), and IL-13 treatment was refreshed. We chose 95 µg/well because optimization done previously (11) showed that human airway epithelial cells exposed to PMa at 50 µg/cm^2 had significantly higher IL-8 production with the least amount of cell death. Briefly, 50 µg/cm^2 × 1.9 cm^2 (area of 24 well plate) = 95ug/well. Notably, the 50 µg/cm^2 is well in line with previous PM toxicity studies and a more physiologically relevant dose for *in vitro* modeling of PM exposures of deployed soldiers (11). The PCLS supernatants were collected for ATP, H_2O_2, and IL-8 measurement 72 h post treatment. To measure AHR, baseline pictures of the airways were taken followed by adding 1, 10, 100, and 1,000 µM of methacholine (Mch) 30 s apart. Images of small airways (diameter < 2 µm) were taken between doses. The area (relative pixel number) within the lumen was traced using the image J freehand tool for all images, and the percent airway constriction was calculated as (1 - post Mch area/baseline area) × 100. The number of airways measured for AHR was between 3 and 9 per condition for every lung subject.

Characterization of PMa and PMc

For PMa, Topsoil from Bagram Air Force Base in Parwan Province of Afghanistan was collected in August 2009 and characterized by the United States Geological Survey in Lakewood, Colorado. Collection and analysis were described previously by our group (11). The bulk topsoil was processed using a dry powder generator (Wright Dust Feeder, CH Technologies, Westwood, New Jersey) to produce respirable size of PM. Samples were analyzed via mass spectroscopy and scanning electron microscope for mineral composition as well as particle size and shape. Samples were found to contain calcite, dolomite, clay, kaolinite, illite, chlorite, muscovite, talc, biotite, feldspar, quartz, oxides, zircon, titanite, synchysite and monazite. The

size of the PMa included 89.46% particles less than 2.5 μm, 10.4% between 2.5 μm and 10 μm, and 0.17% were greater than 10 μm.

For PMc, the topsoil (sand) from the area of China Lake, California was collected and aerosolized at NAMRU Dayton at the Wright Patterson air force base. Particles were run through a particle sizer and the resulting particles had a mean diameter of 1.91 μm. The settled particles were collected from the pan and then sterilized using gamma irradiation. Chemical analysis showed that PMc had similar crustal abundance levels to PMa.

Measurement of ATP

An ATP colorimetric/Fluorometric assay kit (Sigma-Aldrich, St. Louis, MO) was used to quantify ATP levels in supernatants of human PCLS. The Promega GloMax explorer was used to measure the fluorescence intensity at 587 nm for 4 intervals every 30 min.

Measurement of H_2O_2

The Invitrogen Amplex red hydrogen peroxide/peroxidase assay kit was used to quantify H_2O_2 levels in human PCLS supernatants. Samples were incubated at room temperature for 30 min in the dark, and fluorescence was measured using the Biotek microplate reader for a detection at 590 nm.

Enzyme-linked immunosorbent assay

IL-8 levels were measured in PCLS supernatants using a Human IL-8 DuoSet ELISA kit (R&D Systems, Minneapolis, MN, United States) according to the manufacturer's instructions.

Statistical analysis

Parametric data were analyzed using paired *t*-tests for two group comparisons or one-way ANOVA analysis with Holm-Sidak's *post hoc* test for multiple comparisons. Non-parametric data were analyzed using the Mann–Whitney test for two group comparisons. A p value < 0.05 was considered statistically significant.

Results

PMa enhanced airway hyperresponsiveness in IL-13-exposed human precision-cut lung slices

Lung slices treated with PMa alone, as compared to the untreated ones, increased airway constriction in response to the methacholine challenge compared to the control. IL-13 alone trended to increase AHR but did not reach the level of statistical significance ($p = 0.12$). In the presence of both PMa and IL-13, AHR was further significantly increased (Figure 1). To test if PMa may have greater ability to induce AHR as compared to other PM, PMc was used as a control PM for PMa. Unlike PMa, PMc alone did not increase AHR. In the presence of IL-13, PMc was unable to significantly increase AHR ($p = 0.26$). Additionally, AHR in PMc-treated lung slices was significantly less than that in PMa-treated lung slices in the presence of IL-13 (Figure 1).

Role of ATP signaling in AHR induced by PMa and IL-13

Extracellular ATP has been shown to contribute to airway inflammation and AHR in animal models of asthma (18, 19). In addition, previous studies have demonstrated that PM exposure results in mitochondrial dysfunction, such as mitochondrial damage, leading to less intracellular ATP, but more release of ATP into the extracellular space (20). Extracellular ATP binds to its receptors, such as P2Y13, to induce various biological effects (21).

To determine if increased AHR by exposure to PMa and IL-13 may depends on ATP signaling, we used MRS2211, a highly selective antagonist of P2Y13 receptor, in lung slices. As shown in Figure 2A, MRS2211 significantly reduced AHR in slices treated with both PMa and IL-13. MRS2211 also reduced AHR in PMa-treated lung slices (data not shown).

Extracellular ATP was measured to examine the effect of PM and/or IL-13 on ATP release after 72 h of treatment. PMa alone and in combination with IL-13 trended to increase ATP (Figure 2B).

Role of reactive oxygen species in AHR induced by PMa and IL-13 in human-precision cut lung slices

Oxidative stress, due to increased production of reactive oxygen species (e.g., H_2O_2), has been shown to contribute to mitochondrial dysfunction and ATP release induced by other sources of PM (22, 23). We measured H_2O_2 levels in supernatants of lung slices treated with PMa for 72 h in the absence or presence of catalase, an enzyme that converts H_2O_2 into water and oxygen. As shown in Figure 3A, H_2O_2 levels were higher following PMa treatments as compared to non-treated slices, which were not further increased by addition of IL-13. Nonetheless, H_2O_2 levels in lung slices treated with both PMa and IL-13 were still significantly higher than those in untreated lung slices ($p = 0.025$) (Figure 3). Catalase effectively in blocked H_2O_2 production induced by PMa alone or in combination of both PMa and IL-13. Catalase also reduced AHR induced by PMa in combination with IL-13 (Figure 3B).

PMa and IL-13 increased IL-8 production in human-precision cut lung slices

IL-8 is a chemokine for neutrophils that are associated with neutrophilic inflammation in lungs exposed to PM (24, 25). Interestingly, in cultured airway smooth muscle cells, IL-8 was shown to directly induce smooth muscle cell contraction (26), a key contributor to AHR. Here, we found that PMa alone, but not IL-13 alone, significantly increased the levels of IL-8 protein in the supernatants of lung slices (Figure 4). Although the combination of both PMa and IL-13 did not further increase IL-8 production, the

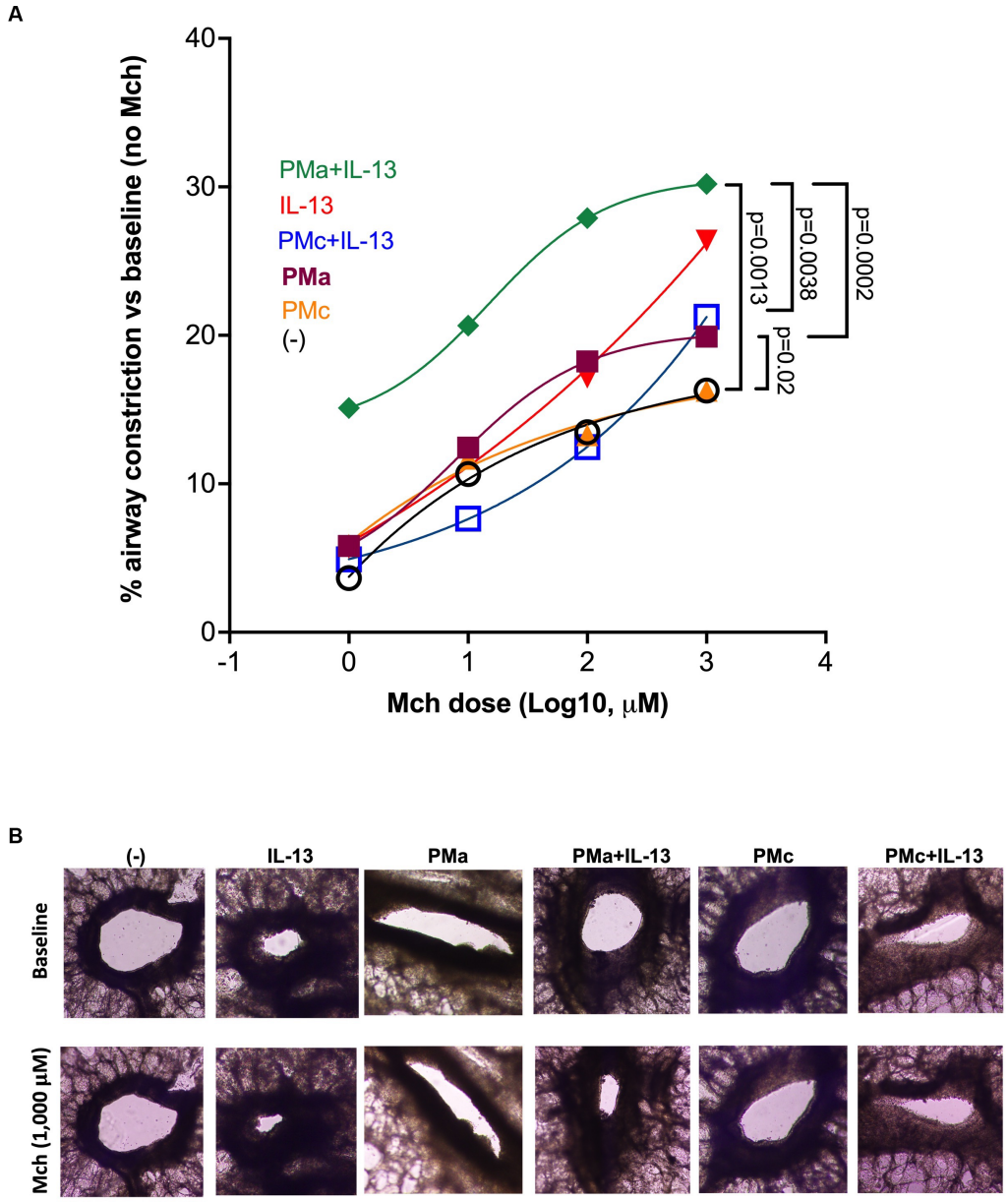

FIGURE 1
PMa increases airway constriction in human precision-cut lung slices exposed to IL-13. **(A)** After 72h, PMa treated PCLS showed an increase in airway constriction and that was significantly increased with the addition of IL-13. Data is represented as a mean from 5 donors. PMa, PM from Afghanistan; PMc, PM from California. **(B)** Representative images from human precision-cut lung slices showing small airway constriction following methacholine (Mch) challenges under different treatment conditions. The images were taken under a phase contrast microscope at x10 magnification.

levels of IL-8 in the combination group was still higher than those in the control group.

Discussion

This study for the first time demonstrates that PMa exaggerated airway constriction in human distal lungs with high type 2 inflammation. Mechanistically, oxidative stress and mitochondrial dysfunction, such as ATP release and signaling, may contribute to worsened airway obstruction induced by both PMa and IL-13 exposures. Our improved understanding of PM-mediated airway obstruction may provide new insights into mechanisms of deployment-related respiratory disease and potential therapeutic approaches.

Various cell culture and animal models have been used to study the effect of PM on lung function. Previous studies in animals have shown that PM increases AHR in the absence or presence of allergen challenges (27, 28). However, there is a lack of direct evidence indicating that PM and in particular PMa, have an effect on airway obstruction in human lungs. Distal airways are the major site of pathology in deployment-related respiratory disease (3, 29). However, cell culture and mouse models do not fully represent the microenvironment in human distal lungs or cannot reflect the

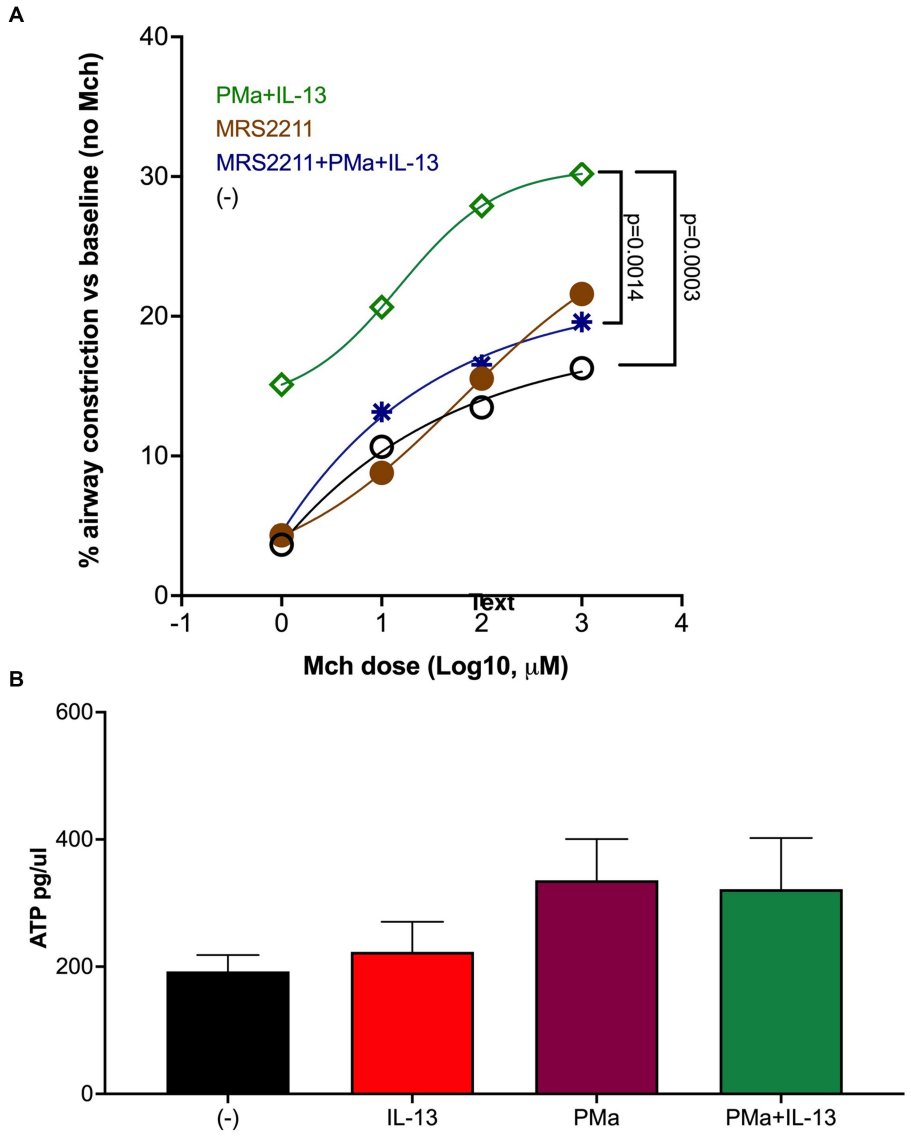

FIGURE 2
Blockade of ATP receptor P2Y13 signaling in human precision-cut lung slices reduces airway constriction. **(A)** MRS2211, a highly selective P2Y13 antagonist, significantly reduced AHR in the PCLS exposed to both PMa and IL-13. Data is presented as a mean from *n*=5 donors. **(B)** ATP levels in supernatants of human PCLS. Data collected from 4 donors.

complexity of human physiological responses. The human lung PCLS model offers several major advantages over other models including intact tissue/organ architecture and native microenvironments (30–33). By using this unique PCLS model, we found that PMa alone significantly increased AHR that is consistent with previous animal studies on the health effects of PM (27, 34). Notably, when PMa was combined with IL-13, PMa further increased AHR. Our findings suggest an exacerbating effect of PMa on airway obstruction in the lungs with a type 2 cytokine-high background. Interestingly, we did not observe the exacerbating effect on AHR of PMc. PM can vary greatly in composition depending on many factors. PMa has a unique composition since it can be coated in burn pit combustion products and diesel exhaust particles, amongst other metals from explosive devises (5, 35). On the other hand, common PM's composition is often associated with traffic-related air pollution (6). Whether the differences in composition of PMa and PMc contribute to the difference AHR response warrants future studies.

How PMa or PMa in combination with IL-13 increases AHR remains unclear. In the current study, we investigated two related mechanisms. First, we focused on ATP signaling as one of the potential mechanisms associated with mitochondrial dysfunction. We found that PMa increased extracellular ATP. While we saw an increase in extracellular ATP, this increase was not significant, which may be due to the short life of ATP being degraded at the time we measured the AHR. ATP release during tissue injury and inflammation is critical to the pathophysiology in asthma including AHR, neutrophilic inflammation, and Th17 response (19, 36). The blockade of ATP-releasing channels by ^{10}Panx peptide has been shown to prevent increased extracellular ATP levels and AHR in an OVA-induced

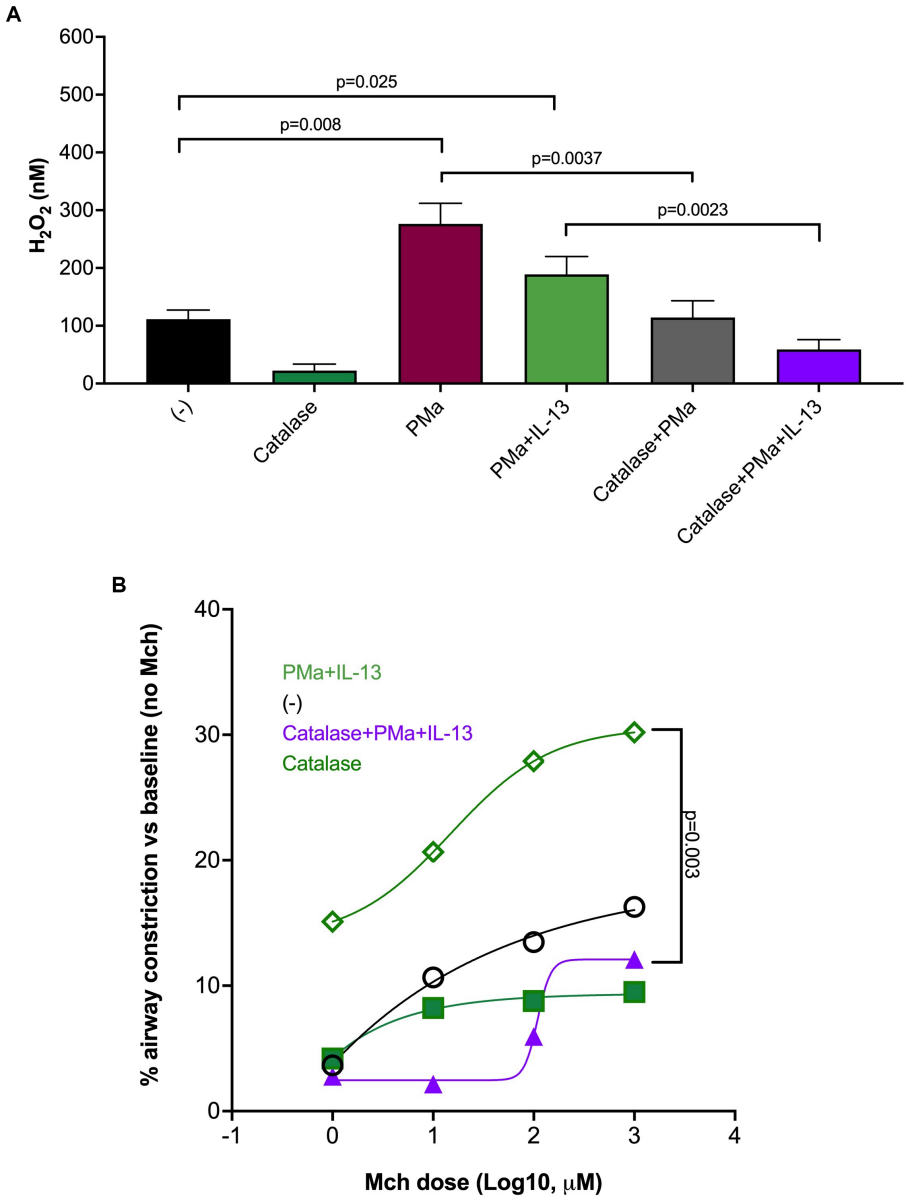

FIGURE 3
Catalase reduces airway constriction in human precision-cut lung slices exposed to IL-13 and PMa for 72h. **(A)** PMa significantly increased H_2O_2 levels that were reduced by catalase. **(B)** Catalase significantly reduced airway constriction in the combination group (PMa+IL-13). Data is represented as mean from 3 donors (n=10 replicates).

allergic asthma mouse model (37). We found that inhibition of ATP by a P2Y3 receptor antagonist MRS2211 reduced AHR in human PCLS exposed to both PMa and IL-13. Our data reveals that AHR induced by PMa and IL-13 may in part be dependent on ATP signaling. Second, we examined the role of ROS in AHR. ROS generation may be responsible for PM-mediated mitochondrial dysfunction (23). Frossi et al. (22) found that oxidative stress can upregulate type 2 inflammation contributing to AHR. We found that PMa increased H_2O_2 release. By using catalase to reduce H_2O_2 levels in human PCLS, we observed inhibition of oxidative stress reduced H_2O_2 levels and AHR in lung slices exposed to PMa and IL-13. Together our data suggest that mitochondrial dysfunction may be one of the mechanisms responsible for increased AHR by PMa and IL-13.

One limitation of this study is that we did not measure mitochondrial activity after PM exposure. Additionally, although we measured airway constriction in PM-exposed PCLS, we did not measure protein markers that may contribute to AHR. These proteins will be considered in our future experiments to improve our understanding of mechanisms by which PMa and IL-13 amplify AHR. We realize the sample size limitation in our study as there were 5 donors included. Nonetheless, all the donor demonstrated similar AHR responses following PMa and IL-13 treatment. Future studies using a larger group of healthy donors are warranted to extend our current study.

Overall, our findings offer novel mechanisms of distal airway obstruction in veterans that were previously deployed in Southeast

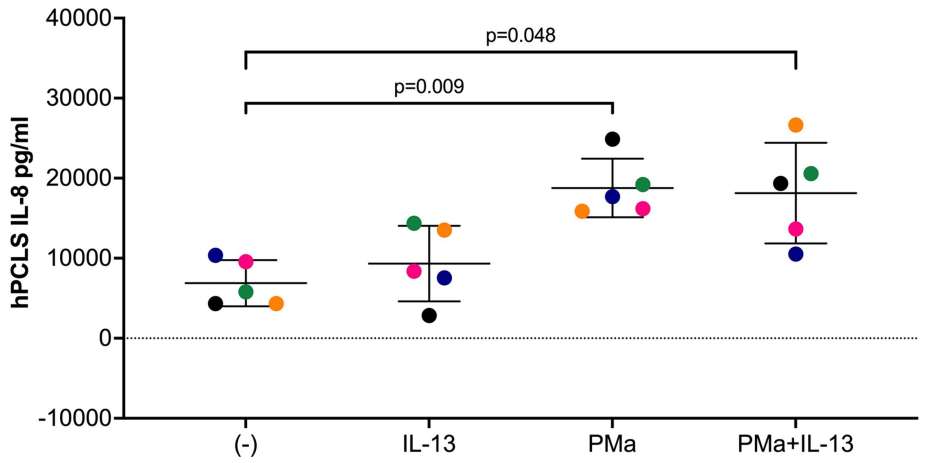

FIGURE 4
IL-8 levels in supernatants of human precision-cut lung slices exposed to IL-13 and/or PMa for 72h. Data is represented as mean±SEM from 5 donors. PMa, PM from Afghanistan; PMc, PM from California.

Asia, and potential new therapies such as the use of antioxidants and ATP receptor antagonists to reduce the disease severity in deployers.

Data availability statement

The original contributions presented in the study are included in the article/supplementary material, further inquiries can be directed to the corresponding authors.

Ethics statement

The studies involving human participants were reviewed and approved by The Institutional Review Board (IRB) at National Jewish Health. Written informed consent for participation was not required for this study in accordance with the national legislation and the institutional requirements.

Author contributions

DC, BD, and HC: conceptualization and investigation. DC, NS, and BD: methodology. DC and NS: validation. DC, NS, HC, and BD: formal analysis. HC, BD, and GD: resources and funding acquisition. DC and HC: data curation and writing—original draft preparation. DC, NS, GD, BD, and HC: writing—review and editing. DC, BD, GD, and HC: visualization. NS and HC: supervision. BD and HC: project administration. All authors contributed to the article and approved the submitted version.

Funding

This work was funded by the Department of Defense (W81WH-16-2-0018).

Acknowledgments

The authors thank Jie Huang, Department of Medicine, National Jewish Health, for her technical assistance in the human precision-cut lung slice experiments, and Heather Lowers and Geoff Plumlee at the United States Geological Survey in Lakewood, Colorado for their efforts in characterizing and analyzing our PM samples.

Conflict of interest

The authors declare that the research was conducted in the absence of any commercial or financial relationships that could be construed as a potential conflict of interest.

Publisher's note

All claims expressed in this article are solely those of the authors and do not necessarily represent those of their affiliated organizations, or those of the publisher, the editors and the reviewers. Any product that may be evaluated in this article, or claim that may be made by its manufacturer, is not guaranteed or endorsed by the publisher.

References

1. Berman R, Min E, Huang J, Kopf K, Downey GP, Riemondy K, et al. Single-cell RNA sequencing reveals a unique monocyte population in Bronchoalveolar lavage cells of mice challenged with Afghanistan particulate matter and allergen. *Toxicol Sci*. (2021) 182:297–309. doi: 10.1093/toxsci/kfab065

2. Rose CS, Moore CM, Zell-Baran LM, Krefft S, Wolff J, Pang K, et al. Small airways and airspace inflammation and injury distinguish lung histopathology in deployed military personnel from healthy and diseased lungs. *Hum Pathol*. (2022) 124:56–66. doi: 10.1016/j.humpath.2022.02.014

3. Garshick E, Abraham JH, Baird CP, Ciminera P, Downey GP, Falvo MJ, et al. Respiratory health after military Service in Southwest Asia and Afghanistan. An official American Thoracic Society workshop report. *Ann Am Thorac Soc*. (2019) 16:e1–e16. doi: 10.1513/AnnalsATS.201904-344WS

4. Engelbrecht JP, McDonald EV, Gillies JA, Jayanty RK, Casuccio G, Gertler AW. Characterizing mineral dusts and other aerosols from the Middle East—part 2: grab samples and re-suspensions. *Inhal Toxicol*. (2009) 21:327–36. doi: 10.1080/08958370802464299

5. Berman R, Rose CS, Downey GP, Day BJ, Chu HW. Role of particulate matter from Afghanistan and Iraq in deployment-related lung disease. *Chem Res Toxicol*. (2021) 34:2408–23. doi: 10.1021/acs.chemrestox.1c00090

6. Tiotiu AI, Novakova P, Nedeva D, Chong-Neto HJ, Novakova S, Steiropoulos P, et al. Impact of air pollution on asthma outcomes. *Int J Environ Res Public Health*. (2020) 17:6212. doi: 10.3390/ijerph17176212

7. Guo C, Sun L, Chen X, Zhang D. Oxidative stress, mitochondrial damage and neurodegenerative diseases. *Neural Regen Res*. (2013) 8:2003–14. doi: 10.3969/j.issn.1673-5374.2013.21.009

8. Qian L, Mehrabi Nasab E, Athari SM, Athari SS. Mitochondria signaling pathways in allergic asthma. *J Investig Med*. (2022) 70:863–82. doi: 10.1136/jim-2021-002098

9. Zhou WC, Qu J, Xie SY, Sun Y, Yao HW. Mitochondrial dysfunction in chronic respiratory diseases: implications for the pathogenesis and potential therapeutics. *Oxidative Med Cell Longev*. (2021) 2021:1–20. doi: 10.1155/2021/5188306

10. Prakash YS, Pabelick CM, Sieck GC. Mitochondrial dysfunction in airway disease. *Chest*. (2017) 152:618–26. doi: 10.1016/j.chest.2017.03.020

11. Berman R, Downey GP, Dakhama A, Day BJ, Chu HW. Afghanistan particulate matter enhances pro-inflammatory responses in IL-13-exposed human airway epithelium via TLR2 signaling. *Toxicol Sci*. (2018) 166:345–53. doi: 10.1093/toxsci/kfy217

12. Profita M, Albano GD, Montalbano AM, Di Sano C, Anzalone G, Gagliardo R, et al. Acetylcholine leads to signal transducer and activator of transcription 1 (STAT-1) mediated oxidative/nitrosative stress in human bronchial epithelial cell line. *Biochim Biophys Acta*. (2013) 1832:1949–58. doi: 10.1016/j.bbadis.2013.06.009

13. Manson ML, Säfholm J, James A, Johnsson AK, Bergman P, Al-Ameri M, et al. IL-13 and IL-4, but not IL-5 nor IL-17A, induce hyperresponsiveness in isolated human small airways. *J Allergy Clin Immunol*. (2020) 145:808–17.e2. doi: 10.1016/j.jaci.2019.10.037

14. Gebski EB, Anaspure O, Panettieri RA, Koziol-White CJ. Airway smooth muscle and airway hyperresponsiveness in asthma: mechanisms of airway smooth muscle dysfunction. *Minerva Med*. (2022) 113:4–16. doi: 10.23736/S0026-4806.21.07283-9

15. Kumar RK, Herbert C, Yang M, Koskinen AM, McKenzie AN, Foster PS. Role of interleukin-13 in eosinophil accumulation and airway remodelling in a mouse model of chronic asthma. *Clin Exp Allergy*. (2002) 32:1104–11. doi: 10.1046/j.1365-2222.2002.01420.x

16. Delmotte P, Sieck GC. Interaction between endoplasmic/sarcoplasmic reticulum stress (ER/SR stress), mitochondrial signaling and ca (2+) regulation in airway smooth muscle (ASM). *Can J Physiol Pharmacol*. (2015) 93:97–110. doi: 10.1139/cjpp-2014-0361

17. Li G, Cohen JA, Martines C, Ram-Mohan S, Brain JD, Krishnan R, et al. Preserving airway smooth muscle contraction in precision-cut lung slices. *Sci Rep*. (2020) 10:6480. doi: 10.1038/s41598-020-63225-y

18. Huang YA, Chen JC, Wu CC, Hsu CW, Ko AM, Chen LC, et al. Reducing lung ATP levels and alleviating asthmatic airway inflammation through adeno-associated viral vector-mediated CD39 expression. *Biomedicine*. (2021) 9:656. doi: 10.3390/biomedicines9060656

19. Zhang F, Su X, Huang G, Xin XF, Cao EH, Shi Y, et al. Adenosine triphosphate promotes allergen-induced airway inflammation and Th17 cell polarization in neutrophilic asthma. *J Immunol Res*. (2017) 2017:1–10. doi: 10.1155/2017/5358647

20. Zeng X, Liu D, Wu W, Huo X. PM. *Environ Sci Pollut Res Int* (2022);29:24445–24456, PM2.5 exposure inducing ATP alteration links with NLRP3 inflammasome activation. doi: 10.1007/s11356-021-16405-w

21. Feng C, Mery AG, Beller EM, Favot C, Boyce JA. Adenine nucleotides inhibit cytokine generation by human mast cells through a Gs-coupled receptor. *J Immunol*. (2004) 173:7539–47. doi: 10.4049/jimmunol.173.12.7539

22. Frossi B, De Carli M, Piemonte M, Pucillo C. Oxidative microenvironment exerts an opposite regulatory effect on cytokine production by Th1 and Th2 cells. *Mol Immunol*. (2008) 45:58–64. doi: 10.1016/j.molimm.2007.05.008

23. Lavrich KS, Corteselli EM, Wages PA, Bromberg PA, Simmons SO, Gibbs-Flournoy EA, et al. Investigating mitochondrial dysfunction in human lung cells exposed to redox-active PM components. *Toxicol Appl Pharmacol*. (2018) 342:99–107. doi: 10.1016/j.taap.2018.01.024

24. Kurai J, Onuma K, Sano H, Okada F, Watanabe M. Ozone augments interleukin-8 production induced by ambient particulate matter. *Genes Environ*. (2018) 40:14. doi: 10.1186/s41021-018-0102-7

25. Valderrama A, Ortiz-Hernández P, Agraz-Cibrián JM, Tabares-Guevara JH, Gómez DM, Zambrano-Zaragoza JF, et al. Particulate matter (PM). *Sci Rep*. (2022) 12:7581. doi: 10.1038/s41598-022-11553-6

26. Govindaraju V, Michoud MC, Ferraro P, Arkinson J, Safka K, Valderrama-Carvajal H, et al. The effects of interleukin-8 on airway smooth muscle contraction in cystic fibrosis. *Respir Res*. (2008) 9:76. doi: 10.1186/1465-9921-9-76

27. Pang L, Zou S, Shi Y, Mao Q, Chen Y. Apigenin attenuates PM2.5-induced airway hyperresponsiveness and inflammation by down-regulating NF-κB in murine model of asthma. *Int J Clin Exp Pathol*. (2019) 12:3700–9.

28. Zhao Y, Zhang H, Yang X, Zhang Y, Feng S, Yan X. Fine particulate matter (PM). *Environ Toxicol Pharmacol*. (2019) 68:155–63. doi: 10.1016/j.etap.2019.03.013

29. Gupta A, Sasse SK, Berman R, Gruca MA, Dowell RD, Chu HW, et al. Integrated genomics approaches identify transcriptional mediators and epigenetic responses to afghan desert particulate matter in small airway epithelial cells. *Physiol Genomics*. (2022) 54:389–401. doi: 10.1152/physiolgenomics.00063.2022

30. Agraval H, Chu HW. Lung organoids in smoking research: current advances and future promises. *Biomol Ther*. (2022) 12:1463. doi: 10.3390/biom12101463

31. Alsafadi HN, Uhl FE, Pineda RH, Bailey KE, Rojas M, Wagner DE, et al. Applications and approaches for three-dimensional precision-cut lung slices. Disease modeling and drug discovery. *Am J Respir Cell Mol Biol*. (2020) 62:681–91. doi: 10.1165/rcmb.2019-0276TR

32. Bailey KE, Pino C, Lennon ML, Lyons A, Jacot JG, Lammers SR, et al. Embedding of precision-cut lung slices in engineered hydrogel biomaterials supports extended. *Am J Respir Cell Mol Biol*. (2020) 62:14–22. doi: 10.1165/rcmb.2019-0232MA

33. Majorova D, Atkins E, Martineau H, Vokral I, Oosterhuis D, Olinga P, et al. Use of precision-cut tissue slices as a translational model to study host-pathogen interaction. *Front Vet Sci*. (2021) 8:686088. doi: 10.3389/fvets.2021.686088

34. Xu M, Zhang Y, Wang M, Zhang H, Chen Y, Adcock IM, et al. TRPV1 and TRPA1 in lung inflammation and airway Hyperresponsiveness induced by fine particulate matter (PM). *Oxidative Med Cell Longev*. (2019) 2019:1–15. doi: 10.1155/2019/7450151

35. Olsen T, Caruana D, Cheslack-Postava K, Szema A, Thieme J, Kiss A, et al. Iraq/Afghanistan war lung injury reflects burn pits exposure. *Sci Rep*. (2022) 12:14671. doi: 10.1038/s41598-022-18252-2

36. Oguma T, Ito S, Kondo M, Makino Y, Shimokata K, Honjo H, et al. Roles of P2X receptors and Ca2+ sensitization in extracellular adenosine triphosphate-induced hyperresponsiveness in airway smooth muscle. *Clin Exp Allergy*. (2007) 37:893–900. doi: 10.1111/j.1365-2222.2007.02719.x

37. Arzola-Martínez L, Benavente R, Vega G, Ríos M, Fonseca W, Rasky AJ, et al. Blocking ATP-releasing channels prevents high extracellular ATP levels and airway hyperreactivity in an asthmatic mouse model. *Am J Physiol Lung Cell Mol Physiol*. (2021) 321:L466–76. doi: 10.1152/ajplung.00450.2020

frontiers | Frontiers in Medicine

TYPE Original Research
PUBLISHED 26 July 2023
DOI 10.3389/fmed.2023.1172622

Check for updates

OPEN ACCESS

EDITED BY
Koji Sakamoto,
Nagoya University, Japan

REVIEWED BY
Shotaro Okachi,
Nagoya University, Japan
Wen-Chun Liu,
Academia Sinica, Taiwan

*CORRESPONDENCE
Simon D. Pouwels
✉ s.d.pouwels@umcg.nl

RECEIVED 23 February 2023
ACCEPTED 14 July 2023
PUBLISHED 26 July 2023

CITATION
Gupta A, Burgess JK, Slebos D-J and Pouwels SD (2023) The development, validation, and *in vivo* testing of a high-precision bronchial epithelial lining fluid sampling device.
Front. Med. 10:1172622.
doi: 10.3389/fmed.2023.1172622

COPYRIGHT
© 2023 Gupta, Burgess, Slebos and Pouwels. This is an open-access article distributed under the terms of the Creative Commons Attribution License (CC BY). The use, distribution or reproduction in other forums is permitted, provided the original author(s) and the copyright owner(s) are credited and that the original publication in this journal is cited, in accordance with accepted academic practice. No use, distribution or reproduction is permitted which does not comply with these terms.

The development, validation, and *in vivo* testing of a high-precision bronchial epithelial lining fluid sampling device

Akash Gupta[1,2,3], Janette K. Burgess[2,3,4], Dirk-Jan Slebos[1,3] and Simon D. Pouwels[1,2,3]*

[1]Department of Pulmonology, University Medical Center Groningen, University of Groningen, Groningen, Netherlands, [2]Department of Pathology and Medical Biology, University Medical Center Groningen, University of Groningen, Groningen, Netherlands, [3]University Medical Center Groningen, Groningen Research Institute for Asthma and COPD (GRIAC), University of Groningen, Groningen, Netherlands, [4]University Medical Center Groningen, W.J. Kolff Institute for Biomedical Engineering and Materials Science-FB41, University of Groningen, Groningen, Netherlands

Introduction: Analysis of respiratory biomarkers or pharmaceutical drug concentrations in bronchial epithelial lining fluid (bELF) using a high-precision sampling method is crucial for effective clinical respiratory diagnostics and research. Here, we utilized a cellulose matrix as an absorptive probe for bELF sampling, subsequently testing the design of a device and sampling technique *in vivo*.

Methods: The absorptive matrix [Whatman® qualitative filter paper (Grade *CF*-12)] was first tested through tissue-contact experiments on porcine airway tissue. The absorption and elution capacity of the matrix, as well as the laboratory processing and analysis method, was validated with a range of Interleukin-8 (CXCL8) and C-Reactive protein (CRP) stock solutions. Subsequently, the device's design was optimized for universal in-house production and both, safe and efficient sampling. The airway sampling method was then tested in a group of 10 patients with Chronic Obstructive Pulmonary Disease (COPD). For each patient, a bELF sample was obtained using the newly developed bELF probe, as well as a reference 20 mL saline bronchial wash sample. Supernatants were assessed, using an immunoassay, for levels of the pro-inflammatory markers CXCL8, Myeloperoxidase (MPO), and CRP. The bELF samples were compared to bronchial wash.

Results: The Whatman® qualitative filter paper (Grade *CF*-12) bELF probes adhered to porcine airway tissue, softening slightly upon wetting. The material maintained architectural integrity following the removal of the probes, leaving no residual fibers on the porcine airway mucosa. The bELF probe design was optimized for bronchoscopic delivery and in-house production. On average, a fully saturated bELF probe carried 32 μL of protein-rich fluid. The mean return of CXCL8 and CRP from samples collected from a serial dilution series (1, 5, 10, 20 ng/mL) was 69% (range 48%–87%). The bELF probe detected, on average, 7 (MPO), 14 (CRP), and 59 (CXCL8) times higher equivalent inflammatory protein concentrations in the collected bELF probe samples compared to the bronchial wash.

Conclusion: The bELF probe is an effective absorptive technology for high-precision bELF sampling without dilution. With a simple in-house production procedure and bronchoscopic sampling technique, this method can be introduced in any bronchoscopic center for a consistent sampling of bELF.

KEYWORDS
airway sampling, COPD, epithelial lining fluid, bronchial wash, biomarkers

1. Introduction

Advancements in clinical respiratory research and diagnostics are leading a shift toward high-throughput multi-omics approaches for profiling heterogeneous lung pathologies (1–4). With this shift, precision in sampling techniques has become increasingly important. Bronchial epithelial lining fluid (bELF) is a critical respiratory specimen for insights into fundamental pathobiological mechanisms of respiratory disease, establishing diagnoses, evaluating prognoses, and monitoring therapy. Constituents of epithelial lining fluid include suspended respiratory and immune cells, microorganisms, toxins, allergens, inhaled medications, and cellular secretory products (e.g., cytokines and growth factors) (5, 6). The conventional methods for sampling bELF, such as bronchial wash, depend on bronchoscopic saline lavage of a target bronchial branch. The sensitivity to detect biomolecules with low abundance is limited due to the extensive dilution of bELF and the absence of a standardized correction method (7). Additionally, the spatial informativity of the identified markers in the collected specimen is limited due to a lack of delineation of the surface area sampled and indiscriminate collection of bELF from downstream sites not visible under direct vision (3, 8).

An effective alternative to saline lavage is the application of a sampling probe, developed from a synthetic or cellulose-based absorptive matrix (9, 10), onto the mucosal layer of the target bronchial wall, collecting bELF through assimilation. The sampling probe collects bELF with no dilution, and sampling is limited to the contact area of the bronchial surface with the probe. These features improve the sensitivity and spatial informativity for detecting biomolecules in bELF.

Olympus first developed the bronchoscopic microsampling (BMS) method and commercialized a synthetic hydroxylated polyester (FHPE) and a cellulose-based absorptive tip into catheter systems for bELF sampling (9). Recently, a respiratory medicine group at Imperial College, together with Hunt Developments (UK) Ltd., commercialized the bronchosorption device, a soft synthetic absorptive tip with a similar catheter system. However, there is still scope for developing additional high-precision bELF sampling device approaches.

In this study, we set out to develop and investigate a novel bELF sampling probe with a high capacity of bELF absorption and reliable output while being simple and inexpensive to produce.

2. Materials and methods

2.1. Testing of absorptive materials

Three absorptive matrices were tested, the Whatman® Grade GF/C Glass microfiber filters (WHA1822090), Whatman® Grade 3 qualitative filter paper (WHA1003185), and Whatman® Grade *CF*-12 qualitative filter paper (WHA10535097; all from Cytiva, Massachusetts, United States).

2.2. bELF probe production and preparation for testing and patient sampling

The probes were produced in a clean working environment within a laminar flow cabinet. Probes were cut from a Whatman® qualitative filter paper (Grade *CF*-12) A4 sheet, Whatman® Glass microfiber filters (Grade GF/C) circles (⌀ 23 mm), Whatman® qualitative filter paper (Grade 3) circles (⌀ 23 mm), using an ethanol-sterilized hole puncher (Ninghai Haibei Stationery Co., Zhejiang, China), producing near-identical oval probes with dimensions of 15x3mm (Figure 1). To prepare for the dilution correction after sample collection, weight measurements of the empty tube and the dry probe were obtained using an analytical/precision weighing balance (0.001 g). A sterile 0.5 mL dry tube was assigned to each cut bELF probe. This tube was first weighed to obtain the weight of the empty tube. The bELF probe was then added to its assigned pre-weighed dry tube (0.5 mL), and the tube was weighed again for the weight of the dry probe. The bELF probes were stored and transported in their assigned tube at room temperature.

2.3. Airway-tissue contact testing

All three absorptive technologies were tested with airway tissue contact and evaluated on the adhesion to the surface and material strength. Freshly harvested porcine lungs were purchased from a commercial vendor (Kroon Vlees, Groningen, Netherlands). Probes cut from Whatman® Glass microfiber filters (Grade GF/C), Whatman® qualitative filter paper (Grade 3), and Whatman® qualitative filter paper (Grade *CF*-12) were applied onto porcine airway tissue. Probes from each matrix were gently pressed against the surface of the freshly harvested wet porcine airway for 30 s. After the removal of the probe,

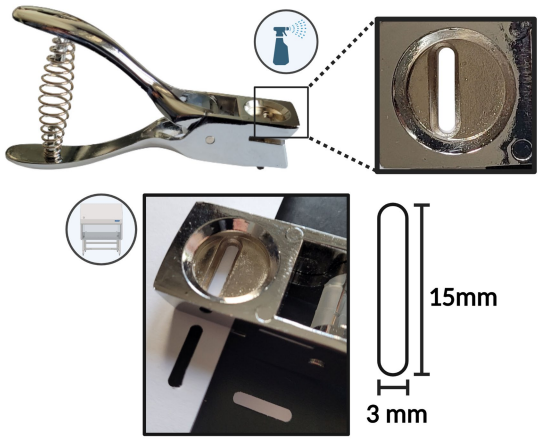

FIGURE 1
Schematic depicting the bronchial epithelial lining fluid (bELF) probe production tools and procedure.

the contact surface of porcine airway tissue was imaged with a camera and evaluated for the deposition of any residual material.

2.4. Absorption capacity and elution efficiency testing

Testing for protein analyte collection and elution capacity was only carried out on the Whatman® qualitative filter paper (Grade *CF*-12) matrix. Two serial dilution series (20, 10, 5, 1 ng/mL) were prepared from a recombinant standard of human interleukin-8 (CXCL8) and human C-reactive protein (CRP; R&D Systems, Minnesota, United States). A sample of each solution from both series was collected to measure the original analyte concentration. For the experimental setup, 40 bELF probes stored in pre-weighed assigned 0.5 mL tubes were used. Two sets of four 1 mL aliquots containing 20, 10, 5, and 1 ng/mL of CXCL8 and CRP were prepared. Five bELF probes were designated for each of the eight solutions. One at a time, a bELF probe was removed from its assigned tube using a clean stainless steel tweezer and submerged for 10 s in its designated solution. Five bELF probe samples were collected from each of the eight serial dilution solutions.

2.5. Primary bELF probe sample processing and dilution-correction method

Immediately after sampling, the wet bELF probe was directly returned to its assigned tube and reweighed for the weight of the collected fluid (Figures 2A-F). Subsequently, 300 µL of elution buffer (0.05%) Tween-20 (P1379) and 1% BSA (A2153; Sigma-Aldrich, Missouri, United States) in PBS was added to the tube containing the wet probe sample (Figure 2G). The tube was then reweighed for the weight of the elution buffer. Next, the sample tubes were shaken in a thermomixer (Eppendorf®, Hamburg, Germany) for 10 min at 600 rotations per minute (RPM) at room temperature (RT) to elute the collected proteins from the wet probe into the elution buffer (Figure 2H). The probe was then removed from the tube using clean stainless steel tweezers. To separate debris from the eluted fluid, the tube was centrifuged for 5 min at 600 g RT, and 250 µL of supernatant was aliquoted into a separate tube and stored at −80°C for further analysis (Figures 2I,J). A dilution factor was calculated for each bELF probe sample using the weight measurements of its assigned empty tube, the dry probe, the wet probe, and the weight of the added elution buffer. For the calculation, it was assumed that the density of the elution buffer and collected bELF was one and that the same concentration of solutes was removed with the wet probe following elution, as remained in the eluted sample (Figure 2K) (11).

2.6. Bronchoscopy procedure and sample collection

The bELF probe and sampling method was tested in 10 patients with severe COPD who were scheduled for a bronchoscopic lung volume reduction procedure under general anesthesia and participated in the "Biological Investigation of Explanted Endobronchial Lung Valves" Study (Bio-EXCEL study, NCT04214587; Group 1; Table 1). The bronchosorption device samples were obtained later from a separate group of 6 current or ex-smokers (Group 2). These patients participated in the "An Integrative Genomic Approach to Solve tHe Puzzle of sevERe earLy-Onset COPD" study (SHERLOCk study, NCT04263961) and were scheduled for a study-related bronchoscopic sampling under general anesthesia (Table 1). Both studies were approved by the UMC-Groningen ethics committee, and all patients provided written informed consent.

Bronchial epithelial lining fluid was collected from a target subsegmental bronchus using the bELF probes and bronchial wash technique. Bronchial epithelial lining fluid was first collected using three bELF probes. The bELF probe was grasped at the short end with biopsy forceps outside the bronchoscope and advanced through the endotracheal tube in front of the bronchoscope to the desired position and gently released on the bronchial wall for the absorption of ELF for an absorption time of 30 s for full saturation of the absorptive matrix. The primary fully-saturated probe was then grasped back with the biopsy forceps and retracted, still in front of the bronchoscope, through the endotracheal tube. Following extraction of the wet probe, the probe was directly returned to its assigned tube and placed on ice. For multiple samples from the same site, the procedure was simply repeated (Figures 2C–E).

After sampling was completed with the bELF probes, a bronchial wash was performed through injection of 20 mL of 0.9% saline solution, followed by immediate recovery. Following the collection of all samples, they were transported to the laboratory on ice (bELF probe, bronchial wash) for further processing within 2 h.

2.7. Primary bELF probe and bronchial wash processing

The collected bELF probes were processed and stored according to the primary processing method detailed above, and a dilution factor was calculated. The bronchial wash was centrifuged at 500 g at 4°C for 10 min, and supernatants were aliquoted. The collected supernatants were stored at −80°C for further analysis.

2.8. Bronchoscopy sampling and primary processing with bronchosorption device

Bronchial epithelial lining fluid was collected from patient group 2 using the bronchosorption catheter system (Mucosal Diagnostics, Midhurst, United Kingdom). One sample was collected from each patient. The sampling and primary processing method was carried out according to the protocol described by Thwaitse et al., and aliquoted supernatants were stored at −80°C for further analysis (12).

2.9. Measurement of analytes

Levels of CXCL8 (DY20), CRP (DY1707), or MPO (DY3174) were measured in duplicate using R&D systems human enzyme-linked immunosorbent assays (R&D Systems, Minnesota, United States) according to the manufacturer's instructions. Absorbance was measured using the EL808 multi-well microplate reader, and the data was analyzed using Gen5™ data analysis software (Biotek® Instruments, Vermont, United States).

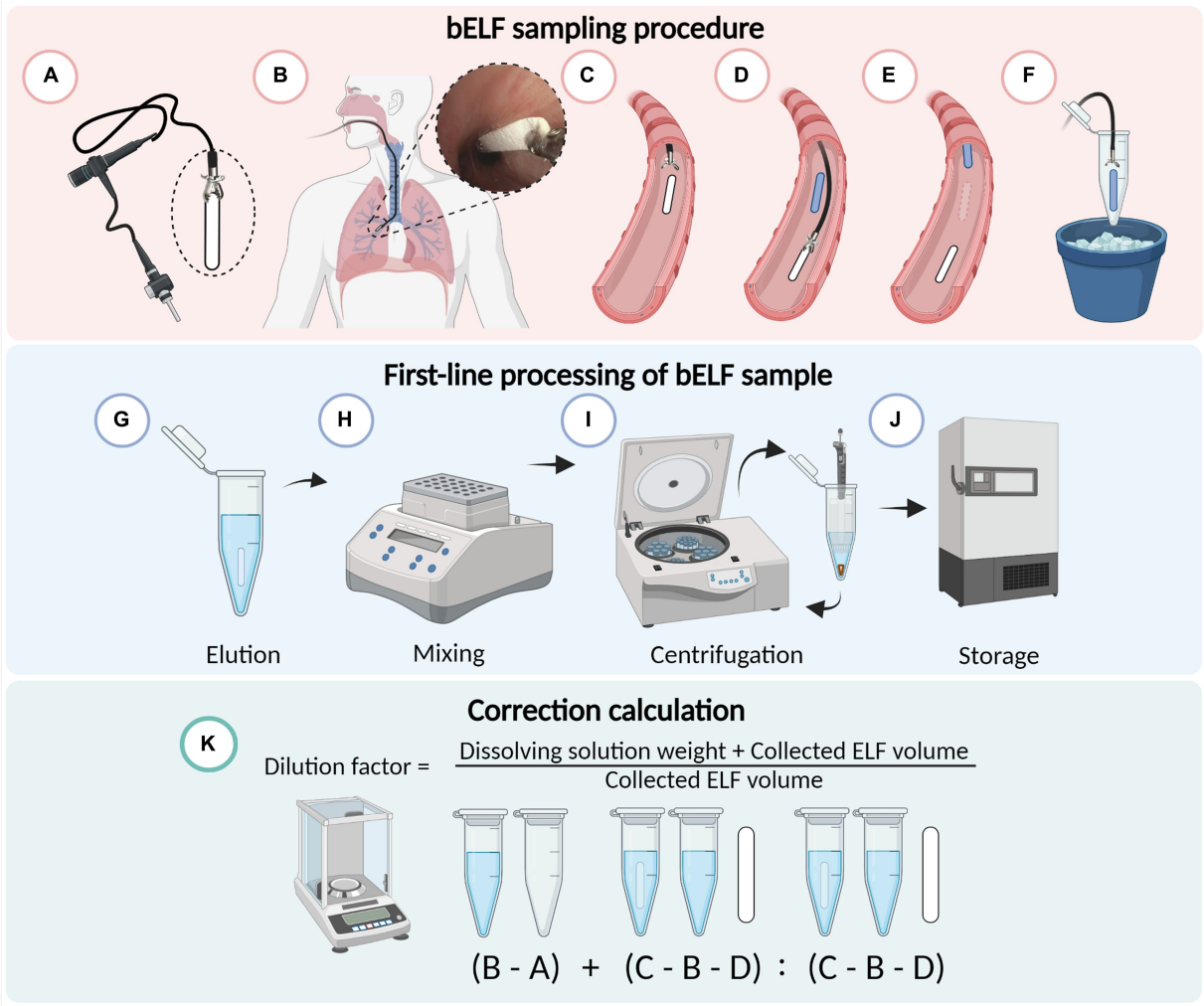

FIGURE 2
Schematic illustrating the bronchial epithelial lining fluid (bELF) probe sampling and laboratory processing protocol. Illustration of the minimally-invasive bronchoscopic bELF sampling procedure **(A–F)**, grasping the bELF probe with a biopsy forceps **(A)**, inserting the forceps and bELF probe through the bronchoscope working channel to the target site **(B)**, gently applying on the airway wall and releasing the bELF probe **(C)**, retracting the biopsy forceps to repeat the sampling protocol with a second bELF probe while waiting for absorption of the first probe **(D)**, removal of the saturated bELF probe **(E)**, storage of bELF probe after sampling on ice **(F)**. Illustration of the bELF probe laboratory processing method **(G–J)**. Submersion of bELF probe in elution buffer **(G)**, elution of collected proteins through shaking in a thermomixer **(H)**, separation of cellular debris from the eluted solution through centrifugation **(I)**, storage of supernatant at −80°C **(J)**. A calculation to correct measurements for dilution **(K)** using the weight of an empty tube **(A)**, tube with elution buffer **(B)**, tube with elution buffer and wet bELF probe **(C)**, and dry bELF probe **(D)**. Figure made in BioRender.com

TABLE 1 Patient characteristics.

	Group 1	Group 2
Age, years Median (range)	65 (55–71)	64 (54–69)
Sex, *n* (male/female)	4/6	4/2
FEV1, %predicted Mean (SD)	26.1 (5.7)	73.3 (42.3)

FEV1, Forced Expiratory Volume; SD, Standard Deviation.

2.10. Statistical analysis

Validation data and patient data were characterized descriptively. Descriptive statistics, including mean, median, and 95% confidence intervals, were used to represent the variables of bELF, bronchial wash, and bronchosorption cytokine concentrations. A Mann–Whitney *U*-test was also performed. The points of sample measurements, above or below the limit of detection, were not included in the statistical analysis but were manually plotted for visual representation. All data were assessed and statistically analyzed using GraphPad Prism version 9.5.1 (GraphPad Software, California, United States). A value of $p \leq 0.05$ was considered significant.

3. Results

3.1. Airway-tissue contact testing

The adhesive properties and material strength of Whatman® filter papers Grade GF/C, Grade 3, and Grade *CF*-12 were evaluated through contact with airway tissue. All three filter papers adhered to

the porcine airway tissue upon wetting. From observation, grade GF/C filter paper adhered the strongest and grade 3 the weakest. The Whatman® Glass microfiber filters (Grade GF/C) softened the most upon wetting, and residual fibers were consistently observed on the airway tissue following the removal of the probe, shown in Figure 3A. The Whatman® qualitative filter paper (Grade 3) remained rigid upon wetting through porcine airway contact, and the matrix remained structurally intact (Figure 3B). Whatman® filter paper Grade *CF*-12 softened slightly when wet but remained structurally intact, with no evidence of residual cellulose fibers remaining on the airway tissues (Figure 3C). Following airway tissue contact testing, the Whatman® Glass microfiber filters (Grade GF/C) and Whatman® qualitative filter paper (Grade 3) were deemed incompatible for bELF sampling and excluded from further testing.

A total of 40 probes, produced from Whatman® filter paper Grade *CF*-12, were submerged in serial dilution series of CXCL8 and CRP (20, 10, 5, and 1 ng/mL; Figure 4). After 10 s of complete submersion, the bELF probes collected, on average, 32 µL (range 24–35 µL) of the solutions. The mean return of CXCL8 and CRP using the bELF probe sampling and processing method was 69% (range 48%–87%). The mean coefficient of variation for the bELF probe sample ($n = 5$) replicates measurements was 0.13 (Range: 0.06–0.19; Figure 4).

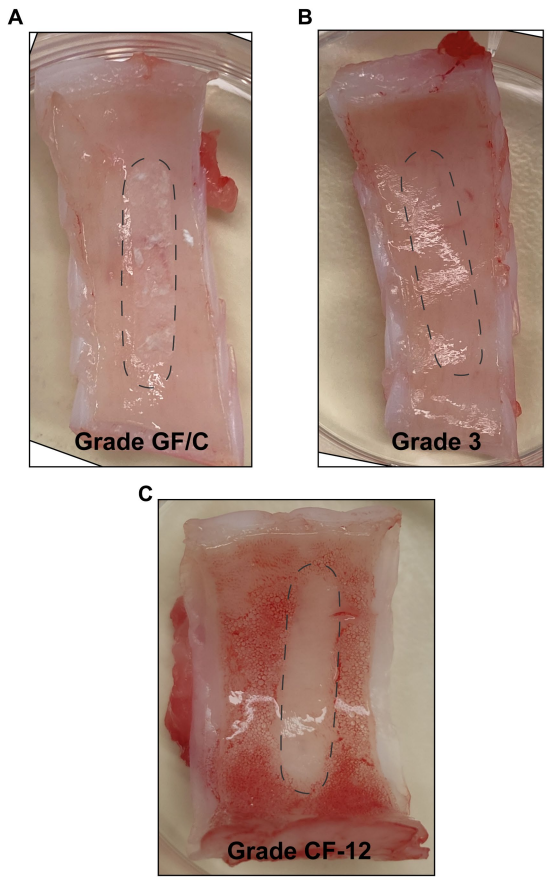

FIGURE 3
Assessment of structural integrity of absorptive matrices through porcine airway-tissue contact. Figures showing the surface of freshly harvested porcine-airway tissue after 30 s of contact with a bELF probe cut from Whatman® Glass microfiber filters (Grade GF/C) **(A)**, Whatman® qualitative filter paper (Grade 3) **(B)**, and Whatman® qualitative filter paper (Grade *CF*-12) **(C)**. The position of the probe during contact is represented with dotted lines.

3.2. Bronchoscopy procedure

The bronchoscopic sampling method was feasible for a trained respiratory physician and was well tolerated by all patients. The mean amount of bronchial epithelial lining fluid collected by the bELF probes was 21 µL (Range 4–46 µL).

3.3. Biomarker analysis

The concentrations of CXCL8, CRP, and MPO were measured in the supernatants of the bELF probe and bronchial wash samples collected from 10 COPD patients (Figures 5A–C). The measured concentrations of CXCL8 and CRP were higher in all epithelial lining fluid samples collected with the bELF probe compared to the sample collected with bronchial wash. For MPO, two patients had a higher concentration of MPO in the bronchial wash compared to the bELF probe measurement. The levels of CRP in the bELF samples of one patient from group 1 fell outside the assay dynamic range (Figure 5B). The measured protein concentration ratios of bELF: Wash were examined for each pair of samples. The median concentration of CXCL8 was 59 times higher ($p < 0.0001$) in bELF samples compared to bronchial wash and for CRP 14 times higher ($p < 0.0001$). The median concentration of MPO was 7 times higher, but there was no difference between the two groups ($p = 0.0892$; Figure 5D).

The concentrations of CXCL8, CRP, and MPO were measured in the supernatants of the bronchosorption samples collected from 6 current and ex-smokers (Figures 6A–C). The levels of CXCL8 and MPO felt outside the assay dynamic range in the bronchosorption samples of two patients from group 2, and CRP levels felt outside for one (Figure 6). The median concentration of CXCL8 measured in the bELF samples was approximately 8 times higher than in the bronchosorption samples ($p = 0.0040$). The median concentration of CRP was approximately 4 times higher ($p = 0.0040$). The median concentration of MPO was 2 times higher, but there was no difference between the two groups ($p = 0.4535$).

4. Discussion

This study explored a novel cellulose-based absorptive matrix as a candidate for a respiratory epithelial lining fluid sampling device. The Whatman qualitative filter paper grade *CF*-12 was selected as the optimal absorptive matrix for the bELF sampling probe due to its maintenance of structural integrity during sampling and absorption and elution efficiency. The bELF probe production, sampling, processing, and correction method were developed to be universally applicable in any bronchoscopy center with basic laboratory equipment. The bELF probe was well-tolerated by patients and returned a higher yield for inflammatory biomarkers in bELF compared to the current standard bronchial wash.

The practice of sampling mucosal surfaces with filter papers is well-established and has been applied previously for the collection of nasal epithelial lining fluid, rectal mucosal fluid, and dental crevicular

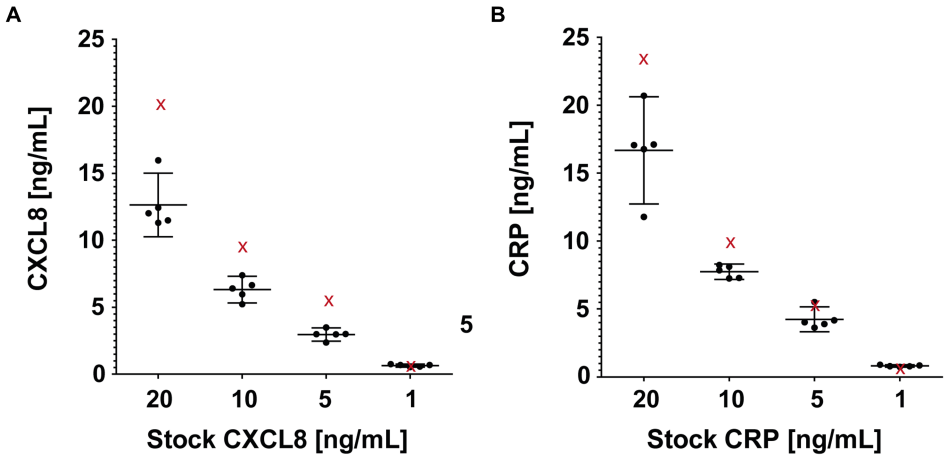

FIGURE 4
Characterization of the absorption capacity and elution efficiency of the bronchial epithelial lining fluid (bELF) probe. The graphs illustrate interleukin-8 (CXCL8) **(A)** and C-Reactive protein (CRP) **(B)** levels measured using enzyme-linked immunosorbent assays in samples collected using a bELF probe (Whatman® grade *CF*-12 filter paper) from a CXCL8 and CRP serial dilution series (20, 10, 5, 1 ng/mL). Represented for each solution in both series are the analyte measurements of a portion aliquoted for the original concentration (red cross) before bELF probe sampling and a set of five bELF probe samples, corrected for dilution (black dot). The bELF probe sample data are represented as mean (95% CI).

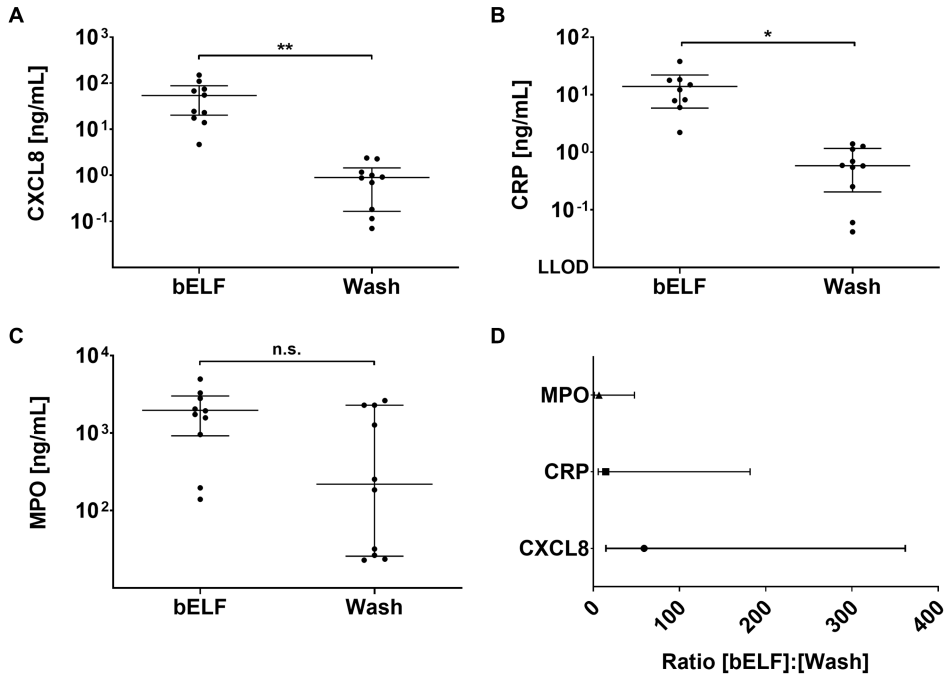

FIGURE 5
Levels of pro-inflammatory proteins obtained from the bronchial epithelial lining fluid (bELF) probe and bronchial wash of a COPD patient group *n* =10. The graphs show the levels of CXCL8 **(A)**, C-Reactive protein (CRP) **(B)**, and Myeloperoxidase (MPO) **(C)** measured using enzyme-linked immunosorbent assays in bELF and bronchial wash collected from 10 COPD patients during routine bronchoscopy. The data are represented as a median (95% confidence interval) with a Mann–Whitney *U*-test. Non-significant (n.s.), $p \leq 0.05$ (*), $p \leq 0.001$(**), Not detected (N.D.) The ratio of pro-inflammatory protein concentrations obtained from the bELF probe and by bronchial wash **(D)**. The data are represented as median (IQR). The lower limit of detection (LLOD).

fluid (13–16). Several filter paper technologies have been explored in the past. In this study, after testing three distinct filter papers, Whatman™ grade *CF*-12 filter papers were found to be the most optimal candidate sampling matrix. The *CF*-12 filter paper technology was developed and optimized for protein analysis with Whatman™ 903 cards, a bio-sample (e.g., blood, urine) collection, and transport product. These filter papers are 100% pure cotton linter with no-wet strength additives. This material composition equipped the bELF probes with high absorption capacity and rapid wicking (17). These features facilitate the collection of bELF from a target site using multiple bELF probes while maintaining a short procedure time and with each bELF probe collecting sufficient volume for protein analysis

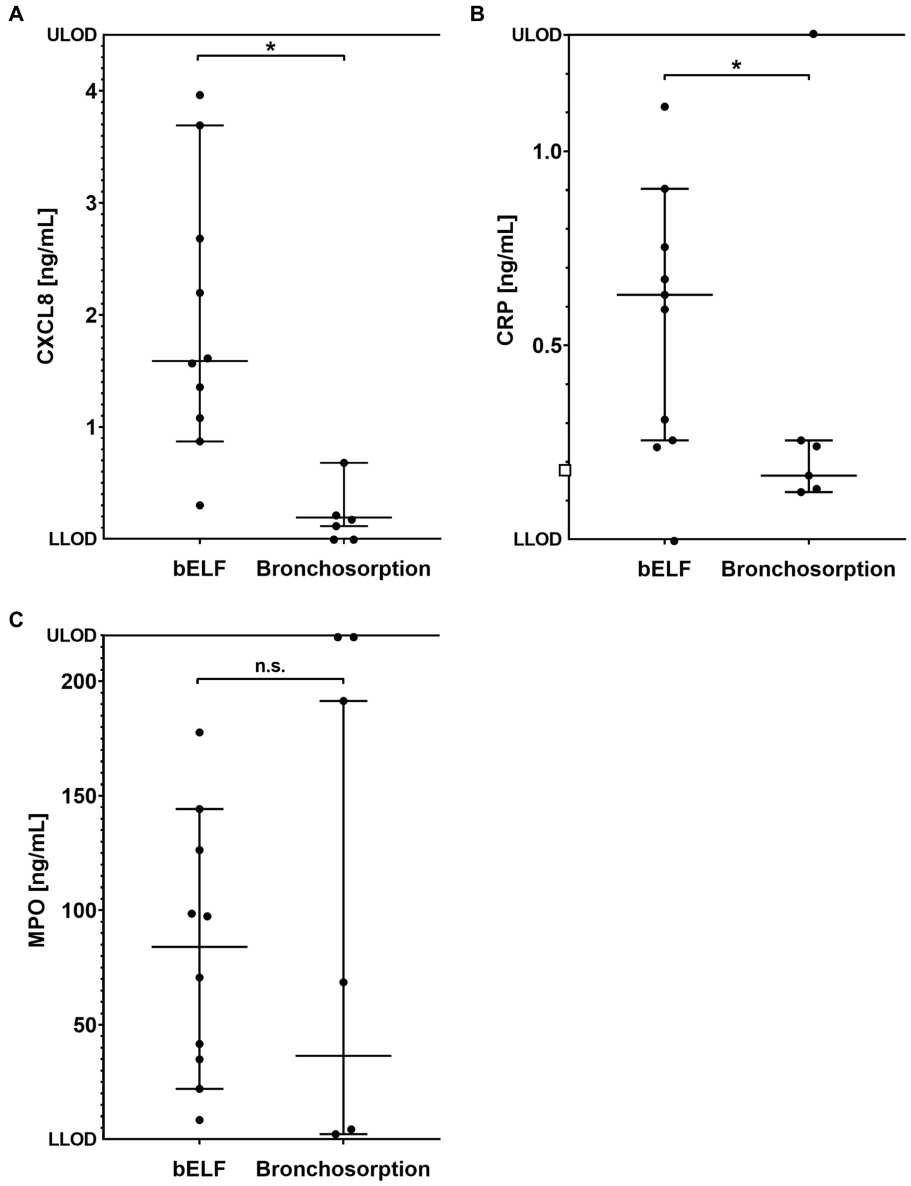

FIGURE 6
Levels of pro-inflammatory proteins obtained from bronchial epithelial lining fluid (bELF) sampled with the bronchosorption device (n = 6) and the bELF probe (n = 10). The graphs show the levels of CXCL8 **(A)**, C-Reactive protein (CRP) **(B)**, and Myeloperoxidase (MPO) **(C)** measured using enzyme-linked immunosorbent assays in samples of bELF collected with the bronchosorption device and the bELF probe from patients during routine bronchoscopy. LLOD, lower limit of detection; ULOD, Upper limit of detection.

with duplicate measurements. Additionally, the wettability and strength of the matrix determined the ease of use and safety of the sampling method. Contact bleeding is an important complication reported previously in sampling asthmatic airways with the BMS probe (18). Injury to the airway mucosa with the BMS probe could be attributed to the use of a hard absorptive matrix or the embedding of a metal wire through the filter paper tip for structural integrity and continuity with the catheter system. From our experience, with careful extrusion and gentle application of the bELF probe, contact bleeding and contamination of the sample could be prevented.

Arguably, the most important property of a sampling matrix is its efficiency in the absorption and elution of analytes. During our controlled experimental setup, the bELF probe sampling and processing method returned, on average, 69% (range 48%–87%) from the serial dilution series of CXCL8 and CRP. The low variability between the replicate measurements highlights the high precision of the measurements. To improve the returned yield, non-specific binding to the inner surfaces of the sample tubes could be reduced by using specific low-protein binding tubes or pre-coating the tubes with a protein matrix, such as albumin. Additionally, to improve protein extraction, parameters of the elution buffer, such as pH and salt content, could be adjusted. Likewise, the time, temperature, and speed of shaking with the thermomixer could be optimized. Lastly, an electrochemiluminescence-based immunoassay could have been employed to improve the sensitivity of the analysis.

The dilution factor calculation was critical to maximize the accuracy of quantified values. Under our controlled experimental setup dipping 40 bELF probes until complete saturation, a relatively small range of dilution factors (13 to 21) was calculated. Dilution

factors calculated from bELF samples collected from the 10 COPD patients ranged from 8 to 78. The small range of dilution factors during the optimization experiments is likely due to a consistent dipping method till full saturation and collection of a uniform PBS-based protein stock solution. The viscosity of bELF remains a challenge for all respiratory sampling methods and was also encountered with the bELF probe when sampling severe COPD respiratory tracts layered intermittently with highly viscous bELF. When samples collected from the same airway segment vary in collected bELF viscosity, the concentrations of suspended analytes may also vary, leading to variability in the quantification of analytes and greater variation across samples from the same segment.

The bELF probe significantly improved spatial informativity and sensitivity in measuring inflammatory biomarkers compared to bronchial wash. The bELF probe samples are obtained from the specifics section of the airway with which the device is in contact. This level of spatial informativity is most relevant for biomarker profiling in heterogenous airway disease, where lavage methods are limited in resolution. For instance, the bELF probe could be used to profile tissue reactions at the implant sites of airway devices (19). Furthermore, quantified levels of inflammatory biomarkers were, on average, multiple times higher with the bELF probe than those measured with bronchial wash. For CXCL8, for example, the bELF samples were measured to be 59 times higher than the bronchial wash obtained from the same segment. This difference introduces the potential for the quantification of low-concentration suspended analytes. The bELF samples collected with the probe in our study were not in contact with blood during the bELF sampling procedure, as sampling was performed with direct visual observation. On the other hand, the bronchial wash may have been contaminated as it was collected from sites, not under direct observation. Blood contamination can significantly alter the measurement of corresponding mediators as analytes may be several magnitudes higher in concentration in blood. Additionally, there is currently no standardized method for correcting for dilution in the bronchial wash (7).

Quantified levels of CXCL8, CRP, and MPO were, on average, higher in the bELF samples measured with the bELF probe than those measured with the commercially-available bronchosorption system. First, it is important to highlight this comparison's limitations, which include the comparison of inflammatory biomarker concentrations of two different patient groups and the falling of several measurements from the limited sample outside of the ELISA dynamic range. Nevertheless, the data obtained shows that the bELF probe is a comparable absorptive matrix for measuring inflammatory biomarkers. Furthermore, the difference in concentrations may be attributed to the lack of dilution correction described in the bronchosorption method (12). Our data shows that, correction with a dilution factor is critical in the measurement of soluble proteins, as the magnitude is similar to the dilution factor of samples obtained with bronchial wash. This calculation was first described by Yamazi et al. for the measurement of drug concentrations with the BMS probe, and can easily be adopted into any bELF sampling method (11).

Guiding the bELF probe requires a degree of bronchoscopy handling competency. Transforming the bELF probe into a single-use catheter-based system, similar to the BMS and bronchosorption devices (9, 10), would improve the ease of use. However, this improvement in handling would provide a higher cost, limiting access for many centers worldwide. With the currently described method, the cost of producing individual bELF probes is nearly negligible. Additionally, open-source capacity would be abandoned through commercialization, limiting community-led improvements. On the other hand, developing a dedicated reusable catheter system for filter paper strips might be an option for further exploration.

The bELF probe is currently an effective alternative to bronchial wash for biomarker analysis, but future studies are necessary. Optimizing elution yields will require further investigation into the impact of viscosity, the type of biomarkers, and elution buffer constituents. Exploration of new applications, such as microbiological and proteomics analysis, will require validation. Additionally, testing for batch variation and implementation in multiple centers is needed to evaluate the replicability of this method.

Overall, the bELF probe is a simple, safe, and effective bronchoscopy-guided technique to generate samples for analyzing biomarkers in bELF from the lower respiratory tract. The bELF probe equips physicians with a reliable diagnostic, prognostic, and monitoring tool for various airway diseases by improving the precision and accuracy of obtained bELF biomarker measurements.

Data availability statement

The raw data supporting the conclusions of this article will be made available by the authors, without undue reservation.

Ethics statement

The studies involving human participants were reviewed and approved by Medical Ethics Review Board University Medical Center Groningen. The patients/participants provided their written informed consent to participate in this study.

Author contributions

AG, JB, D-JS, and SP were involved in the conception and design of the study, were involved in interpretation of the generated data, and were involved in revising the manuscript. AG performed the experimental work, analyzed the data, generated figures, and was involved in drafting the manuscript. D-JS contributed by performing the bronchoscopic sampling. All authors contributed to the article and approved the submitted version.

Funding

This project was co-financed by the Ministry of Economic Affairs and Climate Policy by means of the PPP-allowance made available by the Top Sector Life Sciences and Health to stimulate public-private partnerships, with project code PPP2019-043.

Conflict of interest

The authors declare that the research was conducted in the absence of any commercial or financial relationships that could be construed as a potential conflict of interest.

Publisher's note

All claims expressed in this article are solely those of the authors and do not necessarily represent those of their affiliated organizations, or those of the publisher, the editors and the reviewers. Any product that may be evaluated in this article, or claim that may be made by its manufacturer, is not guaranteed or endorsed by the publisher.

References

1. Brandsma J, Goss VM, Yang X, Bakke PS, Caruso M, Chanez P, et al. Lipid phenotyping of lung epithelial lining fluid in healthy human volunteers. *Metabolomics*. (2018) 14:123. doi: 10.1007/s11306-018-1412-2

2. Lee AJ, Einarsson GG, Gilpin DF, Tunney MM. Multi-omics approaches: the key to improving respiratory health in people with cystic fibrosis? *Front Pharmacol*. (2020) 11:9821. doi: 10.3389/fphar.2020.569821

3. Singh S, Grover V, Christie L, Charles P, Kelleher P, Shah PL. A comparative study of Bronchoscopic microsample probe versus Bronchoalveolar lavage in patients with burns-related inhalational injury, acute lung injury and chronic stable lung disease. *Respiration*. (2015) 89:19–26. doi: 10.1159/000368367

4. Stephenson E, Reynolds G, Botting RA, Calero-Nieto FJ, Morgan MD, Tuong ZK, et al. Single-cell multi-omics analysis of the immune response in COVID-19. *Nat Med*. (2021) 27:904–16. doi: 10.1038/s41591-021-01329-2

5. Meyer KC. Bronchoalveolar lavage as a diagnostic tool. *Semin Respir Crit Care Med*. (2007) 28:546–60. doi: 10.1055/s-2007-991527

6. Rose AS, Knox KS. Bronchoalveolar lavage as a research tool. *Semin Respir Crit Care Med*. (2007) 28:561–73. doi: 10.1055/s-2007-991528

7. Marcy TW, Merrill WW, Rankin JA, Reynolds HY. Limitations of using urea to quantify epithelial lining fluid recovered by Bronchoalveolar lavage. *Am Rev Respir Dis*. (1987) 135:1276–80. doi: 10.1164/arrd.1987.135.6.1276

8. Grover V, Christie LE, Charles P, Kelleher P, Shah P, Singh S. Comparison of a bronchoscopic microsample probe with bronchoalveolar lavage to measure cytokine levels in critically ill patients. *Crit Care*. (2012) 16:P72. doi: 10.1186/cc10679

9. Ishizaka A, Watanabe M, Yamashita T, Ogawa Y, Koh H, Hasegawa N, et al. New bronchoscopic microsample probe to measure the biochemical constituents in epithelial lining fluid of patients with acute respiratory distress syndrome. *Crit Care Med*. (2001) 29:896–8. doi: 10.1097/00003246-200104000-00043

10. Leaker BR, Nicholson GC, Ali FY, Daudi N, O'Connor BJ, Barnes PJ. Bronchoabsorption; a novel bronchoscopic technique to improve biomarker sampling of the airway. *Respir Res*. (2015) 16:102. doi: 10.1186/s12931-015-0268-5

11. Yamazaki K, Ogura S, Ishizaka A, Oh-hara T, Nishimura M. Bronchoscopic microsampling method for measuring drug concentration in epithelial lining fluid. *Am J Respir Crit Care Med*. (2003) 168:1304–7. doi: 10.1164/rccm.200301-111OC

12. Thwaites RS, Jarvis HC, Singh N, Jha A, Pritchard A, Fan H, et al. Absorption of nasal and bronchial fluids: precision sampling of the human respiratory mucosa and laboratory processing of samples. *JoVE*. (2018) 131:e56413. doi: 10.3791/56413-v

13. Carty E, De Brabander M, Feakins RM, Rampton DS. Measurement of in vivo rectal mucosal cytokine and eicosanoid production in ulcerative colitis using filter paper. *Gut*. (2000) 46:487–92. doi: 10.1136/gut.46.4.487

14. Hsiao Y-C, Liu C-W, Robinette C, Knight N, Lu K, Rebuli ME. Development of LC-HRMS untargeted analysis methods for nasal epithelial lining fluid exposomics. *J Expo Sci Environ Epidemiol*. (2022) 32:847–54. doi: 10.1038/s41370-022-00448-3

15. Lamster IB, Ahlo JK. Analysis of gingival Crevicular fluid as applied to the diagnosis of Oral and systemic diseases. *Ann N Y Acad Sci*. (2007) 1098:216–29. doi: 10.1196/annals.1384.027

16. Lamster IB, Mandella RD, Gordon JM. Lactate dehydrogenase activity in gingival crevicular fluid collected with filter paper strips: analysis in subjects with non-inflamed and mildly inflamed gingiva. *J Clin Periodontol*. (1985) 12:153–61. doi: 10.1111/j.1600-051X.1985.tb01374.x

17. Liu Z, Hu J, Zhao Y, Qu Z, Xu F. Experimental and numerical studies on liquid wicking into filter papers for paper-based diagnostics. *Appl Therm Eng*. (2014) 88:280–7. doi: 10.1016/j.applthermaleng.2014.09.057

18. Cohen J, Douma WR, ten Hacken NHT, Vonk JM, Oudkerk M, Postma DS. Ciclesonide improves measures of small airway involvement in asthma. *Eur Respir J*. (2008) 31:1213–20. doi: 10.1183/09031936.00082407

19. Koster TD, Klooster K, Ten Hacken NHT, van Dijk M, Slebos D-J. Endobronchial valve therapy for severe emphysema: an overview of valve-related complications and its management. *Expert Rev Respir Med*. (2020) 14:1235–47. doi: 10.1080/17476348.2020.1813571

frontiers | Frontiers in Medicine

TYPE Brief Research Report
PUBLISHED 09 August 2023
DOI 10.3389/fmed.2023.1182368

Check for updates

OPEN ACCESS

EDITED BY
Emmanuel Twumasi Osei,
University of British Columbia, Canada

REVIEWED BY
Kauna Usman,
University of British Columbia, Canada
Aileen Hsieh,
University of British Columbia, Canada

*CORRESPONDENCE
Irene H. Heijink
✉ h.i.heijink@umcg.nl

†These authors have contributed equally to this work and share first authorship

RECEIVED 08 March 2023
ACCEPTED 28 July 2023
PUBLISHED 09 August 2023

CITATION
Wisman M, Nizamoglu M, Noordhoek JA, Timens W, Burgess JK and Heijink IH (2023) Dysregulated cross-talk between alveolar epithelial cells and stromal cells in idiopathic pulmonary fibrosis reduces epithelial regenerative capacity.
Front. Med. 10:1182368.
doi: 10.3389/fmed.2023.1182368

COPYRIGHT
© 2023 Wisman, Nizamoglu, Noordhoek, Timens, Burgess and Heijink. This is an open-access article distributed under the terms of the Creative Commons Attribution License (CC BY). The use, distribution or reproduction in other forums is permitted, provided the original author(s) and the copyright owner(s) are credited and that the original publication in this journal is cited, in accordance with accepted academic practice. No use, distribution or reproduction is permitted which does not comply with these terms.

Dysregulated cross-talk between alveolar epithelial cells and stromal cells in idiopathic pulmonary fibrosis reduces epithelial regenerative capacity

Marissa Wisman[1,2†], Mehmet Nizamoglu[1,2†], Jacobien A. Noordhoek[1,2,3], Wim Timens[1,2], Janette K. Burgess[1,2,4] and Irene H. Heijink[1,2,3*]

[1]University of Groningen, University Medical Center Groningen, Department of Pathology and Medical Biology, Groningen, Netherlands, [2]University of Groningen, University Medical Center Groningen, Groningen Research Institute for Asthma and COPD (GRIAC), Groningen, Netherlands, [3]University of Groningen, University Medical Center Groningen, Department of Pulmonology, Groningen, Netherlands, [4]University of Groningen, University Medical Center Groningen, W.J. Kolff Institute for Biomedical Engineering and Materials Science-FB41, Groningen, Netherlands

In idiopathic pulmonary fibrosis (IPF) constant epithelial micro-injury and aberrant interactions within the stromal micro-environment lead to abnormal alveolar repair and fibrosis. We hypothesized that alveolar epithelial regenerative responses in IPF are impaired due to disturbed crosstalk between epithelial cells and their stromal niche. We established organoid cultures from unfractionated suspensions and isolated EpCAM$^+$ cells from distal lung tissue of patients with and without IPF. We observed significantly more organoids being formed from unfractionated suspensions compared to isolated EpCAM$^+$ cell cultures, indicating the presence of supportive cells in the unfractionated suspensions. Importantly, lower organoid numbers were observed in unfractionated cultures from IPF lungs compared to non-IPF lungs. This difference was not found when comparing organoid formation from isolated EpCAM$^+$ cells alone between IPF and non-IPF groups, suggesting that crosstalk between the supportive population and epithelial cells is impaired in lungs from IPF patients. Additionally, organoids grown from IPF lung-derived cells were larger in size compared to those from non-IPF lungs in both unfractionated and EpCAM$^+$ cultures, indicating an intrinsic abnormality in epithelial progenitors from IPF lungs. Together, our observations suggest that dysregulated crosstalk between alveolar progenitor cells and the stromal niche affects the regenerative capacity, potentially contributing to alveolar impairment in IPF.

KEYWORDS

idiopathic pulmonary fibrosis, alveolar epithelial repair, epithelial mesenchymal cross-talk, epithelial regeneration, lung organoids

Introduction

Idiopathic Pulmonary Fibrosis (IPF) is a progressive lung disease characterized by aberrant repair responses in the alveoli, leading to fibrosis and rapid lung function decline. A high mortality rate, while having no cure available, illustrates the urgent need to understand IPF pathogenesis to identify new therapeutic strategies (1). The origin of the disease is still unknown,

but ongoing alveolar epithelial micro-injury and aberrant interactions within the stromal micro-environment are thought to induce the abnormal alveolar regeneration and tissue repair (2). The crosstalk between epithelial cells and their stromal niche composed of supportive cells and extracellular matrix (ECM) is critical for alveolar repair (3). The stromal compartment includes fibroblasts, mesenchymal stromal cells, macrophages and endothelial cells, as well as ECM (4). Emerging data suggests that stromal alterations in IPF lead to inadequate alveolar epithelial regeneration (5).

In this study we hypothesized that the crosstalk between alveolar epithelial cells and other cell types present in the fibrotic micro-environment of the lung is disrupted, resulting in reduced regenerative capacity of alveolar epithelial progenitors derived from IPF patients. We studied epithelial regenerative potential using an organoid model where alveolar epithelial progenitors were seeded into a 3-dimensional (3D) hydrogel (Matrigel) with stromal cells to recapitulate critical aspects of alveolar regeneration (6), including self-organization into 3D structures, proliferation and differentiation.

Materials and methods

Subjects

Parenchymal lung tissue was derived from 4 non-IPF donors undergoing tumor resection surgery and 4 IPF donors undergoing lung transplantation surgery (characteristics are shown in Table 1). Tissue derived from the non-IPF donors was taken from anatomically normal tissue as assessed by experienced pathologists, as far away from the tumor region as possible. This protocol was consistent with the Research Code of the University Medical Center Groningen[1] and national ethical and professional guidelines (Code of conduct—in Dutch)[2].

Tissue dissociation

Unfractionated cell suspensions were obtained from parenchymal lung tissue, from which larger airways (>2 mm) were removed if found during visual inspection, as previously described by Kruk et al. (7). Briefly, lung tissue was cut into small sections (1 cm^3) and treated overnight at 4°C with Trypsin/EDTA (0.25%; Gibco, Waltham, MA, United States), supplemented with 1% penicillin (100 U/mL)/streptomycin (100 µg/mL; P/S; Gibco), Collagenase A (2 mg/mL; Roche, Basel, Switzerland) and DNase (0.04 mg/mL, Sigma-Aldrich, Burlington, VT, United States). Subsequently, EpCAM (CD326)$^+$ epithelial progenitors were isolated from this unfractionated cell suspensions from 3 non-IPF and 4 IPF donor (tissue from 1 non-IPF donor did not yield sufficient cell numbers) by negative selection for CD31 and CD45 to deplete endothelial cells and hematopoietic cells (8), followed by a positive selection for CD326 using magnetic beads (human anti-CD31, human anti-CD45, human anti-CD326; Miltenyi Biotec, Bergisch Gladback, Germany) according to manufacturer's instructions. The cell suspensions were then resuspended in Small Airway Growth Medium (SAGM; PromoCell, Heidelberg, Germany), counted manually and kept on ice until use.

TABLE 1 Characteristics of donors included in the study.

	Non-IPF (n = 4)	IPF (n = 4)	p Value
Sex	3 M/1F	3 M/1F	>0.999[#]
Smoking history			0.0285[#]
Former	3	0	
Never	1	4	
Age [median (min–max)]	55 (36–58)	61 (27–68)	0.3143[†]
FEV1% (Pred.) [median (min–max)]	96.5 (70–111)	42.0 (17–64)	0.0286[†]

[#]Indicates p value as assessed by the Chi-square test.
[†]Indicates p value as assessed by the Mann–Whitney test. IPF: Idiopathic pulmonary fibrosis, FEV1 (pred.): Forced expiratory volume in 1 s (predicted).

Organoid culture

MRC-5 human fetal lung fibroblasts (ATCC, Manassas, VA, United States) were cultured in Ham's F12 medium (Gibco) containing 10% fetal bovine serum (FBS; Sigma-Aldrich) and 1% P/S. When confluent, cells were treated with Mitomycin C (0.01 mg/mL; Sigma-Aldrich) for 2 h to inhibit proliferation. Subsequently, cells were trypsinized and resuspended in SAGM, counted manually and kept on ice until use. To generate organoids, unfractionated lung cell suspensions (10.000 cells) or EpCAM$^+$ epithelial cells (5.000 or 10.000 cells depending on the yield from the available tissue) were mixed in a 1:1 ratio with MRC-5 cells. This cell mixture, diluted 2:1 with SAGM, was seeded in 100 µL Matrigel (8.4 mg/mL; Corning, New York, MA, United States) on top of 6.5 mm Transwell inserts (0.4 µm pore size; Corning) and cultured for 7 days in SAGM medium containing 1% FBS and 1% P/S in the basolateral compartment. At day 7, images of the organoid cultures were taken using a Nikon Eclipse Ti-E microscope (Brightfield; Nikon Instruments Europe, Amsterdam, Netherlands) and the organoid numbers and organoid size (diameter) were quantified manually throughout the full z axis of the gel using Nikon Eclipse Ti software (Nikon Instruments) to assess the size of each individual organoid. For the calculations of the diameter, for each organoid the measurement plane was set in the middle of the spheres. To calculate the organoid forming efficiency, for unfractionated cultures organoid numbers were corrected for the number of EpCAM$^+$ cells isolated from the tissue of that donor and the efficiency of EpCAM$^+$ cultures was corrected for the input of epithelial cells (5.000 or 10.000).

Immunohistochemistry

Cytospin slides were prepared from the unfractionated cell suspension directly after dissociation, for immunohistochemical

1 https://www.umcg.nl/documents/770534/2183586/umcg-research-code-2018-en.pdf/9680a460-3feb-543d-7d58-bc9d4f7277de?t=1614951313016

2 https://www.coreon.org/gedragscode-gezondheidsonderzoek

analyses. Slides were fixed with acetone (Merck, Darmstadt, Germany) and blocked with 5% bovine serum albumin (BSA; Sigma-Aldrich)/1 × Phosphate Buffered Saline (PBS; Gibco) and 0.25% Hydrogen Peroxide (Merck)/1 × PBS, both for 30 min at room temperature (RT). The slides were stained overnight with primary antibody solutions for EpCAM (1:1000; Invitrogen, Massachusetts, United States), endothelial cell marker CD31 (1:100; Immunotools, Friesoythe, Germany), stromal cell marker CD90 (1:100; Biolegend, San Diego, CA, United States), or macrophage marker CD68 (1:100; Agilent Dako, Santa Clara, CA, United States) in 1% BSA/0.1% Triton-X (Merck)/1 × PBS. The next day, slides were washed with 1 × PBS and incubated for 1 h at RT with a secondary antibody solution (1:50 Rabbit-anti Mouse (Agilent Dako) in 1% BSA/0.1% Triton-X/1 × PBS). After washing the slides with 1 × PBS, they were incubated for1 hour at RT with a tertiary antibody solution (1:50 Goat-anti Rabbit (Agilent Dako) in 1% BSA/0.1% Triton-X/1 × PBS) where after color was developed using a NovaRed Substrate kit (Vector labs, Newark, CA, United States) according to the company's manual. Hematoxylin solution (Sigma-Aldrich) was used to counterstain the nuclei. From a total cell count of at minimum 150 cells, positive stained cells were counted manually. The presence of bronchiolization in IPF lung samples was identified in hematoxylin and eosin (H&E)—stained sections from paraffin embedded lung tissue taken near the site of tissue used for the organoid cultures.

Statistics

One-way ANOVA with Šídák's multiple comparisons test was used to assess for statistical differences after testing the normality of the data with Q–Q plots and Shapiro–Wilk test. In case of non-parametric data, the Mann–Whitney test was used for comparisons of two groups and the Kruskal–Wallis test for comparison of more than two groups. $p < 0.05$ was considered statistically significant.

Results

IPF lung-derived cells form a smaller number of organoids independent of the number of epithelial cells

Both IPF and non-IPF lung-derived cell suspensions were able to form organoids by day 7 (Figure 1). We first compared organoid formation efficiency between the IPF and non-IPF groups in isolated EpCAM$^+$ cell populations. We observed that IPF and non-IPF-derived EpCAM$^+$ cells were equally well capable of forming organoids, as reflected by both the size of the organoids and the numbers (Figure 2A). Next, we assessed organoid formation efficiency of unfractionated suspensions. The number of EpCAM$^+$ cells isolated from IPF lung tissue was significantly lower compared to the non-IPF group (Supplementary Figure 1). Therefore, we normalized the unfractionated cultures for the number of EpCAM$^+$ cells isolated from these suspensions, and observed when unfractionated organoid cultures were compared between the groups, that significantly less organoids were formed from IPF lung-derived cells compared to non-IPF lung-derived cells (Figure 2A). We also observed significantly more organoids formed from the unfractionated suspensions compared to isolated EpCAM$^+$ cells (Supplementary Figure 2), suggesting the presence of a supportive cell population.

In addition to the number of organoids formed, the size distribution of the organoids was compared between the groups. Notably, IPF-derived cells formed significantly larger organoids compared to the non-IPF group, for both unfractionated (non-IPF organoids mean size 78.45 ± 8.00 µm, IPF organoids mean size 92.70 ± 26.83 µm) and EpCAM$^+$ (non-IPF organoids mean size 64.45 ± 1.47 µm, IPF organoids mean size 82.51 ± 14.42 µm) cultures (Figure 2B).

Cell fractions in unfractionated lung suspensions do not differ significantly between IPF and non-IPF groups

To investigate whether there were differences in the composition of cell types in the unfractionated suspensions between IPF and non-IPF lungs, cytospins of unfractionated suspensions were stained for several markers. As the stromal compartment of the lungs includes various major cell types, we stained for epithelial cells (EpCAM), stromal cells (CD90), macrophages (CD68) and endothelial cells (CD31), which have all been implicated in IPF pathology (3, 9). We were able to identify CD90$^+$, CD68$^+$ and CD31$^+$ cells in the unfractionated suspensions, notably without positive staining for CD31 in the suspension from non-IPF donors, but we did not observe significant differences in the percentages of each type of cell between the non-IPF and IPF groups (Figure 3).

Discussion

In this study, we compared the organoid forming efficiency of EpCAM$^+$ epithelial cell populations and unfractionated cell suspensions from parenchymal regions of IPF and non-IPF lungs. Our results suggest the presence of a supportive cell population in the unfractionated lung suspensions. Of interest, we observed reduced organoid forming efficiency in the unfractionated suspensions from IPF compared to non-IPF lungs. This difference was not present in organoids formed from isolated EpCAM$^+$ cell populations from both IPF and non-IPF lungs, suggesting that dysregulated cross-talk between epithelial cells and other supportive cell populations exists in IPF lungs. In addition to the reduced organoid forming capacity, the organoids derived from IPF lungs were significantly larger compared to non-IPF lung-derived organoids in both unfractionated suspensions and EpCAM$^+$ cell populations. To the best of our knowledge, this is the first report of lower organoid forming capacity in cells isolated from parenchymal tissue of lungs of patients with IPF.

Organoid forming efficiency as an indication of regenerative capacity has been demonstrated for several other lung diseases (10). While fewer numbers of epithelial cells were isolated from the lungs from donors with IPF, our results show reduced numbers of organoids in IPF lung-derived cultures in the unfractionated groups independent of the number of epithelial cells. This was not observed in organoid cultures established from isolated EpCAM$^+$ epithelial cells. This observation does not align with the current school of thought that suggests that the loss of regenerative capacity (specifically their ability

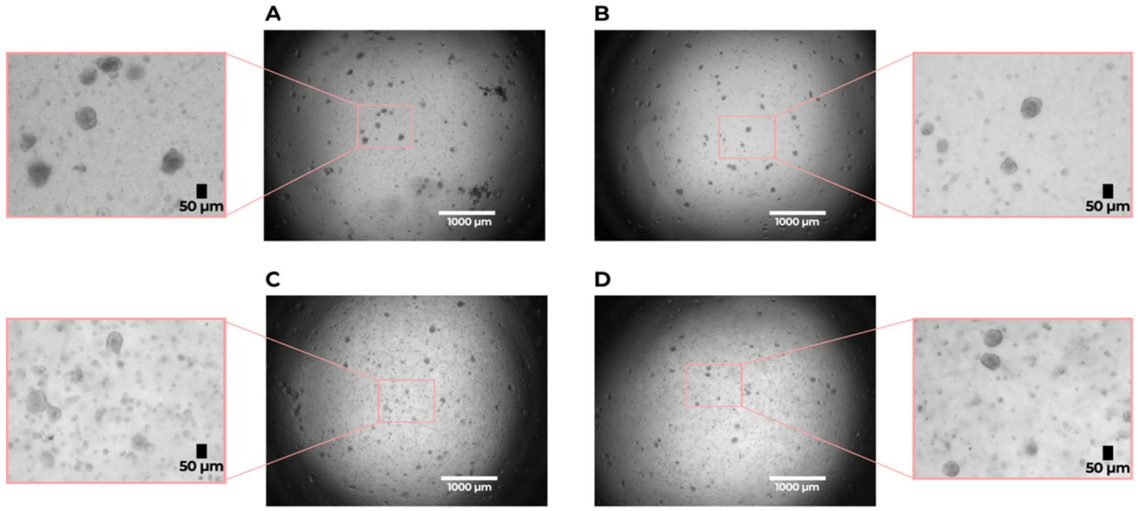

FIGURE 1
Organoid formation by lung alveolar progenitor cells isolated from idiopathic pulmonary fibrosis (IPF) and non-IPF lungs. **(A)** non-IPF (unfractionated), **(B)** non-IPF EpCAM$^+$, **(C)** IPF (unfractionated), **(D)** IPF EpCAM$^+$. Brightfield images were taken on day 7 of the organoid cultures with a 2 × magnification. Scale bar: 1,000 µm. The zoomed in sections show representative images of organoids used for analysis with a size of > 50 µm.

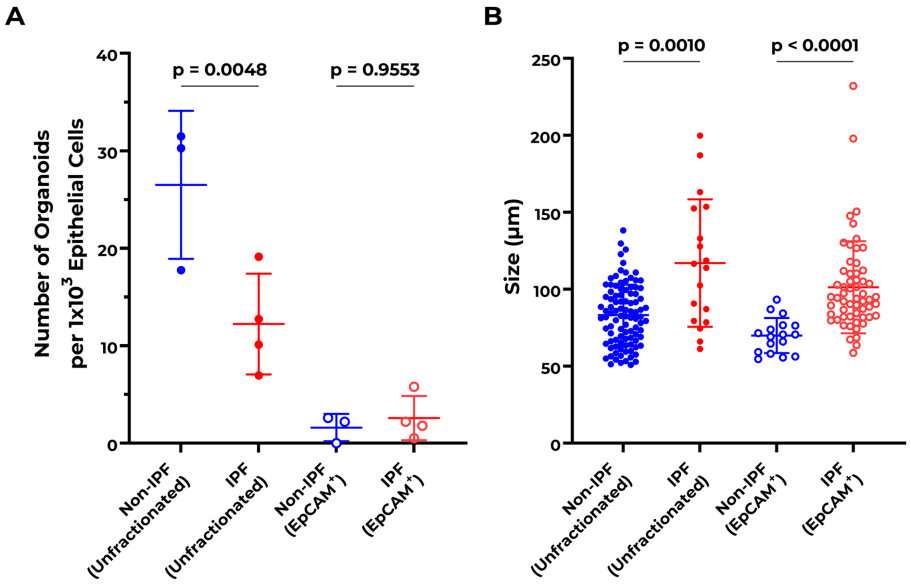

FIGURE 2
Abnormalities in organoid formation of unfractionated lung cell suspensions from IPF patients. **(A)** Quantification of organoid numbers at day 7 comparing non-IPF ($n = 3$) and IPF ($n = 4$) unfractionated and EpCAM$^+$ cultures. Organoid counts of unfractionated suspensions were normalized to the number of isolated EpCAM$^+$ cells per donor. EpCAM$^+$ cultures were corrected for epithelial cell input during the organoid assay. Means ± SD are indicated. One-way ANOVA with Šídák's multiple comparisons test was used to assess for statistical differences after testing the data for normality with Q–Q plots and Shapiro–Wilk test. **(B)** Quantification of organoid size distribution at day 7 comparing non-IPF ($n = 3$) and IPF ($n = 4$) unfractionated and EpCAM$^+$ cultures. The Kruskal–Wallis test was used to assess for statistical differences.

to self-renew) of epithelial cells stems from epithelial–mesenchymal transition or senescence in the epithelial cell population in IPF (11). The comparable organoid forming efficiency seen in isolated EpCAM$^+$ cell populations in IPF and non-IPF groups, relative to the starting number of epithelial cells, indicates that the hampered repair capacity does not result directly from defects in the epithelial progenitor cells. Rather, it may be the result of defective interactions between cells within the stromal niche. In line with previous data from our group (7), our results suggest the presence of a supportive cell population in the unfractionated lung suspensions. Although we did not observe significant differences in the proportions of supporting cell types in the isolated cell populations between IPF and non-IPF, stromal cells, endothelial cells and macrophages were found to be present in the unfractionated suspensions. Notably, we did not detect endothelial cells in the non-IPF suspensions. However, because limited tissue was available yielding low cell counts, we could not examine the individual

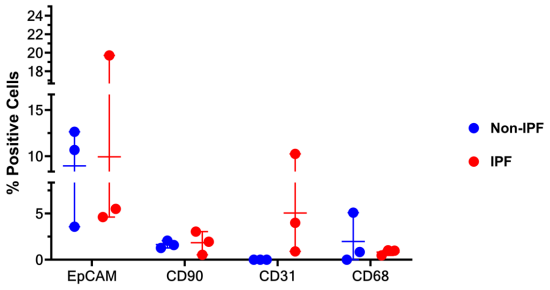

FIGURE 3
Percentage of cells stained positive for EpCAM (epithelial cells), CD31 (endothelial cells), CD90 (mesenchymal cells), and CD68 (macrophages) in unfractionated cell suspension cytospins from IPF and non-IPF lungs. Means ± SD values are shown. Statistical differences between IPF and non-IPF groups were tested using the unpaired *t*-test after verifying data normality with Q-Q plots and Shapiro–Wilk test.

function of the different cell types from the stromal niche. This will be of interest in the future. Furthermore, new multicellular culture models have been used that highlight the importance of a multicellular environment in epithelial regeneration (12–16). It may also be that the fibrotic microenvironment *in vivo* from which these cells were derived has imprinted cells towards different behavior (17); the observed differences in organoid supportive capacity might thus result from dysregulated crosstalk between the epithelial cells and stromal cells dictated by the imprinting from the IPF microenvironment. Nevertheless, we cannot exclude the possibility that an EpCAM$^+$ progenitor population, that may be selectively lost upon isolation of EpCAM$^+$ cells, contributes to the differences in organoid forming ability of unfractionated cell suspensions and EpCAM$^+$ cell populations.

The IPF organoid cultures, both unfractionated and EpCAM$^+$ populations, generated larger organoids compared to non-IPF cultures. This could indicate that epithelial progenitors from IPF lungs display intrinsic differences with respect to proliferation or other characteristics that determine organoid size. The morphology of the epithelial cells in tissue sections adjacent to the regions from where we isolated cells from in the lungs of patients with IPF was checked. Previously published reports indicate bronchiolization of the epithelium in the alveolar region in patients with IPF (18), which may be related to the intrinsic differences observed in IPF-derived epithelial cells. When the H&E-stained sections of IPF lung tissue were examined, presence of bronchiolization of the alveolar epithelium was observed in all IPF patients from whom cells were obtained (Supplementary Figure 3). This is relevant as this is indicative of an active bronchiolization process occurring in the alveolar region in the IPF tissues, which is a form of metaplasia, and the larger organoid formation, potentially due to aberrant proliferation or cell transitioning of epithelial progenitors in the IPF organoids, may be a reflection of such metaplasia (19, 20). Of note, bronchiolization does not indicate the presence of more proximal progenitors cells in distal tissue, but is a form of epithelial cell metaplasia indicating that epithelial progenitors in (or in this case coming from) an inflammatory/fibrotic environment are more prone to differentiate towards a proximal phenotype (18). On the other hand, micro-CT studies have demonstrated that small airways might be the origin of honeycomb cysts in IPF, and thus defects in small airway epithelial progenitors may contribute to alveolar abnormalities observed in IPF as well (21). Further studies on whether the IPF organoids contain more or larger cells, or more swelling due to reduced barrier function or more mucus production would be required to investigate the influence of bronchiolization in parenchymal lung tissue, its repair and its role in abnormalities in the organoid forming process.

Our study reporting initial observations on alveolar regeneration in IPF has some limitations that should be recognized. Although the EpCAM$^+$ cultures from IPF and non-IPF performed equally in their organoid forming capacity, indicating a similar progenitor population, we did not identify specific alveolar progenitor cells. Further, the lack of differences in the numbers of different cell types in the unfractionated cell populations between the groups may be a consequence of the isolation method, which has been optimized for alveolar epithelial cells and not for other cell types. In addition, the generated cell counts may be an underestimation of the total numbers of cells present in the lung tissue as several of the surface markers are known to be sensitive to cleavage by the enzymatic treatment used to isolate cells. Nevertheless, sufficient cell numbers have been isolated in order to support organoid formation effectively, as indicated by our current findings. Further characterization of isolated cell fractions and investigation of the involvement of cellular interactions during the initiation of organoid formation will be of interest in future studies, but was outside of the scope of this discovery study. Moreover, this was not feasible as receiving donor material from IPF and non-IPF patients is very rare, donors need to be matched based on their detailed characterization, and the amount of tissue available is limited.

As mentioned above, the origin of larger organoids from IPF donors requires further investigation. The finding that the organoid forming efficiency differs between IPF and non-IPF lung-derived organoid cultures from unfractionated suspensions, but not isolated epithelial progenitors, suggests that altered interactions between different cell types derived from IPF lungs are responsible for the aberrations in the initiation phase of the organoid formation. Previous research has shown that WNT-signaling influences the ability of epithelial progenitor cells to self-renew and form organoids (22). In mice it has been shown that epithelial progenitors reside in a stromal niche that provides WNT signals to maintain their stemness (23). Thus, we speculate that the WNT signaling pathway might be dysregulated in IPF-derived organoids due to the disturbed crosstalk between epithelial progenitors and stromal cell types. Further studies are needed to investigate whether alterations in the release of WNT ligands from stromal cells, endothelial cells and/or macrophages or in their interaction with epithelial cells occur in IPF.

Conclusion

Overall, our observations indicate that aberrant crosstalk between (alveolar) epithelial cells and stromal cells changes the regenerative capacity of alveolar progenitors in IPF. This dysregulation may contribute to the abnormal alveolar repair in IPF, partly leading to bronchial and squamous metaplasia. In addition, this disturbance might also contribute to an abnormal alveolar micro-environment and ECM interactions in the lung in IPF. Further investigations regarding the contribution of specific stromal cells in epithelial regeneration will be necessary to understand the influence of aberrant alveolar repair in IPF pathophysiology. It will be of interest to investigate the behavior of metaplastic bronchial epithelial cells in culture systems like

organoids to provide further insight into abnormal alveolar repair in IPF. Future research on the interaction of different epithelial cell types along with studying the communication between epithelial and stromal niche cells through excreted mediators/growth factors in multicellular 3D systems will deepen our understanding of IPF pathophysiology.

Data availability statement

The raw data supporting the conclusions of this article will be made available by the authors, without undue reservation.

Author contributions

MW, MN, JB, and IH conceived and designed the study. MW, MN, and JN performed experiments. MW and MN analyzed the data and drafted the manuscript. MW, MN, WT, JB, and IH revised and edited the manuscript. All authors contributed to the article and approved the submitted version.

Conflict of interest

The authors declare that the research was conducted in the absence of any commercial or financial relationships that could be construed as a potential conflict of interest.

Publisher's note

All claims expressed in this article are solely those of the authors and do not necessarily represent those of their affiliated organizations, or those of the publisher, the editors and the reviewers. Any product that may be evaluated in this article, or claim that may be made by its manufacturer, is not guaranteed or endorsed by the publisher.

Supplementary material

The Supplementary material for this article can be found online at: https://www.frontiersin.org/articles/10.3389/fmed.2023.1182368/full#supplementary-material

References

1. Chambers RC, Mercer PF. Mechanisms of alveolar epithelial injury, repair, and fibrosis. *Ann Am Thorac Soc*. (2015) 12:S16–20. doi: 10.1513/AnnalsATS.201410-448MG

2. Selman M, Pardo A. The leading role of epithelial cells in the pathogenesis of idiopathic pulmonary fibrosis. *Cell Signal*. (2020) 66:109482. doi: 10.1016/j.cellsig.2019.109482

3. Kong J, Wen S, Cao W, Yue P, Xu X, Zhang Y, et al. Lung organoids, useful tools for investigating epithelial repair after lung injury. *Stem Cell Res Ther*. (2021) 12:95. doi: 10.1186/s13287-021-02172-5

4. Nizamoglu M, Burgess JK. The multi-faceted extracellular matrix: unlocking its secrets for understanding the perpetuation of lung fibrosis. *Curr Tissue Microenviron Reports*. (2022) 2:53–71. doi: 10.1007/s43152-021-00031-2

5. Chapman HA. Epithelial-mesenchymal interactions in pulmonary fibrosis. *Annu Rev Physiol*. (2011) 73:413–35. doi: 10.1146/annurev-physiol-012110-142225

6. Barkauskas CE, Chung MI, Fioret B, Gao X, Katsura H, Hogan BL. Lung organoids: current uses and future promise. *Development*. (2017) 144:986–97. doi: 10.1242/dev.140103

7. Kruk DMLW, Wisman M, Noordhoek JA, Nizamoglu M, Jonker MR, De Bruin HG, et al. Paracrine regulation of alveolar epithelial damage and repair responses by human lung-resident mesenchymal stromal cells. *Cells*. (2021) 10:2860. doi: 10.3390/cells10112860

8. Barkauskas CE, Cronce MJ, Rackley CR, Bowie EJ, Keene DR, Stripp BR, et al. Type 2 alveolar cells are stem cells in adult lung. *J Clin Invest*. (2013) 123:3025–36. doi: 10.1172/JCI68782

9. Vasse GF, Nizamoglu M, Heijink IH, Schleputz M, van Rijn P, Thomas MJ, et al. Macrophage-stroma interactions in fibrosis: biochemical, biophysical, and cellular perspectives. *J Pathol*. (2021) 254:344–57. doi: 10.1002/path.5632

10. Hughes T, Dijkstra KK, Rawlins EL, Hynds RE. Open questions in human lung organoid research. *Front Pharmacol*. (2022) 13:1083017. doi: 10.3389/fphar.2022.1083017

11. Confalonieri P, Volpe MC, Jacob J, Maiocchi S, Salton F, Ruaro B, et al. Regeneration or repair? The role of alveolar epithelial cells in the pathogenesis of idiopathic pulmonary fibrosis (IPF). *Cells*. (2022) 11:2095. doi: 10.3390/cells11132095

12. Heo H-R, Hong S-H. Generation of macrophage containing alveolar organoids derived from human pluripotent stem cells for pulmonary fibrosis modeling and drug efficacy testing. *Cell Biosci*. (2021) 11:216. doi: 10.1186/s13578-021-00721-2

13. Lee JH, Bhang DH, Beede A, Huang TL, Stripp BR, Bloch KD, et al. Lung stem cell differentiation in mice directed by endothelial cells via a BMP4-NFATc1-Thrombospondin-1 axis. *Cells*. (2014) 156:440–55. doi: 10.1016/j.cell.2013.12.039

14. Lechner AJ, Driver IH, Lee J, Conroy CM, Nagle A, Locksley RM, et al. Recruited monocytes and type 2 immunity promote lung regeneration following pneumonectomy. *Cell Stem Cell*. (2017) 21:120–34.e7. doi: 10.1016/j.stem.2017.03.024

15. Jose SS, De Zuani M, Tidu F, Hortová Kohoutková M, Pazzagli L, Forte G, et al. Comparison of two human organoid models of lung and intestinal inflammation reveals toll-like receptor signalling activation and monocyte recruitment. *Clin Transl Immunol*. (2020) 9:e1131. doi: 10.1002/cti2.1131

16. Leeman KT, Pessina P, Lee J-H, Kim CF. Mesenchymal stem cells increase alveolar differentiation in lung progenitor organoid cultures. *Sci Rep*. (2019) 9:6479. doi: 10.1038/s41598-019-42819-1

17. Upagupta C, Shimbori C, Alsilmi R, Kolb M. Matrix abnormalities in pulmonary fibrosis. *Eur Respir Rev*. (2018) 27:180033. doi: 10.1183/16000617.0033-2018

18. Chakraborty A, Mastalerz M, Ansari M, Schiller HB, Staab-Weijnitz CA. Emerging roles of airway epithelial cells in idiopathic pulmonary fibrosis. *Cells*. (2022) 11:1050. doi: 10.3390/cells11061050

19. Seibold MA, Smith RW, Urbanek C, Groshong SD, Cosgrove GP, Brown KK, et al. The idiopathic pulmonary fibrosis honeycomb cyst contains a mucocilary pseudostratified epithelium. *PLoS One*. (2013) 8:e58658. doi: 10.1371/journal.pone.0058658

20. Schruf E, Schroeder V, Le HQ, Schonberger T, Raedel D, Stewart EL, et al. Recapitulating idiopathic pulmonary fibrosis related alveolar epithelial dysfunction in a human iPSC-derived air-liquid interface model. *FASEB J*. (2020) 34:7825–46. doi: 10.1096/fj.201902926R

21. Tanabe N, McDonough JE, Vasilescu DM, Ikezoe K, Verleden SE, Xu F, et al. Pathology of idiopathic pulmonary fibrosis assessed by a combination of microcomputed tomography, histology, and immunohistochemistry. *Am J Pathol*. (2020) 190:2427–35. doi: 10.1016/j.ajpath.2020.09.001

22. Wu X, van Dijk EM, Ng-Blichfeldt JP, Bos IST, Ciminieri C, Konigshoff M, et al. Mesenchymal WNT-5A/5B Signaling represses lung alveolar epithelial progenitors. *Cells*. (2019) 8:1147. doi: 10.3390/cells8101147

23. Nabhan AN, Brownfield DG, Harbury PB, Krasnow MA, Desai TJ. Single-cell Wnt signaling niches maintain stemness of alveolar type 2 cells. *Science*. (2018) 359:1118–23. doi: 10.1126/science.aam6603

frontiers | Frontiers in Medicine

TYPE Methods
PUBLISHED 12 September 2023
DOI 10.3389/fmed.2023.1214130

Check for updates

OPEN ACCESS

EDITED BY
Congshan Jiang,
Xi'an Children's Hospital, China

REVIEWED BY
John Benjamin,
Vanderbilt University Medical Center, United States
Eleni Papakonstantinou,
Aristotle University of Thessaloniki, Greece

*CORRESPONDENCE
Tillie-Louise Hackett
✉ Tillie.Hackett@hli.ubc.ca

†These authors share first authorship

RECEIVED 29 April 2023
ACCEPTED 22 August 2023
PUBLISHED 12 September 2023

CITATION
Hsieh A, Yang CX, Al-Fouadi M, Nwozor KO, Osei ET and Hackett T-L (2023) The contribution of reticular basement membrane proteins to basal airway epithelial attachment, spreading and barrier formation: implications for airway remodeling in asthma.
Front. Med. 10:1214130.
doi: 10.3389/fmed.2023.1214130

COPYRIGHT
© 2023 Hsieh, Yang, Al-Fouadi, Nwozor, Osei and Hackett. This is an open-access article distributed under the terms of the Creative Commons Attribution License (CC BY). The use, distribution or reproduction in other forums is permitted, provided the original author(s) and the copyright owner(s) are credited and that the original publication in this journal is cited, in accordance with accepted academic practice. No use, distribution or reproduction is permitted which does not comply with these terms.

The contribution of reticular basement membrane proteins to basal airway epithelial attachment, spreading and barrier formation: implications for airway remodeling in asthma

Aileen Hsieh[1,2†], Chen Xi Yang[1,2†], May Al-Fouadi[1,2], Kingsley Okechukwu Nwozor[1,2], Emmanuel Twumasi Osei[1,3] and Tillie-Louise Hackett[1,2*]

[1]Centre for Heart Lung Innovation, St. Paul's Hospital, Vancouver, BC, Canada, [2]Department of Anesthesiology, Pharmacology and Therapeutics, University of British Columbia, Vancouver, BC, Canada, [3]Department of Biology, University of British Columbia, Okanagan, BC, Canada

Rationale: In the healthy lung, the pseudostratified conducting airway epithelium is anchored to the reticular basement membrane (RBM) via hemidesmosome junction complexes formed between basal cells and the extracellular matrix (ECM). The RBM within the healthy lung is composed of the ECM proteins laminin and collagen-IV. In patients with asthma, the RBM is remodeled with collagen-I, -III and fibronectin deposition. The goal of this study was to assess the effect of RBM ECM proteins on basal airway epithelial cell attachment, spreading and barrier formation using real-time electrical cell-substrate impedance sensing (ECIS).

Methods: ECIS 8-well arrays were coated with 50 μg/mL of fibronectin, collagen-I, collagen-III, collagen-IV, or laminin and compared to bovine serum albumin (BSA) or uncoated controls. The airway epithelial cell line (1HAEo-) was seeded 40, 50, 60, and 70 k cells/well and continuously monitored over 70 h to assess cell attachment, spreading and barrier formation using high (64 k Hz) and low (500 Hz) frequency resistance and capacitance. Data were analyzed using a one-phase decay model from which half-life (time cells cover half of the electrode area) and rate-constant (cell-spreading rate/h) were determined and a generalized additive mixed effect model (GAMM) was used to assess ECM proteins over the entire experiment.

Results: High-frequency (64 kHz) capacitance measures demonstrated the half-life for 1HAEo-cells to attach was fastest when grown on fibronectin (6.5 h), followed by collagen-I (7.2 h) and collagen-III (8.1 h), compared to collagen-IV (11.3 h), then laminin (13.2 h) compared to BSA (12.4 h) and uncoated (13.9 h) controls. High-frequency (64 kHz) resistance measures demonstrated that the rate of 1HAEo- cell spreading was significantly faster on fibronectin and collagen-I compared to collagen-III, collagen-IV, laminin, BSA and the uncoated control. Low-frequency (500 Hz) resistance measures demonstrated that 1HAEo-cells formed a functional barrier fastest when grown on fibronectin and collagen-I, compared to the other ECM conditions. Lastly, the distance of 1HAEo-cells from the ECM substrates was the smallest when grown on fibronectin reflecting high cell-matrix adhesion.

Conclusion: Airway epithelial cells attach, spread and form a barrier fastest on fibronectin, and collagen-I and these reticular basement membrane ECM proteins may play a protective role in preserving the epithelial barrier during airway remodeling in asthma.

KEYWORDS

basement membrane, extracellular matrix, cell adhesion, lung, epithelial cells, asthma, barrier function

1. Introduction

The conducting airway epithelium consists of over 10 molecular and morphologically distinct cell types that have specialized functions along the airway tree that can be classified into three categories: basal, ciliated and secretory cells (1–3). The mucociliary epithelium forms a physical barrier to the inhaled environment through the formation of intercellular adhesion complexes between epithelial cells which include: tight junctions, adhesion junctions, desmosomes, intermediate and gap junctions (4–8). While all pseudostratified airway epithelial cells are in contact with the reticular basement membrane (RBM), it is the basal cells which anchor the airway epithelium to the RBM via hemidesmosomes and enable more superficial cells to attach to the RBM via desmosome complexes (8, 9). Basal cells are ubiquitous within the conducting airways, and there is a direct correlation between the number of basal cells and the thickness of the epithelium (7, 8). Thus, from the large to the small conducting airways, as the epithelial thickness decreases the number of basal cells decreases.

The conducting airway RBM readily seen by light microscopy, was initially shown to be composed of three layers by electron microscopy: the lamina lucida, the lamina densa and the reticular lamina. However follow-up studies demonstrated that the layers were likely due to sample processing and that the reticular basement membrane is actually a single layer (10–13). The key functions of the RBM ECM include providing (1) a structural scaffold to support the adhesion of the epithelium, (2) a template for tissue repair, (3) a reservoir for growth factors, and (4) a physical and permeable barrier for cells and proteins (14). Within the airway RBM, collagen-IV, is the main collagen component and is the major structural component forming a network with laminin, that is stabilized by nidogens, heparin and other proteoglycans (15). When the conducting airway epithelium is damaged by inhaled environmental exposures it can dedifferentiate, flatten and migrate rapidly beneath a plasma-derived provisional matrix containing fibronectin to enable reepithelialization; the underlying mesenchymal cells then deposit collagens-I and -III to provide structure to the ECM during repair and growth factors to stimulate epithelial proliferation and differentiation to restore epithelial barrier integrity (16–20). In the conducting airways of patients with asthma, the RBM is thickened and remodeled with increased deposition of fibronectin and collagen types I and III (15, 21, 22). Further, RBM thickening has been shown to correlate with airway hyper responsiveness and disease severity (23, 24). To date, the functional consequences of alterations in RBM ECM proteins on epithelial functions are incompletely understood.

The goal of the study was to understand the role of different RBM ECM proteins on basal airway epithelial homeostasis in the healthy lung, and provide a reference for studies focused on ECM proteins and epithelial function in lung diseases such as asthma. To understand the effect of RBM proteins (collagen-I, -III, and fibronectin) associated with repair and asthma compared to normal RBM proteins (laminin, collagen-IV) on basal airway epithelial functions, we used Electrical Cell-substrate Impedance Sensing (ECIS), which is a continuous, label free, impedance-based method that enables the study of cell attachment, spreading, and barrier function in the sub-nanometer range (25, 26).

2. Materials and methods

2.1. Cell culture

The human airway epithelial (1HAEo-) cell line, was formed from airway epithelial cells from a healthy individual which were immortalized using the origin-of-replication defective SV40 plasmid (pSVori-) (27). 1HAEo- cells have been previously shown to maintain tight junctions and desmosomes and polarity by electron microscopy (27), and were used for all experiments at passage 4–7. Cells were grown in Dulbecco's Modified Eagle Medium, with high glucose (HG-DMEM, GIBCO®, 11,965,118, NY, United States) supplemented with 10% Fetal Bovine Serum (CANADA origin, GIBCO®, 12,483,020, NY, United States) and 1% Penicillin/Streptomycin/Fungizone solution (HyClone™ 100X Antibiotic Antimycotic Solution, SV3007901, GE Healthcare Life Sciences, United States) in a humidified incubator of 5% CO_2 at 37°C.

2.2. Electric cell substrate impedance sensing

2.2.1. Array preparation

The ECIS Zθ instrument and 8 W10+ arrays (Applied Biophysics Inc., NY, United States), with total of 40 circular 250 μm diameter electrodes situated on inter-digitated fingers in each well, were coated with 50 μg/mL of: Collagen-I (Rat Tail, Natural, 354,236, Corning®, NY, United States), Collagen-III (Human, 5,021, Advanced Biomatrix, United States), Collagen-IV (Mouse, Natural, 354,233, Corning®, NY, United States), laminin (Mouse, Natural, 354,232, Corning®, NY, United States), and fibronectin (Human, Natural, 354,008, Corning®, NY, United States) or Bovine serum albumin (BSA, A9418, Sigma, WI, United States). Wells with no coating were used as negative controls

and wells with no cells or coating were used for normalization of electrodes and data. After a one-hour incubation at room temperature, arrays were washed with non-supplemented HG-DMEM twice and stabilized with an electrode-stabilizing solution, L-cysteine (200 µL/well, 10 mM L-cysteine in water, applied biophysics, NY, United States) for another hour at room temperature. After washing and adding 500 µL of supplemented media to all wells, the arrays were hooked to the ECIS platform inside the CO_2 incubator where a second stabilization step that is built into the ECIS software was performed.

2.2.2. Experimental set-up and analysis

After stabilizing the electrodes, cell-free measurements were taken of all wells for 1 h using a multiple frequency mode as recommended by the manufacturer. The run was then paused, and arrays were seeded with 40, 50, 60, or 70 k 1HAEo- cells in each well (except cell-free conditions). The experiment was then run for 72 h and cell resistance and capacitance data were measured in real-time and normalized to cell-free electrode data at time zero (n/n_0). The cell culture media was changed once after 48 h. To assess cell seeding density, in a parallel set-up, cells were cultured in coated 8-well chambered cell culture slides (MatTek, CCS-8, MA, United States) in a similar manner to ECIS arrays for microscopic observation and cell counting. While we did not test cell death directly in these experiments, we did confirm through visual inspection of the plates that the cell membranes were intact (cobble stone appearance) and there was no cell detachment or rounding.

2.3. Statistical analysis

Data from 4 to 7 independent experiments were used for the statistical analysis performed using Graph Pad Prism® 8 (GraphPad Software, Inc. CA, Unites States). One-phase decay and one-phase association exponential models were used to analyze capacitance and resistance data, respectively. *Half-life* (the time required to achieve half-maximal decline/increase in capacitance/resistance of cells growing on different matrices) and *K* (the Spreading rate constant (1/Hr) of these cells) generated from these models were further analyzed for statistical differences using one-way ANOVA followed by Tukey's multiple comparison test. A *p*-value of ≤ 0.05 was considered statistically significant. To compare the normalized capacitance and resistance of different coatings over time, a generalized additive mixed model (GAMM) was used which has a random effect component to take into consideration multiple measures per replicate in the longitudinal ECIS data. From the model:

$$Capacitance\ or\ resistance \sim coating + s(time) + s(time : coating) + (1|Replicate)$$

we were able to test (1) if there is a coating effect, that is, if the normalized capacitance/resistance (averaged throughout time) is different between each pair of the coatings, (2) if there is a time effect, that is, if the normalized resistance/capacitance changes throughout time, and (3) if there is coating-by-time interaction, that is, if the normalized resistance/capacitance of different coatings change differently between each pair of coatings over time. All the modeling was performed using R package "mgcv" in the R statistical computing environment (version 3.5.0).

3. Results

3.1. Optimal cell-seeding density for capacitance and resistance measurements

The human airway epithelial cell line 1HAEo-, was grown in monolayer to model basal airway epithelial cells. To determine the appropriate cell density to measure changes in capacitance (C) and resistance (R) over the time course of the experiment, 1HAEo- cells were seeded 40, 50, 60, 70 k cells per well. Figure 1A illustrates the dynamics of cell adhesion; Phase I cell sedimentation, Phase II cell flattening, Phase III cell spreading and lastly barrier formation in the ECIS® array and electrical current can be used to measure cell–cell and cell-matrix interactions. Transcellular current represented by high-frequency capacitance (64 k Hz), is widely considered a reliable measure of cell attachment (26, 28). Under low resistance frequencies (500 Hz), the majority of the current passes under and in between cells (paracellular current), and thus represents a good measure of barrier function, whereas high resistance frequencies (64 k Hz) are a good measure of cell spreading (26, 28).

As shown by the normalized capacitance values (64 k Hz) in Figure 1B, 1HAEo- cell attachment was fastest on collagen-I coated electrodes for all cell seeding densities compared to uncoated electrodes ($p < 0.05$) and 1HAEo- cell coverage was fastest in wells seeded with 70 k cells and lowest in wells with 40 k cells. The validity of the ECIS data was confirmed by a linear correlation between capacitance (64 k Hz) values and the physical cell counts of 1HAEo- cells in collagen-I and uncoated conditions (Figures 1B,C, $R^2 = 0.94$ and 0.90 respectively). Figure 1D shows the normalized resistance values for 64 kHz, which demonstrates 1HAEo- cell spreading was greater with higher seeding densities (60 and 70 k cells) compared to the lower seeding densities (40 and 50 k cells) on collagen-I coated compared to uncoated electrodes. Lastly, the normalized resistance values for 500 Hz showed that cell–cell contact representing the formation of barrier function was greater with higher seeding densities (60 and 70 k cells) compared to lower seeding densities (40 and 50 k cells) on collagen-I coated compared to uncoated electrodes (Figure 1E). Hence for all other experiments, we choose a 1HAEo- cell seeding density of 70,000 cells.

3.2. Airway epithelial cell attachment on different RBM extracellular matrix proteins

We utilized high frequency capacitance (64 k Hz), to quantify the behavior of basal epithelial cell attachment when exposed to different RBM ECM proteins. Figure 2A shows the normalized capacitance (64 k Hz) curves for 1HAEo- cells grown on normal RBM proteins collagen-IV and laminin, versus asthma-associated RBM proteins fibronectin, collagen-I and -III, a non-specific binding control bovine serum albumin (BSA) and uncoated electrodes. As shown in Figure 2B, the half-life to cover the electrodes was shortest when 1HAEo- cells were grown on fibronectin, collagen-I and -III compared to collagen-IV, laminin, BSA and uncoated controls. To enable assessment of cell attachment over the entire time course of the experiment we used a generalized additive mixed effect model to directly compare the capacitance (64 k Hz) curve shape and position for each ECM protein. The line graph in Figure 2C shows the

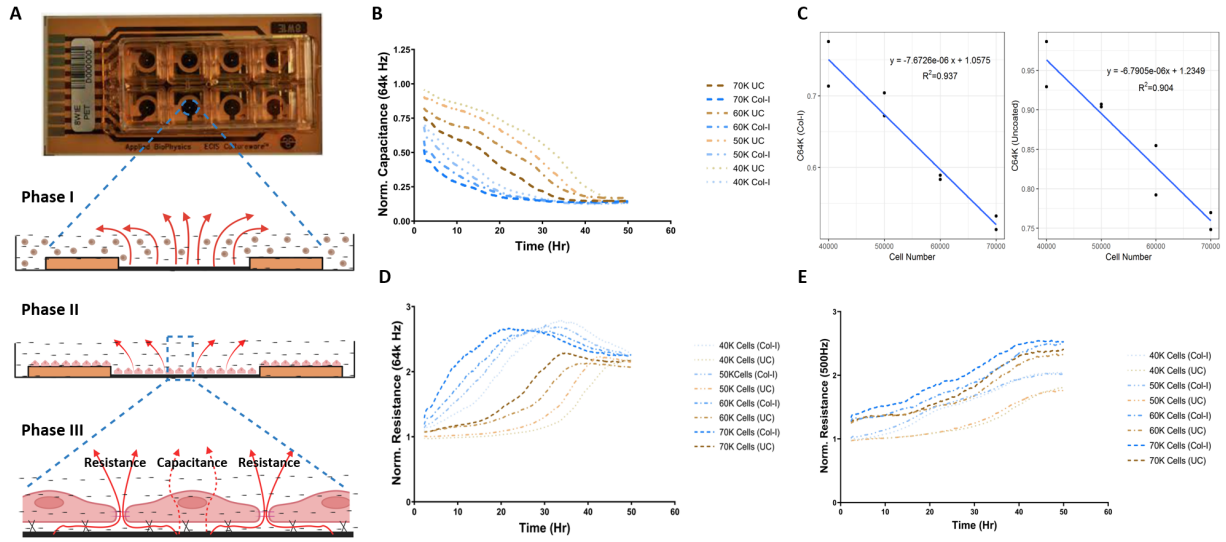

FIGURE 1
Optimal cell-seeding density for capacitance and resistance measurements. **(A)** Image of ECIS 8 well chamber and illustration demonstrating the phases of epithelial cell attachment, spreading, and barrier function measured through the assessment of capacitance and resistance values (figure created with BioRender.com). 1HAEo- cells were seeded at 40 k, 50 k, 60 k and 70 K cells per well on ECIS electrodes with or without collagen-I and assessed for **(B)** normalized Capacitance values at 64 k Hz to measure cell attachment, **(C)** linear relationship between capacitance and total cell number on collagen-I and uncoated electrodes, **(D)** normalized resistance at 64 K Hz to measure cell spreading, and **(E)** normalized resistance at 500 K Hz to measure barrier function. The data represent 2 well replicates per condition. Values were normalized to the cell-free electrode data at time 0 to account for well-to-well variance.

GAMM-modeled capacitance (64 k Hz) for each hour of the experiment. The lower the position and the steeper the slope of the curve indicates that the capacitance (64 Hz) dropped the fastest when 1HAEo- cells grew on an ECM protein. The heatmap in Figure 2D shows the adjusted-*p* value [Benjamini-Hochberg False Discovery Rate (BH-FDR)] from the GAMM model. The upper part (red triangle) of the heatmap compares how the capacitance of each pair of ECM proteins changes differently over time and the lower part (blue triangle) compares the average capacitance of each pair of ECM proteins. In this analysis, 1HAEo- cells grown on fibronectin and collagen-I had the fastest coverage, then collagen-III and -IV, and on uncoated, BSA or laminin 1HAEo- cells had the slowest coverage. These data demonstrate that 1HAEo- cells have a greater preference for fibronectin and fibrillar collagen-I, for cell attachment.

3.3. Airway epithelial cell spreading on different RBM extracellular matrix proteins

Figure 3A, shows the normalized high-frequency resistance (64 k Hz) values for 1HAEo- cells seeded on the different RBM ECM proteins which allow for the assessment of cell spreading. Figure 3B shows the rate constant (k), which is the rate (1/Hr) of cell spreading over the different ECM proteins assessed. 1HAEo- cells spread significantly faster on fibronectin compared to collagen-III, collagen-IV, BSA, laminin and uncoated controls. In addition, cells growing on collagen-I spread significantly faster than collagen-IV, BSA, laminin and the uncoated control. Lastly collagen-III spread significantly faster than laminin and the uncoated control. To assess cell spreading over the entire experiment, the line graph in Figure 3C shows the GAMM-modeled high-frequency resistance (64 k Hz) for each hour of the experiment. The lower the position and the steeper the slope of the line indicates that the resistance (64 k Hz) increased the fastest when 1HAEo- cells spread on an ECM protein. The adjusted-*p* value heatmap in Figure 3D, confirmed that 1HAEo- cells spread the fastest on fibronectin and collagen-I over the time course of the experiment compared to collagen-IV, laminin, BSA and the uncoated control.

3.4. Airway epithelial barrier formation on different RBM extracellular matrix proteins

Figure 4A, shows the normalized low-frequency resistance (500 Hz) values for 1HAEo- cells seeded on the different RBM ECM proteins which allow for the assessment of cell junction formation as a measure of barrier function. Within 50 h, 1HAEo- cells seeded on all RBM ECM proteins reached the same resistance, indicating that cells were fully-confluent and had formed a functional barrier. When we assessed the half-life of cells to form a functional barrier, fibronectin and collagen-I had the shortest half-life to form a functional barrier compared to collagen-IV, laminin, BSA and uncoated controls and collagen-III had a faster half-life than laminin (Figure 4B). The line graph in Figure 4C shows the GAMM-modeled low-frequency resistance (500 Hz) for each hour of the experiment. The adjusted-*p* value heatmap in Figure 4D, confirmed that the rate (curve shape) at which 1HAEo- cells form a barrier is the fastest for fibronectin, collagen-I and -III compared to collagen-IV, laminin, BSA and the uncoated control, but there is no difference in the epithelial barrier formed (curve position) over the time course of the experiment (Figure 4D, 0.05 FDR).

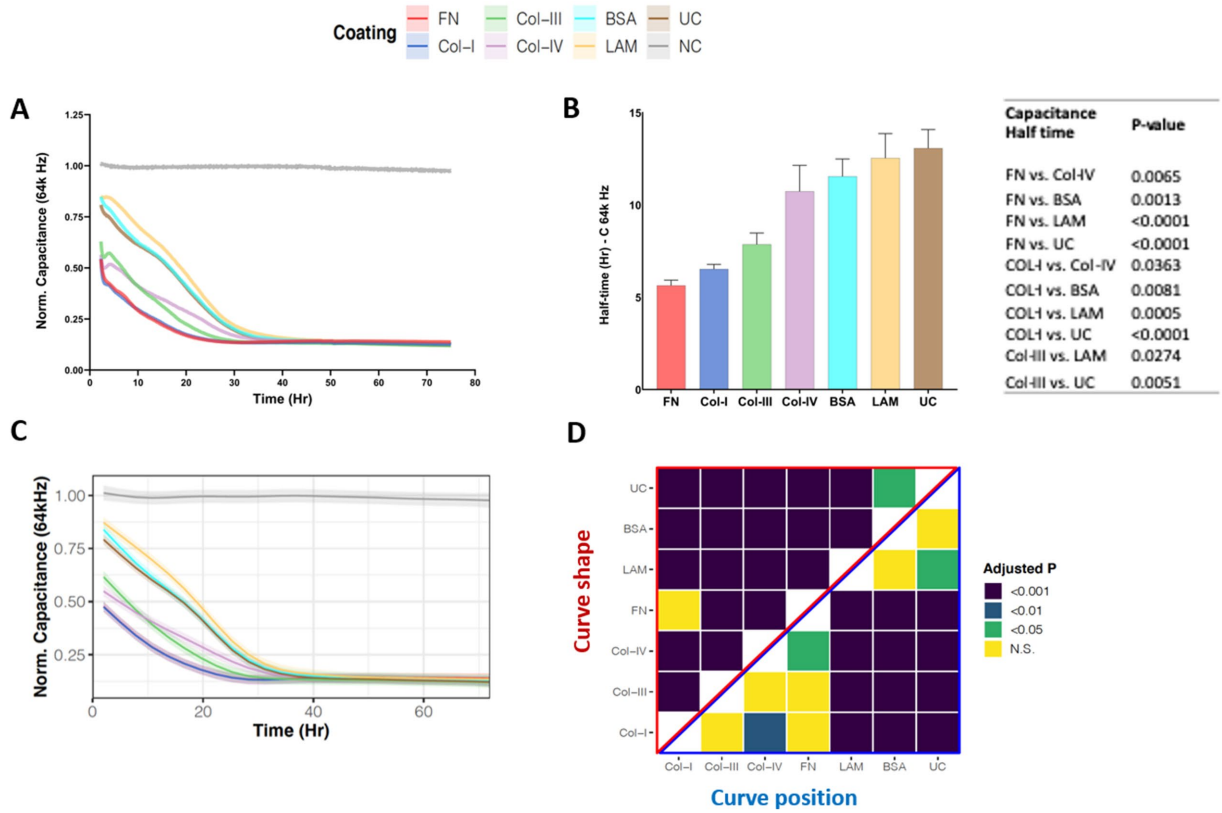

FIGURE 2
Airway epithelial cell attachment on different reticular basement membrane extracellular matrix proteins. 1HAEo- cells were seeded at 70 K cells per well on ECIS electrodes coated with 50 μL/mL of fibronectin (FN, red), collagen-I (Col-I, Blue), collagen-III (Col-III, green), collagen-IV (Col-IV, purple), bovine serum albumin (BSA, turquoise), or laminin (LAM, yellow) and compared to uncoated electrodes (UC, brown) or electrodes with no-cells (NC, grey). 1HAEo- cells were measured in real-time for 70 h and assessed for **(A)** normalized capacitance (64 k Hz) to assess cell attachment, **(B)** for each ECM protein condition the half-life (Hr, hours) of capacitance (64 k Hz) was calculated using a one-phase association model (values shown are mean ± SEM). A one-way ANOVA with Tukey's *post-hoc* test was used and the table shows all significant *p*-values. **(C)** The curves represent the GAMM-modeled normalized capacitance (64 K Hz) for each hour of the experiment and the shading denotes the 95% confidence interval. **(D)** The heatmap shows the adjusted-*p* value (Benjamini-Hochberg False Discovery Rate) from the GAMM-model. The upper part (red triangle) compares how the capacitance of each pair of ECM proteins changes differently over time (curve shape) and the lower part (blue triangle) compares the average capacitance of each pair of ECM proteins (curve position). The data represent $n = 4–7$ experiments, with 2 well replicates per condition. Values were normalized to the cell-free electrode data at time 0 to account for well-to-well variance.

3.5. The physical interaction of cells with different RBM extracellular matrix proteins

To understand the interaction of 1HAEo- cells with the RBM ECM components we calculated the distance between cells and the underlying matrix by calculating the height (h) or distance between cells and electrode surface using the following equation: $h = \rho/(\alpha^2 \times r^2)$, where ρ is the resistivity of the medium, α (cm.ohm0.5) reflects the cell-matrix adhesion, and Rb (ohm.cm2) reflects the cell–cell interactions as previously described (29–32). Figure 5A illustrates cell-matrix adhesion with the distance between the cell and the electrode labeled as "h" (height). As shown in Figure 5B the cell diameter of 1HAEo-s measured using light microscopy was not different when seeded and grown on the difference ECM conditions. As shown in Figure 5C, the distance between the electrode and the cell was smallest for fibronectin, then collagen-1 and -IV, compared to collagen-III and the uncoated control whereas, BSA and laminin coated electrodes had the greatest distance to the cell membrane (Figure 5D).

4. Discussion

In this study, we report that human basal airway epithelial cells adhere, migrate and form a functional barrier more rapidly on the ECM substrates fibronectin and fibrillar collagen-I associated with RBM repair compared to collagen-IV and laminin which are normally found within the healthy RBM. These data form the first comprehensive review of the effect of different basement membrane ECM substrates on airway epithelial attachment, spreading and barrier function using real-time, electrical cell-substrate impedance sensing within the sub-nanometer range. These data have important implications for our understanding of the RBM ECM in epithelial wound repair and how remodeling of the RBM may influence epithelial functions in many respiratory diseases such as asthma.

The most fundamental property of epithelial cells is the generation of an apical domain, which interacts with the external environment and the basolateral domain to enable contact with the reticular basement membrane and neighboring cells. With millions of individual epithelial cells within an epithelium it is essential that each

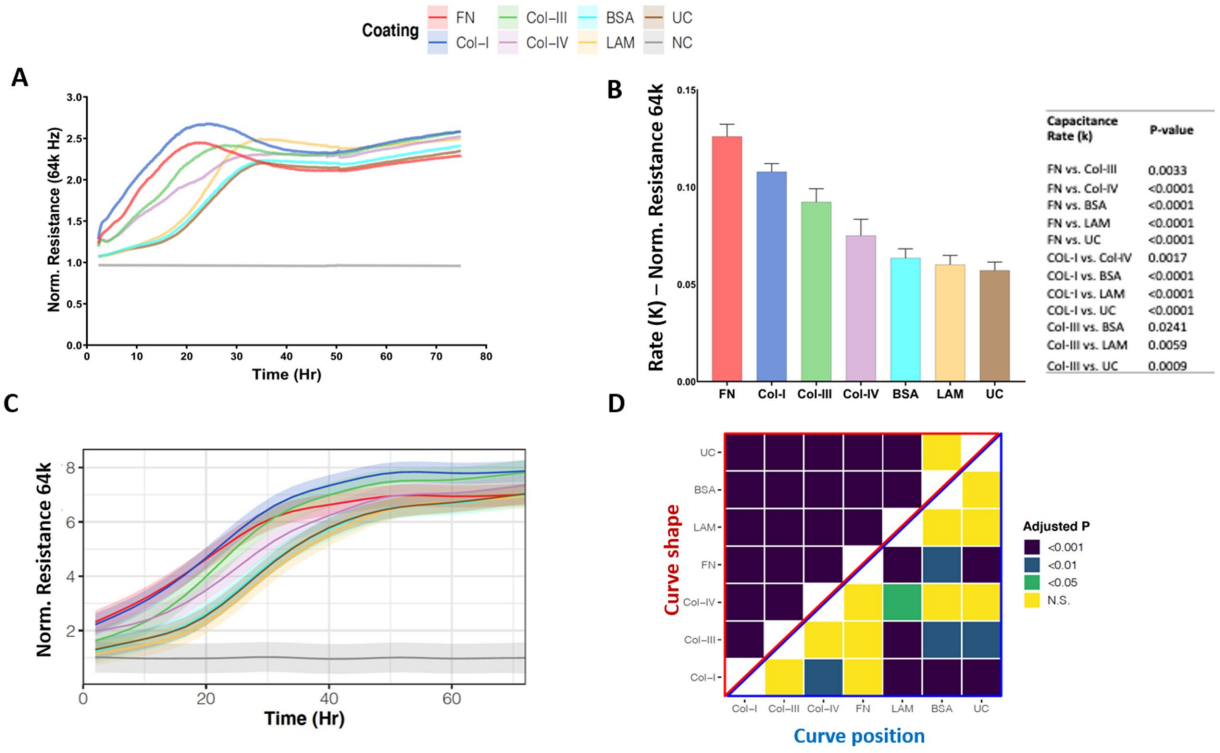

FIGURE 3
Airway epithelial cell spreading on different reticular basement membrane extracellular matrix proteins. 1HAEo- cells were seeded at 70 K cells per well on ECIS electrodes coated with 50 μL/mL of fibronectin (FN, red), collagen-I (Col-I, Blue), collagen-III (Col-III, green), collagen-IV (Col-IV, purple), bovine serum albumin (BSA, turquoise), or laminin (LAM, yellow) and compared to uncoated electrodes (UC, brown) or electrodes with no-cells (NC, gray). 1HAEo- cells were measured in real-time for 70 h and assessed for **(A)** normalized resistance (64 k Hz) to assess cell spreading, **(B)** the rate constant (K, (1/Hr)) for spreading of 1HAEo- cells grown on different matrices were generated by applying a one-phase decay exponential model of these cells (values shown are mean ± SEM). A one-way ANOVA and Tukey's *post-hoc* test was used and the table shows all significant p-values. **(C)** The curves represent the GAMM-modeled normalized resistance (64 k Hz) for each hour of the experiment using a generalized additive mixed model and the shading denotes the 95% confidence interval. **(D)** The heatmap shows the adjusted-p value (Benjamini-Hochberg False Discovery Rate) from the GAMM-model. The upper part (red triangle) compares how the resistance of each pair of ECM proteins changes differently over time (curve shape) and the lower part (blue triangle) compares the average resistance of each pair of ECM proteins (curve position). The data represent $n = 4–7$ experiments, with 2 well replicates per condition. Values were normalized to the cell free electrode data at time 0 to account for well-to-well variance.

cell makes the right decision when to divide, migrate, differentiate, or die. Tight control of these cellular decisions is guided by the mechanical cues from the RBM during epithelial homeostasis and repair. We report for the first time using ECIS that airway epithelial cells attach more rapidly to fibronectin, and fibrillar collagen-1, which are associated with repair and remodeling of the RBM in asthma compared to collagen-IV and laminin which normally form the RBM (15, 21, 22). As cell attachment is a prerequisite for cellular survival and growth (33), the effect of RBM collagen-IV and laminin on cell attachment has been studied since the early 1980s. These studies using radioimmunoassays to assess cell attachment demonstrated that in various cell lines that cell adhesion is promoted primarily by collagen-IV compared to laminin (34, 35). Indeed, our data support these findings demonstrating increased attachment with collagen-IV compared to laminin. Regarding the effect of ECM substrates associated with repair, Hamilton and colleagues, recently investigated the effect of ECM substrates on airway epithelial attachment and differentiation in bioengineered grafts. As part of their study, they investigated the attachment of primary epithelial cells to tissue culture plates coated with collagen-I, collagen-IV, fibronectin, vitronectin and laminin within 30 min using fluorescence cell counting (36). While the authors reported that collagen-IV had greater attachment than laminin in their assay, fibronectin and collagen-I also demonstrated a similar enhanced attachment compared to laminin at 30 min (36). Our data assessed cell attachment using ECIS over 72 h and show the half-life of 1HAEo- cells to cover the electrodes for fibronectin, collagen-I and -III was 6.5, 7.2, 8.1 h respectively, compared to collagen-IV (11.3 h) and laminin (13.2 h) which were within the same range of BSA coated (12.4 h) and uncoated (13.9 h) controls. Our study highlights the importance of being able to study the cells in real-time in order to assess the dynamics of cell attachment which was completed in all ECM conditions at 30 h. This is important, as the process of cell adhesion is characterized by three stages which include; phase I initial attachment of the rounded cell by sedimentation, phase II flattening and attachment of the cell, and Phase III cell spreading and stable adhesion through structural reorganization of the cell cytoskeleton (37, 38) which takes longer than 30 min (Figure 1A). In further support of our findings, several studies have previously reported that fibronectin and collagen-I enhance smooth muscle cell proliferation whereas cells grown on laminin divide more slowly, which may indicate why there is more smooth muscle mass in the airways of asthmatic patients (39, 40). The authors proposed the mechanism behind this response was through the upregulation of the nuclear proliferation marker Ki67 expression. While we did not assess

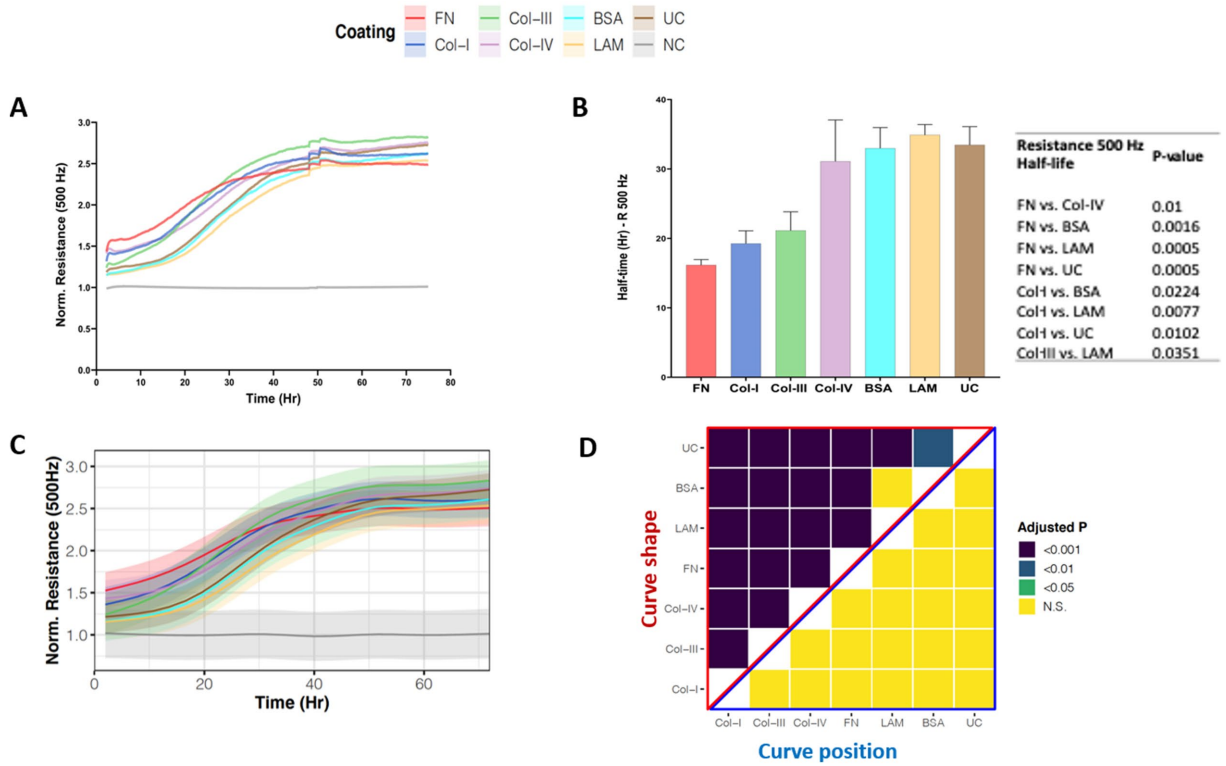

FIGURE 4
Airway epithelial barrier formation on different reticular basement membrane extracellular matrix proteins. 1HAEo- cells were seeded at 70 K cells per well on ECIS electrodes coated with 50 μL/mL of fibronectin (FN, red), collagen-I (Col-I, Blue), collagen-III (Col-III, green), collagen-IV (Col-IV, purple), bovine serum albumin (BSA, turquoise), or laminin (LAM, yellow) and compared to uncoated electrodes (UC, brown) or electrodes with no-cells (NC, gray). 1HAEo- cells were measured in real-time for 70 h and assessed for **(A)** normalized resistance (500 Hz) to assess cell spreading, **(B)** for each ECM protein condition the half-life (Hr, hours) to form a complete barrier measured by resistance (500 Hz) was calculated using a one-phase association model (values shown are mean ± SEM). A one-way ANOVA with Tukey's *post-hoc* test was used and the table shows all significant *p*-values. **(C)** The curves represent the average normalized resistance (500 Hz) for each hour of the experiment using a generalized additive mixed model and the shading denotes the 95% confidence interval. **(D)** The heatmap shows the adjusted-p value (Benjamini-Hochberg False Discovery Rate) from the GAMM-model. The upper part (red triangle) compares how the resistance of each pair of ECM proteins changes differently over time (curve shape) and the lower part (blue triangle) compares the average resistance of each pair of ECM proteins (curve position). The data represent $n = 4–7$ experiments, with 2 well replicates per condition. Values were normalized to the cell-free electrode data at time 0 to account for well-to-well variance.

Ki67 expression directly in our study, we did confirm that the measurement of capacitance (64 kHz) correlates highly with cell number and that the capacitance (64 kHz) increased the greatest when cells were seeded on fibronectin and collagen-I, indicating more cells present. Previous studies of the airway epithelium of asthmatic patients have demonstrated increased numbers of CK5+/p63+ basal cells, and SP progenitor cells and increased expression of Ki67[23,64] (41). While no mechanism for increased numbers of basal cells with Ki67 expression has been proposed in asthma, in support of this hypothesis, fibronectin has been shown to induce cell proliferation and inhibit apoptosis in the human bronchial epithelial cell lines BEAS-2B and 16-HBEs (42). Thus, future work to assess the effect of elevated fibronectin and collagen-I in the RBM of asthmatic patients on Ki67 expression in primary airway epithelial cells would determine if this association is causal or not.

With regards to airway epithelial cell spreading, we found fibronectin and fibrillar collagen-1 demonstrated an enhanced rate of 1HAEo- cell spreading compared to collagen-IV, laminin and BSA controls. In support of our findings, Mereness et al. previously reported using light microscopy that normal human bronchial epithelial cells and primary human pediatric lung epithelial cells spread more over a 3 h timepoint, when grown on either collagen-I and -VI (Collagen-6) versus Matrigel, for which the primary components are: laminin (~60%), collagen-IV (~30%), entactin (~8%) and the heparin sulfate proteoglycan perlecan (~2–3%) (43). Further, Garat and colleagues, using video microscopy experiments, demonstrated that following a scratch wound, alveolar epithelial cells spread and migrate the fastest when grown on fibronectin compared to collagen-I and collagen-IV (44). Compared to the other reported studies ECIS provides the opportunity to assess the cells during the entire experiment so that the rate of cell spreading could be assessed. In terms of the mechanisms for cell attachment and spreading, we did not assess in this study the alterations in integrin expression or localization which are known to be important in hemidesmosome formation with the cell cytoskeleton, due to limitations of imaging the ECIS arrays during the time course of the experiment. In our study, we did assess the effect of the ECM substrates on cell size and height from the electrode and found cells coated on fibronectin had the least distance from the electrode, indicating an earlier and tighter attachment representing Phase III of cell attachment with flattening and stable adhesion through structural reorganization of the cell cytoskeleton. In support of our findings, Kligys et al., have previously

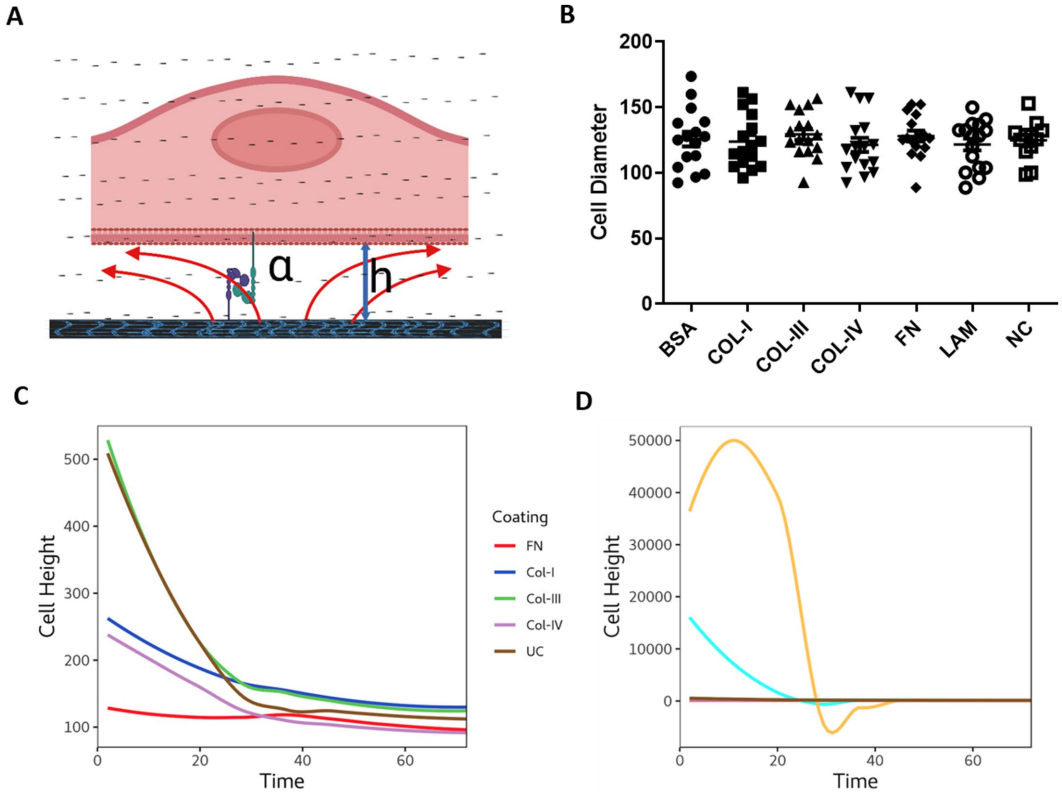

FIGURE 5
The physical interaction of cells with different reticular basement membrane extracellular matrix proteins. **(A)** Illustration demonstrating epithelial cell attachment and distance from the extracellular matrix protein (figure created with BioRender.com). 1HAEo- cells were seeded at 70 K cells per well on ECIS electrodes coated with 50 μL/mL of fibronectin (FN, red), collagen-I (Col-I, Blue), collagen-III (Col-III, green), Collagen-IV (Col-IV, purple), bovine serum albumin (BSA, turquoise), or Laminin (LAM, yellow) and compared to uncoated electrodes (UC, brown) or electrodes with no-cells (NC, gray) and measured for **(B)** Cell diameter using light microscopy (mean ± SD), **(C)** Cell height calculated from the cell radius and alpha values using: $h = \rho/(\alpha^2 \times r^2)$ Cell height at 72 h. Repeated measure ANOVA was used for statistical analysis.

shown with real-time fluorescent imaging that fibronectin impedes the migration of normal bronchial epithelial cells grown on a mixture of laminin and fibronectin and thus enhances their "stickiness" (45).

Lastly, we assessed epithelial barrier function, and found fibronectin and collagen-I significantly decreased the half-life to form a confluent epithelial barrier when measured by low frequency resistance (500 Hz), but all ECM substrates were able to form a patent barrier by 45 h. While no study has directly compared the effect of ECM substrates on epithelial barrier function using ECIS, previous studies using the SV40-transformed bronchial epithelial cell line, 16HBEs, demonstrated a similar finding that on uncoated electrodes it took 70 h to form a confluent monolayer when measured with low frequency resistance (400 Hz) when seeded with 75 K cells (26). Using single, transepithelial resistance measurements using an ohmmeter, Koval and colleagues more recently showed that rat alveolar epithelial cells grown on fibronectin compared to collagen-I and laminin had greater trans-epithelial resistance measures, however after 5 days of culture, alveolar epithelial cells grown on laminin had the greatest transepithelial resistance (46). Together these studies highlight the importance of being able to measure the functional capacity of cells over a significant time course of days or weeks to understand how cells respond to their ECM environment.

In diseases such as asthma, abnormal thickening and remodeling of the RBM develops early in the disease course and is observed in children and adults with mild to severe and fatal asthma, and persists after remission (47, 48). It has been shown that thickening of the airway RBM involves the accumulation of collagens-I, -III and fibronectin (49). While it has been previously proposed that thickening of the airway RBM may lead to defective cross-talk in the epithelial-mesenchymal trophic unit leading to increased inflammation and fibrosis, the data reported in this study highlight that increased deposition of fibronectin and fibrillar collagen-I could potentially be beneficial and enhance attachment of the damaged and defective airway epithelium observed in patients with asthma (41, 50, 51). These data demonstrate that future studies using ECIS will be helpful to determine if there are alterations in airway epithelial attachment, spreading and barrier function, and how this may be altered by the RBM ECM in diseases such as asthma.

While the use of ECIS enabled assessment of cell adhesion, spreading and barrier function in real-time within the same experiment, there are some limitations to note for the study. Firstly, the ECM substrates were studied individually, whereas within the RBM ECM proteins would exist as a matrix with a 3-dimensional organization. While it is not possible to conduct sub-nanometer range ECIS measurement in 3D cultures, further monolayer studies would be beneficially to determine if the combination of ECM proteins may have a greater influence on epithelial cell function. Secondly, in this study we used soluble human-plasma derived fibronectin. Fibronectin

is 500 kDa dimeric glycoprotein with multiple plasma soluble and cellular derived isoforms including three splice variants (52). Cellular fibronectin, has been shown to be 50 times more potent than soluble fibronectin at inducing cell migration and wound repair (53), and is most prominently produced by fibroblasts, chondrocytes, and smooth muscle upon injury to modulate re-epithelization and wound repair (52). Further studies comparing soluble and cellular fibronectin will be helpful to determine the most effective ECM substrates to support epithelial repair and regeneration in grafts. Lastly, this study utilized the human SV40 transformed 1HAEo- epithelial cell line known to maintain epithelial barrier function characteristics, and while the results are comparable to other studies using normal human bronchial epithelial cells it will be important in future studies to determine if there are differences in epithelial cells derived from patients with respiratory diseases such as asthma.

In summary, electrical cell-substrate impedance sensing provides real-time and sensitive measurement to study airway epithelial cell attachment, spreading and barrier formation on different ECM proteins. We found that the RBM ECM substrates fibronectin and collagen-I, which are present within the repairing RBM cause the fastest rate of airway epithelial cell attachment, spreading and barrier formation. As the RBM in individuals with asthma contains increased deposition of fibronectin and collagen-I, we propose that this remodeling may be a protective mechanism to maintain the epithelial integrity of the damaged airway epithelium in asthmatic patients. In future studies, electrical cell-substrate impedance sensing provides an opportunity to assess cell interactions with their ECM microenvironment to study tissue remodeling in the setting of different respiratory diseases with alterations in ECM such as asthma, chronic obstructive disease and idiopathic pulmonary fibrosis.

Data availability statement

The raw data supporting the conclusions of this article will be made available by the authors, without undue reservation.

Author contributions

MA-F, EO, and T-LH conceptualized and designed the experiment. MA-F and AH performed the experiments. MA-F, CY, AH, and T-LH analyzed and interpreted the results. MA-F, CY, KN, and T-LH prepared the figures. MA-F, EO, KN, and T-LH drafted the manuscript. T-LH reviewed the manuscript. All authors read and approved the final version.

Conflict of interest

The authors declare that the research was conducted in the absence of any commercial or financial relationships that could be construed as a potential conflict of interest.

Publisher's note

All claims expressed in this article are solely those of the authors and do not necessarily represent those of their affiliated organizations, or those of the publisher, the editors and the reviewers. Any product that may be evaluated in this article, or claim that may be made by its manufacturer, is not guaranteed or endorsed by the publisher.

References

1. Vieira Braga FA, Kar G, Berg M, Carpaij OA, Polanski K, Simon LM, et al. A cellular census of human lungs identifies novel cell states in health and in asthma. *Nat Med*. (2019) 25:1153–63. doi: 10.1038/s41591-019-0468-5

2. Hallstrand TS, Hackett TL, Altemeier WA, Matute-Bello G, Hansbro PM, Knight DA. Airway epithelial regulation of pulmonary immune homeostasis and inflammation. *Clin Immunol*. (2014) 151:1–15. doi: 10.1016/j.clim.2013.12.003

3. Deprez M, Zaragosi L-E, Truchi M, Becavin C, Ruiz García S, Arguel M-J, et al. A single-cell atlas of the human healthy airways. *Am J Respir Crit Care Med*. (2020) 202:1636–45. doi: 10.1164/rccm.201911-2199OC

4. Heijink IH, Brandenburg SM, Postma DS, van Oosterhout AJM. Cigarette smoke impairs airway epithelial barrier function and cell-cell contact recovery. *Eur Respir J*. (2012) 39:419–28. doi: 10.1183/09031936.00193810

5. Gon Y, Hashimoto S. Role of airway epithelial barrier dysfunction in pathogenesis of asthma. *Allergol Int*. (2018) 67:12–7. doi: 10.1016/j.alit.2017.08.011

6. Nawijn MC, Hackett TL, Postma DS, van Oosterhout AJM, Heijink IH. E-cadherin: gatekeeper of airway mucosa and allergic sensitization. *Trends Immunol*. (2011) 32:248–55. doi: 10.1016/j.it.2011.03.004

7. Evans MJ, Plopper CG. The role of basal cells in adhesion of columnar epithelium to airway basement membrane. *Am Rev Respir Dis*. (1988) 138:481–3. doi: 10.1164/ajrccm/138.2.481

8. Roche WR, Montefort S, Baker J, Holgate ST. Cell adhesion molecules and the bronchial epithelium. *Am Rev Respir Dis*. (1993) 148:S79–82. doi: 10.1164/ajrccm/148.6_Pt_2.S79

9. Knight DA, Holgate ST. The airway epithelium: structural and functional properties in health and disease. *Respirology*. (2003) 8:432–46. doi: 10.1046/j.1440-1843.2003.00493.x

10. Saglani S, Molyneux C, Gong H, Rogers A, Malmström K, Pelkonen A, et al. Ultrastructure of the reticular basement membrane in asthmatic adults, children and infants. *Eur Respir J*. (2006) 28:505–12. doi: 10.1183/09031936.06.00056405

11. Chan FL, Inoue S. Lamina lucida of basement membrane: an artefact. *Microsc Res Tech*. (1994) 28:48–59. doi: 10.1002/jemt.1070280106

12. Shebani E, Shahana S, Janson C, Roomans GMBHR group. Attachment of columnar airway epithelial cells in asthma. *Tissue Cell*. (2005) 37:145–52. doi: 10.1016/j.tice.2004.12.002

13. Chan FL, Inoue S, Leblond CP. The basement membranes of cryofixed or aldehyde-fixed, freeze-substituted tissues are composed of a lamina densa and do not contain a lamina lucida. *Cell Tissue Res*. (1993) 273:41–52. doi: 10.1007/BF00304610

14. Legrand C, Gilles C, Zahm JM, Polette M, Buisson AC, Kaplan H, et al. Airway epithelial cell migration dynamics. MMP-9 role in cell-extracellular matrix remodeling. *J Cell Biol*. (1999) 146:517–29. doi: 10.1083/jcb.146.2.517

15. Liesker JJW, Ten Hacken NH, Zeinstra-Smith M, Rutgers SR, Postma DS, Timens W. Reticular basement membrane in asthma and COPD: similar thickness, yet different composition. *Int J Chron Obstruct Pulmon Dis*. (2009) 4:127–35. doi: 10.2147/COPD.S4639

16. Crosby LM, Waters CM. Epithelial repair mechanisms in the lung. *Am J Physiol*. (2010) 298:L715–31. doi: 10.1152/ajplung.00361.2009

17. Zahm JM, Kaplan H, Hérard AL, Doriot F, Pierrot D, Somelette P, et al. Cell migration and proliferation during the in vitro wound repair of the respiratory epithelium. *Cell Motil Cytoskeleton*. (1997) 37:33–43. doi: 10.1002/(SICI)1097-0169(1997)37:1<33::AID-CM4>3.0.CO;2-I

18. Coraux C, Hajj R, Lesimple P, Puchelle E. Repair and regeneration of the airway epithelium. *Med Sci*. (2005) 21:1063–9. doi: 10.1051/medsci/200521121063

19. Ramos-Lewis W, LaFever KS, Page-McCaw A. A scar-like lesion is apparent in basement membrane after wound repair *in vivo*. *Matrix Biol*. (2018) 74:101–20. doi: 10.1016/j.matbio.2018.07.004

20. Erjefält JS, Erjefält I, Sundler F, Persson CG. Microcirculation-derived factors in airway epithelial repair *in vivo*. *Microvasc Res*. (1994) 48:161–78. doi: 10.1006/mvre.1994.1047

21. Roberts CR. Is asthma a fibrotic disease? *Chest*. (1995) 107:111S–7S. doi: 10.1378/chest.107.3_Supplement.111S

22. Hough KP, Curtiss ML, Blain TJ, Liu R-M, Trevor J, Deshane JS, et al. Airway remodeling in asthma. *Front Med*. (2020) 7:191. doi: 10.3389/fmed.2020.00191

23. Tsurikisawa N, Oshikata C, Tsuburai T, Saito H, Sekiya K, Tanimoto H, et al. Bronchial hyperresponsiveness to histamine correlates with airway remodelling in adults with asthma. *Respir Med*. (2010) 104:1271–7. doi: 10.1016/j.rmed.2010.03.026

24. Berend N, Salome CM, King GG. Mechanisms of airway hyperresponsiveness in asthma. *Respirology*. (2008) 13:624–31. doi: 10.1111/j.1440-1843.2008.01330.x

25. Giaever I, Keese CR. Micromotion of mammalian cells measured electrically. *Proc Natl Acad Sci U S A*. (1991) 88:7896–900. doi: 10.1073/pnas.88.17.7896

26. Heijink IH, Brandenburg SM, Noordhoek JA, Postma DS, Slebos D-J, van Oosterhout AJM. Characterisation of cell adhesion in airway epithelial cell types using electric cell-substrate impedance sensing. *Eur Respir J*. (2010) 35:894–903. doi: 10.1183/09031936.00065809

27. Cozens AL, Yezzi MJ, Yamaya M, Steiger D, Wagner JA, Garber SS, et al. A transformed human epithelial cell line that retains tight junctions post crisis. *Vitro Cell Dev Biol*. (1992) 28:735–44. doi: 10.1007/BF02631062

28. Wegener J, Keese CR, Giaever I. Electric cell-substrate impedance sensing (ECIS) as a noninvasive means to monitor the kinetics of cell spreading to artificial surfaces. *Exp Cell Res*. (2000) 259:158–66. doi: 10.1006/excr.2000.4919

29. Ebrahim AS, Ebrahim T, Kani H, Ibrahim AS, Carion TW, Berger EA. Functional optimization of electric cell-substrate impedance sensing (ECIS) using human corneal epithelial cells. *Sci Rep*. (2022) 12:14126. doi: 10.1038/s41598-022-18182-z

30. Szulcek R, Bogaard HJ, van Nieuw Amerongen GP. Electric cell-substrate impedance sensing for the quantification of endothelial proliferation, barrier function, and motility. *J Vis Exp*. (2014):51300. doi: 10.3791/51300

31. Robilliard LD, Kho DT, Johnson RH, Anchan A, O'Carroll SJ, Graham ES. The importance of multifrequency impedance sensing of endothelial barrier formation using ECIS Technology for the Generation of a strong and durable Paracellular barrier. *Biosensors*. (2018) 8:64. doi: 10.3390/bios8030064

32. *What is ECIS? - Applied biophysics*. (2023). Available at: https://www.biophysics.com/whatIsECIS.php.

33. Lundgren JD, Shelhamer JH, Kaliner MA. The role of eicosanoids in respiratory mucus hypersecretion. *Ann Allergy*. (1985) 55:11.

34. Herbst TJ, McCarthy JB, Tsilibary EC, Furcht LT. Differential effects of laminin, intact type IV collagen, and specific domains of type IV collagen on endothelial cell adhesion and migration. *J Cell Biol*. (1988) 106:1365–73. doi: 10.1083/jcb.106.4.1365

35. Aumailley M, Timpl R. Attachment of cells to basement membrane collagen type IV. *J Cell Biol*. (1986) 103:1569–75. doi: 10.1083/jcb.103.4.1569

36. Hamilton NJI, Lee DDH, Gowers KHC, Butler CR, Maughan EF, Jevans B, et al. Bioengineered airway epithelial grafts with mucociliary function based on collagen IV- and laminin-containing extracellular matrix scaffolds. *Eur Respir J*. (2020) 55:1901200. doi: 10.1183/13993003.01200-2019

37. LeBaron RG, Athanasiou KA. Ex vivo synthesis of articular cartilage. *Biomaterials*. (2000) 21:2575–87. doi: 10.1016/S0142-9612(00)00125-3

38. Hong S, Ergezen E, Lec R, Barbee KA. Real-time analysis of cell-surface adhesive interactions using thickness shear mode resonator. *Biomaterials*. (2006) 27:5813–20. doi: 10.1016/j.biomaterials.2006.07.031

39. Hirst SJ, Twort CH, Lee TH. Differential effects of extracellular matrix proteins on human airway smooth muscle cell proliferation and phenotype. *Am J Respir Cell Mol Biol*. (2000) 23:335–44. doi: 10.1165/ajrcmb.23.3.3990

40. Freyer AM, Johnson SR, Hall IP. Effects of growth factors and extracellular matrix on survival of human airway smooth muscle cells. *Am J Respir Cell Mol Biol*. (2001) 25:569–76. doi: 10.1165/ajrcmb.25.5.4605

41. Hackett T-L, Singhera GK, Shaheen F, Hayden P, Jackson GR, Hegele RG, et al. Intrinsic phenotypic differences of asthmatic epithelium and its inflammatory responses to respiratory syncytial virus and air pollution. *Am J Respir Cell Mol Biol*. (2011) 45:1090–100. doi: 10.1165/rcmb.2011-0031OC

42. Han SW, Roman J. Fibronectin induces cell proliferation and inhibits apoptosis in human bronchial epithelial cells: pro-oncogenic effects mediated by PI3-kinase and NF-kappa B. *Oncogene*. (2006) 25:4341–9. doi: 10.1038/sj.onc.1209460

43. Mereness JA, Bhattacharya S, Wang Q, Ren Y, Pryhuber GS, Mariani TJ. Type VI collagen promotes lung epithelial cell spreading and wound-closure. *PLoS One*. (2018) 13:e0209095. doi: 10.1371/journal.pone.0209095

44. Garat C, Kheradmand F, Albertine KH, Folkesson HG, Matthay MA. Soluble and insoluble fibronectin increases alveolar epithelial wound healing *in vitro*. *Am J Phys*. (1996) 271:L844–53. doi: 10.1152/ajplung.1996.271.5.L844

45. Kligys K, Wu Y, Hamill KJ, Lewandowski KT, Hopkinson SB, Budinger GRS, et al. Laminin-332 and α3β1 integrin-supported migration of bronchial epithelial cells is modulated by fibronectin. *Am J Respir Cell Mol Biol*. (2013) 49:731–40. doi: 10.1165/rcmb.2012-0509OC

46. Koval M, Ward C, Findley MK, Roser-Page S, Helms MN, Roman J. Extracellular matrix influences alveolar epithelial Claudin expression and barrier function. *Am J Respir Cell Mol Biol*. (2010) 42:172–80. doi: 10.1165/rcmb.2008-0270OC

47. Broekema M, Timens W, Vonk JM, Volbeda F, Lodewijk ME, Hylkema MN, et al. Persisting remodeling and less airway wall eosinophil activation in complete remission of asthma. *Am J Respir Crit Care Med*. (2011) 183:310–6. doi: 10.1164/rccm.201003-0494OC

48. HL HUBER, KK KOESSLER. The pathology of bronchial asthma. *Arch Intern Med*. (1922) 30:689–760. doi: 10.1001/archinte.1922.00110120002001

49. Roche WR, Beasley R, Williams JH, Holgate ST. Subepithelial fibrosis in the bronchi of asthmatics. *Lancet*. (1989) 1:520–4.

50. Xiao C, Puddicombe SM, Field S, Haywood J, Broughton-Head V, Puxeddu I, et al. Defective epithelial barrier function in asthma. *J Allergy Clin Immunol*. (2011) 128:549–556.e12. doi: 10.1016/j.jaci.2011.05.038

51. Hackett T-L, Warner SM, Stefanowicz D, Shaheen F, Pechkovsky DV, Murray LA, et al. Induction of epithelial-mesenchymal transition in primary airway epithelial cells from patients with asthma by transforming growth factor-beta1. *Am J Respir Crit Care Med*. (2009) 180:122–33. doi: 10.1164/rccm.200811-1730OC

52. To WSMidwood KS. Plasma and cellular fibronectin: distinct and independent functions during tissue repair. *Fibrogenesis Tissue Repair*. (2011) 4:21. doi: 10.1186/1755-1536-4-21

53. Yamada KM, Kennedy DW. Fibroblast cellular and plasma fibronectins are similar but not identical. *J Cell Biol*. (1979) 80:492–8. doi: 10.1083/jcb.80.2.492

Frontiers in Medicine

Translating medical research and innovation into improved patient care

A multidisciplinary journal which advances our medical knowledge. It supports the translation of scientific advances into new therapies and diagnostic tools that will improve patient care.

Discover the latest Research Topics

See more →

Frontiers

Avenue du Tribunal-Fédéral 34
1005 Lausanne, Switzerland
frontiersin.org

Contact us

+41 (0)21 510 17 00
frontiersin.org/about/contact